

Thèse en cotutelle internationale
entre l'Université Lille 1 et l'Université de Siegen (Allemagne)
présentée en vue de l'obtention du grade de

Docteur de l'Université de Lille 1 Science et Technologies
Discipline Chimie - Spécialité Molécules et Matière condensée

Soutenue publiquement par

Jacob OLCHOWKA

à l'Université de Lille1, le 29 octobre 2015

Structural versus optical properties in selected Bismuth based oxo-salts and compounds

Jury:

Dr. Manuel Gaudon	Maître de Conférences Université de Bordeaux	Rapporteur
Prof. Carsten Engelhard	Professeur des Universités Université de Siegen	Rapporteur
Dr. Florent Boucher	Directeur de Recherches - CNRS Université de Nantes	Examineur
Dr. Olivier Mentré	Directeur de Recherches - CNRS Université de Lille 1	Directeur de thèse
Prof. Claudia Wickleder	Professeur des Universités Université de Siegen	Co-Directeur de thèse
Dr. Marie Colmont	Maître de Conférences Ecole de Chimie de Lille	Invité
Dr. Houria Kabbour	Chargé de Recherche – CNRS Université de Lille 1	Invité

Thèse préparée au sein du lab. UCCS (UMR CNRS 8181) et du lab. Anorganische Chemie II
Ecole doctorale Science de la Matière, du Rayonnement et de l'Environnement

This thesis is a “cotutelle” between the University of Siegen and the University of Lille1.
The thesis work was performed between the 01/10/2012 and the 30/09/2015 under the supervision of Prof. Dr. Claudia Wickleder, Prof. Dr. Olivier Mentré and Dr. Marie Colmont

The most important is not to be optimist or pessimist but to be determined

Acknowledgment

First of all, I would like to thank my thesis directors Dr. Olivier Mentré and Prof. Dr. Claudia Wickleder for giving me the opportunity to carry out my PhD thesis in their research group and also for all of the much appreciated help and advice to guide my work to a successful completion.

I am very thankful to my co-supervisor Dr. Marie Colmont who helped me especially with the experimental part, crystal structures and all the structural aspect during these three years.

I am sincerely indebted to Dr. Houria Kabbour who learn how to performed DFT calculations and to Dr. Matthias Adlung who helped me with decay time measurements.

Then, I would like to thank all the members of my PhD committee Dr. Florent Boucher, Dr. Manuel Gaudon and Prof. Carsten Engelhard who accepted to review my work. Their advices will be very helpful.

I would also like to acknowledge Dr. Thierry Loiseau and Dr. Christophe Volkringer who made me feel the passion for research during my Master thesis.

A PhD work cannot be performed alone and I am obliged to many of my coworkers including Pascal and Fred for the single crystal diffraction, Laurence for the XRD and thermogravimetry measurements, Marielle and Nora for the microscopy, Philippe, Maxence, Jean-Luc for the reactants and Jérémy, Edouard and Romain for informatics and the technical part.

Finally, I would like to thank warmly all my colleagues and my friends from France and Germany with who I spent fabulous three years. We had a lot of fun together during breaks between long hours of work. Some of them are already doctor, Clément (Pub colleague), Guillaume (the hacker), Florent (J-L Mélanchon), Almaz (1st Kirghiz doctor), Fanny (Miss Bourgogne), Sandra (la “cagole”), Rénaud (the “casse-couille”), Giuliano (the fighter), Huayna, Nathalie, Vadim, Vincent, Anne-Lise, Ana, Esperanza, Minfeng And some of them will become doctor soon, Nacho (“Cousous-Duvel”), Konrad (“Bismuth coworker”), Tanguy (just one bier), Sascha (Schweinsteiger), Marine (la Ch’ti), Markus (Sheldon), Margot (princess), Kristina (russian girl), Florence (minion and banana), Raynald (le “stagiaire”), Nico (le Marseillais), Jenny, Manon, Julie, Yann, Aline, Aïda, Bowbag, Blaise, Willis, Xavier, Gaël, Valdu, Denis, Thibault, Nils

Abstract

The development of luminescent materials for future LEDs is currently a hot-topic with respect to energy saving materials and it is an interesting challenge for many researchers to find the luminescent materials of tomorrow. Most of the current commercial LEDs are based on lanthanide activators. The economic and political context leads the European countries to be dependent on the Asian monopole, in terms of the production and exportation of lanthanides. In this context, my PhD work developed in collaboration with the UCCS at Lille, France and the University of Siegen, Germany, deals with the photoluminescence properties of some novel Bi^{3+} oxo-salts phosphors (lanthanide free) studied so far by the french partner for their structural aspects. In the selected phases, one key-parameter is the degree of connectivity between oxo-centered $\text{O}(\text{Bi},\text{M})_4$ tetrahedra, which allows a fine tuning of optical properties from one polytype to another one and tuning the chemical composition. Therefore, one goal of this work concerns the deduction of the important parameters tailoring the Bi^{3+} optical properties, on the basis of simple concepts, e.g. Bi bonding scheme, Bi^{3+} lone pair (LP) stereo-activity, electronic structures ... etc. The investigation of the BiM_2XO_6 ($\text{M}/\text{M}'=\text{Mg}, \text{Cd}, \text{Zn}$ and $\text{X}=\text{P}, \text{As}, \text{V}$) and ABiO_2X ($\text{A}=\text{Ca}, \text{Cd}, \text{Sr}, \text{Ba}$ and $\text{X}=\text{Cl}, \text{Br}$) families validated the pertinence of this study, leading to bright luminescence at room temperature. It mainly shows the strong effect on the excitation edge of the first Bi^{3+} cationic sphere (M,A) mediated by the cationic polarizing power compared to the weak effect of the first anionic coordination sphere (O,X). Dealing with well adapted $\text{Bi}(\text{M},\text{M}')_2\text{XO}_6$, it was also established correlations between the LP stereo-activity and the emission energy. Adding a stoichiometric amount of co-activators such as Mn^{2+} , Pb^{2+} or VO_4^{3-} groups can quench the Bi^{3+} emission. The case of $\text{Bi}^{3+}/\text{Mn}^{2+}$ and $\text{Bi}^{3+}/\text{VO}_4^{3-}$ compounds leads to complete charge transfer $\text{Bi}^{3+} \rightarrow \text{Mn}^{2+}/\text{VO}_4^{3-}$ whereas in the case of $\text{Bi}^{3+}/\text{Pb}^{2+}$ compounds the Pb^{2+} radiative emission is quench due to a $\text{Pb}^{2+} \rightarrow \text{Bi}^{3+}$ charge transfer. It was also shown for BiCdS_2Br that in spite of the presence Bi^{3+} activators, the small and direct bandgap (1.72eV) character leads to semiconductor type (band to band) photoluminescence.

Zusammenfassung

Die Entwicklung lumineszierender Materialien für zukünftige LEDs ist ein wichtiges Thema der heutigen Forschung im Hinblick auf energiesparende Materialien und es ist für viele Wissenschaftler eine interessante Herausforderung den „Leuchtstoff von morgen“ zu entwickeln. Die meisten heutzutage verwendeten kommerziellen LEDs basieren auf Lanthanoiden als Aktivatoren. Wirtschaftliche und politische Hintergründe führen die europäischen Staaten in eine Abhängigkeit des asiatischen Monopols hinsichtlich der Produktion und des Exports dieser Elemente. In diesem Zusammenhang steht meine Dissertation, entstanden in Zusammenarbeit mit der UCCS in Lille, Frankreich und der Universität Siegen, Deutschland, im Zeichen der Charakterisierung der photolumineszierenden Eigenschaften einiger neuer Bi^{3+} -Oxo-basierte Leuchtstoffe (Lanthanoid frei), deren strukturellen Charakteristika bereits durch die französischen Partner untersucht wurden. In den untersuchten Verbindungsklassen ist die Natur und Anzahl der Bindungen zwischen den oxo-zentrierten $\text{O}(\text{Bi},\text{M})_4$ -Tetraedern ein Schlüsselparameter, welche eine Feinjustierung der optischen Eigenschaften von einem Polytypen zum anderen und eine Einstellung der chemischen Komposition ermöglichen. Ein Ziel dieser Arbeit hierfür ist es die optischen Eigenschaften des Bi^{3+} mit Hilfe einfacher Konzepte zu erklären, beispielsweise mit Bi-Bindungsschemata, Stereoaktivitäten der freien Elektronenpaare (LP) am Bi^{3+} , elektronischer Strukturen usw. Die Untersuchung der BiM_2XO_6 ($\text{M}/\text{M}' = \text{Mg}, \text{Cd}, \text{Zn}$ und $\text{X} = \text{P}, \text{As}, \text{V}$)- und ABiO_2X ($\text{A} = \text{Ca}, \text{Cd}, \text{Sr}, \text{Ba}$ und $\text{X} = \text{Cl}, \text{Br}$)-Familien ist von größter Relevanz für diese Arbeit und führt zur Beobachtung starker Lumineszenz bei Raumtemperatur. Es wird besonders der starke Effekt der kationischen Koordinationssphäre (M,A) auf die „Anregungskante“, der durch die kationische Polarisierungsenergie entsteht, im Vergleich zu der schwachen Wirkung der ersten anionischen Koordinationssphäre (O,X) dargestellt. Durch Vergleiche mit der genau untersuchten Verbindungsklasse $\text{Bi}(\text{M},\text{M}')_2\text{XO}_6$ konnte der Zusammenhang zwischen der LP-Stereoaktivität und der Emissionsenergie gezeigt werden. Zugaben von stöchiometrischen Mengen an Co-Aktivatoren, wie Mn^{2+} -, Pb^{2+} - oder VO_4^{3-} -Ionen können die Bi^{3+} -Emission unterdrücken. In den Verbindungen, die $\text{Bi}^{3+}/\text{Mn}^{2+}$ oder $\text{Bi}^{3+}/\text{VO}_4^{3-}$ enthalten findet ein vollständiger Ladungstransfer statt ($\text{Bi}^{3+} \rightarrow \text{Mn}^{2+}/\text{VO}_4^{3-}$). In den Fällen von $\text{Bi}^{3+}/\text{Pb}^{2+}$ -Verbindungen wird die Pb^{2+} -basierte Emission durch einen $\text{Pb}^{2+} \rightarrow \text{Bi}^{3+}$ Ladungstransfer gequencht. Außerdem konnte gezeigt werden, dass trotz Anwesenheit von Bi^{3+} als Aktivator die kleine und direkte Bandlücke (1,72 eV) in BiCdS_2Br zu einer halbleitertypischen (Band-Band) Photolumineszenz führt

Résumé

Le développement de nouveaux matériaux luminescents pour les LEDs du futur, qui ont pour objectifs de préserver l'environnement et de réduire les dépenses énergétiques, est un thème de recherche d'actualité et un défi extrêmement intéressant pour de nombreux chercheurs. Actuellement, la plupart des LEDs commerciales sont des matériaux dopés aux lanthanides. Cependant, la situation économique et politique actuelle est telle que pour l'approvisionnement en lanthanides, les pays européens sont dépendant des pays asiatiques qui ont le monopole sur la production et l'exportation des ceux-ci. Dans ce contexte, mes travaux de thèses effectués en collaboration avec l'UCCS de Lille (France) et l'Université de Siegen en Allemagne ont pour objectifs d'étudier les propriétés photoluminescentes de nouveaux oxydes ou oxohalogénures de Bismuth (sans lanthanides) étudiés préalablement par l'UCCS pour leurs caractéristiques structurales. Dans les phases sélectionnées, la connectivité des tétraèdres oxo-centrés $O(\text{BiM})_4$ est un paramètre clé permettant de jouer sur les propriétés optiques en changeant de polytype ou de composition chimique. De ce fait, un des objectifs de cette thèse est de déterminer les paramètres importants permettant de façonner les propriétés optiques de Bi^{3+} sur les bases de simples concepts tels que la connectivité du Bi, la stéréo-activité de sa paire d'électrons libres ou les structures électroniques...etc. L'étude des familles BiM_2XO_6 ($\text{M}=\text{Mg}, \text{Cd}, \text{Zn}$ et $\text{X}=\text{P}, \text{As}, \text{V}$) et ABiO_2X ($\text{A}=\text{Ca}, \text{Cd}, \text{Sr}, \text{Ba}$ et $\text{X}=\text{Cl}, \text{Br}$) qui possèdent une émission intense à température ambiante valide la pertinence de ces travaux. Les résultats démontrent un effet important de la nature chimique de la première sphère de coordination cationique (M/A) du Bi^{3+} , étudiée du point de vue du pouvoir polarisant des cations (M/A), sur l'énergie d'excitation. Alors que pour ces séries de composés, l'influence de l'anion (O/Cl) est faible. Grâce à une solution solide $\text{Bi}(\text{MM}')_2\text{XO}_6$ bien adaptée, une corrélation entre l'activité de la paire libre et l'énergie d'émission a pu être établie. L'émission du Bi^{3+} peut être éteinte en ajoutant une quantité stœchiométrique de co-activateurs comme Mn^{2+} , Pb^{2+} ou VO_4^{3-} . Un transfert de charge total est détecté dans les cas de $\text{Bi}^{3+}/\text{Mn}^{2+}$ ou de $\text{Bi}^{3+}/\text{VO}_4^{3-}$, ($\text{Bi}^{3+} \rightarrow \text{Mn}^{2+}/\text{VO}_4^{3-}$) alors que dans les composés $\text{Bi}^{3+}/\text{Pb}^{2+}$, l'émission du plomb est éteinte via un transfert de charge $\text{Pb}^{2+} \rightarrow \text{Bi}^{3+}$. Il a également été démontré pour BiCdS_2Br , qui est un semi-conducteur possédant un bandgap direct (1.72eV), qu'une photoluminescence de type semi-conducteur est observée malgré la présence d'activateurs Bi^{3+} .

Table of Content

Abstract	1
Zusammenfassung	2
Résumé	3
Table of Content	5
List of figures	10
INTRODUCTION	19
I. Theory and Background	24
I.1. Basic aspects of luminescence	24
I.2. Decay time.....	27
I.3. Quantum Yield	28
I.4. Quenching Process	29
I.4.1. Quenching via energy transfer	29
I.4.2. Thermal quenching.....	30
I.4.3. Killer centers	31
I.5. Nephelauxetic effect.....	32
I.6. Luminescence of the ns^2 ions	34
I.6.1. Theory of ns^2 ion	35
I.6.2. Photoluminescence of Bi^{3+} cation	38
I.6.2.1. Bi^{3+} as dopant.....	38
I.6.2.2. Photoluminescence of Bismuth based compounds	40
I.6.2.3. Bi^{3+} as sensitizer.....	40
II. Experimental part and methodology	46
II.1. X-ray diffraction.....	46
II.1.1. Single crystal diffraction	47
II.1.2. Powder X-ray diffraction	50
II.1.3. Powder structural refinement	51
II.2. Optical property measurements.....	53
II.2.1. Photoluminescence measurements	53
II.2.2. Decay time measurements.....	55
II.2.3. CIE chromaticity diagram	56
II.3. UV-Vis spectroscopy / Kubelka-Munk method.....	57
II.4. Theory of functional density	59
II.4.1. Introduction to the Density Functional Theory (DFT).....	59

Table of Content

II.4.2.	Background	59
II.4.3.	Electron Density	60
II.4.4.	The Hohenberg-Kohn theorem.....	61
II.4.5.	The Kohn-Sham equations	62
II.4.6.	Exchange and correlation functional.....	63
II.4.7.	Plane Waves	65
II.4.8.	Pseudopotential approach.....	66
II.4.9.	Steps for an electronic calculation	67
II.4.10.	Structural optimization	67
II.5.	Scanning electron microscope.....	68
II.6.	Partial charge calculations and lone-pair localization.....	69
III.	Electronic Structures and Optical properties of $\text{BiM}_2\text{O}_2(\text{XO}_4)$ compounds	72
III.1.	Review of $\text{Bi}_2\text{O}_3\text{-MO}_x\text{-X}_2\text{O}_5$ systems	72
III.1.1.	The antiphase approach	72
III.1.2.	Structural units and Bi...Bi connectivity.....	76
III.1.3.	Empirical rules.....	77
III.2.	$\text{BiM}_2\text{O}_2(\text{XO}_4)$ polymorphs with $n=2$ ribbons.....	79
III.3.	Towards new BiM_2XO_6 phases.....	83
III.3.1.	Accurate crystal Structure of BiCd_2PO_6	83
III.3.2.	Crystal structure of the new $\text{BiPb}_2\text{AsO}_6$ phase.....	88
III.4.	Tuning the optical properties of BiM_2XO_6 compounds.....	93
III.4.1.	M^{2+} influence	93
III.4.1.1.	Synthesis of $\text{BiMM}'\text{PO}_6$ series ($\text{M}/\text{M}'=\text{Mg}, \text{Zn}, \text{Cd}$).....	94
III.4.1.2.	Electronic structures and UV-visible spectroscopy	96
III.4.1.3.	Topology of the Density of States (DOS).....	99
III.4.1.4.	Primary analysis of the M-O-Bi bonding scheme.....	101
III.4.1.5.	Photoluminescence properties and correlations to the structure.....	102
III.4.1.5.1.	Bi-O covalency and excitation	104
III.4.1.5.2.	Excitation Energy above the Bandgap.....	105
III.4.1.5.3.	Emission and Lone Pair activity	108
III.4.1.6.	Analysis of the decay time versus temperature.....	110
III.4.1.7.	Summary	114
III.4.2.	Effect of the XO_4 ($\text{X}=\text{P}, \text{V}, \text{As}$) group	115
III.4.2.1.	Synthesis of BiMg_2XO_6 ($\text{X}=\text{P}, \text{V}, \text{As}$).....	115

III.4.2.2.	Electronic properties	116
III.4.2.3.	Topology of the DOS	119
III.4.2.4.	Photoluminescence properties and correlations	120
III.4.2.5.	Bi-O covalency and excitation	123
III.4.2.6.	Decay Time of BiMg ₂ VO ₆	124
III.4.2.7.	Emission Process	126
III.5.	Solid Solution BiCd ₂ XX'O ₆	126
III.5.1.	Synthesis	126
III.5.2.	Structural characteristics of the mixed compositions	131
III.5.3.	Room temperature PL properties of the mixed compositions	132
III.5.4.	Summary.....	136
III.6.	BiMn ₂ PO ₆ photoluminescence	138
III.6.1.	Synthesis of BiMn ₂ PO ₆	138
III.6.2.	d →d luminescence in BiMn ₂ PO ₆	139
III.7.	Investigation of BiPb ₂ AsO ₆ photoluminescence properties.....	143
III.7.1.	Synthesis of BiPb ₂ AsO ₆	143
III.7.2.	Electronic properties of BiPb ₂ AsO ₆	144
III.7.3.	Luminescent properties.....	146
III.7.4.	Summary.....	147
IV.	Electronic Structures and Optical properties of BiMO(VO ₄) compounds.....	152
IV.1.	Crystal structures and interest for optical properties.....	152
IV.2.	Selection of compounds	154
IV.3.	Synthesis of BiMVO ₅ (M=Mg, Ca, Cd).....	155
IV.4.	Electronic structure calculations	156
IV.5.	Topology of Density of States.....	157
IV.6.	Photoluminescence properties and structural correlation.....	159
IV.7.	Decay time measurements.....	161
IV.8.	Discussion	163
IV.9.	Summary	163
V.	Optical properties of Bi ³⁺ oxyhalides compounds	168
V.1.	The Sillen	168
V.1.1.	Choice and crystal structure of the selected Sillen compounds	168
V.1.2.	Synthesis of the X1 phases.....	173
V.1.3.	Crystal structure of BaBiO ₂ Br.....	173

Table of Content

V.1.4.	Electronic structures calculations of the Sillen X1 phases.....	175
V.1.5.	UV-visible spectroscopy	177
V.1.6.	Topology of the Density of States (DOS)	178
V.1.7.	Photoluminescence properties and correlations to the structure	181
V.1.7.1.	Luminescence properties	181
V.1.7.2.	Differences with previous works	184
V.1.7.3.	Excitation energy	184
V.1.7.4.	Excitation vs. bandgap	186
V.1.8.	Emission and lone pair stereo-activity	187
V.1.9.	Photoluminescence of a disordered X1 phase: CaBiO ₂ Br	188
V.1.9.1.	Synthesis of CaBiO ₂ Br	188
V.1.9.2.	Low temperature photoluminescence	189
V.1.10.	Summary.....	193
V.2.	Investigation of other 2D Bi oxychlorides; the BiA ₃ O ₃ Cl ₃ (A=Sr, Ba) case	193
V.2.1.	Synthesis.....	194
V.2.2.	Structural description of isostructural BiSr ₃ O ₃ Cl ₃ and BiBa ₃ O ₃ Cl ₃	194
V.2.3.	Electronic calculations and UV-vis spectroscopy	197
V.2.4.	DOS topology.....	200
V.2.5.	Room temperature photoluminescence and structural correlation.....	200
V.2.6.	Summary	203
V.3.	Luminescence of Bi versus Pb in PbBi ₄ O ₆ Cl ₂ compound.....	203
V.3.1.	Crystal structure of PbBi ₄ O ₆ Cl ₂	204
V.3.2.	Photoluminescence properties of MBi ₄ O ₆ Cl ₂ (M=Ba, Pb)	206
V.3.3.	Decay time measurement	209
V.3.4.	Summary	210
VI.	Photoluminescence of BiCdS ₂ Br	214
VI.1.	Synthesis.....	214
VI.2.	Structure description of BiCdS ₂ Br	215
VI.3.	Electronic calculations	216
VI.4.	DOS topology.....	217
VI.5.	Photoluminescence properties of BiCdS ₂ Br	218
VI.6.	Decay time.....	219
VI.7.	Discussion	220
VI.8.	Summary	221

Summary and Outlook..... 225
Annex1 229
Annex 2 231

List of figures

Figure I- 1 Basic sketch of luminescence process, “ r ” represents the interatomic distance. .	25
Figure I- 2 Representation of Fluorescence and Phosphorescence processes (ISC means intersystem crossing, S_0 is the ground state, S^* and T^* are two excited states).	26
Figure I- 3 a) Example of monoexponential decay time and b) biexponential decay time (for practical reasons, it is plotted $\ln(\text{Intensity})$ against time).	28
Figure I- 4 Sketch representing possible quenching via energy transfer.	30
Figure I- 5 Sketch representing mechanism of the thermal quenching.	31
Figure I- 6 Sketch representing the effect of the “Nephelauxetic effect” on energy states.	32
Figure I- 7 In blue the case where there is no polarization/low nephelauxetic effect (example of KCl) and in red the case of a strong polarization/high nephelauxetic effect (example of AlCl_3). The electron density of the anion is significantly deformed by the small highly charged cation and the position of excited state is lowered resulting in a red shift.	34
Figure I- 8 Sketch of possible transitions for Bi^{3+} cation and on the right, spectroscopic rules.	36
Figure I- 9 Diagram showing the stereo-activity of the lone pair of electrons, a low stereo-activity faintly shifts the excited state Δr and results on a small Stokes shift (full line). A high stereo-activity induces a larger shift $\Delta r'$, and hence induces a bigger Stokes shift (dashed line).	37
Figure II- 1 a) Picture of an APEX DUO (Bruker-AXS) single crystal diffractometer and b) Zoom from the inside of the chamber.	47
Figure II- 2 a) Picture of a D8 Passeur (Bruker-AXS) diffractometer and b) Zoom from the inside of the chamber.	50
Figure II- 3 Picture of a FluoroMax-4 HORIBA spectrofluorometer	54
Figure II- 4 a) Basic configuration b) Picture of a Fluorolog-3-22 Horiba spectrofluorometer and c) Picture of the chamber for low temperature measurements.	55
Figure II- 5 Representation of the CIE 1931 chromaticity diagram.	56
Figure II- 6 UV reflectance spectrum of BaSO_4 .	57
Figure II- 7 Example of Kubelka-Munk representation with band gap extrapolation for an indirect semiconductor ($n=2$).	58
Figure II- 8 . Representation of the “real” wavefunction and pseudo-wavefunction behaviors (upper part) as well as all electron and pseudopotential (bottom part).	66
Figure II- 9 Self-consistent iteration of a DFT calculation.	67
Figure III- 1 Possible branching between OPb_4 anti-tetrahedra b) Representation of OBi_4 and tetrahedra of the $\delta\text{-Bi}_2\text{O}_3$ crystal structure.	73
Figure III- 2 a) Representation of $\text{Bi}_3\text{Ru}_3\text{O}_{11}$ structure using the oxo-centered approach to show $[\text{Bi}_6\text{O}_4]^{10+}$ tetramers and b) Representation of $\text{La}_4\text{Ru}_6\text{O}_{19}$ with $[\text{La}_4\text{O}]^{10+}$ monomers...	74
Figure III- 3 a) Disorder around phosphorus atoms in $\text{Bi}_{-1.2}\text{M}_{-1.2}\text{PO}_{5.5}$ ($M= \text{Zn}, \text{Mn}$) and b) and projection of the crystal structure showing triple ribbons.	75

Figure III- 4 Representation of two compounds, BiNiPO_5 on the left and BiCu_2PO_6 on the right side using classical structural description (MO_x polyhedra, PO_4 tetrahedra and interstitials Bi^{3+}) and using the anion-centered polyhedra approach, for which it is possible to distinguish infinite chains built on respectively 1 and 2 tetrahedra width.	76
Figure III- 5 Organization between a) ribbons in BiMXO_5 compounds b) double ribbons in BiM_2XO_6 compounds and c) triple ribbons in $\text{Bi}_{-1.2}\text{M}_{-1.2}\text{PO}_{5.5}$ compounds. For the last case tunnels parallel to b are also represented.....	77
Figure III- 6 Representation of ribbons and excrescence for $n= 4, 8$ and 11 . Td sands for tetrahedra.....	78
Figure III- 7 Details of the excrescence for the ribbons $n= 4$ and 6	78
Figure III- 8 a) Representation of infinite one-dimensional $[\text{BiM}_2\text{O}_2]^{3+}$ and b) representation of oxo-centered $\text{O}(\text{Bi}_2\text{M}_2)$ tetrahedron.....	79
Figure III- 9 Examples of BiM_2XO_6 structure: a) BiCd_2VO_6 (SG: $\text{Bb2}_1\text{m}$) b) $\text{BiMg}_2\text{AsO}_6$ (SG: Bbmm) c) BiZn_2PO_6 (SG: Pnma) and d) $\text{BiPb}_2\text{AsO}_6$ (SG: $\text{P2}_1/\text{c}$).....	80
Figure III- 10 Bismuth-oxygen coordination with ideal lone pair (LP) asymmetry. The lone pair of electron is pointing out the double ribbon toward the XO_4 tetrahedra.....	81
Figure III- 11 Rietveld refinement pattern using powder synchrotron X-ray diffraction of BiCd_2PO_6	84
Figure III- 12 Two views of BiCd_2PO_6 structure, along axis b and axis c	86
Figure III- 13 View of the coordination of a) Bismuth b) Cadmium and c) Phosphorus	87
Figure III- 14 a) Representation of $\text{BiPb}_2\text{AsO}_6$ crystal structure and b) view of infinite double ribbons along axis b	91
Figure III- 15 a) View of the coordination of Bismuth b) and c) View of the coordination of Lead atoms d) View of the coordination of Arsenic.	92
Figure III- 16 XRD pattern of BiM_2PO_6 ($\text{M}=\text{Mg}, \text{Zn}, \text{Cd}$)	94
Figure III- 17 XRD pattern of the solid solution $\text{BiMg}_{2-x}\text{Cd}_x\text{PO}_6$	95
Figure III- 18 . XRD pattern of the solid solution $\text{BiMg}_{2-x}\text{Zn}_x\text{PO}_6$	95
Figure III- 19 Band diagrams representation between -3eV and 5eV for a) BiMg_2PO_6 b) BiZn_2PO_6 and c) BiCd_2PO_6 . The minimum of the CB and the maximum of the VB positions are localized by a blue line.....	98
Figure III- 20 Absorption spectra and Kubelka-Munk fit for a) BiMg_2PO_6 b) BiZn_2PO_6 and c) BiCd_2PO_6	99
Figure III- 21 TDOS (bottom) and PDOS diagrams for a) BiMg_2PO_6 b) BiZn_2PO_6 and c) BiCd_2PO_6	100
Figure III- 22 Sketch of the influence of the polarizing power of M^{2+} cations.	101
Figure III- 23 a) Color emission representation in the CIE chromaticity diagram of BiM_2PO_6 ($\text{M}=\text{Mg}, \text{Zn}, \text{Cd}$). b) Picture of BiMg_2PO_6 at room temperature under UV lamp excitation ($\lambda_{\text{ex}}= 254\text{nm}$). c) Room temperature photoluminescence spectra of BiM_2PO_6 ($\text{M}=\text{Mg}, \text{Zn}, \text{Cd}$). The emission spectra are measured exciting at the maxima of corresponding excitation bands and vice versa (see Table III-9).....	103
Figure III- 24 Sketch of the influence of the nephelauxetic effect on Bi^{3+} . Increasing the nephelauxetic effect leads to lower the energy position of Bi^{3+} excited states. This has for consequence to decrease the energy required to reach the excited state $6s6p$	104

List of figures

Figure III- 25 a) Excitation spectra of the solid solution $\text{BiMg}_{2-x}\text{Cd}_x\text{PO}_6$ at room temperature, b) Evolution of the position of excitation maxima of $\text{BiMg}_{2-x}\text{Cd}_x\text{PO}_6$ and $\text{BiMg}_{2-x}\text{Zn}_x\text{PO}_6$ with evidence of a doublet in the central range.	105
Figure III- 26 Comparison between absorption and excitation spectra for a) BiMg_2PO_6 b) BiZn_2PO_6 and c) BiCd_2PO_6	106
Figure III- 27 a) Comparison of absorption and excitation spectra of BiMg_2PO_6 b) A scheme of excitation/bandgap interplay using Bismuth PDOS in the BiM_2PO_6 compounds c) Sketch which explain the energy difference between the absorption and excitation band in Bi^{3+} based compounds.....	107
Figure III- 28 a) Representation of the Bi coordination including the lone pair position b) Diagram showing the stereo-activity of the lone pair of electrons, a low stereo-activity faintly shifts the excited state Δr and results on a small Stokes shift (full line). A high stereo-activity induces a larger shift $\Delta r'$, and hence induces a bigger Stokes shift (dashed line).	108
Figure III- 29 a) Evolution of the cell parameters of the solid solution $\text{BiMg}_{2-x}\text{Cd}_x\text{PO}_6$ b) Evolution of the emission band of $\text{BiMg}_{2-x}\text{Cd}_x\text{PO}_6$ (with x from 0 to 2 with steps of 0.2) c) Correlation between the emission maximum and the cell parameter a (dotted lines are guide of the eyes).....	110
Figure III- 30 a) Temperature dependence excitation spectra for BiMg_2PO_6 b) Sketch representing luminescence processes at low temperature and c) Evolution of the emission maxima energy position and intensity for BiMg_2PO_6	111
Figure III- 31 Temperature dependence emission spectra for BiMg_2PO_6	112
Figure III- 32 a) Decay time of BiMg_2PO_6 for excitation at 266nm and emission at 510nm at room temperature, the lifetime is fitted to 350ns (R^2 adj. = 0,999 fitted linear, the intensity was plotted in $\ln(\text{intensity})$ in order to see the monoexponential behavior) b) Decay time of BiMg_2PO_6 for excitation at 265nm and emission at 516nm at 10K, the two different lifetimes are 37 μs and 286 μs (R^2 adj. = 0,998 fitted exponential).....	113
Figure III- 33 XRD pattern of BiMg_2XO_6 ($X=\text{P, As, V}$) series with reflections indexation... 115	115
Figure III- 34 a-c) Representation of band diagrams for BiMg_2XO_6 d) Zoom on the minimum of the CB and maximum of the VB for $\text{BiMg}_2\text{AsO}_6$ e-g) Kubelka-Munk fits and Tauc plots of BiMg_2XO_6 series and bandgap extrapolation (BG: $\text{BiMg}_2\text{PO}_6=3.76\text{eV}$, $\text{BiMg}_2\text{AsO}_6=3.21\text{eV}$ and $\text{BiMg}_2\text{VO}_6= 3.16\text{eV}$).....	118
Figure III- 35 a-c) Representation TDOS (bottom) and PDOS for a) $\text{BiMg}_2\text{AsO}_6$ b) BiMg_2VO_6 and c) BiMg_2PO_6	120
Figure III- 36 a) Representation of emission color of BiMg_2XO_6 ($X=\text{P, As, V}$) in the chromaticity CIE diagram b) Picture the orange emission of BiMg_2VO_6 at room temperature under UV lamp excitation ($\lambda_{\text{ex}}= 365\text{nm}$) and c) Room temperature photoluminescence of BiMg_2XO_6 ($X= \text{P, As, V}$), The emission spectra are measured exciting at the maxima of corresponding excitation bands and vice versa (see Table III-12).	122
Figure III- 37 Sketch of absorption and emission processes of the VO_4 tetrahedron with T_d symmetry.....	123
Figure III- 38. Decay time measurement of BiMg_2VO_6 at room temperature, $\lambda_{\text{ex}}=340\text{nm}$ and $\lambda_{\text{em}}=510\text{nm}$, the lifetimes are fitted to 18 μs and 104 μs (R^2 adj. = 0,999 fitted linear, the intensity was plotted in $\ln(\text{intensity})$ in order to see the monoexponential behavior).	124
Figure III- 39 Comparison between the absorption and excitation spectra of a) BiMg_2PO_6 b) $\text{BiMg}_2\text{AsO}_6$ and c) BiMg_2VO_6	125

Figure III- 40 Picture of the solid solution powders.....	127
Figure III- 41 Structure representation of $\text{BiCd}_2\text{AsO}_6$ (isostructural to BiCd_2PO_6) and BiCd_2VO_6 (right) in the plan (ab). All the arsenate tetrahedra all up in $\text{BiCd}_2\text{AsO}_6$ whereas their orientation changes in BiCd_2VO_6	128
Figure III- 42 Cell parameters of the three solid solutions refined with Fullprof using pattern matching method.	128
Figure III- 43 a) XRD pattern of BiCd_2XO_6 ($X=\text{P, As, V}$) with reflection indexing. b) XRD pattern of the solid solution $\text{BiCd}_2\text{As}_{1-x}\text{P}_x\text{O}_6$ c) XRD pattern of the solid solution $\text{BiCd}_2\text{V}_{1-x}\text{P}_x\text{O}_6$ and d) XRD pattern of the solid solution $\text{BiCd}_2\text{As}_{1-x}\text{V}_x\text{O}_6$	130
Figure III- 44 Room temperature excitation and emission spectra for the solid solution $\text{BiCd}_2\text{V}_{1-x}\text{P}_x\text{O}_6$	133
Figure III- 45 Room temperature excitation and emission spectra for the mixed composition $\text{BiCd}_2\text{As}_{1-x}\text{V}_x\text{O}_6$	135
Figure III- 46 Sketch representing the photoluminescence of the studied solid solutions.....	137
Figure III- 47 X-ray powder pattern of BiMn_2PO_6 including reflections indexation.	138
Figure III- 48 a) Emission (left) and excitation (right) spectra of BiMn_2PO_6 at 10K and b) Emission color representation in the CIE diagram.	139
Figure III- 49 Sketch representing the attribution of electronic transitions of Mn^{2+} cation to the excitation spectrum of BiMn_2PO_6	140
Figure III- 50 Tanabe-Sugano diagram for a d^5 element in octahedral coordination.	142
Figure III- 51 TDOS and PDOS representation for BiMn_2PO_6 taken from ref [39].....	143
Figure III- 52. X-ray powder pattern of $\text{BiPb}_2\text{AsO}_6$ including reflections indexation from the single crystal data (section 3.3.2).	144
Figure III- 53 . a) TDOS and PDOS representation for $\text{BiPb}_2\text{AsO}_6$. b) Band diagram representation of $\text{BiPb}_2\text{AsO}_6$, the blue lines localize the minimum of the CB and maximum of the VB and show an indirect character. c) Kubelka-Munk fit and extrapolation of the band gap for $\text{BiPb}_2\text{AsO}_6$	145
Figure III- 54 a) Photoluminescence spectra of $\text{BiPb}_2\text{AsO}_6$ and BiMg_2PO_6 at 10K. b) Comparison between the excitation and absorption spectra of $\text{BiPb}_2\text{AsO}_6$. c) Emission color of $\text{BiPb}_2\text{AsO}_6$ at 10K represented in the CIE diagram.....	147
Figure IV- 1 a) The crystal structure of BiCaVO_5 with cis position of M atoms, the projection of the ribbon in the (ab) plan show the Bi...Bi connectivity via Bi-O-Bi bridges b) The crystal structure of BiMnPO_5 with trans position of M atoms, the projection of the ribbon in the (ac) plan show the Bi...Bi connectivity via Bi-O-Bi bridges.	153
Figure IV- 2 XRD pattern of BiMVO_5 ($M=\text{Cd, Ca, Mg}$) with reflections indexation.....	156
Figure IV- 3 Sketch representing the charge transfer $\text{O } 2p \rightarrow \text{V } 3d$	158
Figure IV- 4 TDOS and PDOS of BiMVO_5 ($M=\text{Cd, Ca, Mg}$).....	159
Figure IV- 5 a) Emission color representation on the CIE chromaticity diagram b) Sketch of absorption and emission processes of the VO_4 tetrahedron with T_d symmetry and c) Emission and excitation spectra of BiMVO_5 ($M=\text{Cd, Ca, Mg}$).	160
Figure IV- 6. Room temperature decay time measurements for a) BiCdVO_5 b) BiCaVO_5 and c) BiMgVO_5 . All the decay curves are best fitted with a double exponential behavior and give	

List of figures

two different lifetimes. For BiCdVO_5 and BiCaVO_5 the fitting using a monoexponential behavior give unsatisfactory correlation factors. 162

Figure IV- 7 Sketch representing the influence of Bi^{3+} on VO_4^{3-} photoluminescence. 164

Figure V- 1 a) Structure of ABiO_2Cl (S.G. $I4/mmm$) projected along the b -axis and b) projected along c -axis c) Bismuth-anion coordination and the lone pair position d) Structure of ABiO_2X (S.G. Cmcm) and e) projected along b -axis f) Bismuth-anion coordination for ABiO_2X ($M=\text{Sr}$ and Ba , $X=\text{Cl}$ or Br) and the lone pair position. g) Structure of ABiO_2Cl ($A=\text{Ca}$ and Cd , S.G. $\text{P}2_1/m$) projected along the monoclinic b -axis and h) projected along c -axis i) Bismuth-anion coordination for ABiO_2Cl ($A=\text{Ca}$ and Cd) and the lone pair position. 171

Figure V- 2 a) XRD pattern of ABiO_2Cl ($A=\text{Cd}$, Ca , Sr , Ba) and BaBiO_2Br with indexation of the reflections and b) Profile fitting of BaBiO_2Br in the Cmcm S.G..... 174

Figure V- 3 a), b), c) Band diagrams of ABiO_2Cl ($A= \text{Sr}$, Ba) and BaBiO_2Br . d) Zoom on the bottom of the conduction band for BaBiO_2Cl . e) and f) Band diagrams of ABiO_2Cl ($A= \text{Cd}$, Ca). The blue sticks represent the minima/maxima of the VB/CB, both bandgaps are found indirect. 176

Figure V- 4 Kubelka-Munk representation of ABiO_2Cl ($A=\text{Cd}$, Ca , Sr , Ba) and BaBiO_2Br with extrapolation of the bandgap. 178

Figure V- 5 TDOS and PDOS diagrams for a) SrBiO_2Cl b) BaBiO_2Cl c) BaBiO_2Br d) CdBiO_2Cl and e) CaBiO_2Cl 179

Figure V- 6 a) Room temperature photoluminescence spectra of ABiO_2X ($A=\text{Sr}$, Ba and $X=\text{Cl}$, Br), for BaBiO_2Br $\lambda_{\text{ex}}= 285\text{nm}$ and $\lambda_{\text{em}}=535\text{nm}$, BaBiO_2Cl $\lambda_{\text{ex}}= 299\text{nm}$ and $\lambda_{\text{em}}= 515\text{nm}$, SrBiO_2Cl $\lambda_{\text{ex}}= 267\text{nm}$ and $\lambda_{\text{em}}= 458\text{nm}$ b) room temperature photoluminescence spectra of ABiO_2Cl ($A=\text{Ca}$, Cd) for CdBiO_2Cr $\lambda_{\text{ex}}= 288\text{nm}$ and $\lambda_{\text{em}}=476\text{nm}$, CaBiO_2Cl $\lambda_{\text{ex}}= 277\text{nm}$ and $\lambda_{\text{em}}= 497\text{nm}$. The emission spectra are measured exciting at the maxima of corresponding excitation bands and vice versa. 182

Figure V- 7 Diagram showing the effect of stereo-active lone pair of electrons: a low stereo-activity faintly shifts the excited state $\Delta r \rightarrow$ small Stokes shift (full line). A high stereo-activity induces a larger shift $\Delta r' \rightarrow$ bigger Stokes shift (dashed line).b) Representation of color emission of all the ABiO_2X compounds in the CIE 1931 diagram..... 183

Figure V- 8 . Sketch of the influence of the nature of a) the cation b) the halide. A small cation will strongly polarize the A-O bond and by inductive effect the Bi-O covalency will be lowered. A bigger halide will be more polarized by the Bi and the covalency of Bi-X bond which involves a stronger covalent character..... 185

Figure V- 9 Comparison between the absorption and excitation spectra of the five studied compounds..... 187

Figure V- 10 a) Example of variable Bi-O-Bi connectivity in CaBiO_2Br due to Bi/Ca mixed sites b) XRD pattern of CaBiO_2Br with full pattern indexation..... 189

Figure V- 11. Representation of the chromaticity emission at 10K of CaBiO_2Br in the CIE 1931 diagram. 190

Figure V- 12 Temperature dependence photoluminescence of CaBiO_2Br a) Representation of excitation bands and b) the emission bands..... 191

Figure V- 13 Decay time measurement of CaBiO_2Br at 10K ($\lambda_{\text{ex}}=330\text{nm}$ and $\lambda_{\text{em}}= 552\text{nm}$), the decay curve is fitted with a double exponential behavior ($R^2=0.995$) and gives $\tau_1= 0.099\text{ ms}$ and $\tau_2= 1.128\text{ms}$	192
Figure V- 14 XRD pattern of $\text{BiA}_3\text{O}_3\text{Cl}_3$ ($A=\text{Ba, Sr}$) with reflections indexation from the calculated pattern.....	194
Figure V- 15 Crystal structure of $\text{BiSr}_3\text{O}_3\text{Cl}_3$ with oxo-centered $\text{O}(\text{Sr}_3\text{Bi})$ tetrahedra : (bc) plane (a), (ab) plane (b). c) Representation of the interaction between the Bi atoms and the negative lone pairs. and d) Coordination of Bi atoms for $\text{BiSr}_3\text{O}_3\text{Cl}_3$	196
Figure V- 16 a) and b) Band diagrams representation of $\text{BiSr}_3\text{O}_3\text{Cl}_3$ and $\text{BiBa}_3\text{O}_3\text{Cl}_3$. TDOS (bottom) and PDOS of c) $\text{BiSr}_3\text{O}_3\text{Cl}_3$ d) $\text{BiSr}_3\text{O}_3\text{Cl}_3$. e) and f) represent the Kubelka-Munk fits and Tauc plots with band gap extrapolations for $\text{BiSr}_3\text{O}_3\text{Cl}_3$ and $\text{BiBa}_3\text{O}_3\text{Cl}_3$ (for $A=\text{Sr}$, $BG=3.58\text{eV}$ and for $A=\text{Ba}$, $BG=3.62\text{eV}$).....	199
Figure V- 17 a) Room temperature photoluminescence of $\text{BiA}_3\text{O}_3\text{Cl}_3$ ($A=\text{Ba, Sr}$) and b) Representation of $\text{BiA}_3\text{O}_3\text{Cl}_3$ ($A=\text{Ba, Sr}$) color emission in the CIE 1931 diagram.....	201
Figure V- 18 Comparison between the absorption and excitation spectra for $\text{BiA}_3\text{O}_3\text{Cl}_3$ ($A=\text{Ba, Sr}$).	202
Figure V- 19 Representation of $\text{PbBi}_4\text{O}_6\text{Cl}_2$ crystal structure along axis b.	204
Figure V- 20 Evidence of layered modules in the crystal structures of a) BiOCl , b) $\text{Bi}_2\text{LnO}_4\text{Cl}$, c) (X1) PbBiO_2Cl and d) $\text{PbBi}_4\text{O}_6\text{Cl}_2$ (this work).....	205
Figure V- 21 a) Photoluminescence spectra of $\text{MBi}_4\text{O}_6\text{Cl}_2$ ($M=\text{Pb, Ba}$) at 10K b) Representation of $\text{MBi}_4\text{O}_6\text{Cl}_2$ ($M=\text{Pb, Ba}$) color emission in the CIE 1931 diagram at 10K and c) Representation of $\text{PbBi}_4\text{O}_6\text{Cl}_2$ emission within the color of the spectral range.	207
Figure V- 22 Decay time measurement of $\text{PbBi}_4\text{O}_6\text{Cl}_2$ at 10K. The decay curve is fitted with a triple exponential behavior and gives three lifetime values: $\tau_1=64\mu\text{s}$, $\tau_2=575\mu\text{s}$, $\tau_3=12.6\text{ms}$...	209
Figure V- 23 Sketch representing the energy transfer from Pb^{2+} to Bi^{3+}	210
Figure VI- 1 X-ray powder pattern of BiCdS_2Br with full reflection indexation.	214
Figure VI- 2 a) View of BiCdS_2Br crystal structure along b axis b) Representation of Cadmium chalcobromide slabs in the (bc) plane and c) Bismuth coordination in BiCdS_2Br . + Table with partial charges for BiCdS_2Br and BiCdO_2Br	215
Figure VI- 3 a) DOS of BiCdS_2Br , b) Representation of the band diagram of BiCdS_2Br , a direct bandgap of 1.72eV is found and c) Color emission of BiCdS_2Br at 10K representation in the CIE chromaticity diagram.....	217
Figure VI- 4 Temperature dependence of emission spectra (left) and excitation spectra (right) of BiCdS_2Br	219
Figure S- 1 View in the (bc) plan of the crystal structure of $\text{BiPb}_{0.5}\text{Zn}_{0.5}\text{PO}_5$ and zoom on the infinite ribbon along a-axis.	233
Figure S- 2 Coordination of Bi b) Pb c) Zn and d) P.....	234
Figure S- 3 a) Image of $\text{Bi}_2\text{BaIO}_4\text{H}$ crystals b) EDS spectrum of selected crystals: all the peaks can be indexed to Bi, Ba or I elements c) and d) Tables showing the quantification of the elements.	239
Figure S- 4 Infrared spectrum of $\text{Bi}_2\text{BaIO}_4\text{H}$, O-H bending vibration is evidenced at 1430cm^{-1}	240

List of figures

<i>Figure S- 5 a) Representation of $\text{Bi}_2\text{BaIO}_4\text{H}$ crystal structure in (a,b) plane, b) Cationic layer represented in (a,c) plane and c) Cationic layer of the XI Sillen BaBiO_2Br (S.G. Cmcm) (Chapter V).....</i>	<i>241</i>
<i>Figure S- 6 a) Coordination of the Bi and b) Ba atoms.....</i>	<i>242</i>

INTRODUCTION

Luminescent materials play a crucial role in our daily life, as they can be found in traffic lights, computer screens, smartphones and tablets, Euro banknotes, medical devices, and films for X-rays and light sources. In fact, they have become indispensable.

Recently, a considerable attention has been paid to LEDs (Light Emitting Diode) and especially to white LEDs (WLEDs) due to their attractive advantages in terms of energy saving and ecological features compared to commercial incandescent and fluorescent lamps. WLED are considering as the next generation of solid-state illumination sources. They have higher luminous efficiency and brightness, lower power consumption, more than 10 longer lifetime, they produce much less heat and are Hg-free. All these advantages contribute to the world wide project of energy saving. Different strategies have been developed in order to produce efficient WLEDs. One of the main is to combine chips of the 3 primary colors (blue, green and red) but the shift of color temperature (CR) and color rendering index (CRI) depending on the device temperature makes this kind of WLED unsuitable for commercial applications. These drawbacks can be corrected by pc-WLED (phosphor converted WLED) but the red spectral component deficiency for 1-pc-WLED and the blue absorption of the typical additional red phosphor for 2-pc-WLED lead to respectively an uncomfortable perception for the human eyes and to low luminous efficiency. Then, a strong interest was found for nitride or oxynitride phosphors doped with lanthanides. This type of phosphors has suitable luminescent properties for applications, but due to the synthesis conditions (very high temperature, nitrogen flux and high pressure) and lanthanide price, the cost to prepare raw materials remains critical for commercial applications. It follows that nowadays, the development of new phosphors for commercial applications turns into a very exciting challenge for many researchers.

Moreover, except the blue commercial phosphors which are most of the time direct bandgap semiconductors, $\text{Ga}_{1-x-y}\text{In}_x\text{Al}_y\text{N}$, all the green, yellow or red phosphors are based on lanthanides. The Rare-Earth (RE) sources are however not equitably localized on the Earth. In fact, most of the lanthanides ores are situated in China. When the topic of my thesis was established (end of 2011), China had the monopoly on their productions and their exportations (in 2011 China provides more than 90% of lanthanides, see figure Intro-1a) and take

Introduction

advantage of this to establish quota exportations which drastically increases their prices. For example the price of europium metal was multiply by eight between the 1st trimester of 2011 and august 2011(see figure Intro-1b). This political and economic situation led to a very interesting challenge which consists of replacing lanthanides in phosphors by other activators in order to prevent political and cost dependences.

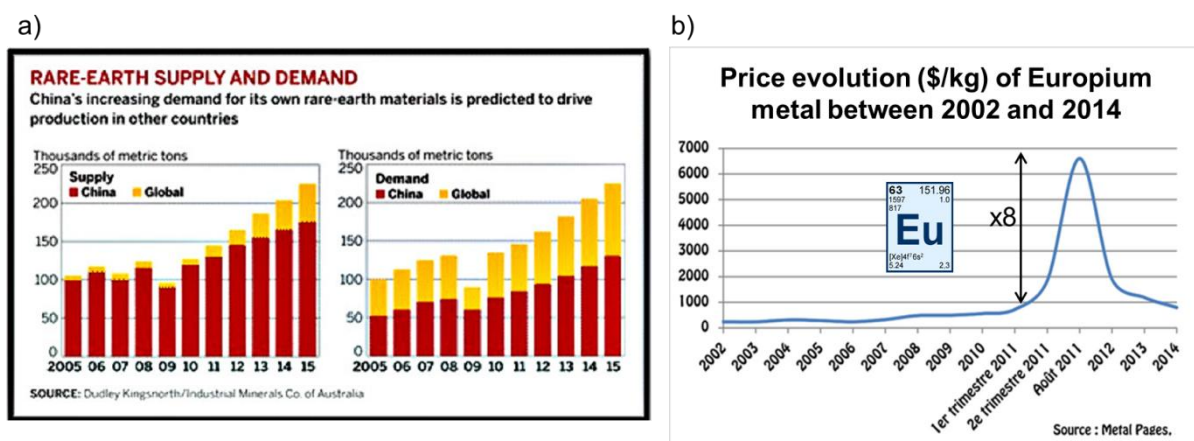


Figure 1 a) Comparison between worldwide and Chinese production and exportation of lanthanides as well as the worldwide demand and b) Evolution of the price of Europium between 2002 and 2014.

There are different possible alternative to replace lanthanide phosphors:

- i) substitute the Ln by transition metal cations. The luminescence properties of these transition metals originate from $d \leftrightarrow d$ electronic transitions, e.g. Mn^{2+} , one of the most study activator exhibits a red emission.
- ii) the OLED (organic LED) could also be a good and promising alternative, they have the main advantage of low cost production.
- iii) the development of quantum dots for which the emission color can be tuned depending on their size .
- iv) replace the lanthanides by ns^2 type ions (Tl^+ , Pb^{2+} , Bi^{3+} , ...), ions possessing a non-bounding pair of electrons on their outer shell (lone pair) responsible for $s^2 \leftrightarrow sp$ radiative transition;

In this thesis, a focus is done on this last option. In fact, it was a great opportunity to combine the knowledge of UCCS group (Univ Lille 1) on the crystallography and specific properties of ns^2 ions (Pb^{2+} , Bi^{3+}) with the expertise on luminescence properties of the Anorganische

Chemie II group (Univ. Siegen) to investigate the relationship between structural and optical properties of selected Bi^{3+} based compounds.

These ions with ns^2 configuration are very advantageous systems because they are able to exhibit extremely bright emission and also efficient excitation due to parity allowed, fast $s^2 \leftrightarrow sp$ electronic transitions. In particular Bi^{3+} based compounds are preferred due to their low toxicity compared to Pb^{2+} , Sb^{3+} or Tl^+ and also due to their large availability. Additionally, their luminescence properties are drastically influenced by the coordination sphere of the emitting cations, which should give a degree of freedom to tune optical properties by chemical substitution in a host-luminescent compound. Furthermore, compared to lanthanides, Bi^{3+} emitters show the advantage to be strong absorbers associated to lower cost. For instance some phases such as $\text{Bi}_4\text{Ge}_3\text{O}_{12}$ are already used for scintillator applications. In the past, the photoluminescence of the ns^2 ions was intensively studied but not very well understood. Especially dealing with Bi^{3+} based frameworks (i.e. stoichiometric ratio of the phosphor), most compounds show complex states of excitation and emission competing transitions, and often display room temperature PL quenching bringing additional experimental difficulties. For example compared to standard Ln^{3+} doped semiconducting phosphors, discrepancies between the absorption bandgap and luminescence excitation at higher energy was sometimes reported but never explained, while no radiative transition is expected in such topology. In this work, we have chosen to investigate bismuth oxo-salts, with a diversity of counter anions (phosphates, arsenates, vanadates, halides) and co-cations. In the related chemical systems, the selected phases show strong structural relationships, bringing arguments for rationalization between the crystal structures and the optical properties. Playing on the chemical nature of both the Bi cationic and anionic coordination sphere and LP stereo-activity results in the possibility to tune the excitation and emission spectra. The influence of the Bi...Bi connectivity in the framework was also studied in different materials and critically high connectivities was pointed out, responsible for the quenching by energy transfer. Energy transfer was also investigated when the Bi^{3+} is co-present with another activator such as Mn^{2+} , Pb^{2+} or VO_4^{3-} groups. The combination of these results give new opportunities to figure out the design of the “ideal” Bi^{3+} based luminescent compound.

Chapter I. Theory and Background

I. Theory and Background

This first chapter deals with the luminescence background necessary in the work that I carried out. First, it describes of the basics of the relevant theory and knowledge useful to understand the main results of the thesis. A brief overview of fundamental concepts such as the decay time, the quantum yield or the quenching effects will be detailed from a theoretical point of view in order to understand their physical origin and main mechanisms. The second part corresponds to a bibliography of the Bi^{3+} luminescence including the Bi^{3+} doped materials, stoichiometric Bi-based compounds and Bi^{3+} used as sensitizers.

I.1. Basic aspects of luminescence

The term “*luminescence*“ was invented by the german physicist G.H. Wiedemann in 1888 and it takes its origin from the greek word “*lumen*“ which means light.¹ Even if this phenomenon was known since the Antiquity, its scientific origin started to be understood only in the middle of the nineteenth century thanks to the work of J. Herschel, E. Becquerel and G. Stokes.

Nowadays, “*luminescence*“ is the common term used for the emission of light from a “cold” material called “phosphor” (\neq *incandescence* where the emission of light comes from heating a material at high temperature, e.g. the filament of metal in bulb lamps).

The luminescence involves usually two main processes, first an electron jumps into a higher energy state after excitation by an external source. It is called the excitation process (or the absorption in some cases). Then, it is followed by vibrational relaxation leading to the relaxed excited state (RES). Such states are unstable and the system tends to return into its fundamental state by emitting a photon, hence it occurs a radiative electronic transition in which an electron returns to the ground state from the higher energy state, it is called the emission process (see figure I-1).

The return to the ground state can be radiative, then a photon is emitted and the luminescence phenomenon is observed at particular energies. It can also be non-radiative. In this second case, the excited electron decays to the ground state without emitting photon. The absorbed energy is mainly transformed into heat and is dissipated in the system, then no emission is observed, the luminescence is quenched. These radiative and non-radiative processes are always in competition against each other, however an efficient phosphor is able to convert most of the absorbed energy into emitted photons. In most of the cases, emission appears at

higher wavelength (lower energy) than excitation. This difference in energy between positions of the maxima band of excitation and emission is called the Stokes shift and corresponds to the energy lost by the system. Graphically, considering a shift Δr between the pertinent interatomic distances of the excited and ground states, smaller is the difference Δr and smaller will be the Stokes shift (see figure I-1) leading to minimize the energy losses by the system.²

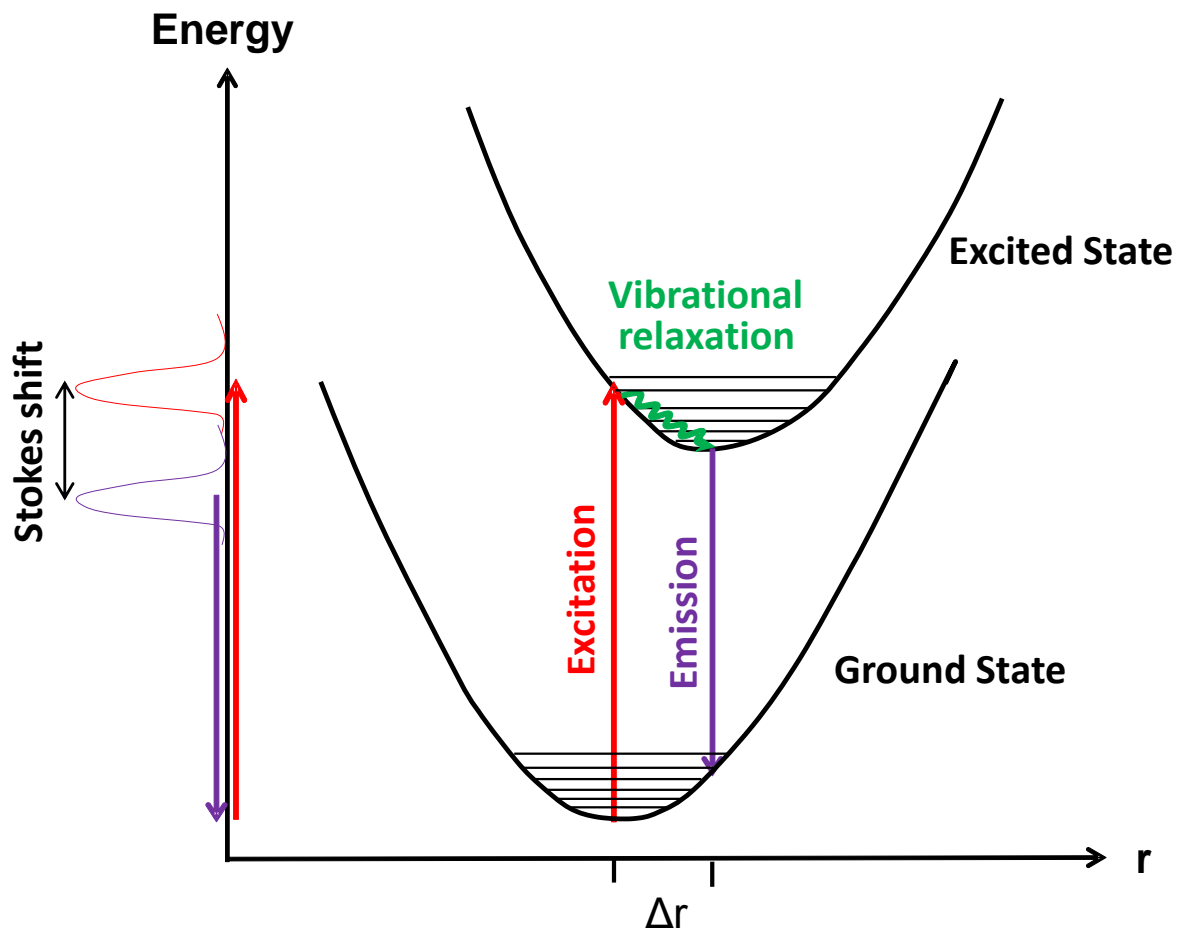


Figure I- 1 Basic sketch of luminescence process, “ r ” represents the interatomic distance.

In this work, only the photoluminescence will be investigated but there are different types of luminescence which are differentiated by the excitation mode. The most common are:

- Chemiluminescence: the excitation is due to a chemical reaction.
- Electroluminescence: a result of an electric current passed through a substance.
- Mechanoluminescence: due to a mechanical action on a solid.
- Photoluminescence: enhanced by absorption of photons.
- Radioluminescence: when a solid is excited by an ionizing radiation.

The photoluminescence includes two different phenomena: fluorescence and phosphorescence. These two phenomena involve different radiative mechanisms of return to the fundamental state. In the fluorescence case, the excited state reached during the light absorption process will be the same electronic state from where the radiative emission starts and the return to ground state transition is allowed by spectroscopic selection rules. Phosphorescence involves a charge transfer from the singlet excited state reached during the excitation (S^*) to another triplet excited state (T^*) from where the return to the ground state (S_0) will happen but it would be forbidden by selection rules (figure I-2). However commonly they are differentiated by the after-glow time. For the fluorescence, the emission process stops very quickly when the excitation source is ceased (10^{-9} to 10^{-5} s) whereas for the phosphorescence, the material can still emit light some seconds, minutes or hours after the excitation process.

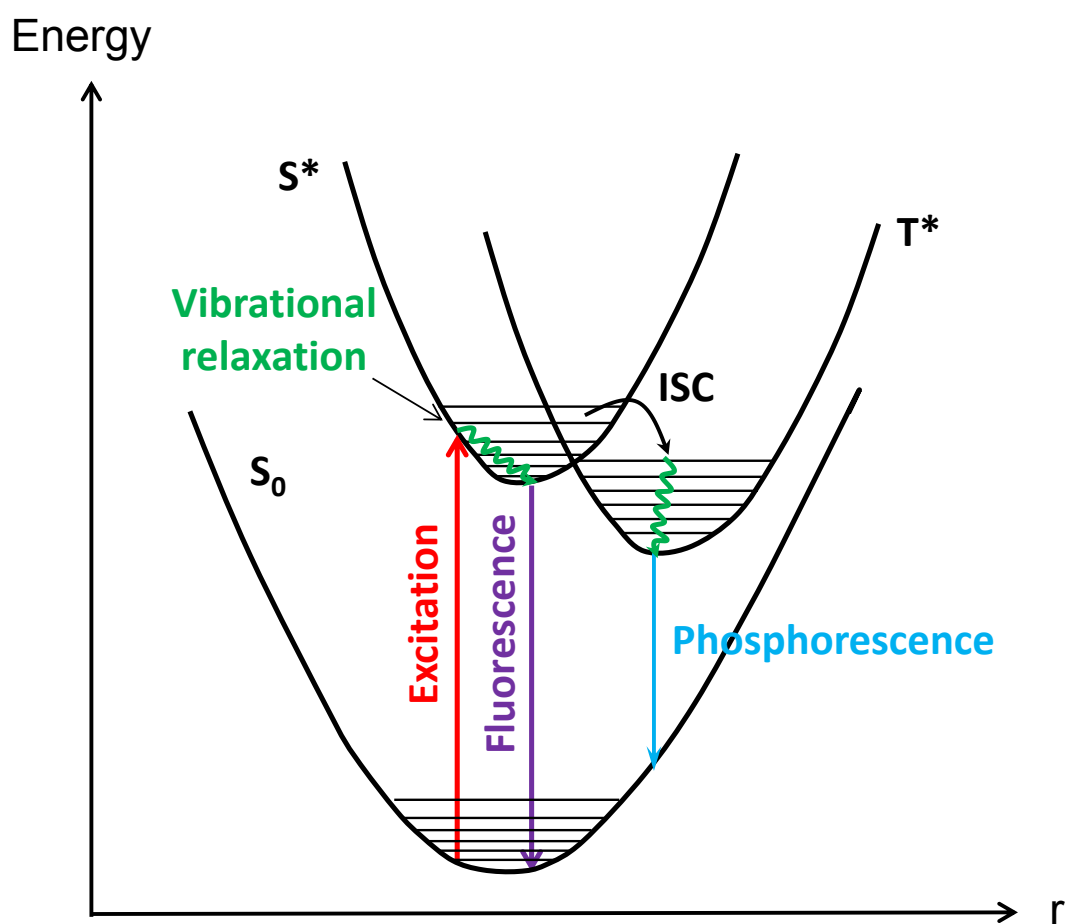


Figure I- 2 Representation of Fluorescence and Phosphorescence processes (ISC means intersystem crossing, S_0 is the ground state, S^* and T^* are two excited states).

Photoluminescence can have different origin, but most of the time it is produced by the intentional incorporation of impurities or defects (extrinsic luminescence) in a host material. These impurities are called “dopants” or “activators” and the materials which exhibit luminescence are named “phosphors”.

These activators can be classified in four types differentiated by the nature of the electronic transitions involving the photoluminescence:

$s^2 \rightarrow sp$ transitions (allowed by selection rules): it concerned Bi^{3+} , Pb^{2+} , Tl^+ , Sb^{3+} , Sn^{2+} ..., all these ions possessing an external lone pair of electrons in their fundamental state.

$f \rightarrow f$ transitions (forbidden by selection rules): Eu^{3+} , Nd^{3+} , Tb^{3+} , Er^{3+} , Pr^{3+} and other trivalent lanthanides (except diamagnetic La^{3+} , Lu^{3+} and Ce^{3+}). These transitions are orbitally forbidden and are expected to be not very intense.

$f \rightarrow d$ transitions (allowed by selection rules): including Eu^{2+} or Ce^{3+} .

$d \rightarrow d$ transitions (forbidden by selection rules): for example in Mn^{2+} , Mn^{4+} , Cr^{2+} , Ti^{3+} .

Also, in semiconductors another type of luminescence can be observed. It happened when donors and accepters act as activators, it involves the transition of a free carrier to a bound carrier or the transition of a bound electron (donor) to a bound hole (acceptor), it is an unlocalized luminescence type.

I.2. Decay time

The decay time or lifetime as well as the quantum yield (see after) are two physical parameters which characterize excited states of the phosphors. The life time corresponds to the average time in which the molecule stays into the excited state before to return into the fundamental state. This value can be calculated knowing the radiative () and non radiative () rates.

Decay time depends on several parameters such as the emitter nature, the type of transition involved or the temperature. For instance transitions allowed by the spectroscopic selection rules will have a shorter decay time than forbidden transitions (i.e. $4f \rightarrow 4f$ transitions in

trivalent lanthanides), (e.g. 2ms for Eu^{3+} against 500ns for Bi^{3+})³⁻⁴ as well as decreasing the temperature in most of the case will increase the decay time for ns² ions.

In absence of non-radiative processes, the radiative rate can be easily deduced from the measurement:

—

The profile of the decay time curve gives access to the number of excited states involved in the radiative emission process (i.e. mono-exponential behavior means only one radiative transition is observed, biexponential behavior shows that two different transitions in competition are involved...) (figure I-3).

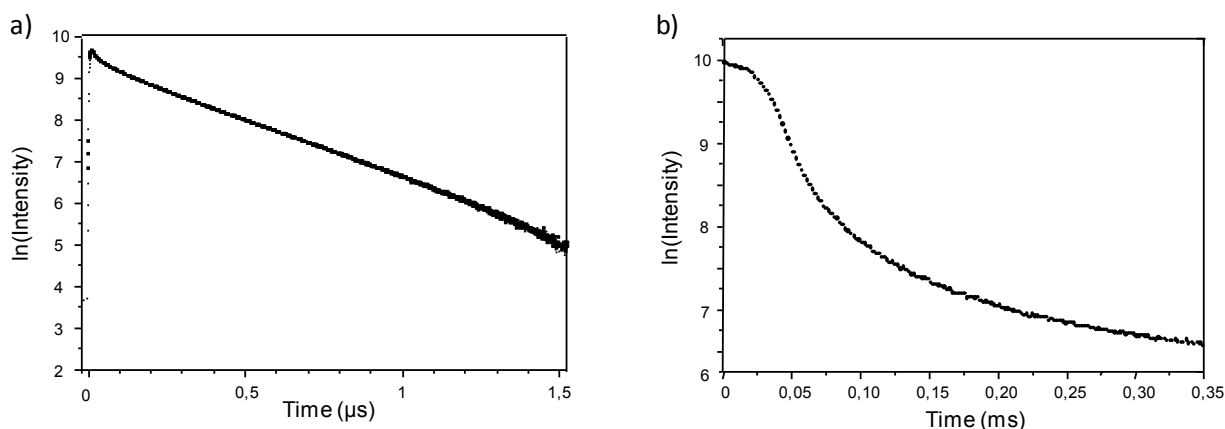


Figure I- 3 a) Example of monoexponential decay time and b) biexponential decay time (for practical reasons, it is plotted $\ln(\text{Intensity})$ against time).

I.3. Quantum Yield

The fluorescence internal quantum yield (IQY) gives the efficiency of the fluorescence process of a phosphor. In other words it corresponds to the probability of the excited state of being deactivated by fluorescence rather than by another, non-radiative mechanism. The internal quantum yield () is defined as the ratio of the number of emitted photons to the number of absorbed photons by a material.

—————

The fluorescence IQY can also be defined by the ratio of the spontaneous emission rate of excited state to the sum of all (radiative and non-radiative) rates of excited state decay:

Where k_r is the rate of spontaneous emission of radiations and k_{nr} is the rate of all non-radiative processes. Other rates of excited state decay are caused by mechanisms other than photon emission and are, therefore, often called "non-radiative rates", which can include: dynamic collisional quenching, near-field dipole-dipole interaction (or resonance energy transfer (FRET)), internal conversion, and intersystem crossing. For instance, the higher the non-radiative rate value k_{nr} , the lower is the quantum yield.

Sometimes the external quantum yield (EQY) is also evoked. It represents the ratio of the number of photons emitted by the phosphor to the number of photons generated by the excitation source. Its value is always lower or equal to IQY.

Before to conclude this paragraph, it is important to notice that a material with a high internal quantum yield has not always a bright luminescence. In fact, the capacity of absorption is also a very important parameter to take account in order to make efficient phosphors.

I.4. Quenching Process

The diminution of emission intensity in photoluminescence is usually related to the term "quenching" which is most of the time undesirable in luminescent materials. This quenching mechanism has different kind of origin but the same effect: it favors the non-radiative process relaxation and hence degrades the emission intensity of the phosphors. Here, the different types of quenching that we can meet for ns^2 ions will be explained more in details.

I.4.1. Quenching via energy transfer

Degradation of luminescence intensity can be due to the resonance energy transfer from the luminescent centers to quenchers which could be defects in the host lattice, unintentional impurities or a center which would not generate an efficient photon. In this case the acceptor

kills the emission and the energy is dissipated into heat. The efficiency of the phosphor also decreases if the concentration of the activator ion is too high, it is called the concentration quenching. The quenching process starts to occur when the optimal/critical concentration of the activator in the host lattice is exceeded. This optimal concentration changes following the nature of the host lattice and the activator. That is the reason why the doping in commercial phosphors never goes over few percentages. When the concentration of activator increases, the average distance between luminescent centers becomes reduced. This case is favorable to energy transfer from an activator ion to another one (resonance energy transfer) and finally to an energy sink via cross-relaxation. Concentration quenching is ascribed to pairing or aggregation of activator ions allowing some of them to act as killer centers and thus, creating a non-radiative return to the ground state (figure I-4). It is also important to note that large Stokes shift reduces energy transfer and therefore concentration quenching.

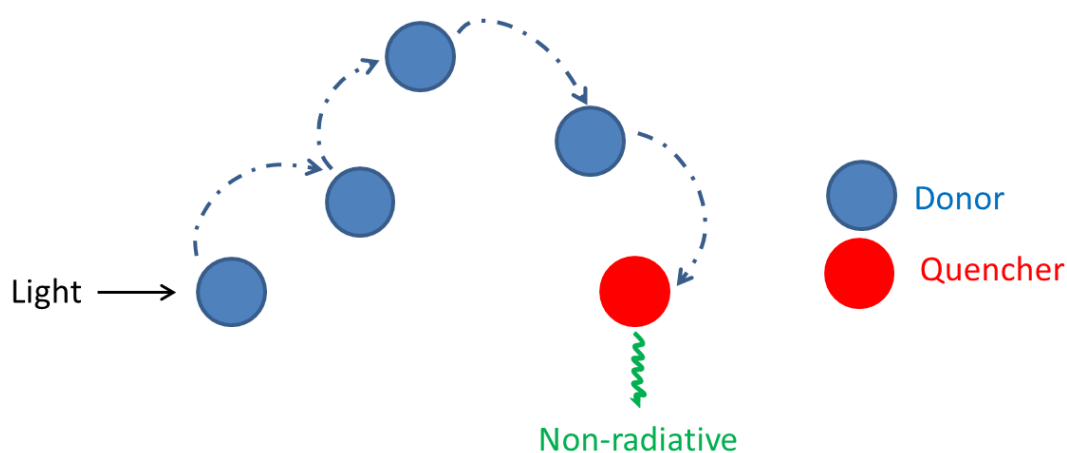


Figure I- 4 Sketch representing possible quenching via energy transfer.

I.4.2. Thermal quenching

The term “thermal quenching” is used to explain decreasing of emission intensity of a phosphor when the temperature rises. It is often the case when the excited state and the ground state curves cross at an energy which is thermally accessible from the relaxed excited state. The figure I-5 is well representative of thermal quenching process. After the excitation process (in red), the system adopts immediately a new equilibrium, the relaxed excited state (in blue). Then the system may undergo a radiative transition (in violet), with emission of photon or when the luminescent center is “thermally activated” the

electron(s) can return to the ground state via the crossing point by a non-radiative way (in green) and the energy is dissipated into heat. A very important Stokes shift increases the probability that the energy (ϵ) between the equilibrium excited state and crossing point of the parabolas is low, hence it increases the thermal quenching (figure I-5).

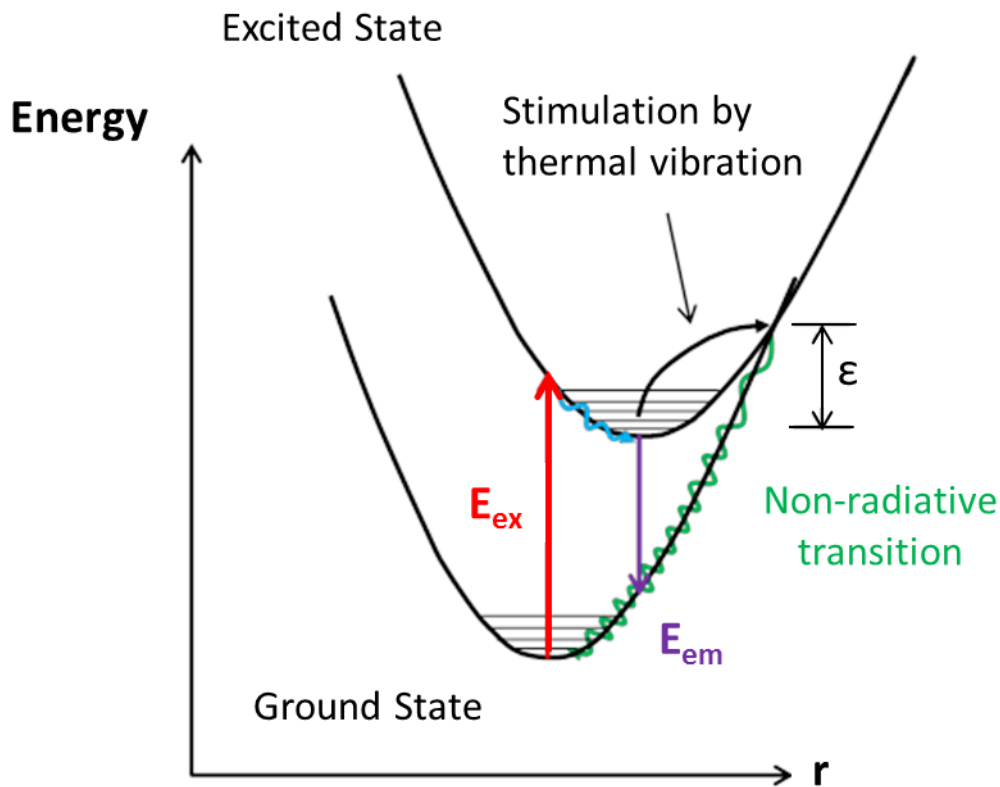


Figure I- 5 Sketch representing mechanism of the thermal quenching.

I.4.3. Killer centers

The luminescent properties of phosphors can be severely damaged or even totally quenched by the intentional or unintentional presence of atoms called killer centers. The most famous of them are the iron group elements: Fe^{2+} , Ni^{2+} , Co^{2+} or the Cu^{2+} .⁵ Even present in very low quantities, they absorb the visible wavelength photons from the phosphor and then relax by emitting photons in the IR range (out of the visible range).⁶ Other killer centers subsist as a deep level traps which generates non radiative path to the fundamental state for the excited emitters.

In order to avoid this type of quenching, it is important to work with reactants as pure as possible and always with a clean stuff.

I.5. Nephelauxetic effect

The concept of nephelauxetic effect (which means “cloud expanding” in Greek) was first introduced by Jørgensen in the 1960's.⁷⁻⁸ This effect is translated by the fact that interelectronic repulsion for a given transition metal is lower in complexes than for the corresponding free ion. This is explained by the formation of metal-ligand bonds which involve overlapping between metal and ligand orbitals, forming a spatially more extended molecular orbital leading to the delocalization of the electronic cloud over a larger area. Decreasing of interelectronic repulsion suggests a wider separation between the same orbital-electrons, as if the electron clouds have “expanded” to some extent.⁹⁻¹⁰ This effect depends on the covalency and the polarizability of metal-ligand (M-L) bonds; hence it depends on the nature of the cation and the ligand(s). When the covalency of a M-L bond increases, the ligand is able to transfer some negative charge to the metal which decreases the partial charge of the given metal and by the way leads to expand its electronic cloud of valence states. From a spectroscopic point of view, this effect shifts the absorption/excitation band to lower energies, i.e. a red shift occurs (see figure I-6 and I-7). It is also noticed that the nephelauxetic effect is more discernible for allowed electronic dipole transitions, and for transitions which involved the outer shell of the electronic configuration. Therefore, this effect can be neglected for the forbidden $4f \rightarrow 4f$ transitions of the lanthanides.

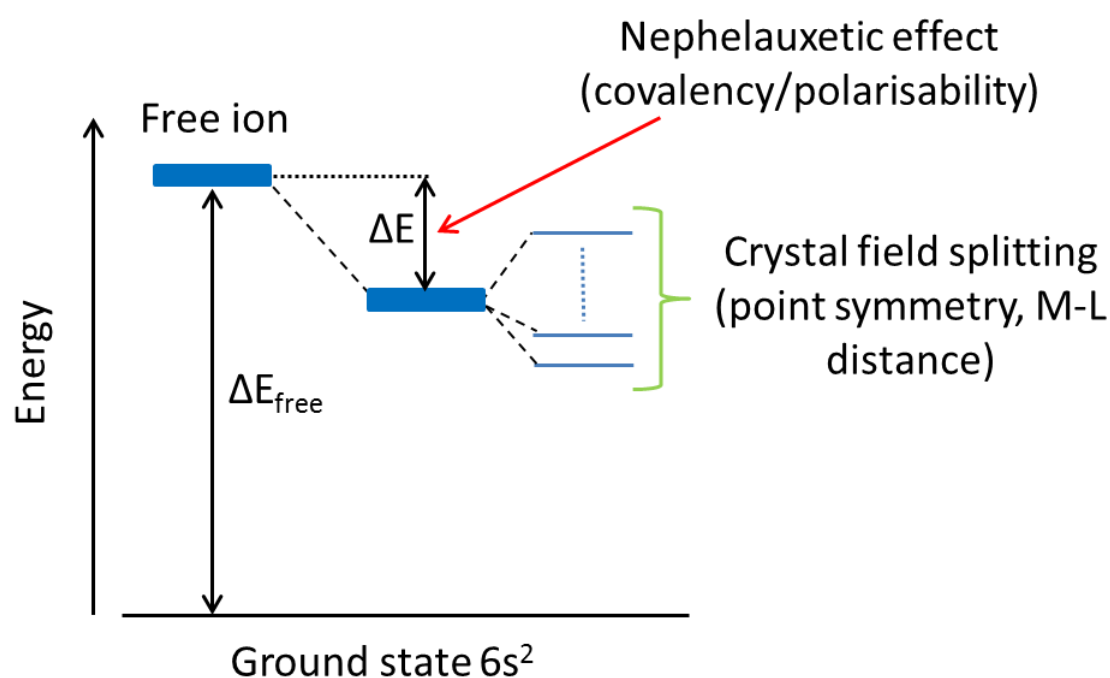


Figure I- 6 Sketch representing the effect of the “Nephelauxetic effect” on energy states.

According to the ref [11], the energies of electronic transitions from the ground 1S_0 level to the excited 3P_0 , 3P_1 , 3P_2 and 1P_1 levels of a free Bi^{3+} ion (E_{free}) are 8.795eV (~141nm), 9.41eV (~132nm), 11.95eV (~104nm) and 14.203eV (~87nm), respectively.

As already mentioned, the nephelauxetic effect depends on the covalency and polarizability of M-L bonds, but the covalency cannot be simply defined by the difference of electronegativity between two atoms on the Pauling scale. In some cases even so-called ionic bonds can have significant covalent character. Covalency between a cation and an anion increases when:

- The cation is small and/or highly charged, in this case the cation is said to be polarizing, and it is able to distort electronic cloud of the neighboring anion and its effect is to increase the electron density between the two atoms compared to an ionic bond. The ability of a cation to deform the electronic cloud of an anion is quantified by the polarizing power.

Polarizing Power is: $\propto \frac{Z}{r^2}$ – where Z is the charge of the cation and r its ionic radius.

- If the anion is large and/or highly negatively charged, then the anion is said to be polarizable. For anions with the same negative charge, the one with the bigger ionic radius is more polarizable ($\text{F}^- < \text{Cl}^- < \text{Br}^- < \text{I}^-$). For anions of similar size, the one who undergoes the greater deformation of his electronic cloud is the greater negative charged (e.g. $\text{S}^{2-} > \text{Cl}^-$).

These rules are called the Fajans' rules.¹²⁻¹³

The polarization of a bond is significant when the cation is highly polarizing and the anion is highly polarizable (see figure I-7).

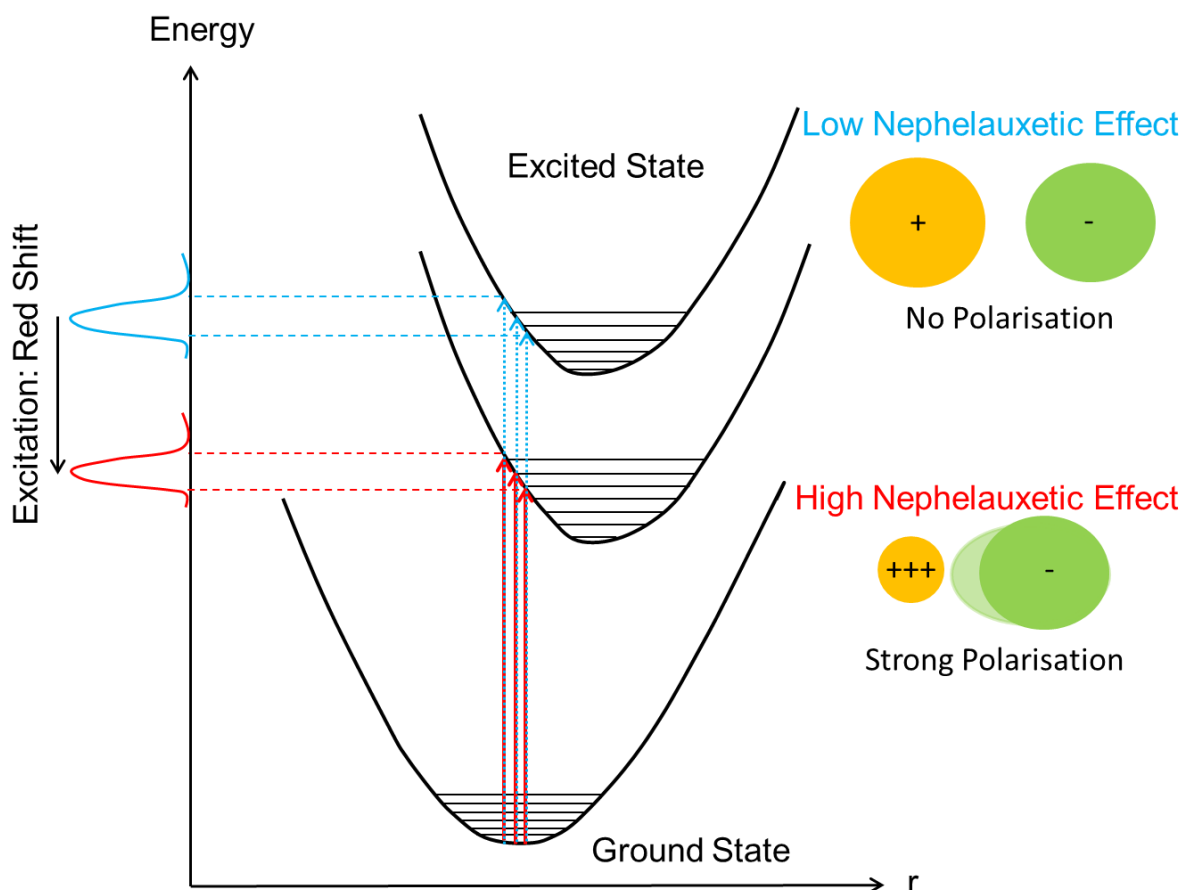
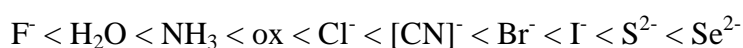


Figure I- 7 In blue the case where there is no polarization/low nephelauxetic effect (example of KCl) and in red the case of a strong polarization/high nephelauxetic effect (example of $AlCl_3$). The electron density of the anion is significantly deformed by the small highly charged cation and the position of excited state is lowered resulting in a red shift.

For a given metal, the ability of ligands to induce this electronic cloud expansion follows the nephelauxetic effect series:



I.6. Luminescence of the ns^2 ions

In this section, the background of the luminescence of ns^2 ions is described, mainly focused on Bi^{3+} ion for the sake of simplicity, but can also be applied to other ns^2 ions. In fact, bismuth is used preferentially as activator instead of lead, antimony or thallium due to its

lower toxicity.¹⁴ Finally a brief review of the literature about the trivalent bismuth luminescence will be presented.

I.6.1. Theory of ns^2 ion

Ions with s^2 configuration (Tl^+ , Pb^{2+} , Bi^{3+} , Sb^{3+} ...) are very advantageous systems, because they are able to exhibit extremely bright emission and also efficient excitation due to parity allowed, fast $s^2 \leftrightarrow sp$ electronic transitions.¹⁵ This transition involves the outer valence shell of the ns^2 ion, hence a strong interaction with the surrounding environment is expected contrary to forbidden $4f \leftrightarrow 4f$ transitions for lanthanides. The ns^2 ions usually have a typical off-center position due to their sterically demanding lone pair of electrons. Hence, its coordination results in short bonds on one side and longer bond distances on the other side. This is known as lone pair or pseudo Jahn-Teller effect. The positions of excitation and emission bands strongly depend on the nature of host lattice, and in this way, it gives access to a large variety of emission wavelengths from blue to red.¹⁶⁻¹⁷

For Bi^{3+} ions, the ground state of the lowest energy configuration $6s^2$ is 1S_0 while the excited configuration $6s6p$ gives rise to a triplet state (3P_0 , 3P_1 , 3P_2) and a singlet state 1P_1 in order of increasing energy. The transition from the ground state 1S_0 to the lower energy excited state 3P_0 is strongly forbidden by the selection rules.¹⁵ Transitions $^1S_0 \rightarrow ^3P_1$ (A-band) and $^1S_0 \rightarrow ^3P_2$ (B-band), are spin forbidden, however, A-band transition becomes allowed by spin-orbit coupling between the 3P_1 and 1P_1 states and in some rare cases, due to vibronic mixing of the 3P_2 with the 1P_1 states, the B-band is detected, but however its intensity is very low. The highest energy transition $^1S_0 \rightarrow ^1P_1$ (C-band) is an allowed electric-dipole transition usually situated in the VUV (high energies) (see figure I-8). The 3P_0 level is assumed to act as a metastable trapping state, i.e. a non-radiative relaxation from 3P_1 to 3P_0 can happen resulting in equilibrium of the Bi^{3+} system.¹⁸ The ratio of population between these two states strongly depends on the temperature. Typically at room temperature, only the emission transition $^3P_1 \rightarrow ^1S_0$ is observed whereas at low temperature $^3P_0 \rightarrow ^1S_0$ becomes significant. The $^3P_{1,0} \rightarrow ^1S_0$ emission is therefore typically characterized by a biexponential decay time. In photoluminescence experiments, only one slightly red shifted emission broad band is observed. This is due to the low energy difference between 3P_1 and 3P_0 states that is referred to as the trap depth.¹⁹

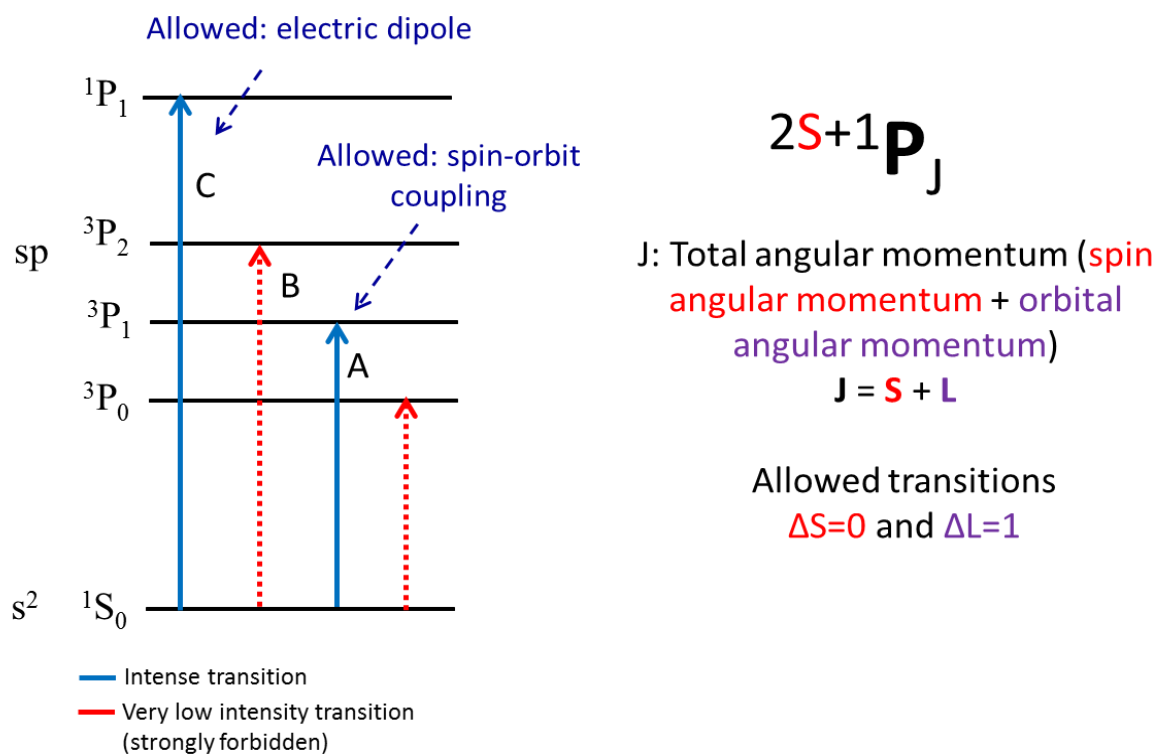


Figure I- 8 Sketch of possible transitions for Bi^{3+} cation and on the right, spectroscopic rules.

Although the emission A-band in most of ns^2 -type based or doped compounds has a simple structure, this A-band in some other cases (e.g. in alkali halide crystals doped with a ns^2 ion) can be composed of two bands: the high-energy band labeled A_T and the low-energy band labeled A_X .²⁰ These bands are ascribed to the coexistence of minima with two different symmetries on the adiabatic potential energy surfaces (APES) of the relaxed excited state and their intensities strongly depend on the temperature. The origin of the two minima is an unclear phenomenon. Sometimes it is referred to a strong spin-orbit (SO) coupling between the 1P_1 and 3P_1 states²⁰ and other publications claim that this phenomenon is mainly governed by the ratio of the spin-orbit coupling, the electron-lattice relaxation and the site symmetry of the ns^2 ion whereas the emission for a strong spin-orbit coupling can be interpreted in term of the SO-split levels 3P_1 and 3P_0 .¹⁵

A fourth transition called D-band can also appear in luminescence spectra, it is attributed to a charge or energy transfer between the Bi^{3+} ion and the host lattice.²¹ This phenomenon takes place when interaction between the s^2 ions and the host lattice is strong. D-level absorption is interpreted as a transition from the Bi^{3+} ground state to the host conduction band states. As

nicely stated by Blasse in his paper “Pandora Box”,²² attribution of excitation and emission bands for ns^2 ions is far from being easy and it is still a subject of controversy.

The energies of excitation and emission bands cannot be exactly predicted by theory but they can be compared between different compounds based on theoretical rules:

The position of excitation band strongly depends on the covalency / polarizability of the ns^2 ion-ligand bonds. An increasing covalency of these bonds leads to a red shift of the excitation band (a shift to lower energy), due to the nephelauxetic effect (see section I.5).⁹

The Stokes shift partly depends on the coordination / site symmetry of the ns^2 ion. Upon excitation, the $6s^2$ ion moves from an off-center position to a position which is closer to the center of the coordination polyhedron. Hence, the larger this relaxation (Δr), the larger is the Stokes shift. This relaxation is usually related to the stereo-activity of the lone pair of electrons: the higher the stereo-activity, the larger is the relaxation. It is easily represented in the potential energy diagram (see figure I-9), where the coordinates of the minimum of the excited state are shifted towards higher metal-ligand distances due to the strong rearrangement of the Bi environment after the excitation process. Usually, low site symmetry leads to a more asymmetrical coordination (high stereo-activity is expected) than high site symmetry and then, a large Stokes shift is expected.

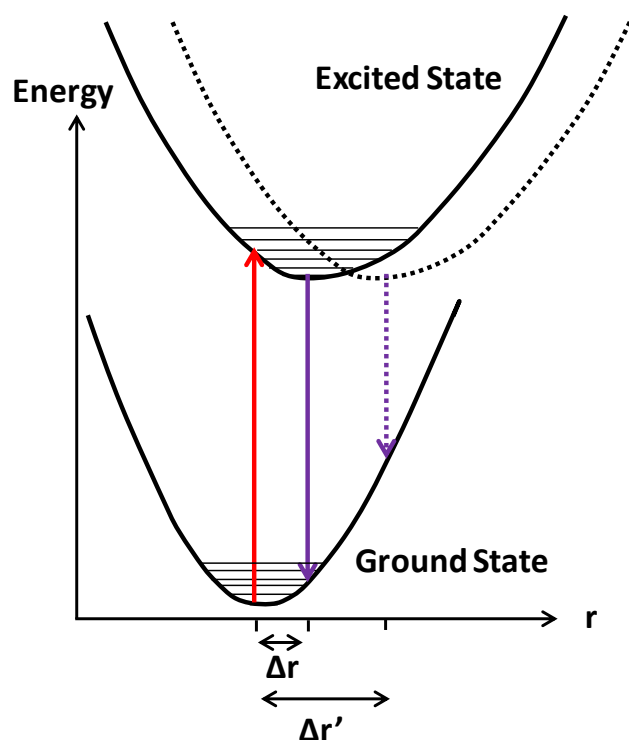


Figure I- 9 Diagram showing the stereo-activity of the lone pair of electrons, a low stereo-activity faintly shifts the excited state Δr and results on a small Stokes shift (full line). A high stereo-activity induces a larger shift $\Delta r'$, and hence induces a bigger Stokes shift (dashed line).

I.6.2. Photoluminescence of Bi³⁺ cation

I.6.2.1. Bi³⁺ as dopant

The photoluminescence of Bi³⁺ as dopant has been studied in a significant number of different hosts since the middle of the last century (silicates,²³ phosphates,²⁴ vanadates,²⁵ aluminates,²⁶ molybdates,²⁷ tungstates,²⁸ borates,²⁹ oxyhalides,³⁰ glasses³¹ and many others). In fact, the easy involvement in chemical combinations (bonding) for the electrons in its p orbital allows to substitute suitably other trivalent cations (Ln³⁺, Y³⁺, Sc³⁺ ...) ³² and makes it a good dopant candidate for phosphors. However, the Bi³⁺ cation can also substitute, in a small amount, divalent cations (i.e. Ca²⁺ in Ca₃Al₂O₆,³³ Zn²⁺ in Zn₂GeO₄,³⁴ Ba²⁺ in Ba₅SiO₄Cl₆).³⁵ In this case, to compensate the excess of positive charge supplied by Bi³⁺, there are different possibilities: M²⁺ vacancies can be created during the preparation process, the formation of interstitial oxygen can balance the excess of charge or three M²⁺ cations are replaced by two Bi³⁺ which will generate two positive defects (Bi_M^{\cdot}) and a negative defect (V''_M).³⁶ When the trivalent bismuth is introduced in a large site as an impurity, it takes an asymmetrical coordination. It was shown by EXAFS measurements in LaPO₄:Bi³⁺ where the Bi³⁺ adopts a more asymmetrical coordination than La³⁺.³⁷ Bi³⁺ ions have attracted much attention due to their emission wavelength which varies from the blue to the red region depending on the host materials¹⁶⁻¹⁷ and also because of its relatively low price compared to lanthanides. The luminescence of Bi³⁺-doped material is nowadays understood even if the assignment of emission bands is sometimes a subject of controversy.²² In 1968, G. Blasse found the relation between the quenching concentration and the critical distance between the same activators.³⁸ Knowing crystal structure parameters and critical transfer distance (R_c) it is easy to find the critical concentration of dopant (χ_c) to not exceed to optimize the emission intensity. Typically, the doping never exceeds few percentages.

— —

Where V is the cell volume and N the number of ions which Bi³⁺ substitutes per unit cell.

In 2012, Lili Wang et al. published a paper in which they are able to “estimate” the position of A and C excitation bands within an accuracy of ±0.50eV for the A-band and ±0.60eV for

the C-band for Bi³⁺ doped compounds using the dielectric theory of the chemical bond for complex crystals.³⁹ They developed empirical relations:

$$E_A = 2.972 + 6.206 \exp(-h_e/0.551)$$

$$\text{And } E_C = 3.236 + 10.924 \exp(-h_e/0.644)$$

where h_e depends on four factors: covalency, coordination number, bond volume polarizability and presented charge which can be calculated knowing the crystal structure of the host and its refractive index n . However, an uncertainty of 0.6eV is very high knowing that usual excitation bands are very broad and hence it could not help for industrial research. In 2011 and 2013, P. Boutinaud developed formulas to predict the position of the excitation of D-band which corresponds to a charge transfer between Bi³⁺ and any type of d⁰ or d¹⁰ cations.⁴⁰⁻⁴¹ The general empirical equation depends on six parameters: the coordination number (CN) of Bi³⁺ and Mⁿ⁺ (the d⁰ or d¹⁰ cation), the shortest distance Bi-Mⁿ⁺ (d_{host}), the ionic radius of the cation that Bi³⁺ substitutes for ($r(\text{host})$) and the electronegativity values (χ) of Bi³⁺ and Mⁿ⁺.

Where $d_{\text{corr}} = d_{\text{host}} + 0.5[r(\text{Bi}^{3+}) - r(\text{host})]$, $k_{\text{CN}'}$ is a constant that is dependent on CN' and an adjustable parameter that is dependent on CN and CN'.

This relation works for Bi³⁺ doped compounds with an uncertainty of 3000cm⁻¹ (0.372eV) which is better than prediction of C-band but it remains high. Moreover this relation cannot be applied for bismuth based compounds. All these empirical methods have their limits and cannot give very accurate results due to the complexity of processes involved in the luminescence of Bi³⁺. Another option to correlate the excitation processes with the structure would be the use of first principles calculations, as it was done successfully for Eu³⁺ doped in BiOCl or for organic compounds,⁴²⁻⁴³ but to my knowledge, it was never attempted for Bi³⁺ doped compounds. However, it has been started to be done for Bi-based compounds⁴⁴⁻⁴⁵ but it only gives information on the nature of the luminescence. It is still impossible to predict the excitation band positions and even less the emission band positions.

I.6.2.2. Photoluminescence of Bismuth based compounds

Concerning stoichiometric Bi-based compounds, their luminescence properties were also studied during the last century, mainly by G. Blasse.⁴⁶⁻⁴⁷ Even if most of them do not emit light at room temperature due to concentration quenching, it is possible to find exceptions which are remarkable due to the very high concentration of activator ions. The spectroscopic assignment of excitation and emission bands typically located in the UV and the visible range respectively, the large Stokes shifts and the temperature dependent decay times were discussed in the literature.⁴⁸ The most famous luminescent Bi-based compound is the $\text{Bi}_4\text{Ge}_3\text{O}_{12}$ (BGO). It was widely investigated certainly because of its application as a scintillation detector. The emission of BGO is characterized by a broad band with a maximum in the blue region around 490nm whereas its excitation is situated in the UV range (max $\approx 290\text{nm}$) and it presents a large Stokes shift (14500cm^{-1}). The origin of its photoluminescence emission was unclear in the past⁴⁹⁻⁵⁰ but recently it was confirmed that the radiative recombination is localized on Bi^{3+} .⁵¹ For other compounds like $\text{K}_3\text{Bi}_5(\text{PO}_4)_6$ or BiBaO_2Cl ,^{45,52} the luminescence undoubtedly stems from Bi^{3+} ions whereas in BiMg_2VO_6 (very close to compounds presented in this work), the emission was very recently attributed to the vanadate groups $(\text{VO}_4)^{3-}$.⁵³ A very puzzling point for many Bi-based compounds is that the excitation band energy starts at higher energy than the bandgap value. It means the activator's discrete excited states are situated inside the conduction band (CB) and not inside the gap or at the bottom of the CB, which is rather uncommon. This particularity has been already reported in several cases⁵⁴⁻⁵⁵ but was never really discussed in the literature. A discussion will be done in this work. It should also be mentioned that inorganic-organic hybrid compounds can also show interesting luminescence properties, as it is the case for $\text{Bi}_2(\text{O})(\text{Pyr})(\text{H}_2\text{O})$ or $\text{Bi}(\text{HPyr})$.⁵⁶

I.6.2.3. Bi^{3+} as sensitizer

Nowadays, trivalent bismuth is more studied as a sensitizer in order to reach higher luminescence efficiencies. In such cases, Bi^{3+} is excited before transferring its energy to another activator ion which finally emits light. Due to the fact that the transition of the A-band is an allowed transition (see section 1.6.1), the Bi^{3+} has a higher absorption cross section than, for example trivalent lanthanides, for which the $4f \rightarrow 4f$ transitions are forbidden. For applications, the other advantage of using Bi^{3+} as sensitizer for white-LEDs is that this ns^2 ion does not absorb in the visible range which avoids a re-absorption of the blue part of emission

spectra. In literature, there are a lot of recent publications in which the Bi^{3+} is used as sensitizer for trivalent lanthanides (Eu^{3+} ,⁵⁷⁻⁵⁸ Sm^{3+} ,⁵⁷ Tb^{3+} ,⁵⁸ Yb^{3+} ,⁵⁸ Nd^{3+} ,⁵⁸ Dy^{3+} ,^{57,59-60} Pr^{3+} ,⁶¹ ...). As it was seen previously for Bi^{3+} as a dopant, it is possible to determine the optimal concentration of the sensitizer with a simple equation by the same formula.³⁸

Moreover, the trivalent oxidation state of the bismuth is not the only one which can generate luminescent emissions. Researchers have also an interest on Bi^{+} ⁶² and Bi^{2+} ⁶³⁻⁶⁴ optical properties, these oxidation states are unstable but can be observed in very small quantities in some host lattices. They are most of the time characterized by an orange/ red luminescence and involve different optical transitions than these presented before for Bi^{3+} .

References :

- [1] Wiedemann, E., *Annalen der Physik*, **1888**, 34, 446.
- [2] García Solè, J.; Bausà, L.E.; Jaque, D., *An Introduction to the Optical Spectroscopy of Inorganic Solids*, Wiley, (2005).
- [3] Zhang, Z.W.; Liu, L.; Song, S.T.; Zhang, J.P.; Wang, D.J., *Current Applied Physics*, **2015**, 15, 248.
- [4] Xu, W.; Peng, M.; Ma, Z.; Dong, G.; Qiu, J., *Optics Express*, **2012**, 20, 15692.
- [5] Klasens, H.A., *Nature*, **1946**, 158, 306.
- [6] Shionoya, S., *Phosphor handbook*, Boca Raton, CRC Press, 231, (1999).
- [7] Jaurgensen, C. K., *Prog. Inorg. Chem.*, **1964**, 4, 73.
- [8] Jaurgensen, C. K., *Adv. Chem. Phys.*, **1963**, 5, 33.
- [9] Tchougreeff, A. L.; Dronskowski, R., *International Journal of Quantum Chemistry*, **2009**, 109 (11), 2606.
- [10] Moens, J.; Jaque, P.; De Proft, F.; Geerlings, P., *ChemPhysChem*, **2009**, 10, 847.
- [11] Gorbenko, V.; Krasnikov, A.; Mihokova, E.; Nikl, M.; Zazubovich, S.; Zorenko, Y., *J. Lumin.*, **2013**, 134, 469.
- [12] Fajans, K., *Naturwissenschaften*, **1923**, 11, 165.
- [13] Fajans, K.; Joos, G., *Zeitschrift für Physik*, **1924**, 23, 1.
- [14] Mohan, R., *Nature Chemistry*, **2010**, 2, 336.
- [15] Blasse, G. and Grabmaier, B. C., *Luminescent Materials*, Springer, Berlin, (1994).
- [16] Timmermans, C.W.M.; Blasse, G., *J. Solid State Chem.*, **1984**, 52, 222.
- [17] Aliev, A.; Olchowka, J.; Colmont, M.; Capoen, E.; Wickelder, C.; Mentré O., *Inorg. Chem.* **2013**, 52, 8427.
- [18] Boulon, G.; Moine, B.; Bourcet, J.C.; Reisel, L.; Kalinsky, Y., *J. Lumin.*, **1979**, 18/19, 924.
- [19] Van der Steen, A.C.; Van Hesteren, J.J.A.; Slok, A.P., *J. Electrochem. Soc.*, **1981**, 128, 1327.
- [20] Yen, W.M.; Shionoya, S.; Yamamoto, H., *Phosphor Handbook* (second edition), Taylor and Francis, (2006).
- [21] Srivastava, A.M. ; Beers, W.W., *J. Lumin.*, **1999**, 81, 293.
- [22] Blasse, G., *J. Lumin.* **1997**, 72, 129.
- [23] Zorenko, Y.; Gorbenko, V.; Zorenko, T.; Malinowski, P.; Jary, V.; Kucerkova, R.; Beitlerova A.; Mares, J.A.; Nikl, M.; Fedorov, A., *J. Lumin.*, **2014**, 154, 525.
- [24] Srivastava, A.M.; Camardello, S.J., *Optical Mater.*, **2015**, 39, 130.
- [25] Kang, F.W.; Peng, M.Y.; Yang, X.B.; Dong, G.P.; Nie, G.C.; Liang, W.J.; Xu, S.H.; Qiu, J.R., *J. Mater. Chem. C*, **2014**, 2, 6068.
- [26] Krasnikova, A.; Lipińska, L.; Mihokova, E.; Nikl, M.; Shalapska, T.; Suchocki, A.; Zazubovich, S.; Zhydachevskii, Ya., *Optical Mater.* **2014**, 236, 1705.
- [27] Kang, F.W.; Peng, M.Y.; Xu, S.H.; Ma, Z.J.; Dong, G.P.; Qiu, J.R., *Europ. J. Inorg. Chem.*, **2014**, 2014, 1373.
- [28] Jin, Y.H.; Hu, Y.H.; Chen, L.; Wang, X.J.; Ju, G.F.; Mu, Z.F., *Radiation Measurements*, **2013**, 51-52, 18.
- [29] Mu, Z.; Hu, Y.; Chen, L.; Wang, X.; Chen, R.; Wang, T.; Fu, Y.; Xu, J., *Displays*, **2014**, 35, 147.
- [30] Wolfert, A.; Blasse, G., *J. Lumin.*, **1985**, 33, 213.
- [31] Torrenço, S.; Paul, M.C.; Halder, A.; Das, S.; Dhar, A.; Sahu, J.K.; Jain, S.; Kir'yanov, A.V.; d'Acapito, F., *J. Non-Cryst. Solids*, **2015**, 410, 82.
- [32] Sun, H.T.; Zhou, J.; Qiu, J., *Progress in Materials Science*, **2014**, 64, 1.
- [33] Ju, H.; Deng, W.; Wang, B.; Liu, J.; Tao, B.; Xu, S., *J. Alloys Compounds*, **2012**, 516, 153.
- [34] Zhang, S.A.; Hu, Y.H.; Chen, R.; Wang, X.J.; Wang, Z.H., *Optical Mater.* **2014**, 36, 1830.
- [35] Lai, S.; Yang, Z.; Wang, R.; Wu, H.; Liao, J.; Qiu, J.; Song, Z.; Yang, Y.; Zhou, D., *J. Mater. Sci.*, **2013**, 48, 8566.

- [36] Yang, Z.W.; Liao, J.Y.; Wang T.Y.; Wu, H.J., Qiu, J.B.; Song, Z.G.; Zhou, D.C., *Mater. Express*, **2014**, *4*, 172.
- [37] Van Zon, F.B.M.; Koningsberger, D.C.; Oomen, E.W.J.L.; Blasse, G., *J. Solid States Chem.*, **1987**, *71*, 396.
- [38] Blasse, G., *Phys. Lett. A*, **1968**, *28*, 444.
- [39] Wang, L.L.; Sun, Q.; Liu, Q.Z.; Shi, J.S., *J. Solid States Chem.*, **2012**, *191*, 142.
- [40] Boutinaud, P.; Cavalli, E., *Chem. Phys. Letters*, **2011**, *503*, 239.
- [41] Boutinaud, P., *Inorg. Chem.*, **2013**, *52*, 6028.
- [42] Yi, J.; Zhao, Z.Y., *J. Lumin.*, **2014**, *156*, 205.
- [43] An, C.A.; Guo, Y.C.; Si, Z.J.; Duan, Q., *J. Fluoresc.*, **2014**, *24*, 847.
- [44] Zhao, L.; Zhang, X.; Fan, C.; Liang, Z.; Han, P., *Phys. B Cond. Matter*, **2012**, *407*, 3364.
- [45] Hizhnyi, Y.A.; Nedilko, S.G.; Chornii, V.P.; Slobodyanik, M.S.; Zatovsky, I.V.; Terebilenko, K.V., *J. Alloys Compounds*, **2014**, *614*, 420.
- [46] Folkerts, H.F.; Zuidema, J.; Blasse, G., *Chem. Phys. Letters*, **1996**, *249*, 59.
- [47] Pei, Z.; van Dijken, A.; Vink, A.; Blasse, G., *J. Alloys Compounds*, **1993**, *204*, 243.
- [48] Oviedo, M.J.; Contreras, O.; Rodriguez, C.E.; Macedo, Z.S.; Hirata, G.A.; McKittrick, J., *Optical Mater.*, **2012**, *34*, 1116.
- [49] Weber, M.J.; Monchamp, R.R., *J. Appl. Phys.*, **1973**, *44*, 5495.
- [50] Moncorge, R.; Jacquier, B.; Boulon, G., *J. Lumin.*, **1976**, *14*, 337.
- [51] Itoh, M.; Katagiri, T.; Mitani, H.; Fujita, M.; Usuki, Y., *Phys. Status Solidi B*, **2008**, *245*, 2733.
- [52] Porter-Chapman, Y.; Bourret-Courchesne, E.; Derenzo, S.E., *J. Lumin.*, **2008**, *128*, 87.
- [53] Barros, A.; Deloncle, R.; Deschamp, J.; Boutinaud, P.; Chadeyron, G.; Mahiou, R.; Cavalli, E.; Brik, M.G., *Optical Mater.*, **2014**, *36*, 1724.
- [54] Polosan, S.; Galca, A.C.; Secu, M., *Solid State Sci.*, **2011**, *13*, 49.
- [55] Brixner, L.H., *Mat. Res. Bull.*, **1978**, *13*, 563.
- [56] Feyand, M.; Koppen, M.; Friedrichs, G.; Stock, N., *Chem. Eur. J.*, **2013**, *19*, 12537.
- [57] Huang, M.N.; Ma, Y.Y.; Xiao, F.; Zhang, Q.Y., *Spectrochimica Acta Part a-Molecular and Biomolecular Spectroscopy*, **2014**, *120*, 55.
- [58] Smola, S.; Rusakova, N.; Korovin, Y., *J. Coord. Chem.*, **2011**, *64*, 863.
- [59] Su, Q.A.; Pei, Z.W.; Lin, J.; Xue, F., *J. Alloys Compounds*, **1995**, *225*, 103.
- [60] Zhang, W.; Liu, S.; Hu, Z.; Liang, Y.; Feng, Z.; Sheng, X., *Materials Science and Engineering B-Advanced Functional Solid-State Materials*, **2014**, *187*, 108.
- [61] Zorenko, Y.; Gorbenko, V.; Savchyn, V.; Zorenko, T.; Nikl, M.; Mares, J.A.; Beitlerova, A.; Jary, V., *J. Lumin.*, **2013**, *141*, 137.
- [62] Bjerrum N.J.; Boston C.R.; Smith J.P., *Inorg. Chem.*, **1967**, *6*, 1162.
- [63] de Jong, M.; Meijerink, A.; Barandiaran, Z.; Seijo, L., *J. Phys. Chem. C*, **2014**, *118*, 17932.
- [63] de Jong, M.; Meijerink, A.; Gordon, R.A.; Barandiaran, Z.; Seijo, L., *J. Phys. Chem. C*, **2014**, *118*, 9696.

Chapter II. Experimental part and methodology

II. Experimental part and methodology

The aim of this work was to find the relation between structure and optical properties of Bi³⁺ based compounds. In order to do that, different characterization methods to investigate physical and chemical properties of the concerned phosphors were used. Basically, for each compound, the “purity” of the sample was checked with powder X-ray diffraction. Room and low temperature photoluminescence analyses were performed to get positions and shapes of excitation and emission bands. Decay time measurements gave more information on the nature of emission transitions. UV-Vis spectra showed the absorption edge of the semi-conductors and a Kubelka-Munk fit allowed to obtain the bandgap value. Density Functional Theory (DFT) calculations helped to determine the orbital composition of the valence and conduction bands as well as the nature (direct or indirect) of the gap. Single crystal measurement gave the structure of the compounds. Other technique like MEB analyses, Infra-Red, BET, quantum yield measurements were also used for specific cases. To resume, this chapter “Experimental methods” will present the main techniques and devices used during this thesis.

II.1. X-ray diffraction

X-ray diffraction is based on the interaction of a monochromatic X-ray beam with crystalline matter, this results in an elastic and coherent scattering of radiation with a specific wavelength in certain directions perfectly defined in the space which are characteristic of the crystal structure of the compounds.

Single crystal diffraction: This technique allows a very accurate measurement of the diffracted intensities during the data collection by controlling the crystal orientation. Reflections have an excellent spatial resolution which makes it the preferred technique to determine the crystal structure of new crystalline compounds.

Powder diffraction: Mainly used to identify crystalline phases. Nevertheless, this technique can also be a good alternative to do structural refinement in absence of single crystals. However, powder diffraction has an important drawback compared to single crystal diffraction, since this method only allows a monodimensional projection of the reciprocal space network which is in reality 3-dimensional. This has for consequences important losses of information leading to reflection covering, in particular for low symmetry structures or big

unit cells and hence, making it very difficult to extract intensity factors needed to solve the structure.

II.1.1. Single crystal diffraction

Single crystal measurements were performed using an APEX DUO (Bruker-AXS) single crystal diffractometer. It combines molybdenum and copper X-ray sources with a highly accurate 4-axis KAPPA goniometer and is equipped with a bi-dimensional CCD-4K detector. A low-temperature Oxford Cobra Plus system enables measurements from room temperature down to 100K (in order to reduce thermal vibrations or to observe an eventual structure transformation) (figure II-1).

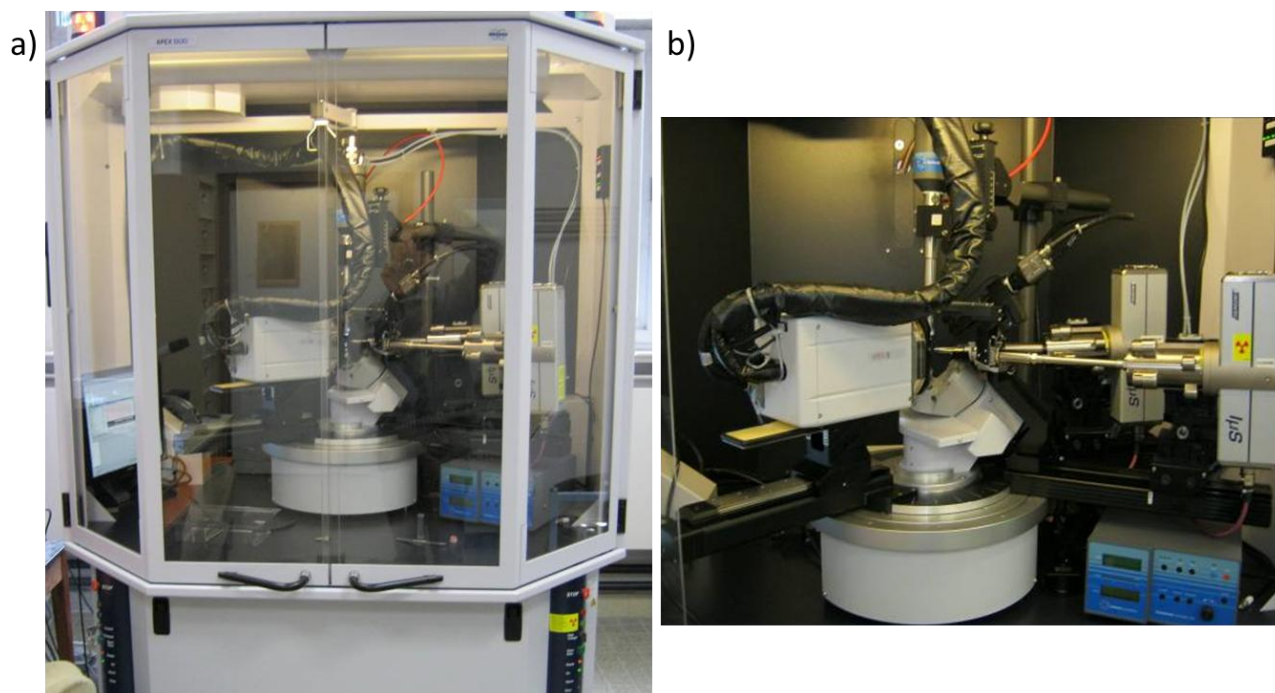


Figure II- 1 a) Picture of an APEX DUO (Bruker-AXS) single crystal diffractometer and b) Zoom from the inside of the chamber.

The crystal is deposited on the extremity of a thin glass fiber stacked on a goniometric head which allows the orientation of the crystal in all the space directions and at the same time, keeping it in the X-ray beam focus. The selection of a good quality crystal is a very important step which can take several hours sometimes. In fact, poor crystal quality will always give bad data, making the structure resolution very difficult.

Experimental part and methodology

Once the crystal is centered, a first and quick test based on 3 runs of 12 images with a scanning along Ω angle (rotation about an axis perpendicular to the beam) and an exposure time of 20s is started. It allows to determine the symmetry (Laue group) and the cell parameters of the single crystal. These information will define the parameters used for the data collection which corresponds to a scanning of the reciprocal sphere in order to harvest all the reflections with an intensity $I \geq 3\sigma(I)$ needed to resolve the structure.

The single crystal structural determination (or structural elucidation) consists of the determination of the electron density distribution corresponding to the position of atoms in the unit cell from the data obtained by X-ray diffraction. Data acquisition was done with the APEX DUO (Brüker-AXS) single crystal diffractometer cited before.

The intensities diffracted by atomic planes are measured for all the lattice family planes (written with Miller indices h, k, l) of the Ewald sphere depending on the symmetry of the crystal. Bragg's law is respected for each lattice plane (hkl) in diffraction position.

where λ is the wavelength of the radiative source (Mo $K\alpha$ or Cu $K\alpha$), d the spacing between diffracting planes, θ the incident angle and n an integer number.

Then, we proceed to the structural determination.

The diffracted beam is characterized by its amplitude which is a vectorial size: The relation between the F_{hkl} module called structure factor, and the atomic positions is given by the following equation:

With N = number of atoms in a unit cell

= atomic form factor of the atom j

, and = atomic coordinates of the atom j

The electron density at each point (x,y,z) is proportional to the Fourier transform of the structure factor. It is defined in terms of a Fourier series:

—

with V is the volume of unit cell

The density of electrons allows to find the atom positions: the atomic positions correspond to the maxima of electronic density. The experimental measurements give access to the intensities of the diffracted beams which are proportional to the square of the structure factor.

These collected intensities are extracted and corrected for Lorentz-polarization factor with the software SaintPlus 6.025 from Bruker.¹ This correction is needed because the entire planes (hkl) passing through positions in which they satisfied the condition for reflection do not occupy such positions in equal lengths of time during the crystal rotation. Moreover absorption corrections linked to the geometry of the crystal are done with the software SADABS.²

Structural resolution: As the cell parameters and the Laue group were determined before the collection of intensities, the first step is to find the right space group. It is defined following the extinction rules with XPREP program (SHELX).³ Then different possibilities exist to solve the structure.

Concerning the structure elucidation, in a first time direct methods for the determination of the position of heavy atoms were used.³ After that, the structure was refined with Jana 2006⁴ using the least squares method including the lighter atom positions like oxygen and the anisotropic atomic displacement parameters for heavy atoms. Finally, depending on the cases, isotropic extinction parameters and site occupancy factor (SOF) can also be refined.

The refinement advancement is controlled by several parameters as the GOF (goodness of fit), wR (weighted R-factor) and especially by the reliability coefficient (R) which represents the average of relative error on structure factors.

These parameters allow to judge the quality of the refinement, they should as lower as possible.

II.1.2. Powder X-ray diffraction

Two different diffractometers were used to get XRD powder pattern:

For room temperature measurements, the D8 Passeur from Bruker-AXS was used (figure II-2). This device is equipped with a rapid linear Lynxeye detector and an auto sampler with 90 positions working in transmission as well as in reflection geometry, using $\text{CuK}_{\alpha 1}$ ($\lambda_1=1.54056\text{\AA}$) and $\text{CuK}_{\alpha 2}$ ($\lambda_2=1.54439\text{\AA}$) radiation with intensities $I_{\lambda_1}/I_{\lambda_2} = 0.5$. It enables a quick switch between the para-focusing Bragg-Brentano geometry to parallel beam geometry without realignment system. In the θ/θ configuration the sample holder is fixed whereas the X-ray tube and the detector turn around the sample with an angle θ .

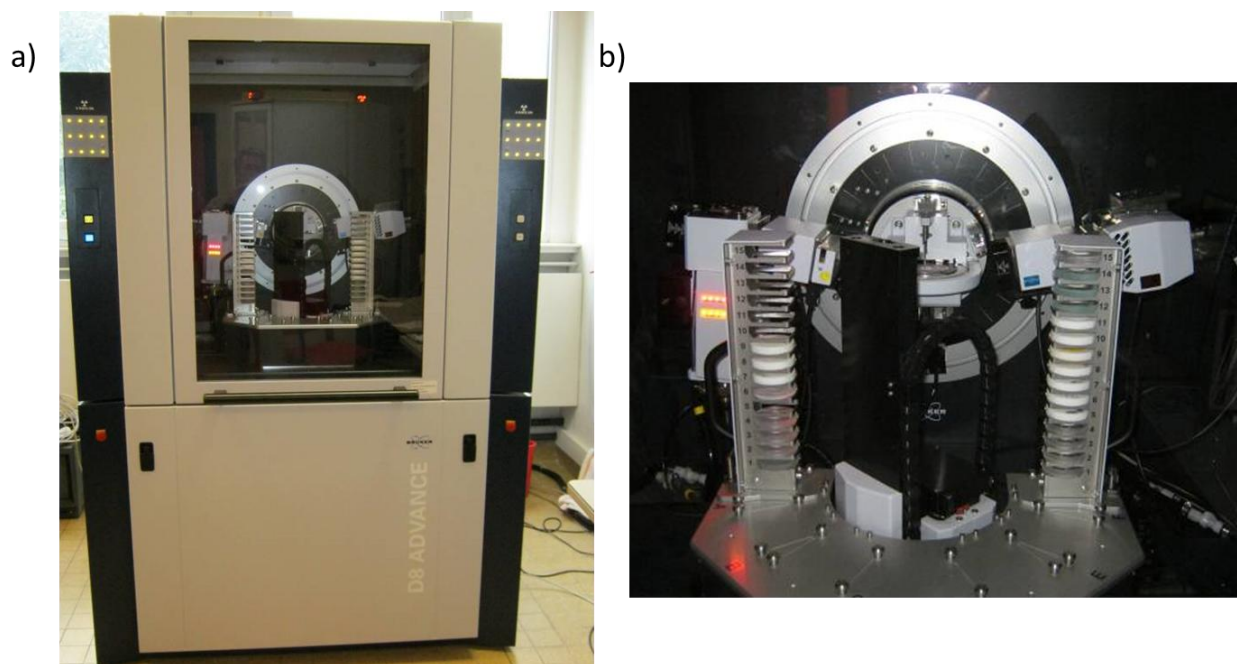


Figure II- 2 a) Picture of a D8 Passeur (Bruker-AXS) diffractometer and b) Zoom from the inside of the chamber.

Sometimes the resolution qualities of the measurements provided by the diffractometers were not enough good to perform a powder structural refinement. Then, in order to get higher resolution diffractogram, samples were collected on the Synchrotron 11-BM beamline at the Advanced Photon Source (APS, Argonne National Laboratory) with a wavelength of $\lambda=0.4137\text{\AA}$. This shorter wavelength of the synchrotron X-ray beam compared to $\text{CuK}_{\alpha 1}$ ($\lambda_1=1.54056\text{\AA}$) of our diffractometer provides greater structural information for the sample,

by enabling more observations over a wider Q-range (especially for smaller d-spacing and Q is the scattering vector), which is essential for correct pattern indexing and it also strongly reduces or eliminates fluorescence problems for most samples. The higher energy radiation source reduces the sample absorption which allows using the transmission geometry even for compounds based on heavy elements to avoid the preferential orientation problem common for reflection geometry instruments.

All the characteristics and advantages of the Argonne Synchrotron diffractometer are resumed on the website page <http://11bm.xray.aps.anl.gov/faq.html>.

The phase identifications of the sample were done with EVA or Match software. The sample's diagram is compared by a computer treatment to a database called powder diffraction file (PDF) after a previous selection of possible elements present in the sample. This comparison is done on two main criteria which are the peak positions and their intensities. This method is useful to show if the sample is pure, and if not, by selecting extra peaks which not belong to the desired phase and by making a DIF file, it is in most of the cases possible to identify the impurities. Another advantage of this method is that it allows distinguishing different allotropic forms for a same compound.

II.1.3. Powder structural refinement

The data analyses were carried out by the Rietveld method.⁵ When the growing of single crystal with an adequate size for single crystal diffraction measurement is difficult, this method is a good alternative to find out a structural model of the material. Rietveld analysis gives access to information like cell parameters of the unit cell, space group, atomic positions, site occupations and atomic displacements (isotropic or anisotropic)... This technique relies on a comparison of intensities and the profile of an observed diagram with a calculated one where the calculated one is based on the hypothesis of a correct structural model. These types of refinement were carried out with Fullprof software.⁶⁻⁷

The first step of the refinement is a “profile matching” also called “Le Bail method”⁸ consists on the refinement profile parameters without the knowledge of the crystalline structure. For this the approximate cell parameters should be known or can be found by doing an indexing with software as DicVol.⁹ The aim of this step is to determine the best profile function which

Experimental part and methodology

corresponds to the experimental diffraction pattern. During my thesis it was done following this order:

The background points were peaked manually from the input diffractogram file with WinPlotter program (included in Fullprof Suite).¹⁰ Typically the background was composed of 40-50 points. Then the 2θ zero point and the cell parameters were refined to adjust the position of the calculated peaks whereas the background is kept fix. After that, the parameters W , V and U of the Caglioti formula ($H^2 = U \tan^2\theta + V \tan\theta + W$ where H represents the FWHM) were refined in this order to adjust the peak profile.¹¹ The peak profile is described as a mixture of Gaussian and Lorentzian behavior and in the cases in this thesis, the Pseudo-Voigt profile ($V_p(2\theta) = \eta L(2\theta, H) + (1 - \eta) G(2\theta, H)$) fits the best. Then the η parameter (proportion between Gaussian and Lorentzian behavior) must be also refined. At the end, if necessary, the asymmetrical parameters were finally refined at low 2θ angles. To match the experimental and theoretical profiles, the least-squares method is used. It gives an output factor χ^2 which shows the agreement between experimental and simulated profile (the χ^2 parameter has to tend as close as possible to 1 in order to consider a refinement as “good”).

For the second step (structural refinement), a high quality diffractogram measured over a wide 2θ range is required to allow a good refinement. The Rietveld method is based on a least-squares approach to characterize measured data points of a diffraction pattern, I_{obs} , with an analytic function, I_{calc} , taking into account unit cell parameters, atomic positions, anisotropic and/or isotropic temperature vibrations and site occupancies. The refinement process minimizes the following function:

where w is the weighting factor and σ is the standard deviation of

Different reliability factors enable to judge of the quality of the refinement:

The weighted profile R-factor:

$$\frac{\sum w |I_{obs} - I_{calc}|}{\sum w I_{obs}}$$

The unweighted profile R-factor:

The expected R-factor:

$$\frac{R}{\sqrt{N - P - C}}$$

where N, P and C are respectively the number of independent observations, the number of refined parameters and the number of constraints between these two parameters.

The goodness of fit (GOF):

$$\frac{R}{\sqrt{N - P - C}}$$

However, profile R-factors measure GOF for structure + peak shape + background, then some problems can happened:

With very good counting statistics and minor profile problems one gets high R & R_p values. Whereas with poor counting statistics and high backgrounds, the R & R_p values will be low and these good output data come from fitting background. Finally, it is also very important to judge quality of refinement from the plot of the fit.

II.2. Optical property measurements

II.2.1. Photoluminescence measurements

The photoluminescence measurements were carried out on two different spectrofluorometers:

For room temperature measurements the FluoroMax-4 HORIBA spectrofluorometer was used (figure II-3). It is equipped with a 150W Xenon source which allows excitations from 250nm to 850nm. By adjustable slit widths, high resolution spectra can be obtained. Its emission-

Experimental part and methodology

detector electronics employ photon counting for low light level detection and high signal/noise ratios. Photon-counting concentrates on signals that originate from fluorescence photons, ignoring the smaller pulses originating in photomultiplier-tube electronics. It is also equipped with a spacious sample chamber to allow the use of a wide variety of accessories for special samples.

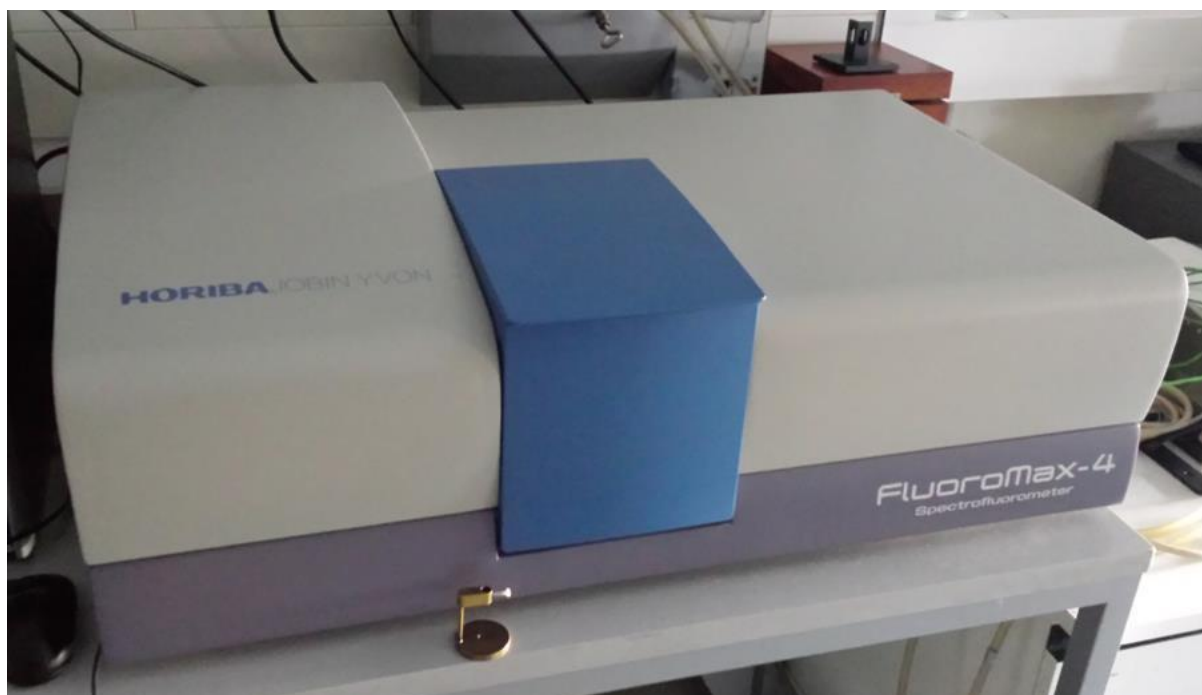


Figure II- 3 Picture of a FluoroMax-4 HORIBA spectrofluorometer

The low temperature and temperature dependent photoluminescence measurements were done with a Fluorolog-3-22 Horiba spectrofluorometer (figure II-4b). It has a 450W Xenon arc lamp and is equipped with double excitation and emission monochromator and a photomultiplier tube (PMT). The excitation spectra can be measured in the range 240-600nm whereas the emission spectra can be detected between 290 and 850 nm. It has adjustable slit widths (0-15nm) in order to obtain high resolution spectra. As for the FluoroMax device, a spacious sample chamber is available and can be equipped with a liquid Helium closed-cycle cryostat in order to measure the optical properties down to 10K (figure II-4c).

All the samples were sealed in a quartz tube under vacuum before measurements for practical reasons and also in order to prevent possible contaminations (dust, humidity...) of the phosphors. Each excitation spectrum was measured while keeping the emission wavelength fixed, and likewise, the emission spectra were taken while exciting at a fixed wavelength. The emission spectra were also corrected for the photomultiplier sensitivity and the excitation

spectra were corrected for the lamp intensity. This latter correction takes into account that the output of the xenon lamp is not uniform throughout the entire wavelength range and gratings change their efficiency. The corrected spectrum becomes useful for comparing data between instruments and for theoretical work.

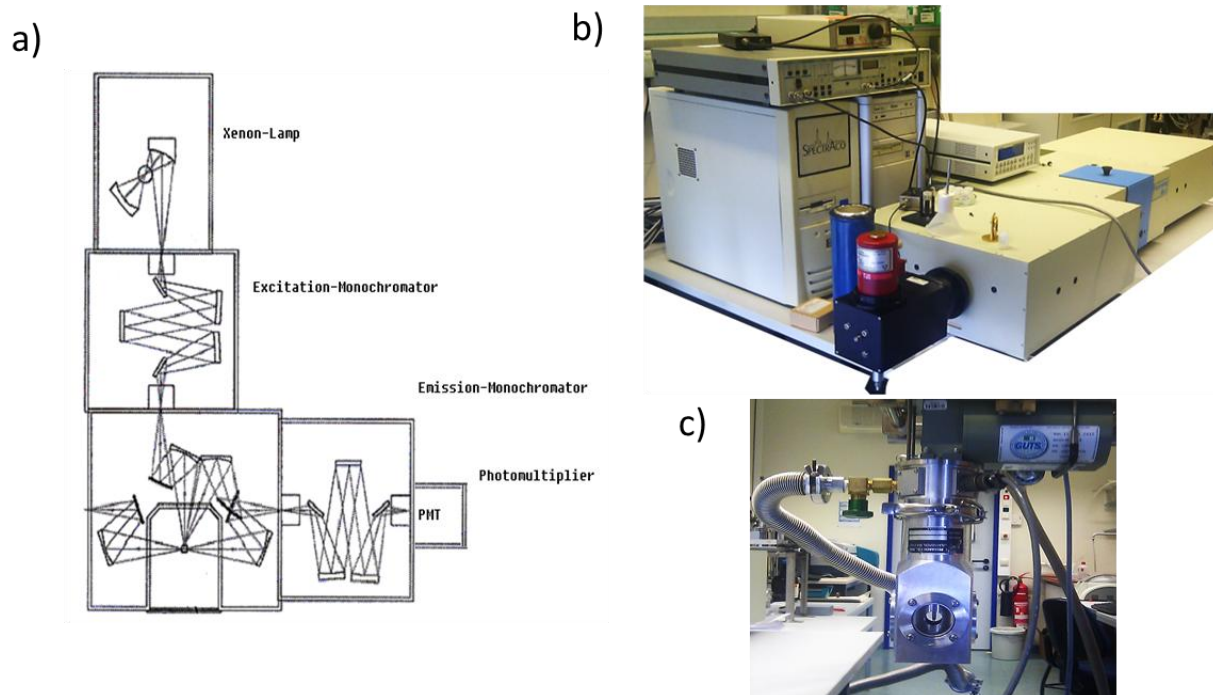


Figure II- 4 a) Basic configuration b) Picture of a Fluorolog-3-22 Horiba spectrofluorometer and c) Picture of the chamber for low temperature measurements.

II.2.2. Decay time measurements

For phosphors with decay times higher than $10\mu\text{s}$, measurements were performed using the Fluorolog-3-22 Horiba spectrofluorometer whereas for compounds with low decay time measurements (lower than $10\mu\text{s}$), a frequency-shifted Nd:YAG laser (Spectra Physics Quanta Ray Indi 40) with a repetition rate of 10 Hz and a pulse width of 8 ns was used. The excitation wavelength is fixed depending on the excitation spectrum of the sample. For the detection of desired emission wavelength, a single monochromator (Jobin Yvon) was employed that allows a resolution down to 5 nm. The decay signal was recorded with a photomultiplier tube attached to an oscilloscope (Tektronix, 500 MHz).

II.2.3. CIE chromaticity diagram

The CIE chromaticity diagrams was created by the “Commission Internationale de l’Eclairage” and have for aim to try to produce a color space based on measurements of human color perception. Different diagrams were created and improved during the last century (CIE 1931, CIELUV, CIELAB, CIEUVW...) whereas the most widely used remains the CIE 1931 chromaticity diagram. The latest CIE 1931 diagram will also be used in this work. The diagram represented figure II-5 represents an internationally agreed method for the mapping of human color perception in terms of two CIE parameters x and y . The spectral colors are distributed around the edge of the "color space" as shown, and that outline includes all of the perceived hues and provides a framework for investigating color.

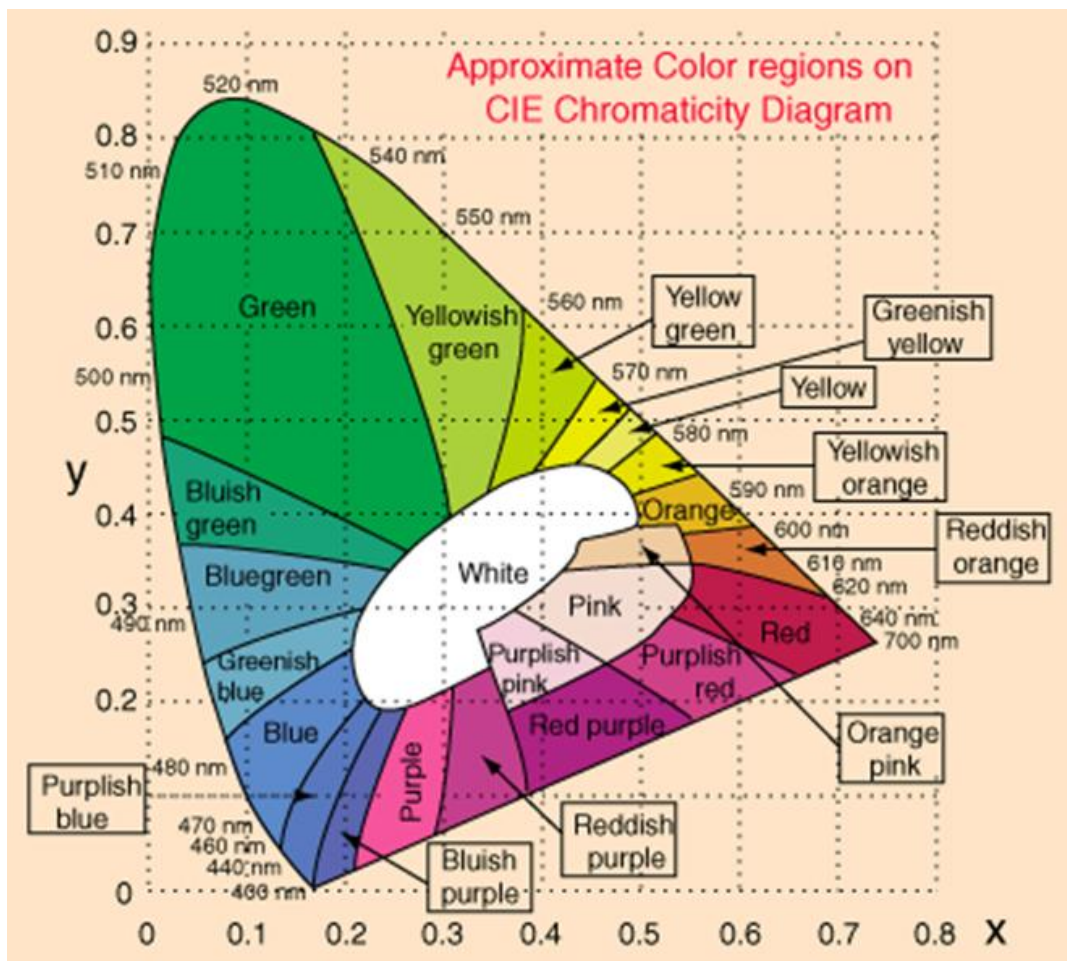


Figure II- 5 Representation of the CIE 1931 chromaticity diagram.

The diagrams in this thesis were obtained by means of the software ColorCalculator. The color representations in the CIE 1931 diagram were always calculated with the entire emission corrected spectrum.

II.3. UV-Vis spectroscopy / Kubelka-Munk method

UV/Vis spectra have been collected at room temperature with a Perkin Elmer Lambda 650 spectrophotometer in the range of 250–800 nm with 1 nm slits and using a 150 mm integration sphere designed for the characterization of the optical properties of solids. Before each measurement, a blank measurement with BaSO₄ was performed. This material has the peculiarity to show no absorption in the regarded spectral range ($\approx 0\%$ absorbance or $\approx 100\%$ reflectance, see figure II-6). Basically two spectra were collected for each sample, a basic absorbance spectrum to figure out in which wavelength region the material absorbs and a reflectance spectrum useful to determine the optical band gap.

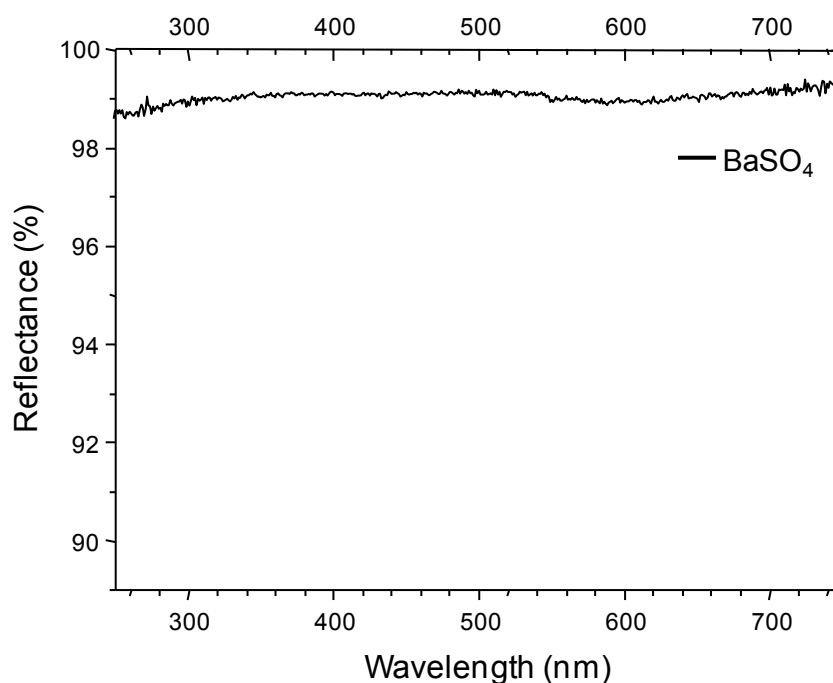


Figure II- 6 UV reflectance spectrum of BaSO₄.

There are lots of methods to determine the energy band gap of semiconductors using the diffuse reflectance spectroscopy.¹² In this work, are used the most common method using Kubelka-Munk function¹³⁻¹⁴ and Tauc plot.¹⁵ The model proposed by Kubelka and Munk describes the light behavior travelling inside a light-scattering homogeneous layer which results in a complete diffusion. First the acquired diffuse reflectance spectra is converted to the Kubelka-Munk function . The denotes the reflectance considered for a sample with an infinite thickness (when thickness of the sample is much bigger than an individual

Experimental part and methodology

particle) and the sample holder has no influence on the reflectance values. Moreover, to get good results, the particle size should be homogeneous.

The Kubelka-Munk function:

$$\frac{(1-R_{\infty})^2}{R_{\infty}}$$

where R_{∞} is the absolute reflectance, k is the molar absorption coefficient and s is the scattering coefficient.

For semiconductor samples, a Tauc plot can be constructed:

Here, E_g is the energy in eV () and $F(R_{\infty})^{1/n}$, the Kubelka-Munk function. n denotes the nature of the transition: $n=1/2$ for a direct transition $n=2$ for an indirect transition

The optical band gap is finally determined by the E_g value at the intersection of the line tangent to the plotted curve inflection point with the horizontal axis (figure II-7).

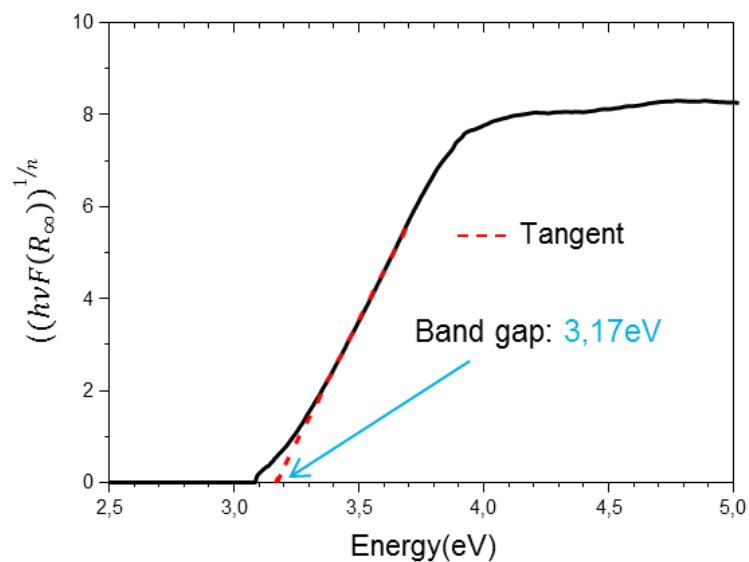


Figure II- 7 Example of Kubelka-Munk representation with band gap extrapolation for an indirect semiconductor ($n=2$).

II.4. Theory of functional density

In the case of a quantum system with more than two particles (fermions), a so-called N-body system, the Schrödinger equation does not have an analytic solution. Then it is necessary to make some approximations in order to solve it numerically. In quantum chemistry two main approaches are used: The Hartree-Fock method¹⁶⁻¹⁷ and the density functional theory (DFT).¹⁸ In this thesis, the last approach was employed for the calculation of the projected and total density of states as well as the band structure of many semiconductors/insulators.

II.4.1. Introduction to the Density Functional Theory (DFT)

Density functional theory (DFT) is a recent and powerful approach based on the determination of the electronic density $n(\mathbf{r})$ rather than the many-electron wavefunction Ψ_{el} . In this approach multi-electronic interactions (correlation and exchange phenomena) are simulated thank to an exchange-correlation functional . Nowadays, DFT is one of the most used methodologies to study the electronic structure in solid matter due to its ability of giving rise to accurate results at low cost. As it will be shown in the following parts, in practice, approximations are required to implement the theory and the development of these last ones defines the precision of results.

II.4.2. Background

Solving the Schrödinger equation for a quantum system with N electrons and M nuclei results into determine E and Ψ , respectively the total energy of the system and the total wavefunction. The knowledge of E and Ψ gives access to physical, chemical and electronic properties of system.

The Hamiltonian operator includes two main contributions: kinetic energy operator and the potential energy operator . Its exact expression for a many-body system is:

$$\hat{H} = \underbrace{-\frac{\hbar^2}{2} \sum_{\alpha} \frac{1}{m_{\alpha}} \nabla_{\alpha}^2 - \frac{\hbar^2}{2m_e} \sum_i \nabla_i^2}_{\hat{T}} + \underbrace{\sum_j \sum_{i>j} \frac{e^2}{r_{ij}} + \sum_{\alpha} \sum_{\alpha>\beta} \frac{Z_{\alpha} Z_{\beta} e^2}{r_{\alpha\beta}} - \sum_{\alpha} \sum_i \frac{Z_{\alpha} e^2}{r_{i\alpha}}}_{\hat{V}}$$

Nuclei kinetic energy
Electron kinetic energy
Electron-electron repulsion
Nuclear-Nuclear repulsion
Nuclear-electron attraction

Where m_{α} and m_e are the masses of the nuclei α and electrons respectively, Z is the nuclear charge, r_{ij} the distance between the electrons i and j , $r_{\alpha\beta}$ the distance between nuclei α and β . This N-body Hamiltonian operator can be simplified within the Born-Oppenheimer approximation,¹⁹ in which it is considered that the kinetic energy of nucleus can be neglected ($m_{\alpha} \gg m_e$) due to important difference of mass between nuclei and electrons ($m_{\alpha} \sim 1800 m_e$). The nucleus-nucleus repulsion term then becomes a fixed external potential to electrons and hence nuclear and electronic dynamics can be decoupled ($\Psi_{\text{tot}} = \Psi_{\text{el}} \Psi_{\text{nuc}}$). Then, the Hamiltonian operator becomes:

with

$$\hat{H}_{\text{el}} = -\frac{\hbar^2}{2m_e} \sum_i \nabla_i^2 + \sum_j \sum_{i>j} \frac{e^2}{r_{ij}} - \sum_{\alpha} \sum_i \frac{Z_{\alpha} e^2}{r_{i\alpha}}$$

and

$$\hat{H}_{\text{nuc}} = \sum_{\alpha} \sum_{\alpha>\beta} \frac{Z_{\alpha} Z_{\beta} e^2}{r_{\alpha\beta}}$$

II.4.3. Electron Density

However the determination of the electronic wavefunction Ψ_{el} is a complex problem mainly because this function is depending on $4N$ variables ($3N$ spatial variables and N spin variables), and contrary to the electron density $n(\mathbf{r})$, the wavefunction is not an observable. The electron density $n(\mathbf{r})$, which is a positive function depending only on the three spatial variables (x, y, z), represents the probability of finding any of the N electrons within the

volume element dV . This function is defined such that $\int n(\mathbf{r}) dV = N$, with N as the number of electrons, and vanishes at infinity.

In 1927, Thomas²⁰ and Fermi²¹ were the first authors to propose a model in which the total energy of an electronic system is a functional of the electronic density ($E[n]$). They considered a homogeneous electron gas (HEG) in order to obtain the following expression of the kinetic energy operator:

By considering the classical formulation of electron-electron and electron-nucleus interactions, the famous Thomas-Fermi energy functional can be obtained as :

However, because of the strong approximation applied on the kinetic energy expression and the absence of electronic exchange and correlation interaction, the last formula give in general bad results. But this first attempt is really interesting because it shows that the total energy of any electronic system can be expressed as a functional of the electronic density if some approximations are applied. That's why the Thomas Fermi model is now considered as the starting point of the development of DFT formalism.

II.4.4. The Hohenberg-Kohn theorem

The work done by Hohenberg and Kohn²² and published in 1964 constitutes the basis of all DFT based codes. The two Hohenberg and Kohn theorems show that the ground state energy E_0 of a given electronic system is a unique functional of the electron density $n(\mathbf{r})$. Moreover, for a given external potential $V_{ext}(\mathbf{r})$, it can be shown that the ground state energy can be obtained by minimizing the energy functional with respect to the electron density. When the density is the true ground-state electron density, this minimizes the energy functional.

Theorem I: For any system of electrons in an external potential $V_{ext}(\mathbf{r})$, this potential is determined uniquely, except for a constant, by the ground state density $n_0(\mathbf{r})$.

$$\begin{array}{ccc}
 V_{\text{ext}}(\mathbf{r}) & \xleftarrow{\text{HK}} & n_0(\mathbf{r}) \\
 \downarrow & & \uparrow \\
 \Psi_i(\{\mathbf{r}\}) & \Rightarrow & \Psi_0(\{\mathbf{r}\})
 \end{array}$$

Knowing the ground state, it is possible to determine the external potential and hence the ground state wavefunction which gives access to all the electronic properties of the system.

Theorem II: An universal functional for total energy E in terms of the density $n(\mathbf{r})$ can be defined for any external potential $V_{\text{ext}}(\mathbf{r})$. Thus, for any particular $V_{\text{ext}}(\mathbf{r})$, the exact ground state energy of the system is the global minimum value of this functional, and the density $n(\mathbf{r})$ that minimizes the functional is the exact ground state density $n(\mathbf{r})$. Here the word “universal” means “whatever the V_{ext} ” and V_{ext} includes the attraction potential electron-nucleus and all kind of external potential like magnetic field or electric field. To resume this second theorem: minimizing E for a given V_{ext} gives n_0 and E_0 .

Ultimately, the expression of total energy could therefore be written as follows:

Where E_{xc} corresponds to electronic exchange functional. However the analytical expression of E_{xc} and E_{c} are unknown. Thus these theorems show E and n_0 are two linked quantities but they did not demonstrate how to calculate the first one from the second one.

II.4.5. The Kohn-Sham equations

One year after the publication of Hohenberg and Kohn theorems, Kohn and Sham were successful in developing a system of equations which allows finding out the exact electron density.²³ They introduced a concept system of fictitious and non-interacting particles for which the ground state electron density is the same electron density as for the interacting system. Thus the Hamiltonian operator for such systems can be expressed as follows:

–

Where V_{KS} is the effective potential applied on non-interacting system in order to obtain a ground state electronic density equal to the electronic density of the interacting system

($n_{KS}(\mathbf{r}) = n_0(\mathbf{r})$). The total energy of the interacting system can therefore be formulated as follows:

with

Where the exchange correlation energy combines all non-analytical terms. The electronic correlation energy is therefore defined as the difference between kinetic energies of non-interacting and interacting system. Thus, the effective Kohn-Sham potential V_{KS} can be defined as follows:

$$\text{-----}$$

Finally, within the Kohn-Sham formalism, the electronic structure of any compound can be obtained by solving the Schrödinger equation for N one-electron orbitals.

—

And the link between electronic density and one-electron wavefunction can be easily made as follows:

The Kohn-Sham method is exact but unfortunately any exact formulation exists for exchange correlation functional which regroups all the multi-electronic effects. Thus, some approximations have to be applied to solve the Kohn-Sham scheme.

II.4.6. Exchange and correlation functional

The first approximation proposed for this functional is based on a local approach of the density (LDA, local density approximation). This approach considers that exchange and correlation effects are localized properties which depend only on the electron density $n(\mathbf{r})$ at the point \mathbf{r} . LDA approach is based on the approximation of a static HEG model.

This approach is exact for homogeneous electron gas and gives accurate results for systems where the density has very small spatial variations, such as metals.

GGA-type (generalized gradient approximation) functionals are an improved version of LDA. These functionals take into account variations of the electron density around the point r . Exchange correlation energy is hence functional of the electron density and its gradient.

In this way, GGA methods favor density inhomogeneity more than LDA methods. Meta-GGA is still more accurate than GGA because it also includes the second derivative of the electron density (Laplacian term).

Since some years, many new hybrid functionals have been developed. They are more efficient because they incorporate a portion of exact exchange from Hartree–Fock theory with exchange and correlation from other sources. Typically they are constructed with a fitted linear combination of different terms with specific parameters. One of the most commonly used hybrid versions is B3LYP, (Becke, three-parameter, Lee-Yang-Parr).²⁴ Finally, it is important to notice that even if the exchange and correlation functionals become more and more efficient, treatment of strongly correlated electron systems (i.e. lanthanides) are not very reliable. In this case, other approaches like LDA+U or LDA+DMFT type are used in order to improve the treatment of electronic states close to the Fermi level of a solid. For DFT calculations presented in this thesis, GGA PW91 type of exchange and correlation functional were used.²⁵

During this work, VASP (Vienna Ab-initio Simulation Package) code has been employed in order to do first principle calculations.²⁶ It is based on DFT formalism as presented before, and allows to access to a quantitative estimation of the total energy of considered systems. This periodic code allows a geometrical optimization with the possibility to relax the lattice shape, volume and the atomic positions at the same time. VASP code is based on the Blöchl's formalism called PAW (projector-augmented wave) formalism in order to calculate wavefunctions for periodic system like crystalline solids.²⁷ Thus the VASP simulations combine pseudopotentials and a plane wave basis set.

II.4.7. Plane Waves

The plane waves are the basis functions used in the VASP code, as they are well suitable to describe electronic structure in periodic systems. Indeed, in a perfect crystal, a periodic potential $V(\mathbf{r})$ is applied on electrons. Thus, the electronic wavefunction corresponds to the product of plane waves with a periodic function (Bloch's theorem):

avec

In the reciprocal space, the periodic electronic wavefunction can be expressed as:

— —

Where \mathbf{G} is a vector of the reciprocal space ($\mathbf{G} = n_1 \cdot \mathbf{b}_1 + n_2 \cdot \mathbf{b}_2 + n_3 \cdot \mathbf{b}_3$, with \mathbf{b}_i a vector of the first Brillouin zone). Thus, it is necessary to sample with \mathbf{k} points the first Brillouin zone in order to calculate the electronic wavefunctions. Finally, the electronic structure of periodic system can be obtained by solving a finite number of Schrödinger equations on a finite number of \mathbf{k} points.

—

To solve the last equation, it is necessary to develop each wavefunction $\psi_{\mathbf{k}}$, also called band, on an infinite number of reciprocal vectors \mathbf{G} . However in practice, electronic wavefunctions are defined on a finite number of plane waves. Thus, a cut-off energy E_{cut} corresponding to the energy of the highest band is needed and it can be defined as:

—

This last parameter is essential because an enhancement of the cut-off energy induces systematically an enhancement of the accuracy of periodic DFT calculations. Nevertheless, a very large number of plane waves are necessary to describe strong electronic density variations close to the atomic nucleus. Hence, to make the structural electronic processing more efficient, they need to be gathered with pseudopotentials.

II.4.8. Pseudopotential approach

There exist different ways to simplify the electronic calculation with respect to the electron-nucleus interaction. A chemical bond results in sharing electrons between two atoms. However, not all electronic states contribute to the formation of a chemical bond. One can usually distinguish between two different states: the *core states* which are spatially close to the nucleus and nearly not influenced by the atomic environment, and the *valence states* located at the outermost shell of the atom. It is a good approximation to assume that only the valence electrons are involved into a chemical bond and hence contribute to most of physical and chemical properties of the studied compounds. Based on that, a pseudopotential is used to replace the complicated effects of the motion of the core electrons of an atom and its nucleus. In this way, under a defined cut-off radius around each core, the valence wavefunctions are replaced by pseudo-wavefunctions with significantly fewer nodes, thus easier to be described by plane waves (figure II-8). For our calculations, we used specifically the ultra-soft pseudopotentials (USPP)²⁸ library available with the VASP code.

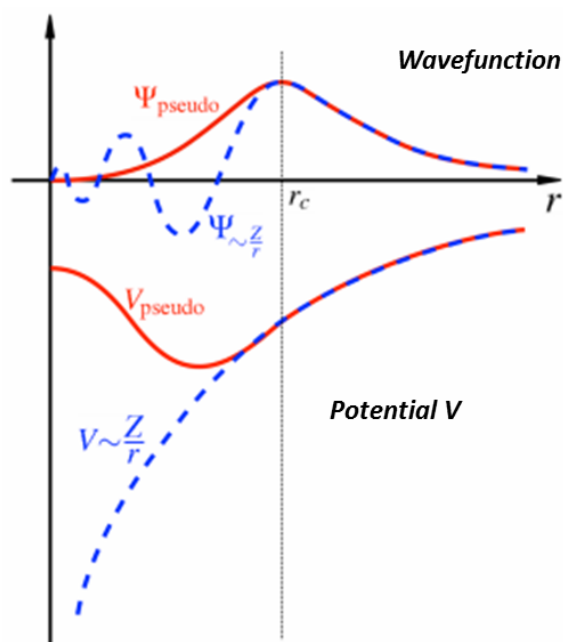


Figure II- 8 . Representation of the “real” wavefunction and pseudo-wavefunction behaviors (upper part) as well as all electron and pseudopotential (bottom part).

II.4.9. Steps for an electronic calculation

The electronic density of the system which minimizes the total energy for the system is obtained following a self-consistent-field (SCF) variation process. An initial density is introduced and it represents the sum of atomic density of the unit cell. This density is used to get access to the Coulomb potential by Poisson's equation.

The Coulomb potential corresponds to the sum of Hartree potential (V_{el-el} contribution) and nuclear potential $V_{nuc-nuc}$. Afterwards, the effective potential is obtained by adding the exchange and correlation term. Then, the electronic Hamiltonian is built up with the effective potential and the electronic density and finally the Kohn-Sham equations are solved giving as results the eigenfunctions and eigenvalues of the electronic Hamiltonian. A new electronic density is then obtained by summing the square module of the mono-electronic wavefunction over the entire occupied states. A mix of the electronic density and is reintroduced in the cycle until the convergence criteria are reached (i.e. the electronic density (or its corresponding electronic energy) is stable)(see figure II-9.).

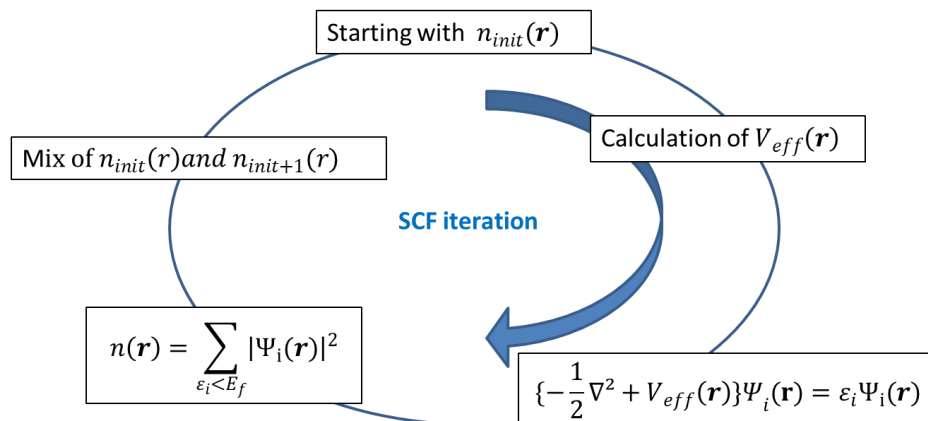


Figure II- 9 Self-consistent iteration of a DFT calculation.

II.4.10. Structural optimization

A structure optimization consists on searching a minimum in the potential energy surface (PES) of a system. Technically, with the approach that we used, this exploration is resumed in

shifting atomic positions into directions dictated by atomic forces in order to find the most stable system (lowest total energy). For each ionic step, SCF total energy calculations are done and atomic forces are recalculated. The forces acting on atoms are obtained differentiation of the total energy with respect to the atomic positions.

It is possible to evaluate forces on atoms due to the Hellman-Feynman theorem. For the fundamental state we have:

$$\mathbf{F}_i = -\nabla_{\mathbf{r}_i} E_{\text{SCF}}$$

where

$$\mathbf{F}_i = -\nabla_{\mathbf{r}_i} E_{\text{SCF}}$$

The convergence is finished when the atomic forces become negligible and the crystalline structure obtained is stable. For our calculations, the relaxation is stopped if all forces are smaller than the $3 \cdot 10^{-2} \text{ eV/\text{Angst}}$ (EDIFFG tag).

II.5. Scanning electron microscope

The scanning electron microscope (SEM) is a supplementary technique to study and characterize samples in solid states chemistry. SEM is a type of electron microscope that gives images of a sample by scanning it with a high-energy beam of electrons in a raster scan pattern. During the sample's scanning by the electron beam, many interactions happened: absorption and electron energy losses, diffusion and diffraction of the electrons, emission of Auger or secondary electron, emission of photon ...²⁹ All these effects can be exploiting for imaging, by using the right detection method to transform the results of interaction between electrons and matter into an electric signal. The SEM is mainly based on the analysis of secondary electrons (generated as ionization products) paired with back-scattered electrons to generate images of the sample. In the secondary electrons mode, we have access to information about the topography of the sample whereas in back-scattered electrons mode, information on the composition can be find out.

The Hitachi S4700 microscope was used in order to get images of our samples. It is also equipped with a microanalysis EDS (Energy-dispersive X-ray spectroscopy) system which uses the X-ray emitted by the sample to characterize its atomic composition. A quantitative analysis can also be performed however light elements ($Z < 11$) are detected and quantified with difficulty because they are low energy X-ray subject to strong absorption by the specimen and moreover the electrons involved in generating the characteristic X-rays are also the valence electrons involved in chemical bonding of the element.

II.6. Partial charge calculations and lone-pair localization

Partial charge calculation: The Henry's model for determination of partial charges using scales of atomic electronegativity and hardness implemented in the program PACHA was chosen in this work. This software uses a "non-empirical" method to determine partial charges from the crystal structure and two *ab initio* parameters per chemical element: a configuration energy and the radius of the most diffuse valence orbital.³⁰ The partial charges were calculated using as input files the CIF files got by single crystal or powder refinements or downloaded from ICSD (Inorganic Crystal Structure Database).³¹

Lone-pair localization: The theory enabling the localization of the lone-pair electrons (LP) in a crystal structure was developed by Verbaere *et al.*³² It is based on the local electric field calculation in the whole crystal using Ewald's method.³³ It was incorporated in the computer program HYBRIDE.³⁴ Under the influence of the local electric field E_{Loc} , at the cation center the LP is displaced by an amount d such that $q \cdot d = \alpha \cdot E_{Loc}$. α is the polarizability and a partial charge model can be chosen. The program splits the polarizable cation into a mobile -2 charge for the lone pair electrons and a stationary charge for the nucleus and the core orbitals.

In fine, on the basis of structural data and partial charge calculated using PACHA, a roughly access to LP activity and its approximate position can be determined (at least the relative activity along a solid-solution is meaningful).

References

- [1] SAINT: Area-Detector Integration Software; Siemens Industrial Automation, Inc.: Madison, **1996**.
- [2] SADABS: Area-Detector Absorption Correction; Siemens Industrial Automation, Inc.: Madison, **1995**.
- [3] Sheldrick, G.M., SHELXS 97, Program for Solution of Crystal Structure, University of Göttingen, Germany, **1997**.
- [4] Petricek, V.; Dusek, M.; Palatinus, L., JANA2006, Structure Determination Software Programs, Institute of Physics, Praha, Czech Republic, **2006**.
- [5] Rietveld, H., *J. Applied Crystallography*, **1969**, 2, 65.
- [6] Rodriguez-Carvajal, J., *IUCR satellite meeting 'Powder Diffraction'* Toulouse, **1990**.
- [7] Rodríguez-Carvajal, J., *IUCR Commission on Powder Diffraction Newsletter*, **2001**, 26, 12.
- [8] Le Bail, A.; Duroy, H.; Fourquet, J.L., *Mater. Research Bulletin*, **1988**, 23, 447.
- [9] Boultif, A.; Louer, D., *J. Appl. Crystallography*, **1991**, 24, 987.
- [10] Roisnel, T.; Rodriguez-Carvajal, *Mater. Sci. Forum*, **2001**, 378–381, 118.
- [11] Caglioti, G.; Paoletti, A.; Ricci, F.P., *Nucl. Instrum. Methods*, **1958**, 3, 223.
- [12] Nowak, M.; Kauch, B.; Szperlich, P., *Review of Scientific Instruments*, **2009**, 80, 046107.
- [13] Kubelka, P.; Munk, F., *Z. Tech. Phys.*, **1931**, 12, 593.
- [14] Kubelka, P., *J. Opt. Soc. Am.*, **1948**, 38, 448.
- [15] Tauc, J., Optical Properties of Solids, F. Abeles (Ed.), North Holland Publishers, Amsterdam, **1970**.
- [16] Hartree, D.R., *Proc. Cambridge Philos. Soc.*, **1928**, 24, 89.
- [17] Fock, V., *Z. Phys.*, **1930**, A 61, 126.
- [18] Ramachandran, K.I. et al., Computational Chemistry and Molecular Modeling, Springer **2008**.
- [19] Born, M.; Oppenheimer, R., *Annalen der Physik*, **1927**, 389, 457.
- [20] Thomas, L.H., *Proc. Cambridge Philos. Soc.*, **1927**, 23, 542.
- [21] Fermi, E., *Rend. Accad. Naz. Lincei*, **1927**, 6, 602.
- [22] Hohenberg, P.; Kohn, W., *Phys. Rev.*, **1964**, 136, B864.
- [23] Kohn, W.; Sham, L.J., *Phys. Rev.*, **1965**, 140, A1133–A1138.
- [24] Becke A.D., *J. Chem. Phys.*, **1993**, 98, 5648.
- [25] Perdew, J. P.; Wang, Y., *Phys. Rev. B*, **1992**, 45, 13244.
- [26] Kresse, G.; Furthmüller, J. Vienna Ab-initio Simulation Package (VASP); Institut für Materialphysik: Vienna (<http://www.vasp.at/>), **2012**.
- [27] Blöchl, P. E., *Phys. Rev. B*, **1994**, 50, 17953.
- [28] Vanderbilt, D., *Phys. Rev. B*, **1990**, 41, 7892.
- [29] Eberhart, J.P., Structural and Chemical Analysis of Materials, John Wiley and sons, Ltd, Chichester, **1991**.
- [30] Henry, M., *Chem. Phys. Chem.*, **2002**, 3, 561.
- [31] <https://icsd.fiz-karlsruhe.de/search/index.xhtml>.
- [32] Verbaere, A.; Marchand, R. and Tournoux, M.J., *Solid State Chem.*, **1978**, 23, 383.
- [33] Ewald P.P., *Ann. Phys.*, **1921**, 64, 253.
- [34] Morin, E.; Wallez, G.; Jaulmes, S.; Couturier, J. and Quarton, M. *J. Solid State Chem.*, **1998**, 137, 283.

Chapter III. Electronic Structures and
Optical properties of $\text{BiM}_2\text{O}_2(\text{XO}_4)$
compounds

III. Electronic Structures and Optical properties of BiM₂O₂(XO₄) compounds

III.1. Review of Bi₂O₃-MO_x-X₂O₅ systems

Since the discovery of the great conductivity properties in the high temperature phase Bi₄V₂O₁₁ and its stabilization¹ by the partial substitution of vanadium for different metal, the ternary system Bi₂O₃-MO_x-V₂O₅ (M=various metal cations) was deeply investigated. In addition to the discovery of the broad BIMEVOX series,² at the UCCS laboratory, this chemical system has been extended to other Bi₂O₃-MO_x-X₂O₅ ones where M= various metal and X=V, P or As, i.e. a tetrahedral cation. This study gave rise to an extended series of new compounds which exhibit different interesting physical and chemical properties, such as ionic conductivity, non-linear optical properties, catalytic properties, photoluminescence properties, ferroelectricity or ferroelasticity...³⁻¹⁰

In these systems two features implied to go into an original descriptive formalism: i) the coordination polyhedron of Bi³⁺ which is very asymmetric and does not allow clear relationship between related compounds. ii) the predominant disorder character that occur on some Bi/M mixed sites and XO₄ configuration for a lot of compounds especially in the X=P phosphate case. It follows that the anion-centered polyhedra approach was used to describe the crystal structure of the concerned compounds. It will be presented in the next section, leading to empirical rules common to most of the structures that was handled in this work within the Bi₂O₃-MO_x-X₂O₅ systems. A special focus will be given to BiM₂XO₆ (M= Mg, Zn, Cd, Pb, Mn and X= P, V, As) series that concern a large part of this PhD work.

III.1.1. The antiphase approach

To my knowledge, the first article mentioning an anion-centered polyhedra approach, which is an alternative route to the standard description of polyhedra centered on cations, was published in 1968.¹¹ Later, a multitude of studies were done, and they demonstrated the utility of the “anti-polyhedra” structural description. This approach is especially useful for crystalline structures showing a cationic disorder or having a framework based on large cations (where the anionic polyhedra is not well defined or very irregular). This artful

approach allows to highlight anti-polyhedral successions and also to establish structural filiations of compounds hardly described by other means. More specifically, the widespread OM₄ tetrahedra occupy a privileged role with this approach. At this level, the numerous and systematic works of Filatov's and Krivovichev's teams which applied this concept to a lot of phase diagrams¹²⁻¹⁵ must be highlighted. Taking the lead chemistry as an example, the figure III-1a shows the wide range of possible branching between OPb₄ anti-tetrahedra leading to multiple dimensionalities of the framework.

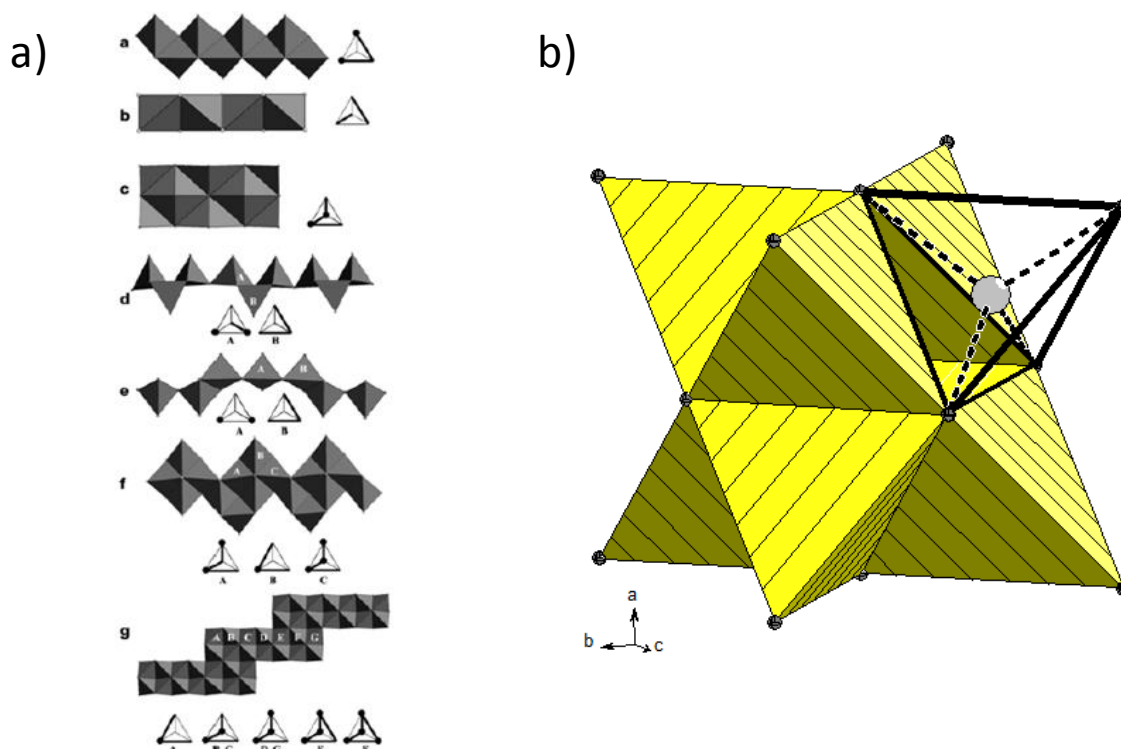


Figure III- 1 Possible branching between OPb₄ anti-tetrahedra b) Representation of OBi₄ and tetrahedra of the δ -Bi₂O₃ crystal structure.

In this thesis, a description based on O(Bi,M)₄ tetrahedra, centered on the oxygen (oxo-centered) was used. Concerning the chemistry of bismuth, these models were established by analogy with the δ -Bi₂O₃^{4,7,8,16} which crystallized in the fluorine-type structure described by association of $\frac{3}{4}$ th OBi₄ and $\frac{1}{4}$ th □Bi₄ tetrahedra (present due to one fourth of vacancy on the oxygen site) linked by sharing edges (figure III-1b).

All the compounds studied in this thesis can be related to the ideal structure of δ -Bi₂O₃, which is in real rather disordered.¹⁷⁻¹⁹ At the UCCS, after handling bismuth phosphates structure strongly disordered, this concept was used and generalized to most of the so-called bismuth oxides or oxo-salts. For example, compounds which adopt the 3D KSbO₃-type crystal structure such as Bi₃M₃O₁₁ (M=Ru, Os, Pt)²⁰⁻²¹ and La₄Ru₆O₁₉,²² possess a subnetwork of polymerized OBi₄ or isolated OLa₄ tetrahedra. Then, it is very useful to consider these structural units centered on oxygen and their connectivity in order to distinguish the different topological series (see figure III-2.).

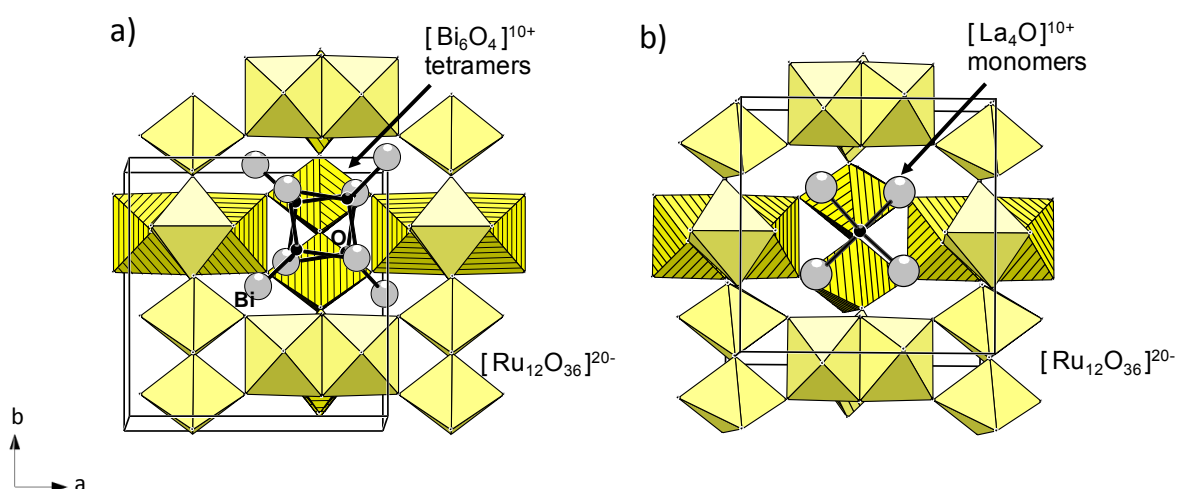


Figure III- 2 a) Representation of Bi₃Ru₃O₁₁ structure using the oxo-centered approach to show [Bi₆O₄]¹⁰⁺ tetramers and b) Representation of La₄Ru₆O₁₉ with [La₄O]¹⁰⁺ monomers.

Speaking more specifically about the phases investigated during this thesis work, the structural description is well adapted for several reasons:

► For some of the studied structures, there is a disorder on the cationic site (M/Bi) (figure III-3.). These sites are situated at the border of chains or ribbons systematically formed by connected O(Bi,M)₄ anti-tetrahedra. This specific disorder leads to another disorder on the anionic environment of these sites and prevents a clear visualization of the structures with a classical description based on a network built on connected MO_x polyhedra.

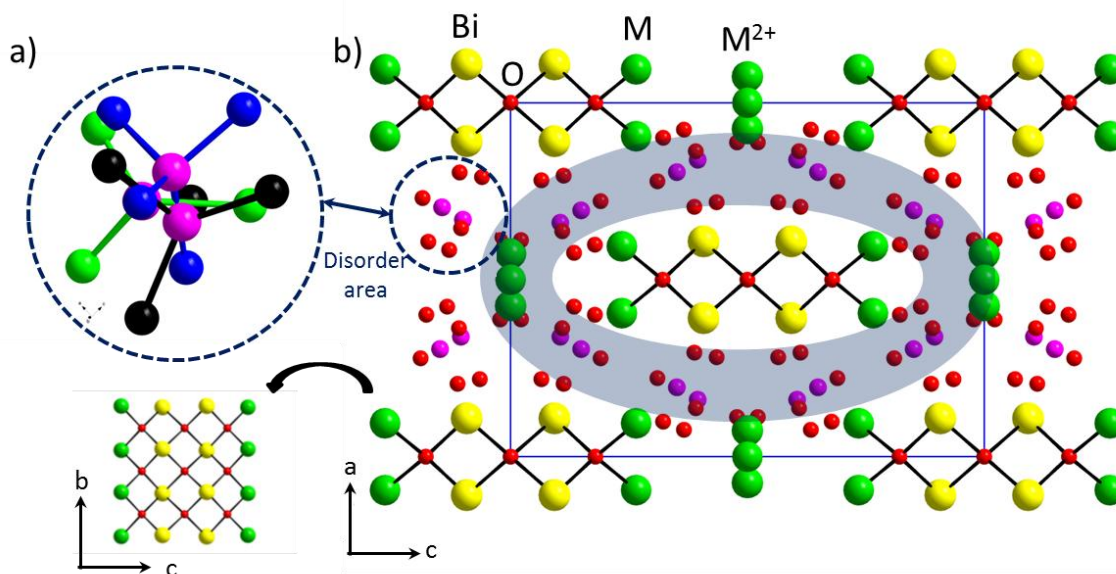


Figure III- 3 a) Disorder around phosphorus atoms in $\text{Bi}_{1.2}\text{M}_{1.2}\text{PO}_{5.5}$ ($M = \text{Zn}, \text{Mn}$) and b) and projection of the crystal structure showing triple ribbons.

► It allows to establish a systematic topological relation between the different compounds. In fact, almost of the studied phases can be described by the association of two different structural elements which are XO_4 groups ($X = \text{P}, \text{V}, \text{As}$) and ribbons of variable width built on $\text{O}(\text{Bi}, \text{M})_4$ oxo-centered tetrahedra sharing edges. In the case of phosphates, these polycationic ribbons are infinite along a crystallographic axis, assigned by convention, to the b axis and the cell parameter b is equal $\sim 5.2 \text{ \AA}$ which corresponds to the height of two $\text{O}(\text{Bi}, \text{M})_4$ tetrahedra sharing edge. The ribbons often lie parallel to each others and run along the a -axis which is equal to $\sim 11.5 \text{ \AA}$ due to the specific arrangement of ribbons and their surrounding XO_4 tetrahedra. The third lattice parameter is specific to each compound. The figure III-4 demonstrates the relation between the structure of $\text{BiMO}(\text{PO}_4)$ and that of $\text{BiM}_2\text{O}_2(\text{PO}_4)$ described following the standard and the anti-structure concept. In these two structures, it is possible to distinguish chains of $\text{O}(\text{Bi}, \text{M})_4$ tetrahedra and double chains (double ribbons) which contain the periodic element responsible for the parameter $b \sim 5.2 \text{ \AA}$.

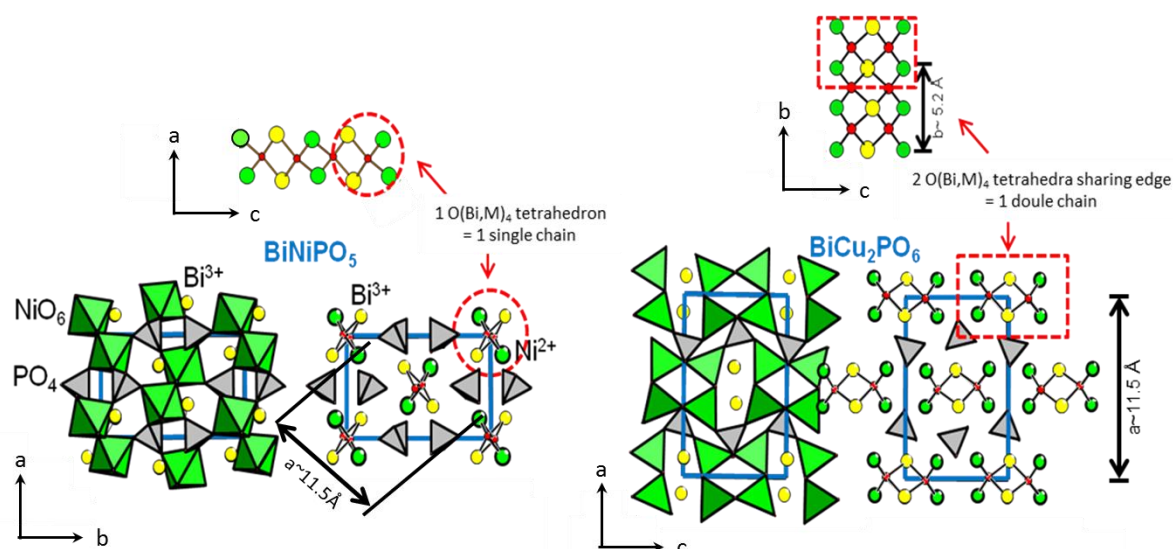


Figure III- 4 Representation of two compounds, BiNiPO_5 on the left and BiCu_2PO_6 on the right side using classical structural description (MO_x polyhedra, PO_4 tetrahedra and interstitials Bi^{3+}) and using the anion-centered polyhedra approach, for which it is possible to distinguish infinite chains built on respectively 1 and 2 tetrahedra width.

III.1.2. Structural units and Bi...Bi connectivity

The structures are composed of ribbons isolated by XO_4 tetrahedra. The topologies leading to parallel orientations between the ribbons are predominant for the compounds issues from the ternary system $\text{Bi}_2\text{O}_3\text{-MO}_x\text{-P}_2\text{O}_5$. The figure III-5 shows structures with mono ribbons ($n=1$), double ribbons ($n=2$) and triple ribbons ($n=3$) where n corresponds to the number of tetrahedra sharing edge regarding the width. One key parameter for the optical properties being the Bi...Bi connectivity, ruling the luminescence concentration quenching, more or less suitable topologies can be observed from this anti-phase description. For instance, for $n=1$, 2 and 3 each Bi is connected to 1 or 2, 2 or 5 another Bi^{3+} by Bi-O-Bi bridges with different paths.

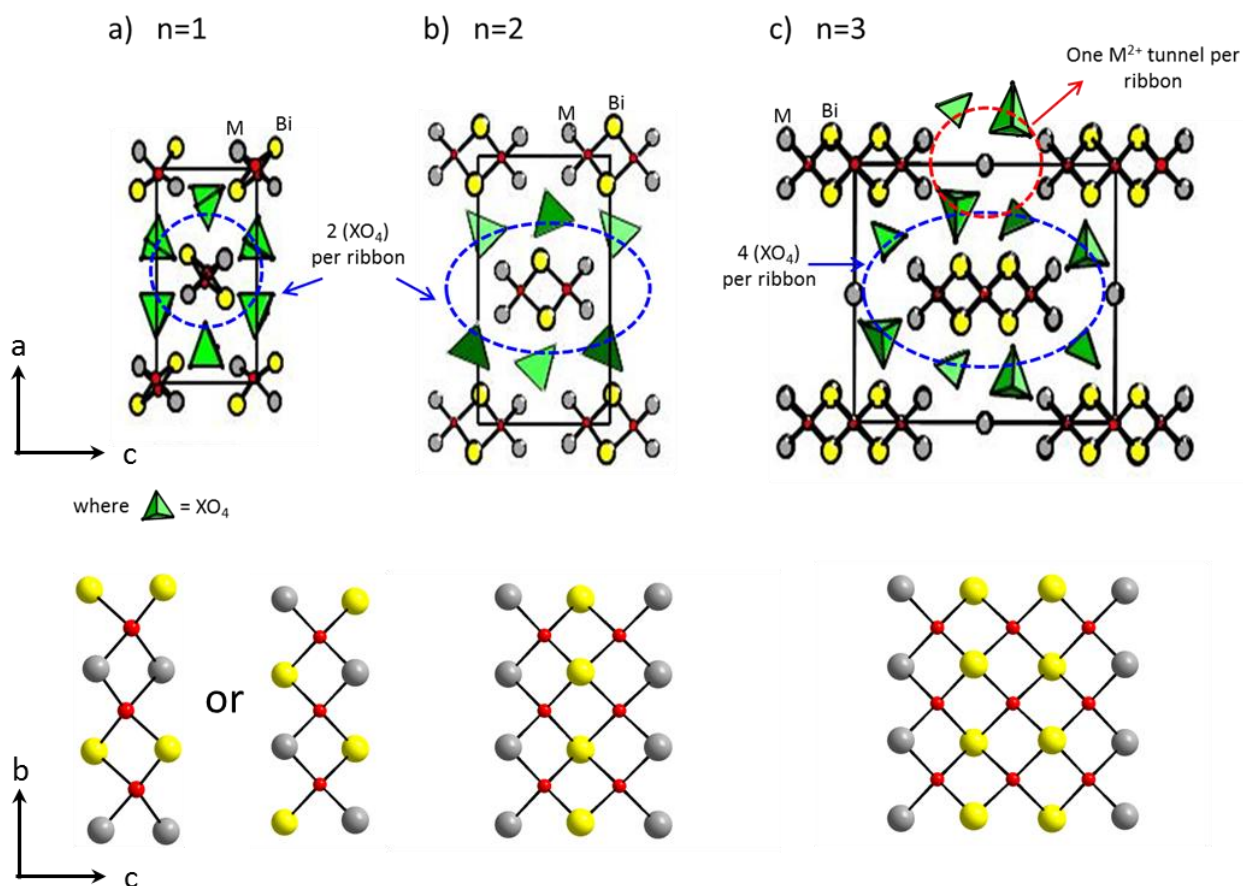


Figure III- 5 Organization between a) ribbons in BiMXO₅ compounds b) double ribbons in BiM₂XO₆ compounds and c) triple ribbons in Bi_{-1.2}M_{-1.2}PO_{5.5} compounds. For the last case tunnels parallel to b are also represented.

III.1.3. Empirical rules

During last years, several compounds with variable width have been characterized, and from this study some empirical structural rules have been deduced. These rules are verified in the case of phosphates and stem from the relative size of PO₄ compared to OBi₄ groups which are imbricated.

- (1) The width of the ribbons is formed by the association of $n=1,2,3 \dots$ tetrahedral up to infinite layers. As discussed above, the figure III-5 shows three examples of compounds with this structure, BiMXO₅ for $n=1$, BiM₂XO₆ for $n=2$ and Bi_{1.2}M_{1.2}PO_{5.5} for $n=3$.
- (2) For compounds with the ribbon size $n>3$, an additional (O-Bi)⁺ decoration coming in addition to the ribbons for stabilization with surrounding XO₄ groups is found (Figure

III-6.). These additional decorations are located in the XO₄ interlayer space. A maximum of only two subsequent XO₄ can surround a ribbon taking into account the steric considerations.

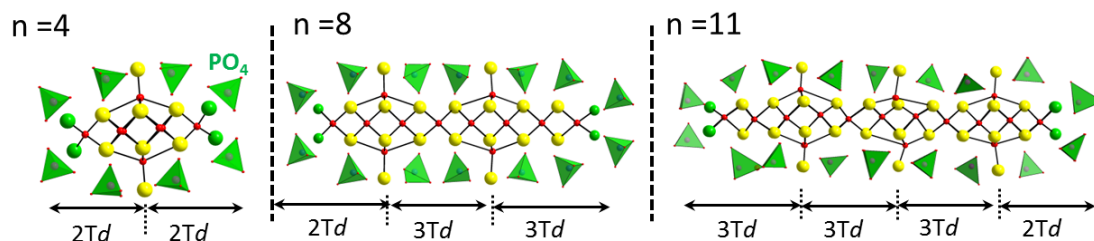


Figure III- 6 Representation of ribbons and excrescence for $n= 4, 8$ and 11 . Td stands for tetrahedra.

(3) This excrescence formed by additional $(O-Bi)^+$ takes place perpendicularly to ribbons. The oxygen atom is five coordinated (it is bonded to four Bi^{3+} cations from the ribbon and to the Bi^{3+} coming from the excrescence) (figure III-7).

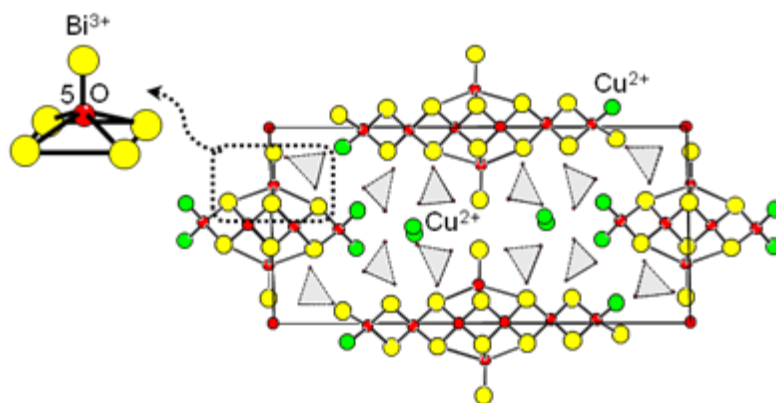


Figure III- 7 Details of the excrescence for the ribbons $n= 4$ and 6 .

Ribbons with different width can get together inside a same compound (Figure III-7.) Only OBi_4 tetrahedra can be present inside the ribbon whereas at its extremities may host Bi^{3+} , M^{2+} or mixed sites (Bi^{3+}/M^{2+}). The presence of the latest statistic disorder sometimes induces a strong disorder in the inter ribbon space (XO_4 orientation and tunnel occupancy).

Other rules have been gathered and used to design new materials,²³ however, they are useless here and hence won't be detailed. These four presented empirical laws will be used in this

thesis as well as in the Annex2 part to describe new compounds which were evidenced during this work.

III.2. BiM₂O₂(XO₄) polymorphs with n=2 ribbons

Due to the large number of phases with the BiM₂XO₆ formula, the first target of this work was to play on optical properties by chemical doping on the various crystallographic sites. Contrarily to main phases discuss above, these series is essentially formed of fully ordered compounds except for solid-solution members. First, a panorama of the structural properties of these series will be given. Chronologically, since the report of BiMg₂VO₆,⁴ a large number of isotopic compounds of general formula BiM₂XO₆ (M= Ca, Mg, Mn, Zn, Cu, Cd, Pb and X= As, V, P), have been prepared which highlights the versatility of the concerned crystal structure (see Table III-1). In addition depending on M and X, a diversity of physical specificities has been reported such as ferroelectricity in BiCa₂VO₆,⁷ or second harmonic generation for BiCd₂VO₆ and BiCd₂AsO₆.²⁴ Dealing with M magnetic ions it was established that BiCu₂PO₆ is a frustrated two-leg S=1/2 ladder system.²⁵⁻²⁷ However little was reported about the luminescence properties of these phases except a brief mention for light emission in BiMg₂VO₆ by Sleight *et al.*⁴ and only very recently, significant room temperature Bi³⁺ luminescence was reported for BiMg₂VO₆ and BiMg₂PO₆.²⁸ In this context, the investigation of the M²⁺ and X⁵⁺ roles is relevant for full-rationalization.

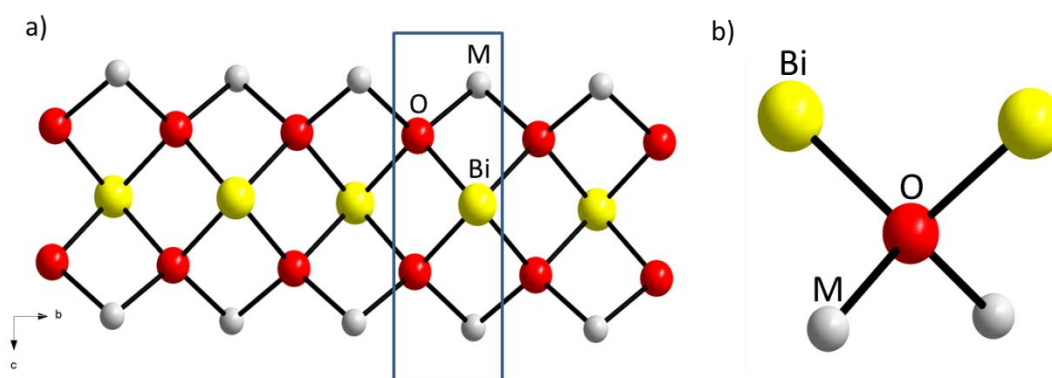


Figure III- 8 a) Representation of infinite one-dimensional $\infty[\text{BiM}_2\text{O}_2]^{3+}$ and b) representation of oxo-centered $\text{O}(\text{Bi}_2\text{M}_2)$ tetrahedron.

The crystal structure of BiM₂XO₆ was already discussed above (see figure III-5b). It is built on infinite one-dimensional $\infty[\text{BiM}_2\text{O}_2]^{3+}$ polycations with n=2 oxo-centered $\text{O}(\text{Bi}_2\text{M}_2)$ tetrahedra sharing edges (see figure III-8) and separated by isolated $(\text{XO}_4)^{3-}$ groups.²⁹ The

crystal symmetry and exact orientations between all sub-units vary depending on the crystal structures/nature of M^{2+} and X^{5+} cations. For instance, the figure III-9 evidences the orientations of the XO_4 polyhedra in four different polymorphs. Focusing on the (a,c) projection one can remark different tilting and twisting compared to the ribbons, from all XO_4 groups “up” in $Bb2_1m$ to transverse orientation in the three other forms. The distortion of the ribbon is also variable.

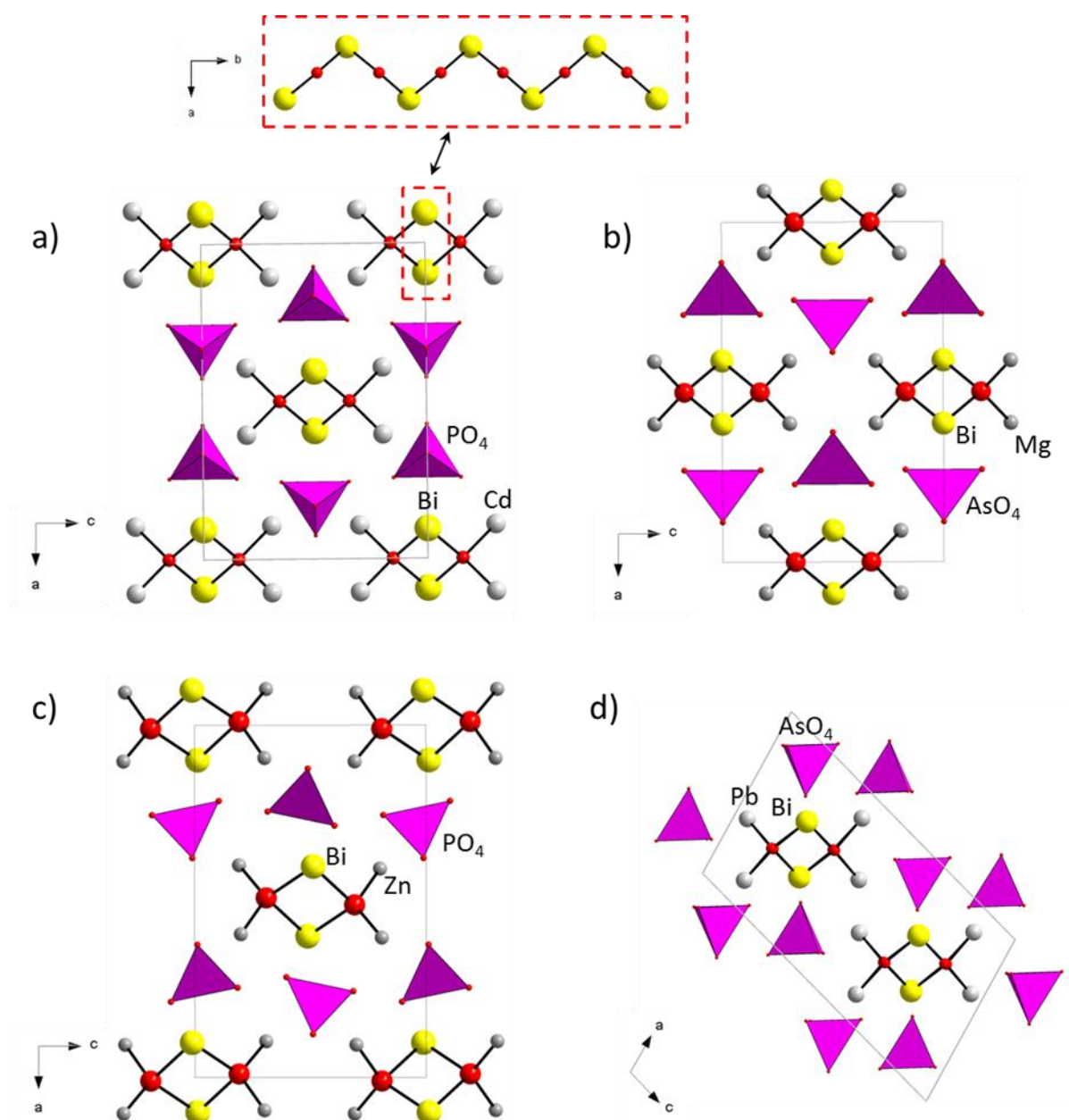


Figure III- 9 Examples of BiM_2XO_6 structure: a) BiCd_2VO_6 (SG: $Bb2_1m$)
 b) $\text{BiMg}_2\text{AsO}_6$ (SG: $Bbmm$) c) BiZn_2PO_6 (SG: $Pnma$) and d) $\text{BiPb}_2\text{AsO}_6$ (SG: $P2_1/c$).

The positions at the border of the oxo-centered double ribbons are occupied by the divalent M^{2+} ions whereas Bi^{3+} are located at their centers (see figure III-8-9.) and form 1D zigzag chains growing along the b -axis. The Bi^{3+} coordination is typical of ns^2 ions, characterized by 4 short Bi-O bonds at one side and longer Bi-O bonds (connected to $(XO_4)^{3-}$ groups) at the other side. It follows that the stereo-active lone pair points out externally to the ribbon towards the tetrahedral groups.³⁰⁻³¹ (see figure III-10).

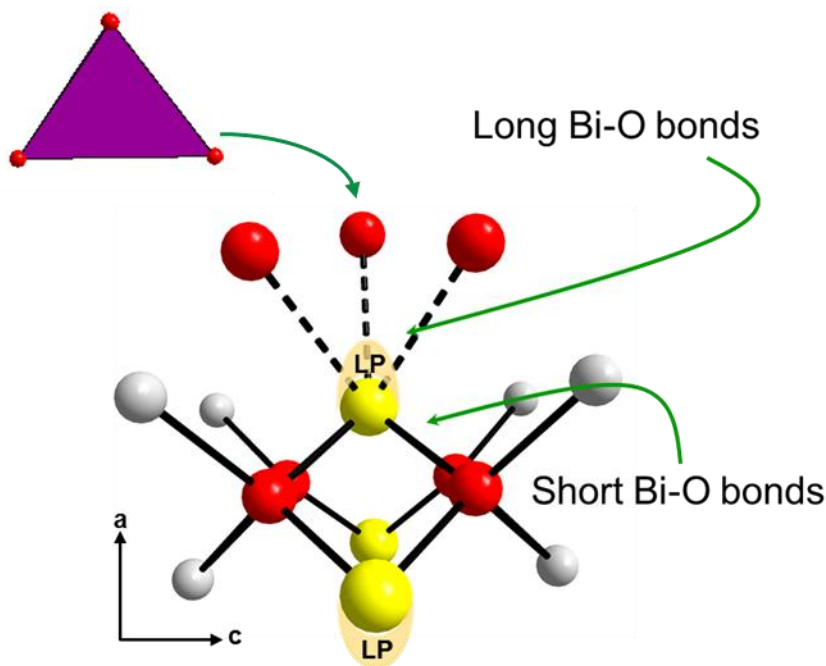


Figure III- 10 Bismuth-oxygen coordination with ideal lone pair (LP) asymmetry. The lone pair of electron is pointing out the double ribbon toward the XO_4 tetrahedra.

The Table III-1 indexes most of the BiM_2XO_6 compounds known until now from the literature and from this work. The only reported exception belongs to $BiZn_2VO_6$ compound, it crystallizes in the primitive $P-1$ space group.³²⁻³³ Due to unavailable CIF file, the crystal structure of $BiZn_2VO_6$ cannot be represented here but instead of infinite $(BiZn_2O_2)^{3-}$ chains, $BiZn_2VO_6$ contains discrete Bi_2O_{12} dimers; it does not contain fluorite-like slabs of edge-sharing OBi_2M_2 tetrahedra as we have seen previously.³²⁻³³

Table III-1 Crystalline characteristics of BiM₂XO₆ phases. For practice reasons the space groups *C mcm* is converted into *B bmm* and *C mc2₁* into *B b2₁m* in order to always have a unit cell with the same orientation (*a*~12, *b*~5.5 and *c*~8Å)

Compound	Space Group	a (Å)	b (Å)	c (Å)	β (°)	Z	Ref
BiZn ₂ PO ₆	<i>P nma</i>	11.8941(3)	5.2754(2)	7.8161(2)		4	[34]
BiMg ₂ PO ₆	<i>P nma</i>	11.8948(3)	5.2743(1)	7.8088(2)		4	[35]
BiMg ₂ PO ₆	<i>B bmm</i>	11.888(3)	5.273(2)	7.801(2)		4	[16]
BiMg ₂ VO ₆	<i>P nma</i>	12.2475(3)	5.4431(2)	7.9160(2)		4	[4]
BiMg ₂ AsO ₆	<i>B bmm</i>	12.1637(8)	5.3898(4)	7.9142(5)		4	[16]
BiCd ₂ PO ₆	<i>B b2₁m</i>	11.952(10)	5.374(10)	8.505(10)		4	This work
BiCd ₂ VO ₆	<i>B b2₁m</i>	11.4611	5.6455	8.6451		4	[35]
BiCd ₂ AsO ₆ (a)	<i>B b2₁m</i>	11.949(2)	5.4407(7)	8.618(1)		4	[24]
BiCa ₂ VO ₆	<i>B b2₁m</i>	11.9608(1)	5.5459(5)	8.8932(7)		4	[7]
BiCa ₂ AsO ₆	<i>B b2₁m</i>	11.9723(11)	5.5453(5)	8.8848(8)		4	[35]
BiCu ₂ PO ₆	<i>P nma</i>	11.776(1)	5.1730(6)	7.7903(6)		4	[36]
BiCu ₂ VO ₆	<i>P 2₁/n</i>	13.471(1)	7.812(1)	15.760(1)	113.10(1)	12	[9]
BiCu ₂ AsO ₆	<i>P nma</i>	12.253(1)	5.280(1)	7.577(1)		4	[8]
BiPb ₂ PO ₆	<i>P bnm</i>	11.473(6)	5.930(4)	9.079(10)		4	[37]
BiPb ₂ VO ₆	<i>P 2₁/m</i>	15.0501(5)	5.9011(3)	7.5355(5)	101.5657	4	[38]
BiPb ₂ AsO ₆	<i>P 2₁/c</i>	8.2662(4)	5.6274(3)	14.3152(7)	106.663(2)	4	This work
BiMn ₂ PO ₆	<i>P nma</i>	12.031(1)	5.3652(5)	8.1225(7)		4	[39]
BiMn ₂ VO ₆	<i>P nma</i>	12.002(1)	5.4421(5)	8.2378(7)		4	[39]
BiMn ₂ AsO ₆	<i>P nma</i>	12.009(1)	5.3734(4)	8.2092(7)		4	[39]

III.3. Towards new BiM₂XO₆ phases

Many attempts using different synthesis methods (solid state, hydrothermal, Pechini) have been performed during this thesis to prepare BiM₂XO₆ isostructural compounds with various M²⁺ and X⁵⁺ cations. For instance, BiCd₂PO₆ was mentioned but not published⁴⁰ while BiPb₂AsO₆ appears to be an original phase. Both phases have been investigated in this work. Dealing with large M²⁺ ions (Ba²⁺, Sr²⁺, Ca²⁺) the synthesis of hypothetical compounds BiSr₂XO₆, BiBa₂XO₆ (X= P, V or As) or BiCa₂PO₆, remain unsuccessful and leads most of the time to mixtures of BiXO₄, M₃(XO₄)₂ or M₂X₂O₇ and unidentified phases. This experimental failure is obviously related to the large M²⁺ ionic radius combined with the high “rather symmetrical” coordination required for these cations (by comparison with Pb²⁺).

III.3.1. Accurate crystal Structure of BiCd₂PO₆

To prepare BiCd₂PO₆, a stoichiometric mixture of Bi₂O₃, CdO and (NH₄)₂HPO₄ was ground and heated first at 500°C during 12h to decompose the (NH₄)₂HPO₄ and finally at 800°C for 24h in an alumina crucible. Several intermediate grindings are required to obtain the pure phase. Finally, a white powder was obtained at the end of the reaction.

—

—

The structure of BiCd₂PO₆ was preliminary analyzed by Rietveld refinement using Fullprof software against high-resolution synchrotron powder diffraction data, collected on the 11-BM beamline at the Advanced Photon Source (APS, Argonne National Laboratory) with a wavelength of 0.4137Å. The outside of 0.8mm diameter capillary was coated by sample powder mixed with silicone grease and then put into a 1.5 mm diameter kapton capillary in order to decrease absorption of the compound related to the presence of cadmium. The 2θ range for the fit is [0.5°-50°]. A zone from 7.48 to 7.75° 2θ was excluded because of the presence of a weak intensity reflection which not belongs to the title compound. The powder pattern of BiCd₂PO₆ shows similarities with that of BiCd₂AsO₆ (*Bb2₁m*),²⁴ and in this way, the atomic positions of the latest compound were used as starting model for refinement. Furthermore, extinction conditions indicate a B-centered Bravais lattice (hkl, h+l=2n) and no

reflection refute the possibility to have an axis 2_1 along $(0k0, k=2n)$ or a mirror b perpendicular to $(0kl, k=2n)$. Extinctions have been verified by electron diffraction. The $Bb2_1m$ model quickly converged to relatively reasonable factor structure values (see Table III-2 and XRD pattern in figure III-11). Refinement was also tried in the $Bbmm$ space group leading to higher agreement factors and abnormally high thermal parameters. The refinement parameters are given in the table III-2 and atomic positions in the table III-3. More recently, BiCd₂PO₆ single crystals were “accidentally” grown and their structure determination comforts the Rietveld refinement (see the measurement and structural refinement parameters table III-2). Crystals are seriously twinned and this should be responsible for rather high R values.

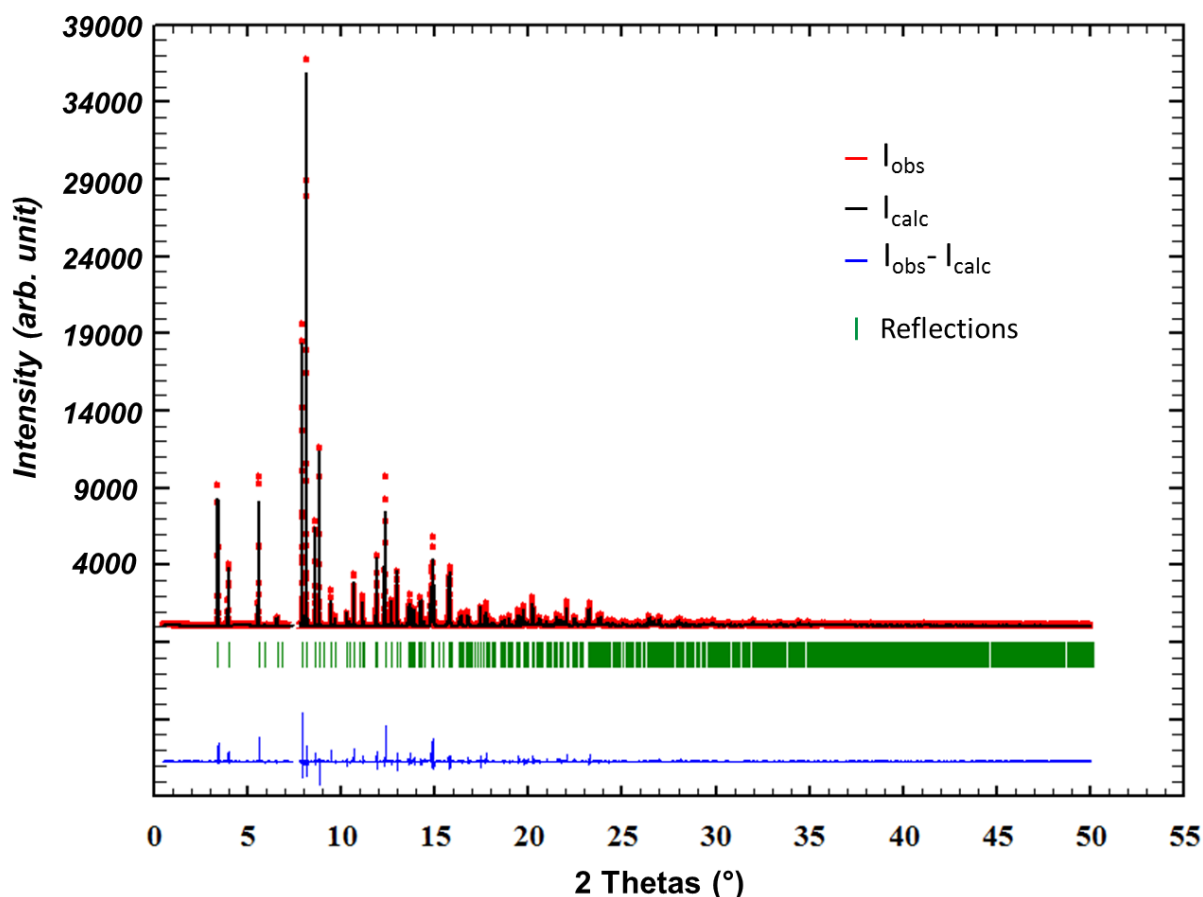


Figure III- 11 Rietveld refinement pattern using powder synchrotron X-ray diffraction of BiCd₂PO₆.

Table III-2. Crystal data, synchrotron and single crystal measurements, refinement parameters of BiCd₂PO₆.

BiCd₂PO₆			
Crystal data	Single	Synchrotron	
crystal			
Crystal symmetry	Orthorhombic	Orthorhombic	
Space group	<i>B</i> <i>b</i> 2 ₁ <i>m</i> (36)	<i>B</i> <i>b</i> 2 ₁ <i>m</i> (36)	
a (Å)	11.977 (2)	11.952(1)	
b (Å)	5.3773(7)	5.374(1)	
c (Å)	8.5245(10)	8.505(1)	
V (Å ³)	549.02 (13)	546.31(1)	
Z	4	4	
Dx (g/cm ³)	6.7821	6.818	
(mm ⁻¹) (0.7107Å)	42.086	-	
Appearance	Yellow platelet	White powder	
Crystal size (mm)	0.16 x 0.11 x 0.04	-	
Data collection			
λ (Å)	0.71073	0.4137	
Scan mode	ω and φ	transmission	
θ(min-max)(°)	2.93 – 40.34	0.5<2θ<50 (0.003°) step	
R(int) (%)	5.5	-	
	-11 ≤ h ≤ 15	-	
Reciprocal space recording	-19 ≤ k ≤ 20	-	
	-8 ≤ l ≤ 9	-	
Refinement			
Meas., obs./indep.all	3134,	-	
(obs=I>3σ(I))	1045/839	-	
No. of Refined parameters	92	-	
Refinement method	F	Rietveld	
R1(F ²)(obs) / R1(F ²)(all) (%)	5.3 / 11.67	R _{wp}	21.7
wR2(F ²)(obs) / wR2(F ²)(all) (%)	9.64 / 9.85	R _p	20.3
GOF(obs) / GOF(all)	4.23 / 3.85	R _f	8.34
Δρmax/ Δρmin (e Å ⁻³)	6.42 / -4.24	R _{BRAGG}	6.30
Extinction coefficient	407 (16)	χ ²	3.74

Table III-3. Atomic positions and atomic displacement parameters (\AA^2) for BiCd_2PO_6 (Synchrotron data).

Atom	Wyckoff	x	y	z	B_{iso} (\AA^2)
Bi1	4a	0.90557(7)	0.11214	0	Aniso
Cd1	8b	0.10606(12)	0.1117(5)	0.30364(10)	Aniso
P1	4a	0.6850(7)	0.642(3)	0	1.747
O1	8b	0.000(2)	0.371(7)	0.1556(9)	2.279
O2	4a	0.167(2)	0.357(5)	1/2	2.279
O3	4a	0.074(3)	0.791(7)	1/2	2.279
O4	8b	0.744(2)	0.727(4)	0.850(3)	2.279

	B_{11}	B_{12}	B_{13}	B_{21}	B_{22}	B_{23}
Bi	0.01245	0.00307	0.01554	0	0	0
Cd	0.0304	0.00439	0.00802	0	0.00443	0

Crystal description of BiCd_2PO_6 :

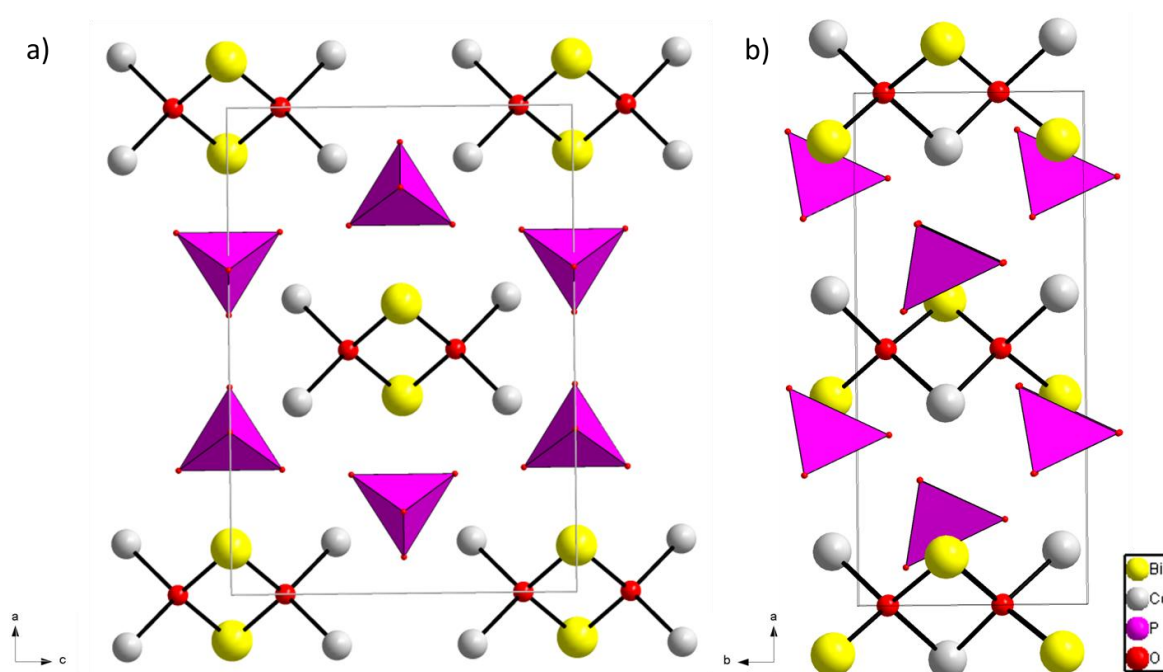


Figure III- 12 Two views of BiCd_2PO_6 structure, along axis b and axis c .

BiCd₂PO₆ crystallizes in the orthorhombic non-centrosymmetric space group *Bb2₁m* and it is isostructural to BiCd₂AsO₆,²⁴ BiCa₂VO₆⁷ and BiCd₂AsO₆.³⁵ Bi atoms have a typical asymmetric environment characterized by a stereo-active lone pair with four short Bi-O bonds on one side (2.17/2.23 Å) and the three longer bonds on the other side to oxygens of PO₄ tetrahedra. A bond valence sum of 3.19 was calculated for Bi³⁺ in its coordination (see figure III-13a).

Cd is found in a seven-coordination environment with bond lengths to oxygen from 2.21 to 2.90 Å, and giving rise to a bond valence sum of 1.97.

The P atoms which have a bond valence sum of 4.95, are localized in a regular tetrahedral environment with P-O bonds ranging from 1.53 to 1.55 Å and angles comprised between 103 and 113° (see figure III-13).

As for its isostructural compounds, the orientation of the (PO₄)³⁻ tetrahedra is non-centrosymmetric and polar, all the tetrahedra are pointing in the same direction along the crystallographic axis *b* (see figure III-12). This particularity fits with the tendency evoked by Evans²⁴ in which a large cation M²⁺ like Ca²⁺ or Cd²⁺ favors the formation of centered orthorhombic non-centrosymmetric phases.

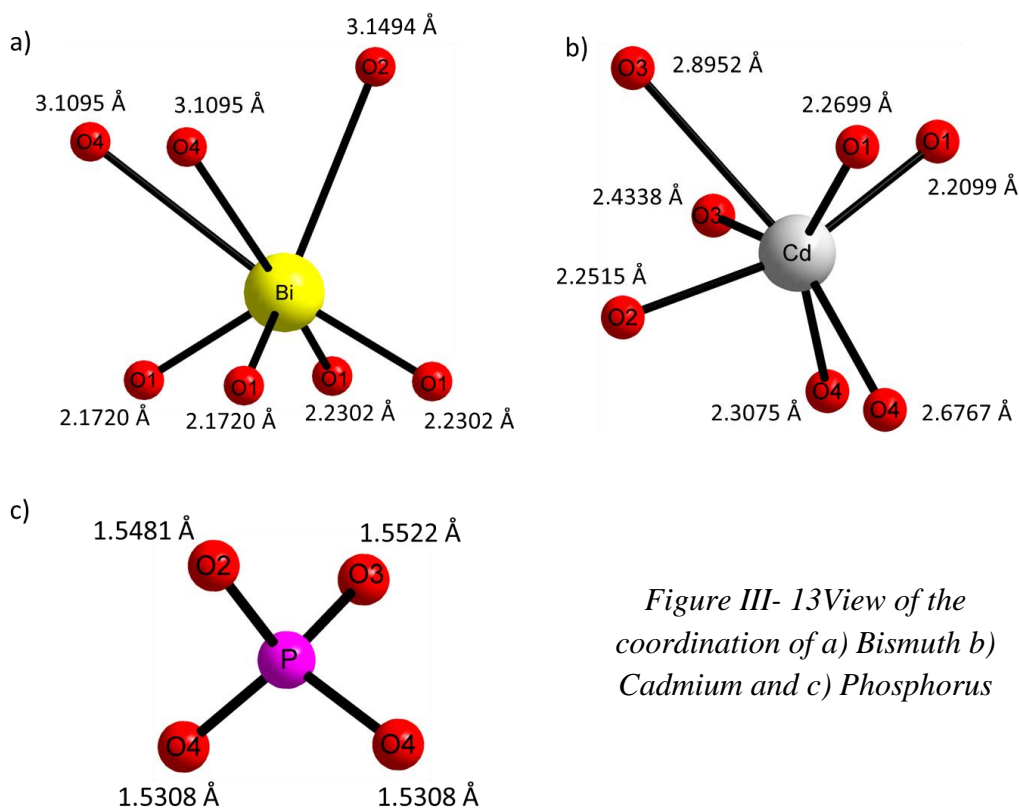
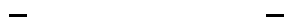


Figure III- 13View of the coordination of a) Bismuth b) Cadmium and c) Phosphorus

III.3.2. Crystal structure of the new BiPb₂AsO₆ phase

The synthesis of the novel BiPb₂AsO₆ involves a stoichiometric mixture of Bi₂O₃, PbO and As₂O₅ grounded with acetone and heated at 780°C during 36h in an alumina crucible according to the reaction:



The synthesized yellowish-white powder was subsequently melted at 1050°C, cooled down to 600°C with a rate of 3°C/h and then to room temperature at a rate of 15°C/h in order to get single crystals. A yellowish plate-like single crystal of BiPb₂AsO₆ was isolated from the melt and mounted on a glass fiber. It was refined in the monoclinic space group $P2_1/c$, which consists of a new form for BiM₂XO₆ phases.

The crystal structure refinement performed in the space group converged to relatively good reliability factors. In a first time, the Pb and Bi atoms were located by analogy with the other members of the BiM₂XO₆ (Bi in the middle of the double ribbon and Pb at the borders), then the bond valence calculations confirmed the right positions ordering between these atoms. At the last cycles of the refinement, anisotropic displacements were considered for heavy atoms (Bi, Pb and As) whereas isotropic displacements were kept for oxygen atoms. Results and refinement are listed table III-4 and atomic positions, displacement parameters are listed table III-5.

Table III-4. Crystal data, measurement and structural refinement parameters for BiPb₂AsO₆

BiPb₂AsO₆	
Crystal data	
Crystal symmetry	Monoclinic
Space group	<i>P2₁/c</i>
a (Å)	8.2662(4)
b (Å)	5.6274(3)
c (Å)	14.3152(7)
β (°)	106.663(2)
V (Å ³)	637.940(6)
Z	4
D _x (g/cm ³)	8.267
(mm ⁻¹) (0.7107Å)	87.165
Appearance	Yellow platelet
Crystal size (mm)	0.20 x 0.12 x 0.03
Data collection	
λ (Mo Kα) (Å)	0.71073
Scan mode	ω and φ
θ(min-max)(°)	2.57 - 33.17
R(int) (%)	5.5
Reciprocal space recording	-12 ≤ h ≤ 11 -8 ≤ k ≤ 8 -22 ≤ l ≤ 22
Refinement	
Meas., obs./indep.all	11231, (obs=I>3σ(I))
No. of Refined parameters	92
Refinement method	F
R1(F ²)(obs) / R1(F ²)(all) (%)	3.88 / 4.94
wR2(F ²)(obs) / wR2(F ²)(all) (%)	4.98 / 5.16
GOF(obs) / GOF(all)	1.87 / 1.70
Δρmax/ Δρmin (e Å ⁻³)	6.16 / -4.12
Extinction coefficient	407 (16)

Table III-5. Atomic positions and atomic displacement parameters (\AA^2) for BiPb₂AsO₆.

Atom	Wyckoff	x	y	z	U _{iso} or U _{eq} (\AA^2)
Bi1	4e	0.62497	0.26683	0.21688	0.01662(12)
Pb1	4e	0.13928	0.26820	0.13033	0.02101(13)
Pb2	4e	0.60463	0.24468	-0.04223	0.01256(11)
As1	4e	1.13541	0.26248	0.38937	0.0117(3)
O1	4e	0.61864	0.01653	0.33647	0.0164(12)
O2	4e	1.27909	0.25972	0.32678	0.0336(18)
O3	4e	0.62307	0.50770	0.34185	0.0165(12)
O4	4e	0.93993	0.24271	0.31611	0.0314(18)
O5	4e	1.16903	0.03830	0.47115	0.0336(17)
O6	4e	1.15382	0.50764	0.45818	0.0437(20)

	U ₁₁	U ₂₂	U ₃₃	U ₁₂	U ₁₃	U ₂₃
Bi1	0.0151(2)	0.01978(19)	0.01292(19)	0.00078(10)	0.00063(13)	0.00021(10)
Pb1	0.0157(2)	0.0263(2)	0.0194(2)	0.00053(11)	0.00242(15)	0.00132(11)
Pb2	0.01137(18)	0.01333(17)	0.01404(19)	0.00037(9)	0.00536(12)	0.00078(9)
As1	0.0038(4)	0.0163(4)	0.0143(5)	-0.0002(2)	0.0012(3)	-0.0001(3)

Crystal description of BiPb₂AsO₆

While the most of the compounds of the BiM₂XO₆ series crystallize in an orthorhombic space group, BiPb₂AsO₆ crystallizes in the monoclinic non-centrosymmetric space group $P2_1/c$. This is due to the larger ionic radii and the asymmetric coordination of the Pb²⁺ ions. For instance monoclinic distortion have already been observed for BiPb₂VO₆.³⁸ Once again, the structure can be described as the association of complex infinite one-dimensional polycations $\infty[\text{BiPb}_2\text{O}_2]^{3+}$ (along axis “b”) and arsenate tetrahedra (see figure III-14.a,b).

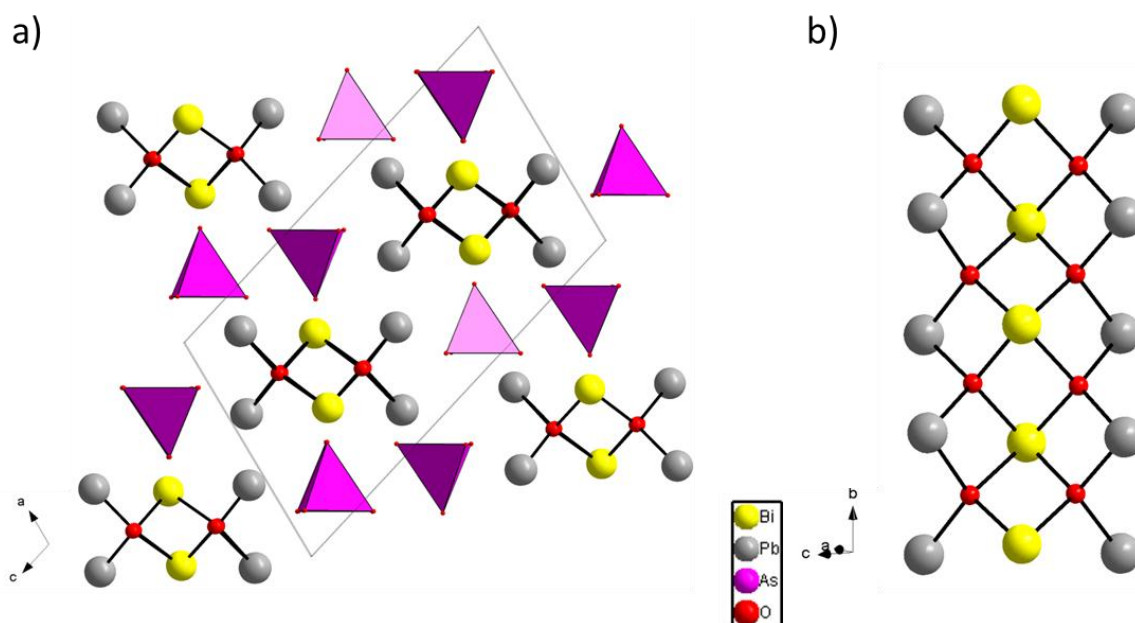


Figure III- 14 a) Representation of BiPb₂AsO₆ crystal structure and b) view of infinite double ribbons along axis b.

The bismuth ion is found to be seven-fold coordinated with oxygen ions and adopts a less pronounced off-centered coordination than for the other members of the BiM₂XO₆ series. However, it is still coordinated with four short Bi-O bonds on one side (from 2.23 to 2.46 Å) and three longer Bi-O bonds on the other side (from 2.54 to 3.05 Å). Within this coordination a bond valence of 2.607 is calculated for the bismuth (see figure III-15a).

There are two different Pb sites in this structure, Pb1 is found in a eight-fold coordination with four Pb1-O bonds on each side from 2.374 to 3.170 Å and a bond valence of 2.055 is calculated for this cation. On the other hand, Pb2 is found in a uncommon asymmetric five-fold coordination with four oxygen ions bonding at one side (from 2.222 to 2.804 Å) and a bond length of 2.8043 Å for O2 at the other side. In this coordination, the bond valence for Pb2 is equal to 2.096. The high coordination number for Pb1 suggests a low stereo-activity of

the lone-pair of Pb1 whereas the lone pair of electrons for Pb2 should be strongly stereo-active (see figure III-15b-c).

Arsenic bonds to four oxygen atoms in a slightly distorted tetrahedral coordination. Bond distances range from 1.659 to 1.689 Å and angles from 103.78 to 111.81° (see figure III-15d).

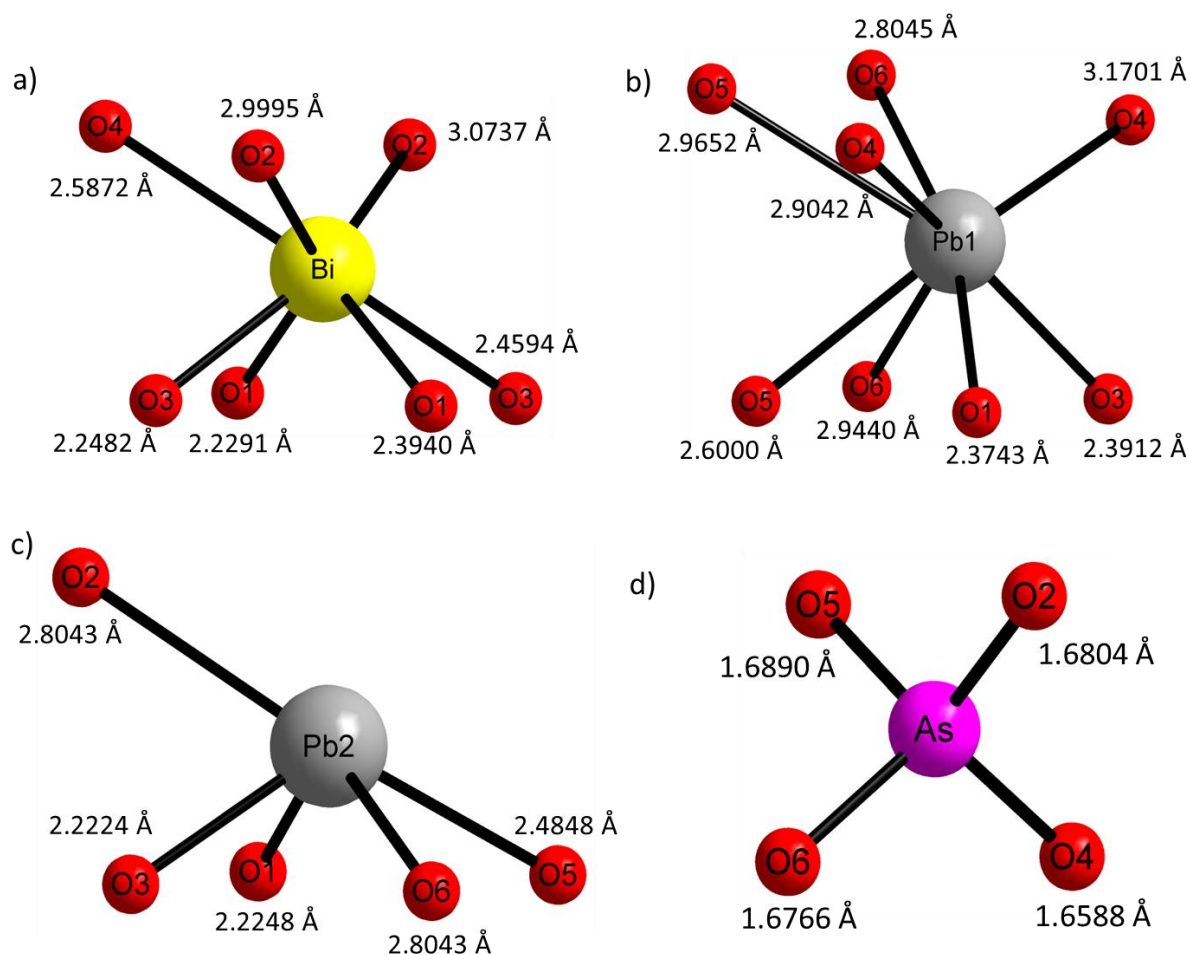


Figure III- 15 a) View of the coordination of Bismuth b) and c) View of the coordination of Lead atoms d) View of the coordination of Arsenic.

III.4. Tuning the optical properties of BiM₂XO₆ compounds

Focusing on the photoluminescence properties, only approximately the half of compounds indexed in table III-1 do not emit radiation at room temperature for some physical reasons:

Table III-6. Room temperature photoluminescence of BiM₂XO₆ series.

Room temperature photoluminescence	BiMg ₂ PO ₆ , BiZn ₂ PO ₆ , BiCd ₂ VO ₆	BiMg ₂ VO ₆ , BiCa ₂ VO ₆ , BiCa ₂ AsO ₆	BiMg ₂ AsO ₆ , BiCd ₂ PO ₆
Photoluminescence quenched at R.T.	BiPb ₂ PO ₆ , BiCu ₂ PO ₆ , BiMn ₂ PO ₆ , BiCd ₂ AsO ₆	BiPb ₂ VO ₆ , BiCu ₂ VO ₆ , BiMn ₂ VO ₆	BiPb ₂ AsO ₆ , BiCu ₂ AsO ₆ , BiMn ₂ AsO ₆

- For compounds containing divalent copper for example, the Cu²⁺ cations act as killer centers and quench the luminescence.⁴¹
- For lead compounds the problem is different, the Pb²⁺ is an ns² ion emitter as well as Bi³⁺. Both ions have similar optical properties and then, a concentration quenching occurs.
- Mn²⁺ cation is also an emitter⁴² and the high concentration of this last one paired with high concentration of Bi³⁺ also quench the luminescence at room temperature. However, at low temperature (10K) a characteristic luminescence of Mn²⁺ is observed and will be presented later in this chapter.
- And finally, strangely BiCd₂AsO₆ does not show any luminescence properties, the reason will be discussed later in this chapter.

On the other hand, all these compounds possess only one Bi site symmetry which makes easier the study of the relation between the luminescence properties and the chemical and structural environment of the ns² emitter.

III.4.1. M²⁺ influence

In this section the influence of the nature of the cation M²⁺, situated on the second sphere of the bismuth coordination, on the optical properties (electronic structure, reflectance, photoluminescence) of the BiM₂PO₆ (M= Mg, Zn, Cd) series and in its solid solution

BiMM'PO₆ will be investigated and discussed. These isostructural compounds offer the possibility to study the structure-optical relationship of bismuth compounds changing only on one chemical key parameter.

III.4.1.1. Synthesis of BiMM'PO₆ series (M/M'=Mg, Zn, Cd)

Polycrystalline powder samples were prepared by conventional solid state reaction between Bi₂O₃, CdO or MgO or ZnO and (NH₄)₂HPO₄ in stoichiometric amount. In a first stage, ZnO, MgO and Bi₂O₃ were heated overnight at 600°C for decarbonation. After grinding in a small amount of acetone, mixtures have been preheated at 500°C for 12h to decompose (NH₄)₂HPO₄. The reaction was complete after annealing at 800°C (770°C for BiZn₂PO₆) for 48h in an alumina crucible in air. Several intermediate grindings were necessary to obtain single crystalline-phases especially for magnesium-base compound. The solid solutions BiMg_{2-x}Cd_xPO₆ and BiMg_{2-x}Zn_xPO₆ were synthesized in the same way. All as-prepared samples are white powders, their purities were confirmed by XRD measurements (all the reflections are indexed to calculated pattern)^{12,29} and their cell parameters were refined using Fullprof software in the pattern matching mode (see figure III-16-17-18). Dealing with end-members compounds, the crystal data and other parameters discussed latter are gathered in the table III.7. They have been used for electronic structure calculations.

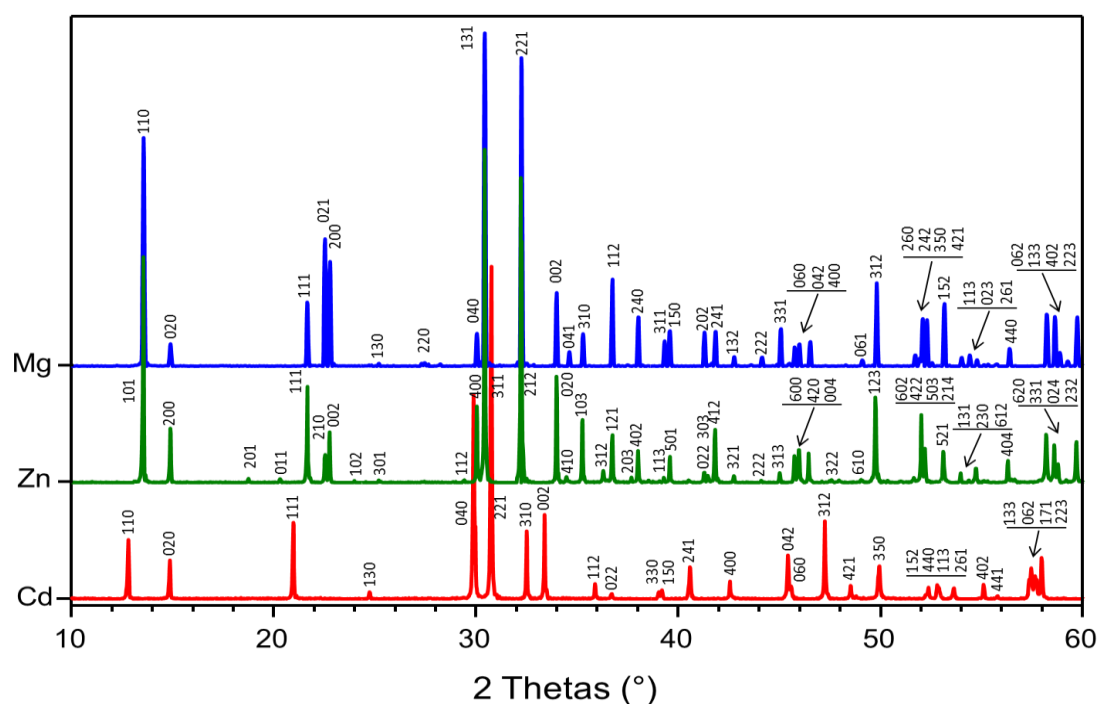


Figure III- 16 XRD pattern of BiM₂PO₆ (M=Mg, Zn, Cd)

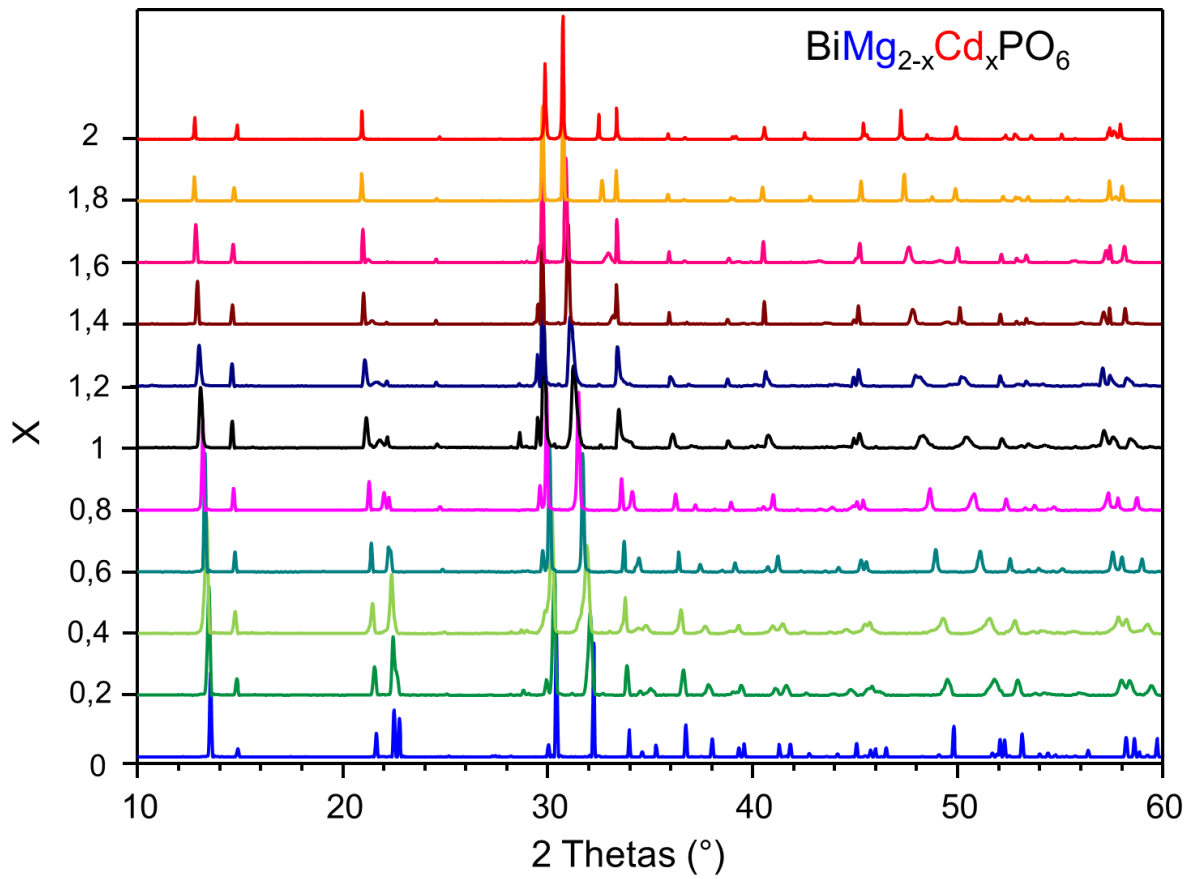


Figure III- 17 XRD pattern of the solid solution $\text{BiMg}_{2-x}\text{Cd}_x\text{PO}_6$

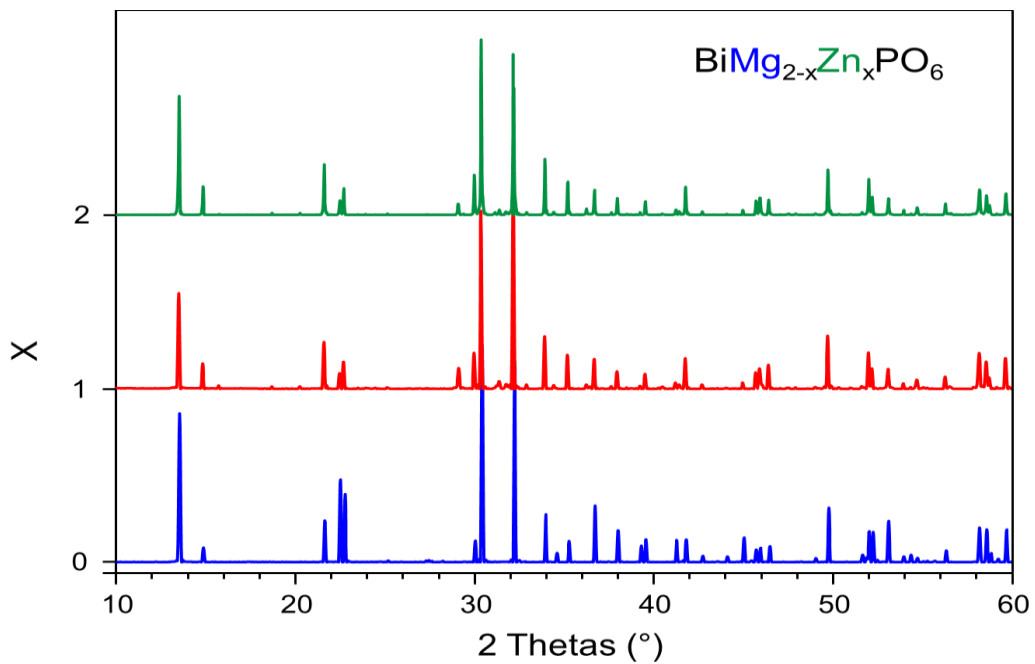


Figure III- 18 . XRD pattern of the solid solution $\text{BiMg}_{2-x}\text{Zn}_x\text{PO}_6$

Table III-7. Selected crystal data, Partial charges, Bi-Lp lengths and BVS for BiM₂PO₆ (M=Mg, Zn, Cd).

Compound	BiMg ₂ PO ₆ , ref. [12]	BiZn ₂ PO ₆ , ref. [29]	BiCd ₂ PO ₆ , this work
Crystal system	orthorhombic	orthorhombic	orthorhombic
Space group	<i>Bbmm</i>	<i>Pnma</i>	<i>Bb2₁m</i>
<i>a</i> (Å)	11.888(3)	11.8941(3)	11.9522(10)
<i>b</i> (Å)	5.273(2)	5.2754(2)	5.3744(10)
<i>c</i> (Å)	7.801(2)	7.8161(2)	8.5047(10)
Cell Volume (Å ³)	489.90(3)	490.43(3)	546.30(1)
Refinement type	XRD Single crystal	XRD Single crystal	synchr. powder XRD
Bi-O bonds (Å) (average)	4 x 2.196(3) 2 x 3.320(8) 4 x 3.346(5) (2.881)	2 x 2.301(20) 2 x 2.338(20) 1 x 2.937(24) 2 x 3.063(7) 2 x 3.570(11) (2.831)	2 x 2.172(30) 2 x 2.230 (30) 2 x 3.110(30) 1 x 3.150 (20) 2 x 3.534 (20) (2.805)
Partial charges (using Pacha)	Bi: 0.211 Mg: 1.375 P: 0.390 O1: -0.559 O2: -0.516 O3: -0.600	Bi: 0.411 Zn1: 0.886 Zn2: 0.901 P: 0.525 O1: -0.462 O2: -0.457 O3: -0.438 O4: -0.443	Bi: 0.428 Cd: 0.925 P: 0.449 O1: -0.454 O2: -0.471 O3: -0.467 O4: -0.440
Bi-LP length (Å) (using Hybride)	0.21	0.13	0.22
Bond Valence Sum	Bi: 3.09 Mg: 2.02	Bi: 2.52 Zn1: 2.08 Zn2: 2.15	Bi: 2.94 Cd: 1.99

III.4.1.2. Electronic structures and UV-visible spectroscopy

Density functional theory (DFT) calculations were performed using the Vienna *ab initio* simulation package (VASP).⁴³ The calculations were carried out within the generalized gradient approximation (GGA) for the electron exchange and correlation corrections using the Perdew-Wang (PW91) functional and the frozen core projected wave vector method.⁴⁴⁻⁴⁵ The full geometry optimizations were carried out using a plane wave energy cutoff of 550eV and 10 *k* points in the irreducible Brillouin zone for each compounds. All structural optimizations converged with residual Hellman-Feynman forces on the atoms smaller than 0.03 eV/Å and

led to reasonable structures regarding the distances and the local geometries. The cell parameters found after the full structural relaxation fit well with the experimental one. The error on cell parameters does not exceed 2.1% (on the *c* parameter for BiCd₂PO₆) (table III-8).

Table III-8. *Comparison between experimental and theoretical cell parameters (orthorhombic symmetry) of BiM₂PO₆ after full structural relaxation.*

Compound	Cell parameters	Experimental	Theoretical	Deviation from exp.
BiMg ₂ PO ₆	<i>a</i> (Å)	11.888(3)	12.0970	1.8%
	<i>b</i> (Å)	5.273(2)	5.3428	1.3%
	<i>c</i> (Å)	7.801(2)	7.8894	1.1%
BiZn ₂ PO ₆	<i>a</i> (Å)	11.8941(3)	12.1243	1.9%
	<i>b</i> (Å)	5.2754(2)	5.3379	1.2%
	<i>c</i> (Å)	7.8161(2)	7.9152	1.3%
BiCd ₂ PO ₆	<i>a</i> (Å)	11.9522(10)	12.1243	1.4%
	<i>b</i> (Å)	5.3744(10)	5.4296	1.0%
	<i>c</i> (Å)	8.5047(10)	8.6816	2.1%

Then, the relaxed structures were used to perform accurate calculations of the electronic structure. For the later, a plane wave energy cutoff of 400eV, an energy convergence criterion of 10⁻⁶ eV and 20 *k* points in the irreducible Brillouin zone were used. For the band diagram calculations, the *k* points were chosen according to the symmetry of the sample in order to investigate the entire Brillouin zone.

The figure III-19a-c represents the band structures of the BiM₂PO₆ (*M*= Mg, Zn, Cd) compounds calculated between -3eV to 5eV. For all three compounds the maximum of the valence band (VB) and the minimum of the conduction band (CB) are located at different *k* points of the Brillouin zone, which indicates indirect bandgaps. It allows reducing the electrons/holes recombination probability after photo-excitation and make of these compounds exciting candidates for enhanced photocatalytic activities.⁴⁶ For *M*=Mg, a minimum indirect bandgap of 3.62eV between the VB at the Gamma point and the CB at the Y2 point was obtained, while for *M*=Zn it is 2.75eV between the Gamma point (VB) and the Z point (CB). Concerning *M*=Cd, it is difficult to directly define the nature of the bandgap due to the low-dispersed band at the top of the VB between the calculated Gamma points. However, numerically, there is also an indirect bandgap of 2.64 eV between the Gamma point (VB) and the Z point (CB) whereas the value of a direct bandgap at the Z points is very close, i.e. 2.65eV. Note that for BiMg₂PO₆, these results differ from the direct bandgap announced by Barros *et al.*²⁸ even though a comparable value (3.58eV). This difference most probably

stems from the *Pmcn* model used in their calculations from ref.[35], with unrealistic Mg1-O2 ($d=1.739\text{\AA}$) smaller than the sum of ionic radii ($r\text{Mg}^{2+}_{\text{coord.IV}}=0.57\text{\AA}$, $r\text{O}^{2-}_{\text{coord.IV}}=1.38\text{\AA}$).

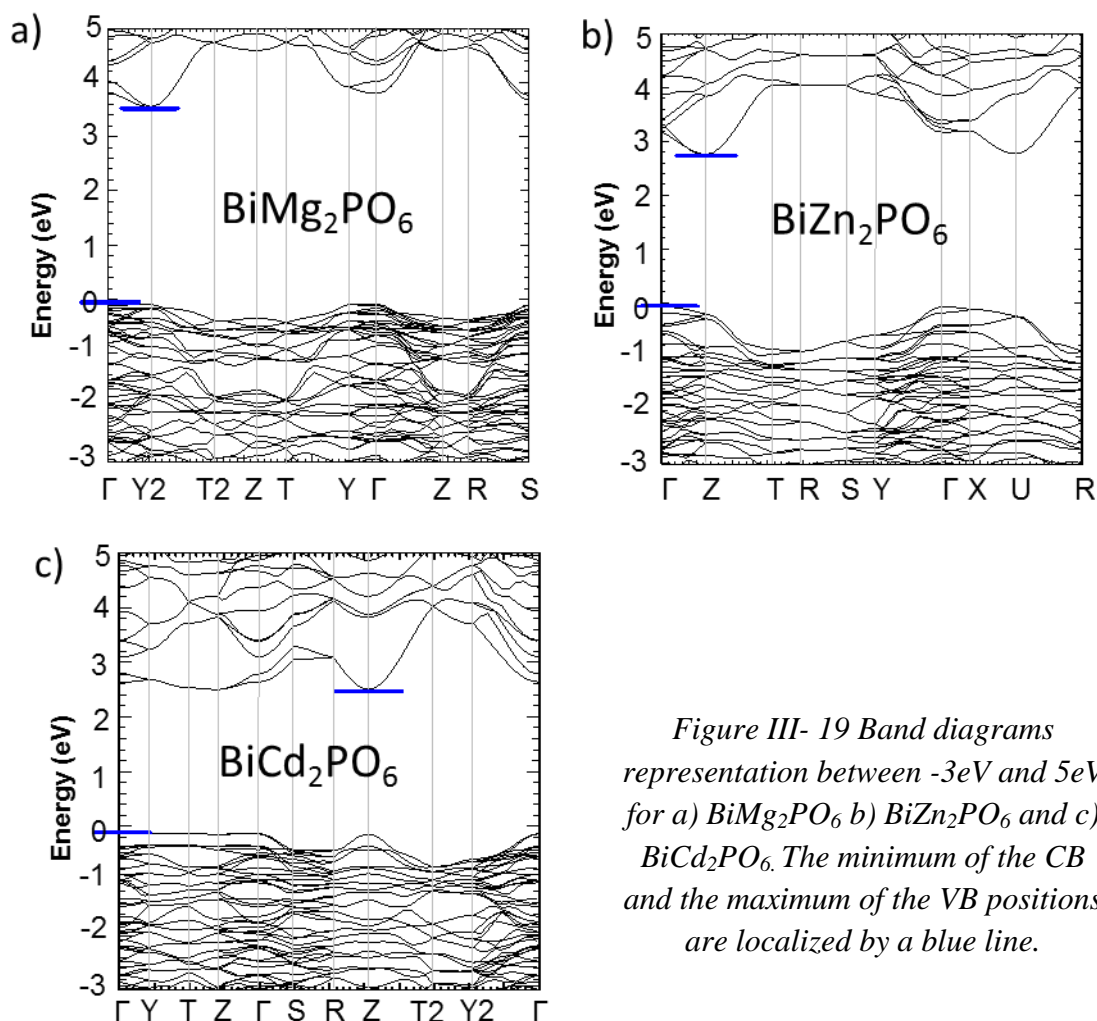


Figure III- 19 Band diagrams representation between -3eV and 5eV for a) BiMg₂PO₆ b) BiZn₂PO₆ and c) BiCd₂PO₆. The minimum of the CB and the maximum of the VB positions are localized by a blue line.

The reflectivity measurements were done in order to determine the experimental optical bandgaps. Kubelka-Munk fits ($F(R) = (1 - R)^2/2R$) and Tauc plots were used, as presented in figure III-20. Absorption spectra show comparable shapes with existence of weak low-energy tails, ascribed to minor shallow defect levels. The BiCd₂PO₆ spectrum is also characterized by an intense shoulder between 2.5 and 3.5eV. It may be due to the particular band structure dominated by the low energy low-dispersed band in most of the Brillouin zone. The indirect gaps have been extrapolated to $E_{\text{ind.}} = 3.76$ (vs. $E_{\text{GGA}} = 3.62\text{eV}$), 3.12 (vs. $E_{\text{GGA}} = 2.75\text{eV}$) and 2.62eV (vs. $E_{\text{GGA}} = 2.64\text{eV}$) respectively for M= Mg, Zn and Cd. The experimental values are well compatible with their calculated values although the experimental ones are a bit higher (except for M=Cd). This is accounted by the standard underestimation of the bandgap energies by DFT calculations.

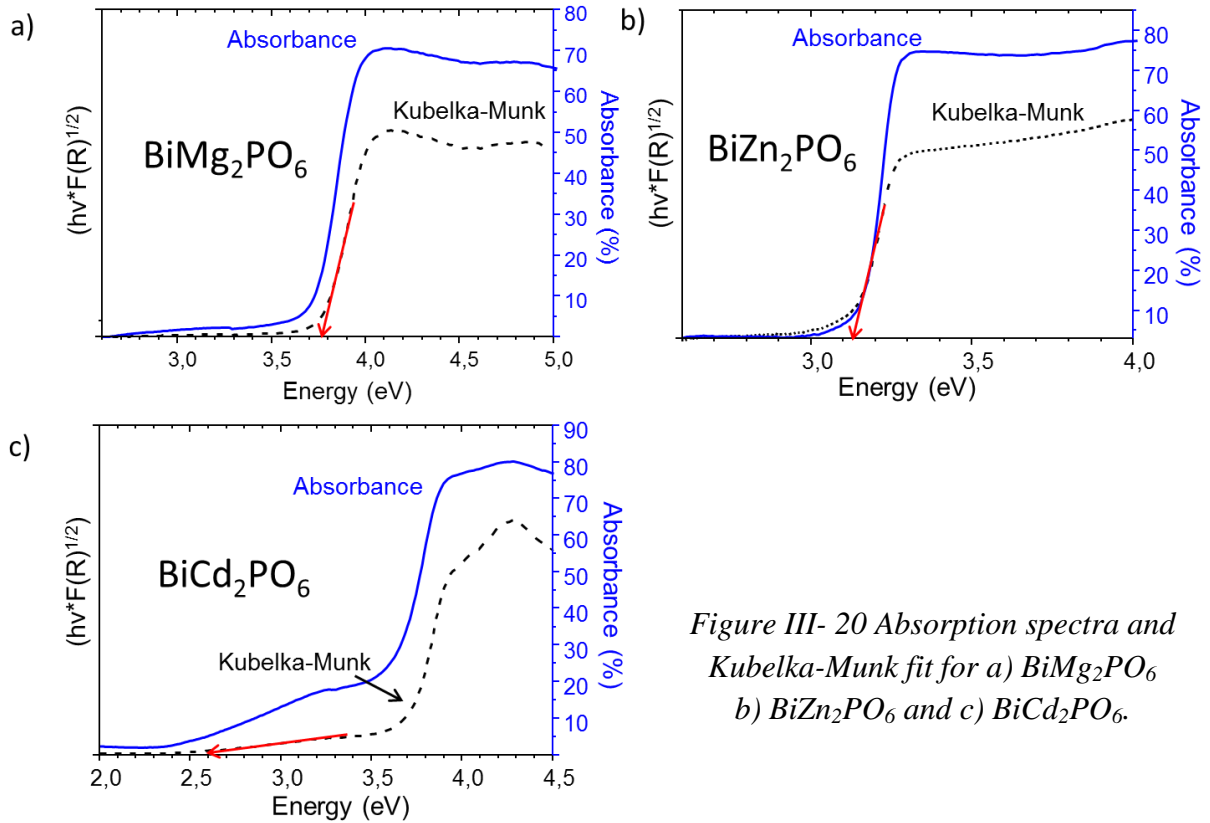


Figure III- 20 Absorption spectra and Kubelka-Munk fit for a) BiMg₂PO₆ b) BiZn₂PO₆ and c) BiCd₂PO₆.

III.4.1.3. Topology of the Density of States (DOS)

In this case, only the density of states of the oxygens present in the ribbon are represented. It is well established that, for post-transition lone-pair metal oxides (Tl⁺, Pb²⁺, Bi³⁺),³⁰⁻³¹ that i) strong interactions between the cation s and oxygen p orbitals results in anti-bonding states with a large degree of cationic s character at the top of the valence band, and ii) the interactions between nominally empty cationic p states (Bi³⁺ : 6s² 6p⁰) with the anti-bonding orbitals results in the familiar lone pair asymmetric electron density within distorted coordination. In the three investigated compounds, this behavior is verified by the presence of mixed O 2p, Bi 6s, Bi 6p states at the Fermi level. In details, the figure III-21a presents the total density of states (TDOS) and partial density of states (PDOS) calculated for BiMg₂PO₆. The highest VB part (-5,5 to 0eV) is essentially dominated by P 3p, O 2p and Bi 6p states, and a small contribution of Bi 6s states just below the Fermi level. The intermediate VB part (-9.6 to -7.1eV) is mainly composed of Bi 6s, P 3s, and Mg (s and p) states. The lowest energy part is mainly contributed by P 2p, O 2s states, and by a small amount of Bi 6s and 6p. In the conduction band (CB) (~3.6 to 11.2eV), the lower energy part between 3,6 and 6,5eV originates from the contribution of the O 2p and Bi 6p and Bi 6s states. The TDOS and PDOS for BiZn₂PO₆ are illustrated in Figure III-21b. Similarly to the BiMg₂PO₆ situation, it can also

be separated into three main sections. The principal and highest part (-6,9 to 0.0eV) is mainly composed of Zn 3d states and an appreciable contribution of O 2p and P 3p states with a small amount of Bi 6p states. Due to the contribution of the Zn 3d states, this near-Fermi level section is more extended that in the Mg²⁺ case. The second part from ~-10.1 to -8.2eV is shifted to lower energy compared to BiMg₂PO₆ and is composed of Bi 6s and P 3s states. The last part from ~-18.6 to -16.3eV is mainly composed of P 3s and O 2s. The bottom of the CB is essentially composed of Zn 4s, O 2p and Bi 6p and Bi 6s states.

The TDOS for BiCd₂PO₆ is represented in the figure III-21c and shows more similarities to BiZn₂PO₆ than to BiMg₂PO₆ (due to Cd²⁺ and Zn²⁺ d states). The VB can again be described by three parts. The higher from -7.1 to 0eV is mainly attributed to O 2p, Bi 6p and P 3p states as observed for the other compounds. In addition, it is found a large contribution of the Cd 4d states together with a small contribution from Bi 6s states just below the Fermi level. The second part from ~-9.9 to -7.8eV originates from Bi 6s and P 3s states. The last part from -18.2 to -15.9eV is generated from P 3p, O 2s and a very low contribution of Bi 6s and 6p states. Here again, the bottom of the CB is essentially composed of O 2p, Bi 6p and Bi 6s with adjunction of Cd 5s states.

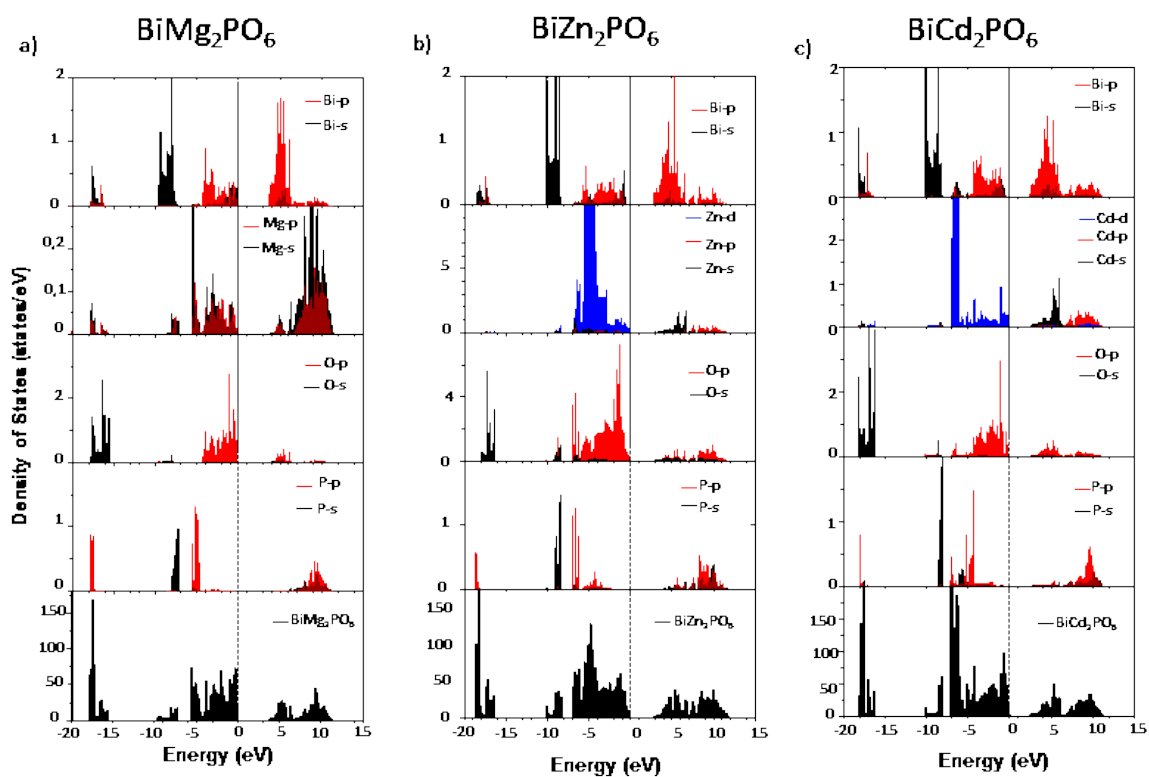


Figure III- 21 TDOS (bottom) and PDOS diagrams for a) BiMg₂PO₆ b) BiZn₂PO₆ and c) BiCd₂PO₆.

III.4.1.4. Primary analysis of the M-O-Bi bonding scheme

The chemical nature of the divalent cations on the M²⁺ site is expected to lead to sizeable electronic cloud expansion along the M-O-Bi subunits, a key-feature for optical properties discussed below. Accordingly the M²⁺ polarizing power, defined as the charge/radius ratio (*i.e.* q/r), provoking the electronic cloud elongation of the neighboring O²⁻ ions, follows the order $M = \text{Mg} (q/r = 3.03) > \text{Zn} (q/r = 2.94) > \text{Cd} (q/r = 2.30)$. At the same time, greatest electronegativity of the small ions is probably also important and a most important residual charge on the smallest Mg ions was calculated, see table III-7, but this parameter is rather hard to take into account. Increasing the M²⁺ polarizing power induces a more polarized M-O bond which decreases the oxygen electronegativity,⁴⁷ and it follows by inductive effects that inversed polarizations are expected on the next Bi-O bonds (see figure III-22), *i.e.* the Bi-O covalency increasing along the sequence (Mg-O-Bi) → (Zn-O-Bi) → (Cd-O-Bi). This is in good agreement to the Bi-O average bond lengths (M=Mg: 2.881Å) → (M=Zn: 2.831Å) → (M=Cd: 2.805Å). A similar tendency is shown after analysis of the DOS, as described in the next part. This effect could more simply be viewed as a compressive effect of the sizeable M-O unit on the next O-Bi unit.

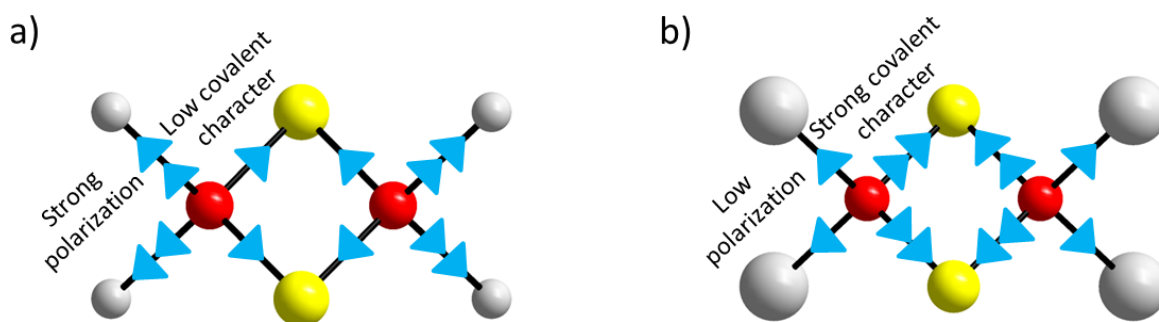


Figure III- 22 Sketch of the influence of the polarizing power of M²⁺ cations.

This effect can also be estimated from the DOS topologies. Focusing on the M-O bonds at the top the VB, BiMg₂PO₆ shows a strong degree of hybridization between the Mg 3s/3p and the O 2p levels. For BiZn₂PO₆, O 2p states are mixed with the Zn 3d states which are localized into a strong peak, providing a lower overlap scheme than for BiMg₂PO₆. In the case of BiCd₂PO₆, the Cd 4d states are mainly localized in the intermediate part of the VB and almost do not mix with O 2p states (mainly located in the highest VB area). It results into a sizeable

covalent character of the M-O bonds, increasing from $M= \text{Cd} < \text{Zn} < \text{Mg}$ as deduced from empirical polarizing power values.

III.4.1.5. Photoluminescence properties and correlations to the structure

BiMg₂PO₆ and BiZn₂PO₆ show a greenish-white luminescence at room temperature whereas BiCd₂PO₆ a bluish-white one. The coordinates representing their emission color on the chromaticity diagram (CIE 1931) are: $x=0.2684$ $y=0.3452$ for BiMg₂PO₆, $x=0.2733$ $y=0.3556$ for BiZn₂PO₆ and $x=0.2657$ $y=0.3252$ for BiCd₂PO₆ (figure III-23a). The emission which is comparable for the three phosphors, consists of a broad ($\Delta= \sim 16000\text{cm}^{-1}$) band in the visible region (with a maximum at $\sim 19600\text{cm}^{-1}$ to $\sim 20000\text{cm}^{-1}$). These bands can be assigned to the Bi³⁺: ³P₁ → ¹S₀ transition whereas the excitation (A-band) is significantly shifted between the three compounds even if it remains in the UV region (32680-37764cm⁻¹), see figure III-23b. All the photoluminescence characteristics are reported in the table III-9.

Table III-9. Photoluminescence characteristics for BiM₂PO₆ (M=Mg, Zn, Cd) and comparison between our results and the recently published by Boutinaud for BiMg₂PO₆

Compound	BiMg ₂ PO ₆	BiMg ₂ PO ₆ [28]	BiZn ₂ PO ₆	BiCd ₂ PO ₆
Excitation maximum	37767 cm ⁻¹ (4,68eV)	36364 cm ⁻¹ (4,51eV)	36765 cm ⁻¹ (4,56eV)	32680 cm ⁻¹ (4,05eV)
Emission maximum	19608 cm ⁻¹ (2,43eV)	19608 cm ⁻¹ (2,43eV)	19608 cm ⁻¹ (2,43 eV)	20048 cm ⁻¹ (2,48eV)
Emission FWHM	7140 cm ⁻¹ (0,89eV)	-	6680 cm ⁻¹ (0,83eV)	7820 cm ⁻¹ (0,97eV)
Stokes Shift	18156 cm ⁻¹ (2,25eV)	16756 cm ⁻¹ (2,08eV)	17157 cm ⁻¹ (2,13eV)	12632 cm ⁻¹ (1,57 eV)
Ionic radius M ²⁺	Mg ²⁺ : 0,66 Å	Mg ²⁺ : 0,66 Å	Zn ²⁺ : 0,68 Å	Cd ²⁺ : 0,87 Å

CIE 1931

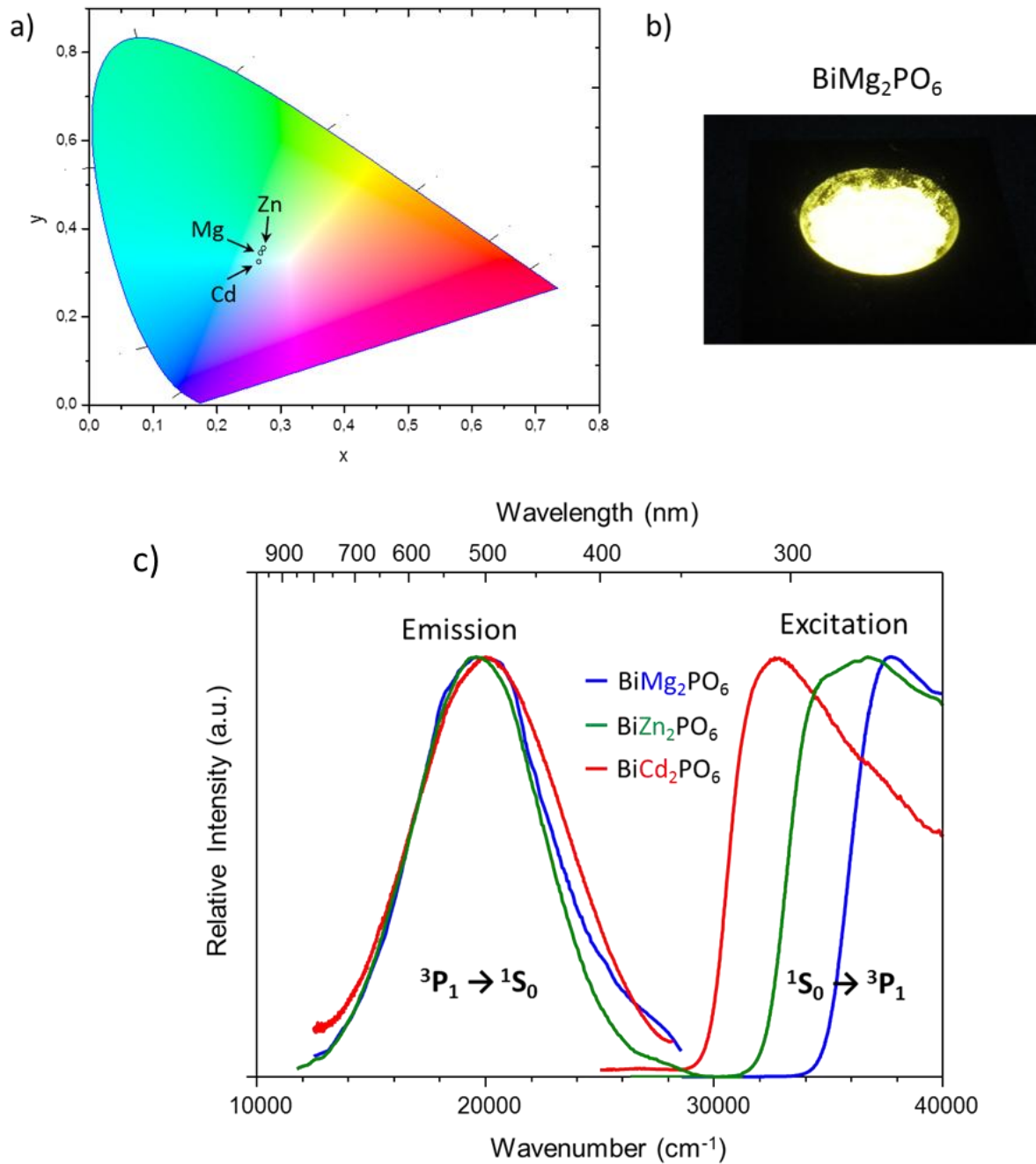


Figure III- 23 a) Color emission representation in the CIE chromaticity diagram of BiM_2PO_6 ($M=\text{Mg}, \text{Zn}, \text{Cd}$). b) Picture of BiMg_2PO_6 at room temperature under UV lamp excitation ($\lambda_{\text{ex}}=254\text{nm}$). c) Room temperature photoluminescence spectra of BiM_2PO_6 ($M=\text{Mg}, \text{Zn}, \text{Cd}$). The emission spectra are measured exciting at the maxima of corresponding excitation bands and vice versa (see Table III-9).

III.4.1.5.1. Bi-O covalency and excitation

- Focusing on the excitation process, a progressive redshift of the maximum occurs from M=Mg²⁺ to Zn²⁺ and then to Cd²⁺, i.e. when the M²⁺ ionic radii increases. It matches perfectly with the relative covalency of the M-O bonds deduced from the PDOS diagrams and from relative cationic polarizing powers, considering the electronic cloud expansion and expected nephelauxetic effect.⁴⁸⁻⁴⁹ In essence, the lower polarization of M²⁺-O bonds has for effect to increase the nephelauxetic effect concerning Bi³⁺ leading to a lowering of the ¹S₀ → ³P₁ transition energy (figure III-24.).

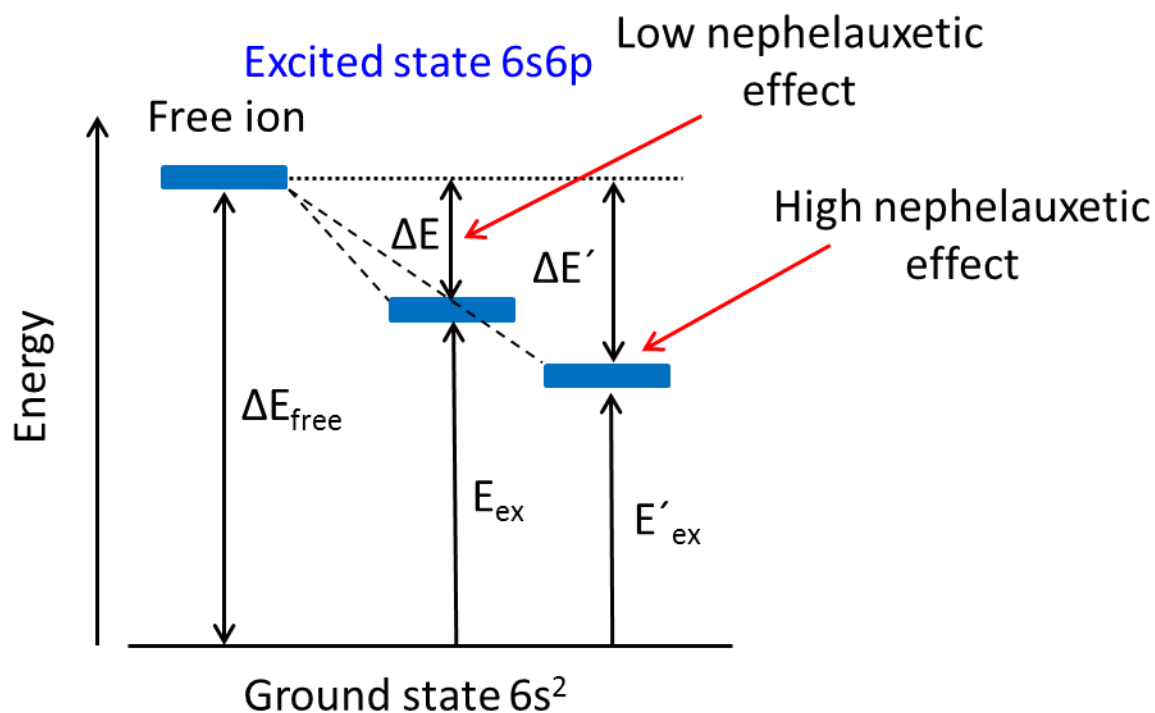


Figure III- 24 Sketch of the influence of the nephelauxetic effect on Bi³⁺. Increasing the nephelauxetic effect leads to lower the energy position of Bi³⁺ excited states. This has for consequence to decrease the energy required to reach the excited state 6s6p.

- The redshift of the excitation bands was also experimentally verified in the BiMg_{2-x}Cd_xPO₆ (strong effect) and BiMg_{2-x}Zn_xPO₆ (weak effect) solid solutions on increasing x, see figure III-27. It was observed for the mixed Mg/Cd compounds a splitting of the band into a doublet between x ~0.6 to ~1.4, although single phases are observed by XRD (Figure III-17 and 27). It most probably denotes appreciably different local environments of Bi (Mg neighbors vs. Cd

neighbors) in this x range. Indeed it was already pointed out by ³¹P NMR spectroscopy the drastic influence of the 1st and 2nd M²⁺ cationic sphere on the phosphorus chemical shift in the BiMg_{2-x}Cd_xPO₆ solid solution.⁵⁰ Similarly, it involves a distribution of local M/M' structures around Bi³⁺ in the mixed M/M' systems.

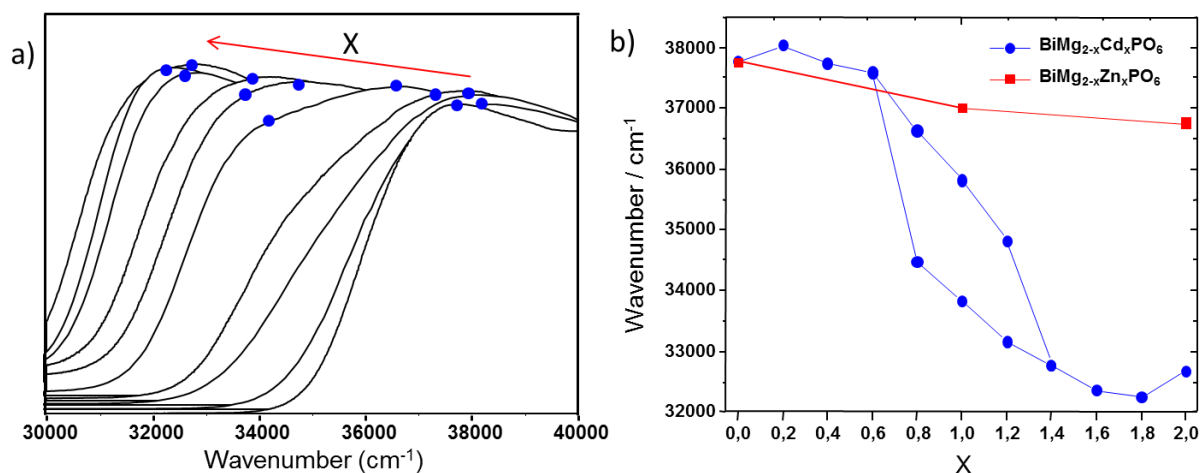


Figure III- 25 a) Excitation spectra of the solid solution BiMg_{2-x}Cd_xPO₆ at room temperature, b) Evolution of the position of excitation maxima of BiMg_{2-x}Cd_xPO₆ and BiMg_{2-x}Zn_xPO₆ with evidence of a doublet in the central range.

III.4.1.5.2. Excitation Energy above the Bandgap

In general it is admitted that, if the excitation is at higher energies than the bandgap, a light emission would not be observed since photo-ionization or photo-conductivity would occur instead. Even if intriguing, the scrupulous examination of the literature shows similar behaviors for other stoichiometric Bi based compounds, e.g. glass-ceramic Bi₄Ge₃O₁₂,⁵⁴ Bi₂Al₄O₉⁵⁵ or previous report of BiMg₂PO₆²⁸ ($E_{ex}/E_{GAP} = 4.54\text{eV}/3.6\text{eV}$, $4.28\text{eV}/3.65\text{eV}$, $4.51\text{eV}/3.58\text{eV}$ respectively). Such discrepancies are in general not pointed out in the publications, only in the case of KPb₂Cl₅ it led to controversial assignment of the excitation spectra⁵⁶⁻⁵⁷. Typically in all compounds described above this critical situation where the excitation energy is much higher than the bandgap is observed. What are the experimental proofs and reasons for so atypical features?

- The absorption spectrum shows a multiplet structure (mainly non-radiative) in which the second component is situated at the same energy than the excitation band (radiative process).

It is found for M= Mg, Zn and Cd compound $E_{ex}/E_{GAP} = 4.68\text{eV}/3.76\text{eV}$, $4.56\text{eV}/3.12\text{eV}$, $4.05\text{eV}/2.6\text{eV}$ (see figure III-26).

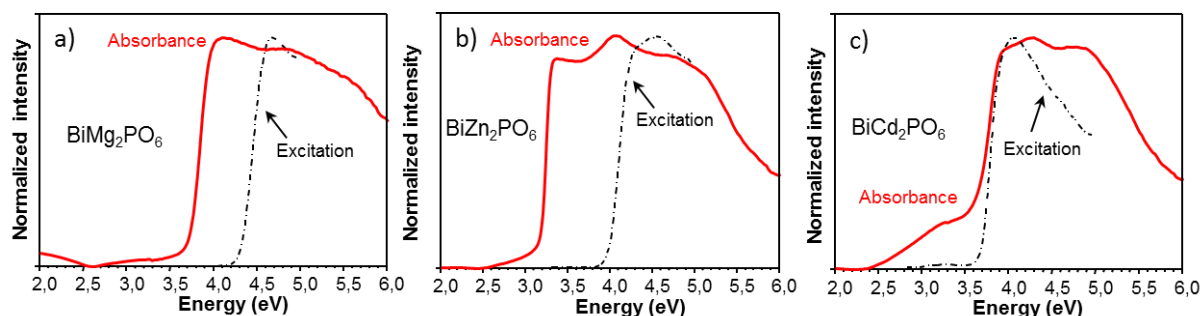


Figure III- 26 Comparison between absorption and excitation spectra for a) BiMg₂PO₆ b) BiZn₂PO₆ and c) BiCd₂PO₆.

- The calculated DOS give good opportunities to probe the fast Bi³⁺: $^1S_0 \rightarrow ^3P_1$ excitation, even though “ground states” calculations are not well representative of the excited states. However in a context of non-correlated electrons at the Fermi level, the calculated DOS mimic adequately empty states above the Fermi level and give good “prints” for VB \rightarrow CB transitions. At least, in the literature, several works have already correlated experimental luminescent results and *ab-initio* calculations in the fundamental state.⁵¹⁻⁵³ For BiM₂PO₆ series, these examinations of the DOS show that the Fermi edge does not systematically contain a Bi 6s contribution (e.g. see BiZn₂PO₆ and BiCd₂PO₆, figure III-24). Therefore the energy difference $\Delta(s^2 \rightarrow sp)$ between the highest VB Bi 6s states and the lowest CB Bi 6p states was estimated from the DOS leading to the values $\Delta(s^2 \rightarrow sp) \sim 3.2$ eV (M=Cd) < ~ 3.5 eV (M=Zn) < ~ 4.0 eV (M=Mg). These values still differ remarkably from the experimental excitation energies (i.e. Maximum of excitation at 4.05eV (M=Cd), 4.56eV (M=Zn) and 4.68eV (M=Mg)).

- The reasons for this difference are twofold: on one hand, the transition from the ground state to the lowest Bi 6s6p state (3P_0) is totally forbidden and will not be observed in the excitation spectra. On the other hand, the Stokes shift (the shift of excited states of M-L axis) has to be taken into account; it will shift the excitation spectra to higher energy (see figure III-27c). These results suggest, at least from the relative viewpoint the possibility for a probing of fast electronic transitions from basic DFT DOS calculations, even if the calculated transitions will be underestimated due to the two reasons mentioned previously. Then, one can consider that the excited states of bismuth are discrete levels in the CB, in good agreement with the

$\Delta(s^2 \rightarrow sp)$ rationalization detailed above (the 3P_0 states are not involved in the luminescence process at room temperature). Yet no clear explanation for this behavior (photoemission instead of photo-ionization or photo-conductivity) can be provided but at least the well matching of the excitation energies $\Delta s^2 \rightarrow sp$ calculated from the DOS can be noted. The radiative and non-radiative absorptions are sketched in the figure III-27, where the electronic $s \rightarrow p$ jump falls in the CB at the $6s-6p$ hybridization energy. At this stage, this presumption appears favored by $6s^2$ ions and may be preferred in indirect bandgap situations.

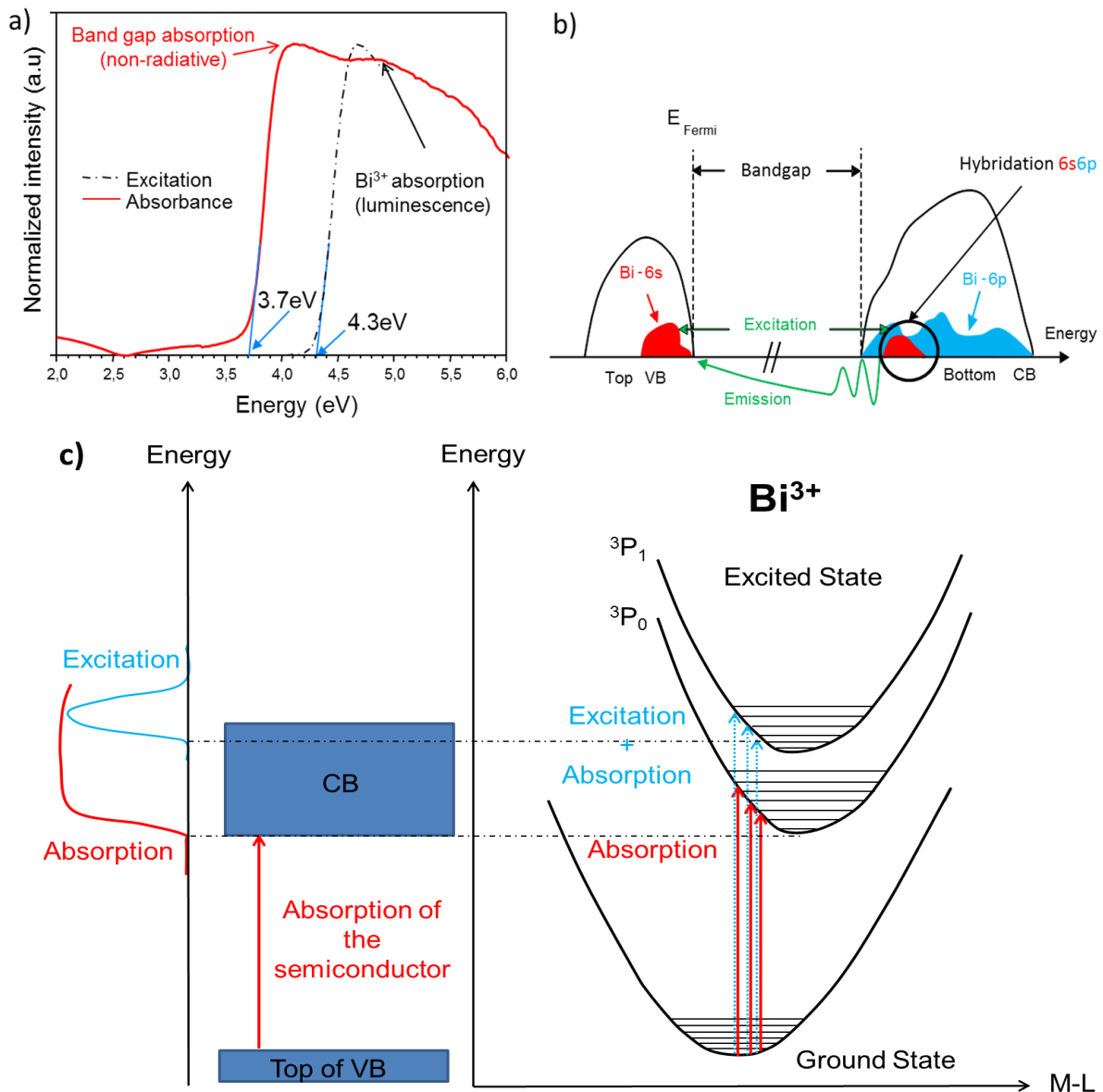


Figure III- 27 a) Comparison of absorption and excitation spectra of BiMg_2PO_6 b) A scheme of excitation/bandgap interplay using Bismuth PDOS in the BiM_2PO_6 compounds c) Sketch which explain the energy difference between the absorption and excitation band in Bi^{3+} based compounds.

III.4.1.5.3. Emission and Lone Pair activity

In the three compounds, the Bi³⁺ lone pairs (Lp) are pointing outside the BUs and have a strong stereo-chemical activity characterized by distinct short and long Bi-O bond distances, see table III-7. The Lp is shifted from Bi³⁺ centers along the *a*-axis (figure III-28a), as verified from the LP localization using the Verbaere method described in the experimental part (Chapter II). For these calculations, the partial charge determined using WinPacha have been used (see experimental part Chapter II).

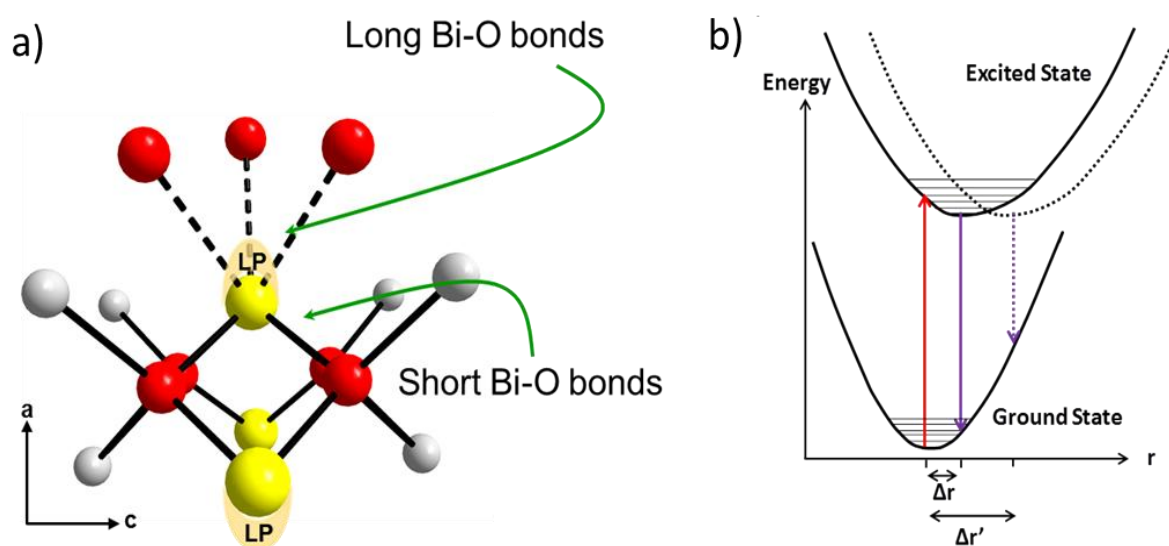


Figure III- 28 a) Representation of the Bi coordination including the lone pair position b) Diagram showing the stereo-activity of the lone pair of electrons, a low stereo-activity faintly shifts the excited state Δr and results on a small Stokes shift (full line). A high stereo-activity induces a larger shift $\Delta r'$, and hence induces a bigger Stokes shift (dashed line).

The calculated Bi-Lp distances are given in the table III-7. The $6s^1 6p^1 \rightarrow 6s^2$ emission is achieved through multiple vibrational relaxations, whereas, the respective contributions of each components are difficult to distinguish especially dealing with excited states. However, due to the mixed sp nature of excited states the lone-pair stereo activity is most presumably decisive on the emission process whereas, no clear evidence of this effect was given in the literature in absence of adequate chemical system. Based on these empirical calculations (see Table III-7), the Bi-Lp separation is found very close for the three Mg, Zn and Cd compounds in agreement with their comparable *a* lattice parameters (11.89_{-Mg-}, 11.89_{-Zn-} and 11.95_{-Cd-} Å) and is pointing out from the double ribbons toward the phosphates along axis *a*. Concomitantly, the energy of the emission maximum remains nearly unchanged between the

three compounds, i.e. Max emission: 2.43eV (M=Zn and Mg) and 2.48eV (M= Cd) respectively. Moreover, the Bi(Mg_{2-x}Zn_x)PO₆ solid solution also shows slight changes of both the *a* lattice parameter and the emission band energy (Max emission: 2.42eV for BiMgZnPO₆ with *a*=11,909 Å).

Strikingly, the very unusual evolution as a function of *x* of the lattice parameters along the Bi(Mg_{2-x}Cd_x)PO₆ solid solution gives good playground for the analysis of the LP effect. This lattice evolution was previously reported by our group⁵⁰: The cell *b* and *c* parameters increase with the respect of Cd²⁺ versus Mg²⁺ ionic radii whereas the *a* parameter increases up to *x*=1.2 and then decreases until *x*=2 (figure III-29a). This unusual concave plot was explained in ref. [50]. For *x*=1.2 the stress caused by the bigger Cd²⁺ cations induce tilting of the phosphates leading to a relaxation of the “*a*” cell parameter. As for the end-members, for all intermediate compositions, the RT emission spectra are characterized by a broad band in the visible range. A progressive redshift of the peak is observed from *x*=0 (BiMg₂PO₆) to *x*=1.2 and turns into a blue-shift from *x*=1.2 to *x*=2 (BiCd₂PO₆). Indeed the correlation between the *a*-parameter and the emission energy is obvious and unique to our knowledge, but validates the geometry of the excited state is strongly influenced by the lone pair activities (see figure III-29b-c). In fine, the lowest energy emission would correspond to the highest lone pair stereo-activity. It shows that the future prospection for performant luminescent Bi-based compounds with low Stokes shifts for energy saving should be oriented towards compounds with the most symmetrical Bi³⁺ coordination.

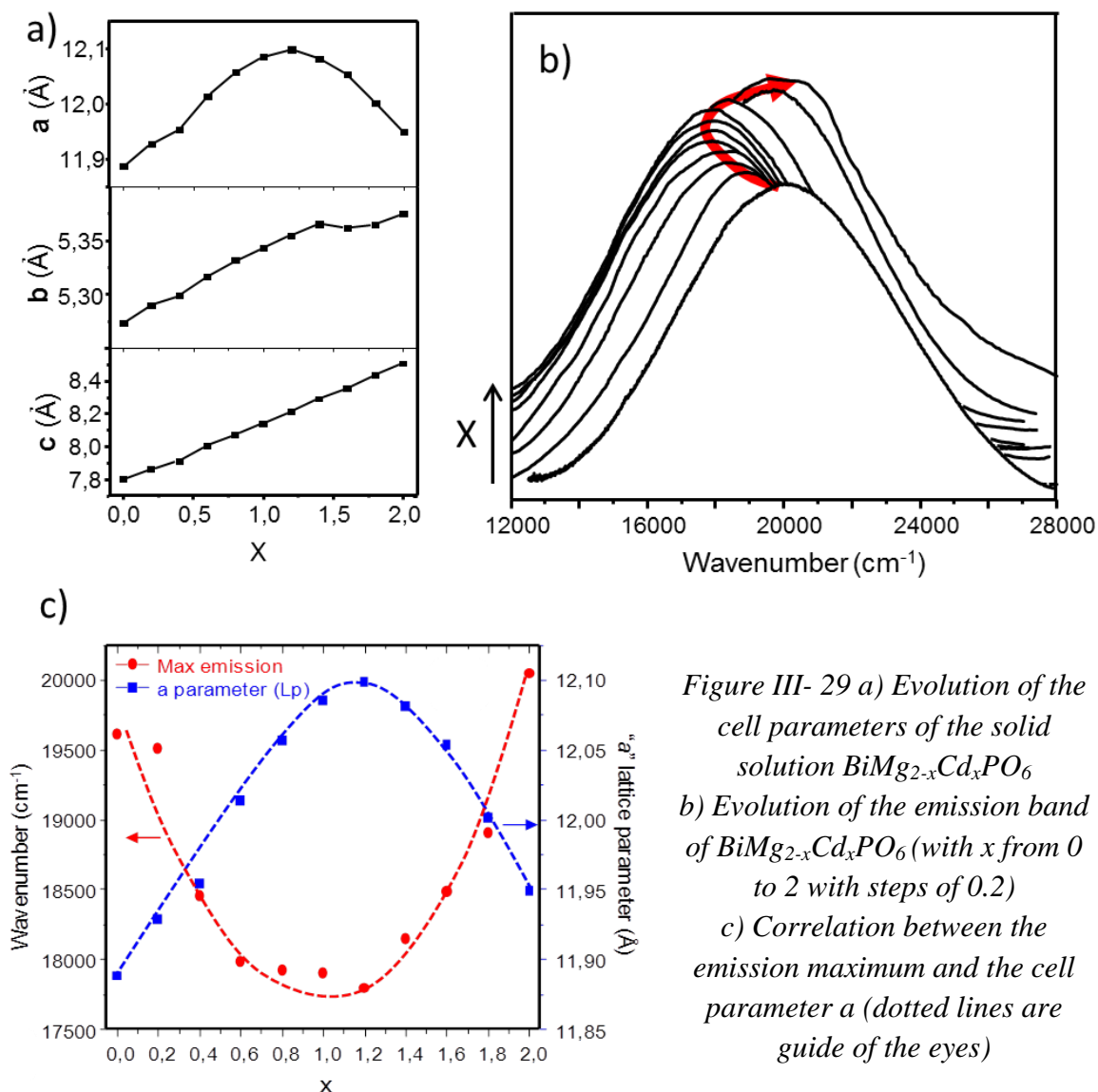


Figure III- 29 a) Evolution of the cell parameters of the solid solution $\text{BiMg}_{2-x}\text{Cd}_x\text{PO}_6$ b) Evolution of the emission band of $\text{BiMg}_{2-x}\text{Cd}_x\text{PO}_6$ (with x from 0 to 2 with steps of 0.2) c) Correlation between the emission maximum and the cell parameter a (dotted lines are guide of the eyes)

III.4.1.6. Analysis of the decay time versus temperature

A more detailed study was done for BiMg_2PO_6 including the temperature dependence of the luminescence, the decay time at room and low temperature. Taking into account that room and low temperature have to be measured on different systems, the decay time dependence cannot unfortunately be measured.

The excitation and emission intensities increase cooling down the sample to 30K and then decrease to 10K. This general behavior is simply explained by the thermal quenching and a similar thermal evolution anomaly below 30K was reported for Pb_2OSO_4 or $\text{La}_2\text{Zr}_2\text{O}_7$: Bi^{3+} .⁵⁸⁻⁵⁹ Concerning the excitation bands, when the intensity increases, a slight and progressive blue shift occurs which could be the consequence of change of the Bi-O bonds covalency with

temperature (figure III-30a). It was already shown for BiMg₂VO₆ compound that bond distances change upon temperature: the four short Bi-O bond lengths change from 2,1899Å (x2) and 2,2221Å (x2) at 100K to 2,1821Å (x2) and 2,2143Å (x2) at 250K .¹⁰ Then, in good agreement with the previous analyzes, the shorter Bi-O bonds at higher temperature increase the covalency and shift of the excitation toward lower energy is observed.

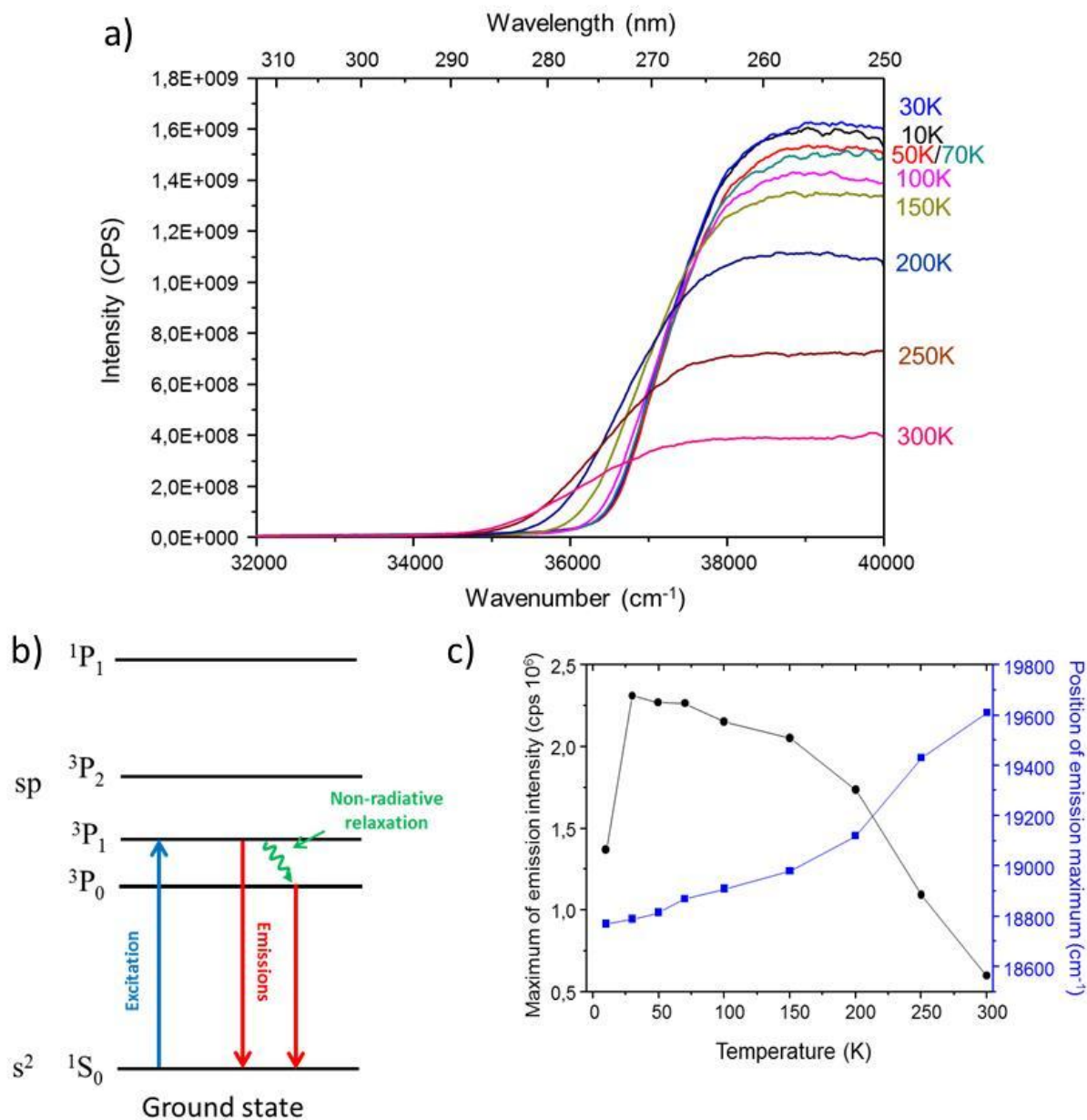


Figure III- 30 a) Temperature dependence excitation spectra for BiMg₂PO₆
 b) Sketch representing luminescence processes at low temperature and c) Evolution of the emission maxima energy position and intensity for BiMg₂PO₆.

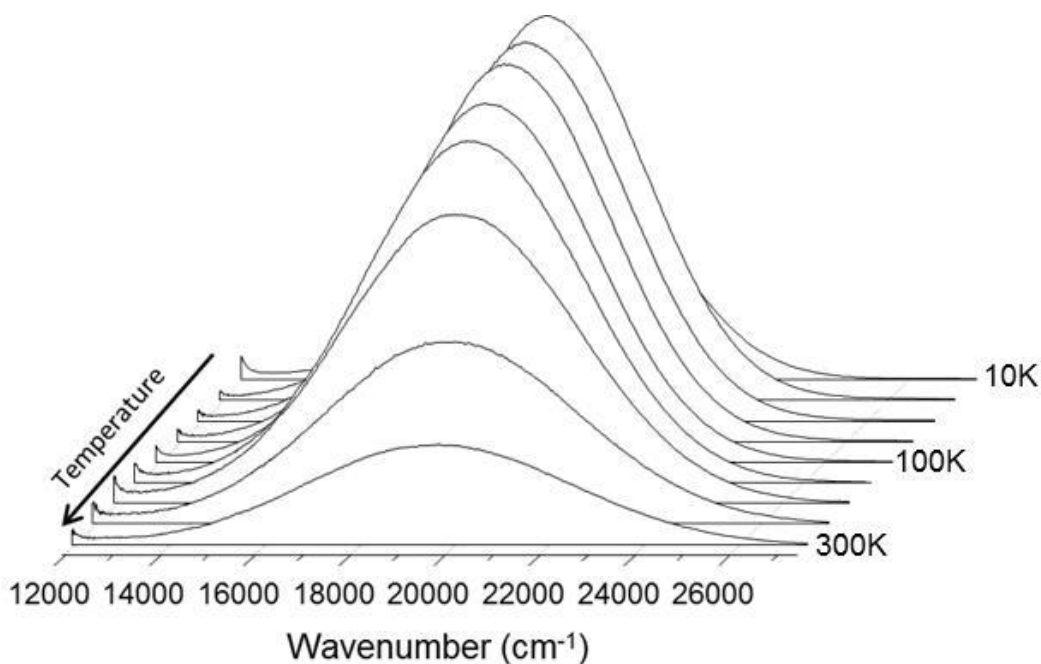


Figure III- 31 Temperature dependence emission spectra for BiMg₂PO₆.

Due to lower thermal atomic displacement at low temperature, the non-radiative relaxation from ³P₁ to ³P₀ excited states is favored and a pronounced thermodynamic equilibrium between ³P₁ to ³P₀ states happens (at room temperature only the ³P₁ state is considered occupied after excitation) (see figure III-30b). Moreover, as the ³P₀ state is situated below the ³P₁ level, this has for consequence to shift the emission toward higher energies upon cooling as it is observed figure III-30c-31. Even if theoretically two distinct emission bands are present, by time resolved spectroscopy it is not possible to observe separately these two bands due to their similar time dependence and their close energy positions.

This thermal equilibrium phenomenon is also demonstrated by the decay time measurements for which at 10K a double exponential behavior is fitted by opposition with the monoexponential at room temperature.

At room temperature, the decay time measurement shows a monoexponential behavior fitted to $\tau=350\text{ns}$ value. The decay expression used to fit the curve was $I = I_0 + A \cdot \exp(-t/\tau)$ (see figure III-32a). The character of this behavior means that only one radiative transition is observed during the emission process and the relatively short lifetime fits with a parity allowed transition. Moreover, this result is in good agreement with the literature reported value of $\sim 500\text{ns}$ for the Bi³⁺: ³P₁ → ¹S₀ transition.⁶⁰ In the other hand, at 10K the decay curve was fitted using a double exponential behavior, $I = I_0 + A_1 \cdot \exp(-t/\tau_1) + A_2 \cdot \exp(-t/\tau_2)$, giving two different lifetimes: $\tau_1=37\mu\text{s}$ and $\tau_2=586\mu\text{s}$ (see Figure III-32b). This double

emission corresponds plausibly to $^3P_1 \rightarrow ^1S_0$ transition for the lower value $\tau_1=37\mu\text{s}$ and $^3P_0 \rightarrow ^1S_0$ forbidden transition for the higher one ($\tau_2=286\mu\text{s}$).

The difference of the decay time value between 300K (350ns) and 10K (37 μs) for the $^3P_1 \rightarrow ^1S_0$ transition can also be explained by the temperature quenching.

In conclusion, the low temperature as well as the decay time measurements confirm that at room temperature only one transition for the emission is observed ($^3P_1 \rightarrow ^1S_0$) whereas at low temperature a thermodynamic equilibrium between 3P_1 to 3P_0 states is created and both radiative transition $^3P_1 \rightarrow ^1S_0$ and $^3P_0 \rightarrow ^1S_0$ are observed. Moreover, decreasing the temperature, no red shift of the excitation or any new excitation band appear at lower energies than the $^1S_0 \rightarrow ^3P_1$. Thus, it can be conclude that only one transition for the excitation process is observed $^1S_0 \rightarrow ^3P_1$ and the electrons cannot reach directly the 3P_0 from the ground state even at 10K. This result concerns the BiMg₂PO₆ phase but could reasonably be assumed for other compounds of the series.

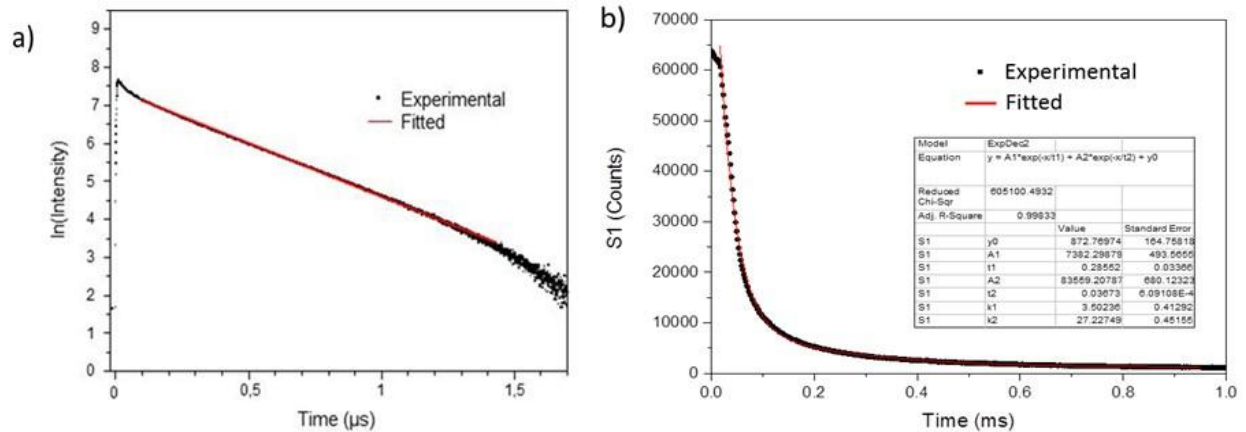


Figure III- 32 a) Decay time of BiMg₂PO₆ for excitation at 266nm and emission at 510nm at room temperature, the lifetime is fitted to 350ns (R^2 adj. = 0,999 fitted linear, the intensity was plotted in ln(intensity) in order to see the monoexponential behavior) b) Decay time of BiMg₂PO₆ for excitation at 265nm and emission at 516nm at 10K, the two different lifetimes are 37 μs and 286 μs (R^2 adj. = 0,998 fitted exponential).

III.4.1.7. Summary

In this part, the fully rationalized optical properties of the BiM₂PO₆ (M= Mg, Zn, Cd) and of the solid solution BiMM'PO₆ compounds comfort the intrinsic nature of the unquenched luminescence though atypical behaviors. Indeed, the excitation/emission processes may occur via excited states located above the bandgap, they are not fully hampered by non-radiative photo-ionization. The arrangement of Bi³⁺ ions in 1D-zigzag chains results in a limited Bi-Bi connectivity together with important Stokes shifts also play against self-quenching of the emission in the BiM₂PO₆ structural type. Contrarily, it is most probable that the greatest Bi-Bi connectivities inside broader ribbons of related Bi/M-oxophosphates would be a critical limit for luminescence. For the BiM₂PO₆ (M= Mg, Zn, Cd) compounds, it is also shown that a significant tuning of the excitation energy is allowed by substitution of M²⁺ cations, through inductive covalent effects inside the M-O-Bi subunits accordingly to the nephelauxetic effect. When the polarizing power of M²⁺ increases (Mg > Zn > Cd), the covalent Bi-O character decreases, shifting the excitation band to higher energy, as confirmed by 1st principle calculations. It was also shown that the excitation bands are situated at higher energies than the absorption edge, this is explained by the fact that the lowest energy excited state of Bi³⁺ (³P₀) is not involved in the excitation process and Stokes shift has to be taken account. Additionally, to the best of my knowledge it is shown for the first time the dependence of the emission energy on the lone pair stereo-activity, in an atypical mixed M/M' series. The correlation is such that less pronounced LP stereo-chemical activities lead to a shift of the emission band to higher energies. Finally one could propose that low polarizing power cations associated with Bi³⁺ is a favorable field of investigation for energy saving lamps (low excitation energy). Blue shift or redshift of the emission could ideally be reached playing on the lattice volume and lone pair activity towards a stronger or weaker electronic asymmetry respectively. In the following part will be investigated the role of the chemical nature of XO₄ (X= P, As, V) tetrahedra through the tuning the size of the XO₄ groups.

III.4.2. Effect of the XO₄ (X=P, V, As) group

After the rationalization of the effect of the M chemical nature, it is relevant to investigate and discuss the influence of the nature of the X⁵⁺ cation. In other words the chemical nature of tetrahedra surrounding the double ribbons in the BiM₂XO₆ phases was analyzed using same concepts as previously. It was shown in the section 3.4.1 that playing on the chemical nature of M²⁺ cation influences the excitation energy position by inductive effect on the covalent character of Bi-O bonds and the emission could be correlated to the stereo-activity of the Bi's lone pair of electrons. In this section, the BiMg₂XO₆ (X= P, V, As) series and also mixed compositions BiCd₂(XX')O₆ will be investigated.

III.4.2.1. Synthesis of BiMg₂XO₆ (X=P, V, As)

Polycrystalline powder samples of all stoichiometric phases and mixed compositions were prepared by conventional solid state reaction between Bi₂O₃, MgO, V₂O₅, As₂O₅ and (NH₄)₂HPO₄. After grinding in a small amount of acetone, the phosphorus mixtures have been preheated in a first time at 500°C for 12h to decompose (NH₄)₂HPO₄ before to complete the reaction at 800°C during 48h. The vanadium and arsenic compounds were directly heated at 800°C in alumina crucible in air and isothermed for 48h. Several intermediate grindings were necessary to obtain single crystalline-phases. The purity of each sample was confirmed by XRD (figure III-33).^{4,16} Concerning the colors, BiMg₂PO₆, BiMg₂AsO₆ are white powders whereas BiMg₂VO₆ is yellow.

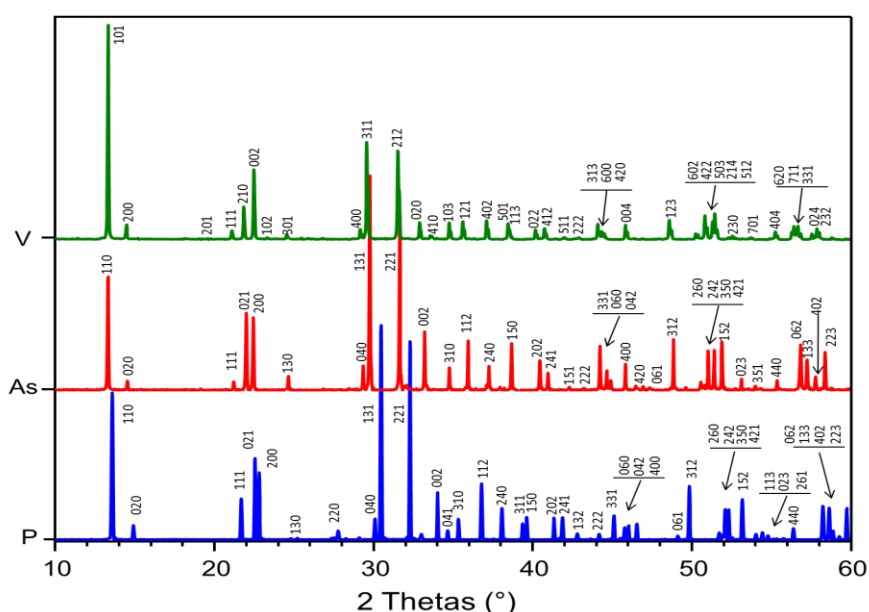


Figure III- 33 XRD pattern of BiMg₂XO₆ (X=P, As, V) series with reflections indexation.

Table III-10. All the crystallographic data concerning the BiMg₂XO₆ (X=P, As, V) series.

Compound	BiMg ₂ AsO ₆ , ref. [16]	BiMg ₂ VO ₆ , ref. [4]	BiMg ₂ PO ₆ ref. [16]
Crystal system	orthorhombic	orthorhombic	orthorhombic
Space group	<i>Bbmm</i>	<i>Pnma</i>	<i>Bbmm</i>
a (Å)	12.1637(8)	12.2475(3)	11.888(3)
b (Å)	5.3898(4)	5.4431(2)	5.273(2)
c (Å)	7.9142(5)	7.9160(2)	7.801(2)
Cell Volume(Å ³)	518.85(10)	527.72(3)	489.01(30)
Refinement type	XRD Single crystal	XRD Single crystal	XRD Single crystal
Bi-O bonds (Å) (average)	4 x 2.2196(243) 2 x 3.3742(578) 4 x 3.4458(366) (2.941)	2 x 2.1938 (91) 2 x 2.2116(91) 1 x 3.2193(241) 2 x 3.3215(139) 2 x 3.5776(157) 1 x 3.6509(241) (2.948)	4 x 2.1955(33) 2 x 3.3200(76) 4 x 3.3458(46) (2.881)
Partial charges (using Pacha)	Bi: 0.210 Mg: 1.391 As: 0.344 O1: -0.562 O2: -0.603 O3: -0.503	Bi: 0.022 Mg: 1.139 V: 0.390 O1: -0.546 O2: -0.782 O3: -0.715	Bi: 0.211 Mg: 1.375 P: 0.390 O1: -0.559 O2: -0.516 O3: -0.600
Bi-LP length (Å) (using Hybride)	0.07	0.77	0.21
Bond Valence Sum	Bi: 2.31 Mg: 2.02	Bi: 2.80 Mg: 2.02	Bi: 3.09 Mg: 2.02

III.4.2.2. Electronic properties

Density functional theory (DFT) calculations were performed using the Vienna *ab initio* simulation package (VASP).⁴³ The calculations were carried out within the generalized gradient approximation (GGA) for the electron exchange and correlation corrections using the Perdew-Wang (PW91) functional and the frozen core projected wave vector method.⁴⁴⁻⁴⁵ The full geometry optimizations were carried out using a plane wave energy cutoff of 550eV and 10 *k* points in the irreducible Brillouin zone for each compounds. All structural optimizations converged with residual Hellman-Feynman forces on the atoms smaller than 0.03 eV/Å and led to reasonable structures regarding the distances and the local geometries. The error on cell parameters does not exceed 2.3% (on the *a* parameter for BiMg₂AsO₆) which is acceptable (table III-11).

Table III-11. Comparison between experimental and theoretical (after full relaxation) cell parameters for BiMg₂XO₆ (X=P, As, V).

Compound	Cell parameters	Experimental	Theoretical	Deviation from exp.
BiMg ₂ PO ₆	<i>a</i> (Å)	11.888(3)	12.0970	1.8%
	<i>b</i> (Å)	5.273(2)	5.3428	1.3%
	<i>c</i> (Å)	7.801(2)	7.8894	1.1%
BiMg ₂ AsO ₆	<i>a</i> (Å)	12.1637(8)	12.4422	2.3%
	<i>b</i> (Å)	5.3898(4)	5.4553	1.2%
	<i>c</i> (Å)	7.9142(5)	7.9813	0.8%
BiMg ₂ VO ₆	<i>a</i> (Å)	12.2475(3)	12.3887	1.2%
	<i>b</i> (Å)	5.4431(2)	5.5157	1.3%
	<i>c</i> (Å)	7.9160(2)	7.9928	1.0%

Then, the relaxed structures were used in order to perform accurate calculations of the electronic structure. For the calculation of the density of states (DOS) and projected density of states (PDOS), a plane wave energy cutoff of 400 eV, an energy convergence criterion of 10⁻⁶ eV and 20 *k* points in the irreducible Brillouin zone were used. For the band diagram calculations, the *k* points were chosen according to the symmetry of the sample in order to investigate the entire Brillouin zone. Finally, the band diagrams for the BiMg₂XO₆ (X=P, As, V) series were represented between -3eV and 5eV and present an indirect bandgap (see figure III-34a-d.).

Electronic properties of BiMg₂PO₆ were already described in the previous part, and will not be described in details again. However, its electronic properties can be compared to these of the two other compounds of the BiMg₂XO₆ (X=P, As, V) series. The three concerned compounds display an indirect band gap of 3.62 eV, 3.37 eV and 3.19eV respectively for X=P, X=As and X=V. For BiMg₂VO₆, the band gap value is in good agreement with the one found by Barros et al.²⁸ (3.26eV). Concerning BiMg₂AsO₆, the indirect band gap is not obvious and accurate zoom was needed to confirm it. From the calculations, the minimum of the CB is situated at the Y point and the “exact” maximum of the VB in between the Y and Gamma points. However there is only 0.01eV difference between the lowest indirect transition (3.37eV) and the lowest direct transition (3.38eV) situated at the Y point, see figure III-34d. The calculated gaps of the BiMg₂XO₆ (X=As and V) are comparable although slightly higher than the experimental values found by extrapolation of Kubelka-Munk representations and Tauc plots fits ((E_{ind.} = 3.21 (vs. E_{GGA} =3.37eV), 3.16 (vs. E_{GGA} =3.19eV) respectively for X=As and X=V) (figure III-34e-g).

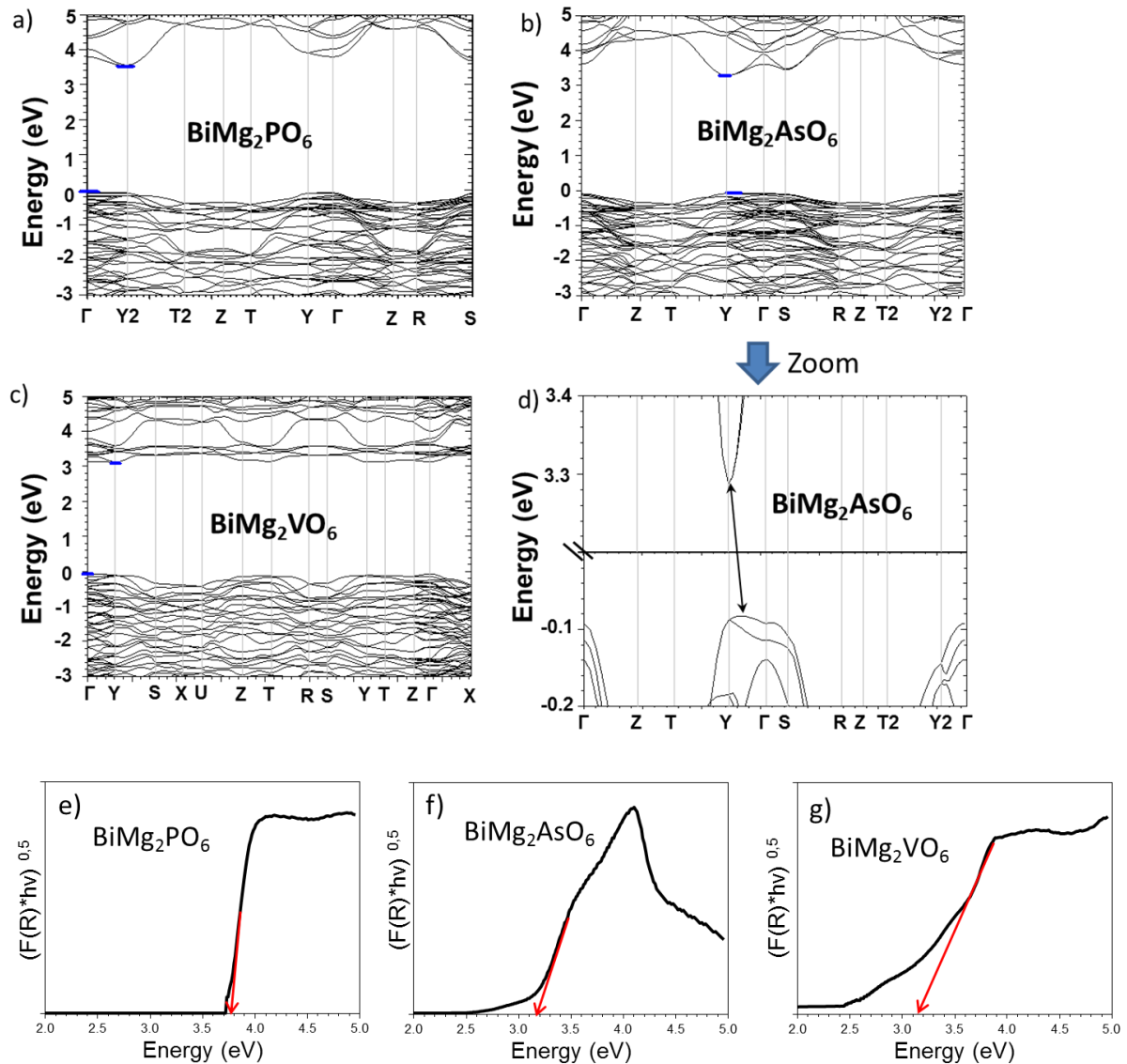


Figure III- 34 a-c) Representation of band diagrams for BiMg_2XO_6 d) Zoom on the minimum of the CB and maximum of the VB for $\text{BiMg}_2\text{AsO}_6$ e-g) Kubelka-Munk fits and Tauc plots of BiMg_2XO_6 series and bandgap extrapolation (BG: $\text{BiMg}_2\text{PO}_6=3.76\text{eV}$, $\text{BiMg}_2\text{AsO}_6=3.21\text{eV}$ and $\text{BiMg}_2\text{VO}_6= 3.16\text{eV}$).

III.4.2.3. Topology of the DOS

The figure III-35 presents the total density of states and partial density of states calculated for BiMg₂XO₆ (X=P, As, V) series.

- The electronic properties of BiMg₂PO₆ were already described in detail previously and its DOS are plotted here as a model for comparison.
- For BiMg₂AsO₆, the highest VB part (-5,1 to 0eV) is mainly dominated by O 2p, Bi 6p and As 3d/4p states, a low contribution of Bi 6s states localized just below the Fermi level is also found. Whereas the O 2p and Bi 6p states cover all the highest part of the VB, the As 3d states are situated between ~-3 and 0eV and the As 4p states between ~-5.1 and 2eV. On the other hand, the lowest part conduction band (CB) (~3.37 to 6.5eV), originates from the contribution of the O 2p, As 4s and Bi 6p states and also of Bi 6s states 4 and 6eV.
- The TDOS and PDOS for BiMg₂VO₆ are illustrated in figure III-35b. Similarly to the BiMg₂PO₆ and BiMg₂AsO₆ situation, the contribution of Mg can be neglected. The highest part of the VB (-4,4 to 0.0eV) is essentially composed of O 2p, Bi 6s/6p and V 3d states and a small contribution of V p and V s states is found. Whereas the three first cited states are presented at the Fermi level, the V 3d states are localized between -4.4 and -1eV. The lowest part of the CB (3.19 to 6.4eV) for BiMg₂VO₆ differ from these of X=P and X=As. In the vanadium compound it is essentially composed of V 3d states even if noticeable contributions of Bi 6p, V p and O 2p states and small contribution of Bi 6s are found.

It is important to recall that in the case of changing M in BiM₂PO₆ compounds led to sizeable bonding parameters inside the Bi-O-M links, and the degree of M-O covalency was directly observed in the DOS (see section 3.4.1.4). Here playing with X, this feature does not seem true anymore and DOS show similar degree of Mg, Bi and O states.

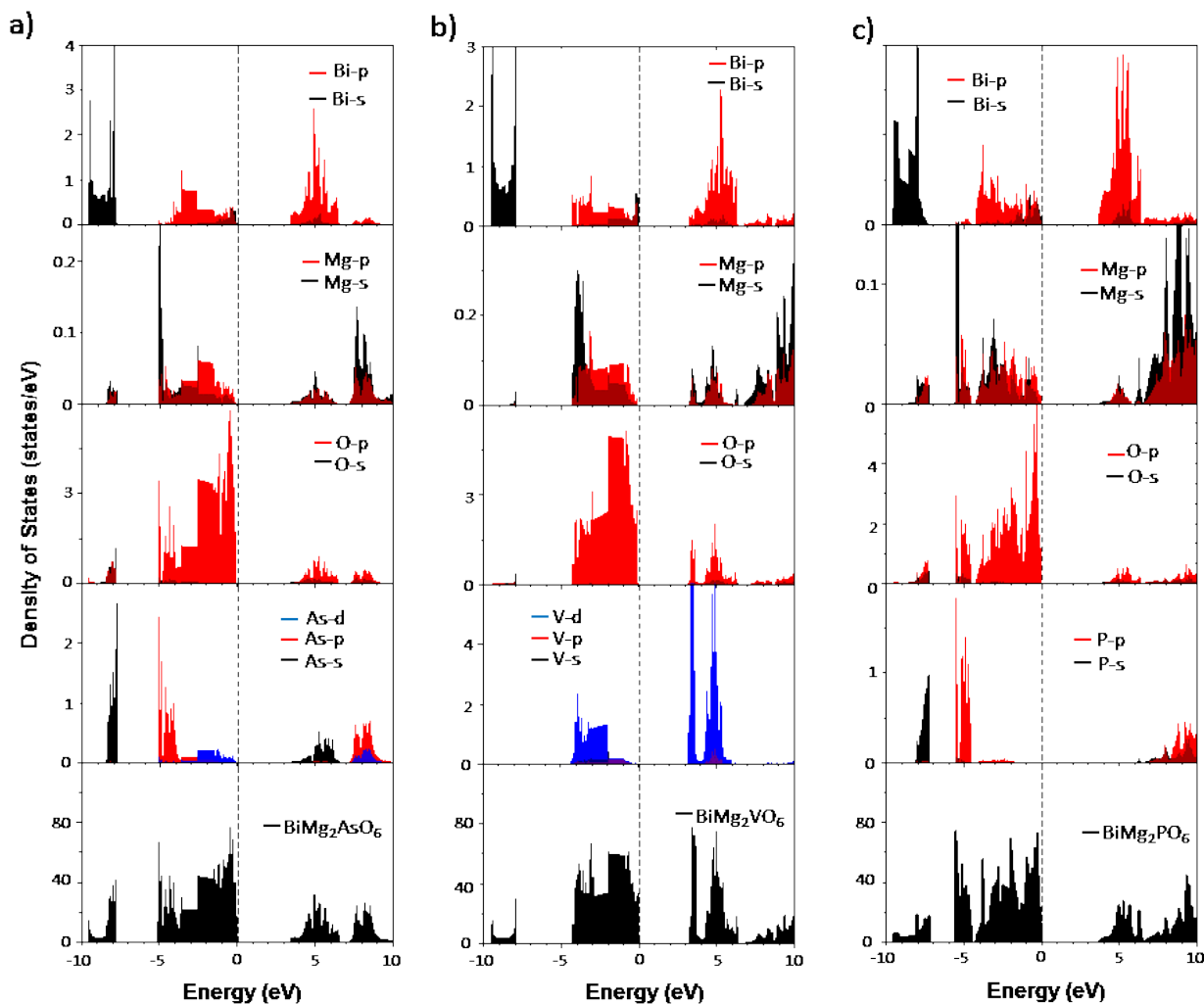


Figure III- 35 a-c) Representation TDOS (bottom) and PDOS for a) BiMg₂AsO₆ b) BiMg₂VO₆ and c) BiMg₂PO₆.

III.4.2.4. Photoluminescence properties and correlations

The luminescence of BiMg₂PO₆ was already discussed but is compared here with the two other phosphors. All the three compounds exhibit photoluminescence emission at room temperature. The coordinates representing their emission color on the chromaticity diagram (CIE 1931) are: x=0.2684 y=0.3452 for BiMg₂PO₆ (greenish-white emission), x=0.3178 y=0.3948 for BiMg₂AsO₆ (greenish white emission) and x=0.4677 y=0.4635 for BiMg₂VO₆ (orange emission) (figure III-36a-b.).

Excitation: Focusing on the excitation now, the energy position band follows the same trend than emission for the three compounds (maximum at 37767cm⁻¹, 36710cm⁻¹ and 29760cm⁻¹ respectively for BiMg₂PO₆, BiMg₂AsO₆ and BiMg₂VO₆), see figure III-36c. Due to the limits of our spectrofluorometer, the excitation spectra at higher energies than 40000cm⁻¹ (250nm) cannot be recorded. Hence, the exact character of the excitation band for BiMg₂XO₆ (X = As, P) cannot be observed but on the other hand the excitation band of BiMg₂VO₆ clearly exhibits at least a doublet character with a second maximum at ~36840cm⁻¹ which is not the case in the previous report (only a singlet).²⁸ All the photoluminescence characteristics are reported Table III-12.

Emission: For the three compounds, the emission is situated in the visible range and is characterized by a broad band (between 12000 and 16000cm⁻¹). Contrarily to what was observed changing M²⁺ (very weak influence on the emission energy), the emission is situated at significantly different energies for the three isostructural compounds. Compared to BiMg₂PO₆ (maximum at 19608cm⁻¹), the emission of BiMg₂AsO₆ is slightly shifted to lower energies (maximum at 18940cm⁻¹) whereas the red shift of BiMg₂VO₆ emission band is more significant (maximum at 16420cm⁻¹).

Table III-12. Room temperature photoluminescence characteristics for the BiMg₂XO₆ (X=P, As, V) series.

Compound	BiMg ₂ PO ₆	BiMg ₂ AsO ₆	BiMg ₂ VO ₆	BiMg ₂ VO ₆ ref[28]
Excitation maximum	37767 cm ⁻¹ (4,68eV)	36710 cm ⁻¹ (4,55eV)	29760 cm ⁻¹ (3,69eV)	28985 cm ⁻¹ (3,59eV)
Emission maximum	19608 cm ⁻¹ (2,43eV)	18940 cm ⁻¹ (2,35eV)	16420 cm ⁻¹ (2,04 eV)	15873 cm ⁻¹ (1,97eV)
Emission FWHM	7140 cm ⁻¹ (0,89eV)	6725 cm ⁻¹ (0,83eV)	5590 cm ⁻¹ (0,69eV)	-
Stokes Shift	18156 cm ⁻¹ (2,25eV)	17770 cm ⁻¹ (2,20eV)	13340 cm ⁻¹ (1,65eV)	13112 cm ⁻¹ (1,63 eV)
Ionic radius M ²⁺	P ⁵⁺ : 0,17 Å	As ⁵⁺ : 0,335 Å	V ⁵⁺ : 0,355 Å	V ⁵⁺ : 0,355 Å
PP of X ⁵⁺	29.4	14.9	14.1	14.1
CIE coordinates	x= 0.2684 y= 0.3452	x= 0.3178 y= 0.3948	x= 0.4677 y= 0.4635	- -

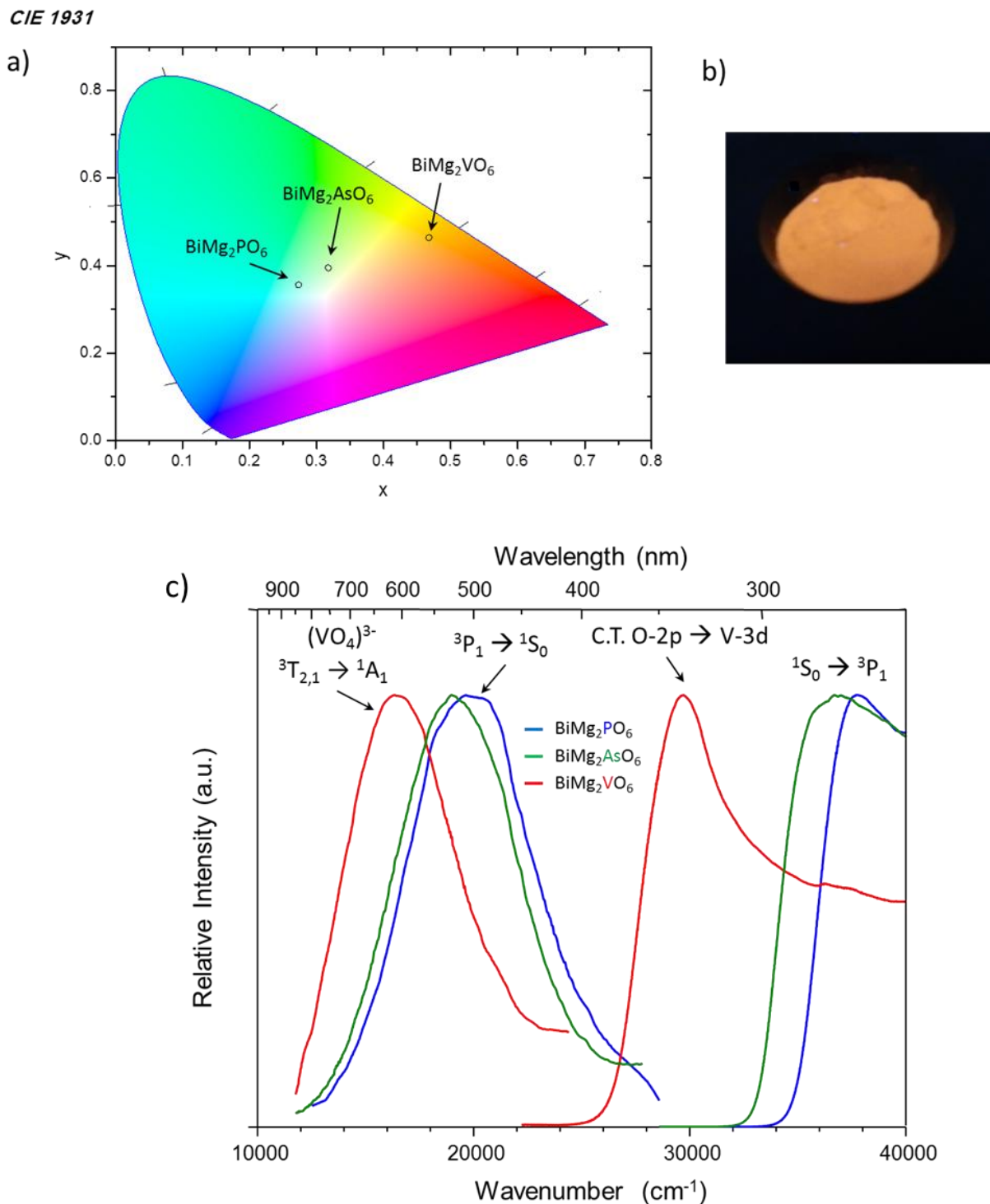


Figure III- 36 a) Representation of emission color of BiMg_2XO_6 ($X=\text{P, As, V}$) in the chromaticity CIE diagram b) Picture the orange emission of BiMg_2VO_6 at room temperature under UV lamp excitation ($\lambda_{\text{ex}}=365\text{nm}$) and c) Room temperature photoluminescence of BiMg_2XO_6 ($X=\text{P, As, V}$), The emission spectra are measured exciting at the maxima of corresponding excitation bands and vice versa (see Table III-12).

III.4.2.5. Bi-O covalency and excitation

The excitation and emission bands of BiMg₂XO₆ (X = P and As) are undoubtedly ascribed to the Bi³⁺: ¹S₀ → ³P₁ (excitation) and ³P₁ → ¹S₀ (emission) transitions whereas for BiMg₂VO₆ a doubt can subsist due to the presence of (VO₄)³⁻ groups which also exhibit a characteristic broad band emission in the visible range.⁶¹⁻⁶³

Charge transfer in vanadates

Vanadates are well known to exhibit efficient photoluminescence properties which can be understood from the molecular orbital theory.⁶⁴ The excitation band of vanadates is commonly ascribed to a charge transfer from oxygen 2p orbitals to the central vanadium 3d orbitals inside the (VO₄)³⁻ groups. This absorption is attributed to the transition from the ground state ¹A₁ to the excited states ¹T₂ and ¹T₁ of the vanadate complexes and the emission band of vanadates groups take its origin from the radiative ³T₂ → ¹A₁ and ³T₁ → ¹A₁ transitions (see figure III-37).⁶⁵

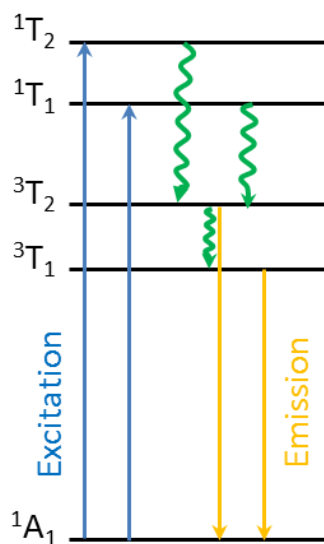


Figure III- 37 Sketch of absorption and emission processes of the VO₄ tetrahedron with T_d symmetry.

In the previous report,²⁸ the photoluminescence of BiMg₂VO₆ was attributed to (VO₄)³⁻ groups, on the base of a large Stokes shift for the emission and by means of DOS and PDOS for the excitation. It seems reasonable to ascribe the excitation to a charge transfer from O 2p orbitals to the central V 3d orbitals inside the (VO₄)³⁻ groups due to the difference of density of state between the V 3d and Bi 6s-6p on the bottom of the conduction band and moreover the excitation of (VO₄)³⁻ is often found around 350nm (28570cm⁻¹) in the literature.⁶⁵⁻⁶⁶

Additionally, in the previous part it was also shown (by comparison of the PDOS/absorption spectra with the excitation spectra) that the excitation process of Bi³⁺ do not involve a transition from the Bi 6s states situated at the top of the VB to the lower energy Bi 6p states situated in the CB but to higher energy Bi 6p states which comforts of the “Vanadate” excitation. However, for the emission, knowing that the Stokes shift in BiMg₂AsO₆ and BiMg₂PO₆ is also very large and the photoluminescence originates from Bi³⁺ transitions, additional experiments are needed to confirm this hypothesis. That is the reason why in this work the decay time of BiMg₂VO₆ was measured.

III.4.2.6. Decay Time of BiMg₂VO₆

At room temperature, the decay time measurement of BiMg₂VO₆ shows a biexponential behavior fitted to $\tau_1=18\mu\text{s}$ and $\tau_2=104\mu\text{s}$ values (excitation at 29760cm^{-1} and detecting the emission at 16420cm^{-1}). The two linear parts of the decay curve were fitted using the $I = I_0 + A \cdot \exp(-t/\tau)$ equation (see figure III-38). The figure III-38 shows that the higher component τ_2 is majority in the emission process, and the lifetime deduced is about three order of magnitude higher than for BiMg₂PO₆ ($\tau=350\text{ns}$). Looking into the literature, the radiative decay rate of (VO₄)³⁻ groups at 300K is about $200\mu\text{s}$,⁶⁷ although this value can vary depending on the energy transfer efficiency in the vanadates, basically the decay time decreases increasing the energy transfer efficiency.⁶⁸ Thus, it confirms the emission can be attributed to the (VO₄)³⁻ groups. The small part fitted to $\tau_1=18\mu\text{s}$ at the beginning of the decay curve should correspond to the charge transfer from Bi³⁺ to vanadate groups.

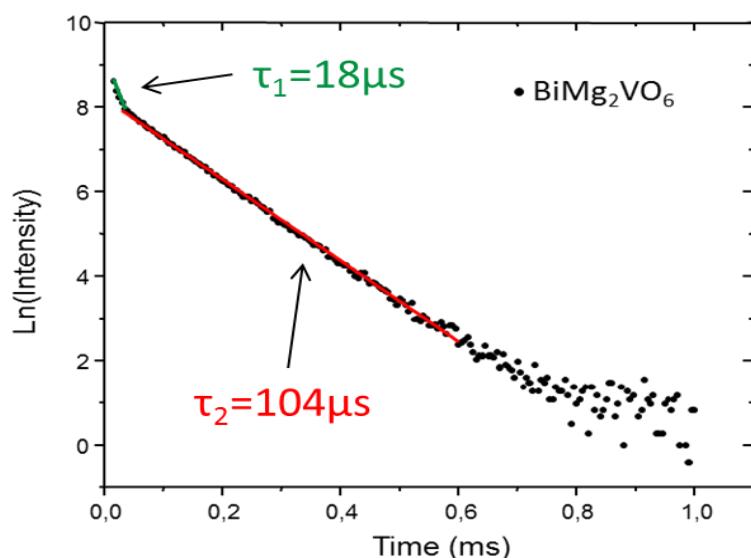


Figure III- 38. Decay time measurement of BiMg₂VO₆ at room temperature, $\lambda_{ex}=340\text{nm}$ and $\lambda_{em}=510\text{nm}$, the lifetimes are fitted to $18\mu\text{s}$ and $104\mu\text{s}$ ($R^2 \text{ adj.} = 0,999$ fitted linear, the intensity was plotted in $\ln(\text{intensity})$ in order to see the monoexponential behavior).

These results do not let the possibility to correlate the excitation and the emission between the three isostructural compounds BiMg₂XO₆ (X= P, As, V). However it is still possible to compare BiMg₂PO₆ with BiMg₂AsO₆.

Playing on the covalent character of long Bi-O bonds connected to XO₄ groups, one could think that the effect on excitation band would be negligible but it is not the case (figure III-36c). Focusing on the excitation process, a redshift occurs from X = P⁵⁺ to As⁵⁺, i.e. when the X⁵⁺ ionic radius increases. It matches perfectly with the relative covalency of the X-O bonds deduced from the PDOS diagrams and from the cationic polarizing powers of X⁵⁺ (z/r= 29.4 for P⁵⁺ and 14.9 for As⁵⁺), considering the electronic cloud expansion and expected nephelauxetic effect.⁴⁸⁻⁴⁹ In essence, the lower polarization of X⁵⁺-O bonds leads to more covalent Bi³⁺-O²⁻ bonds which has for effect to a lowering of the ¹S₀ → ³P₁ transition energy.

The figure III-39 shows the comparison between the absorption and excitation spectra for the BiMg₂XO₆ series. For BiMg₂AsO₆ the same particularities are observed than for the BiM₂PO₆ series (the lower energy excited state of Bi³⁺ (³P₀) is not involved in the excitation process and the displacement between the excited and the ground-state potential minima in the configurational coordinate model shifts the excitation to higher energy). The beginning of the absorption starts about 1.7eV before the excitation. However, this behavior is less pronounced concerning BiMg₂VO₆ (~1eV) and can easily be explained by the fact that within the (VO₄)³⁻ groups the two first excited states (³T₁ and ³T₂) are not involved in the excitation process.

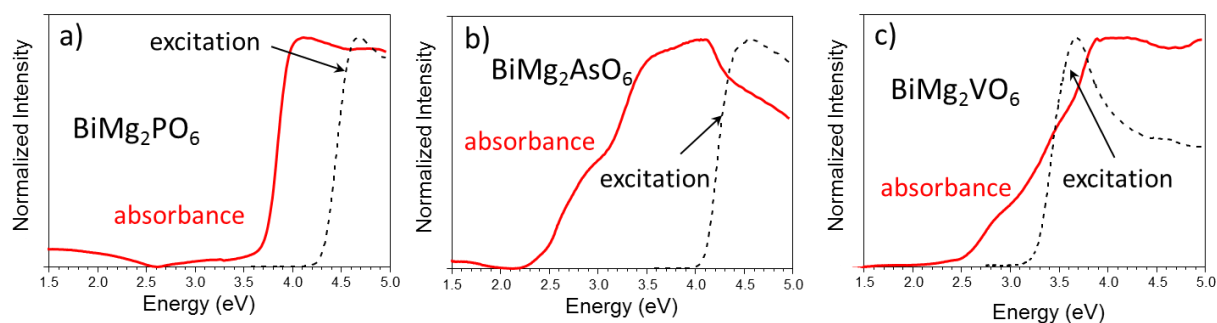


Figure III- 39 Comparison between the absorption and excitation spectra of a) BiMg₂PO₆ b) BiMg₂AsO₆ and c) BiMg₂VO₆.

III.4.2.7. Emission Process

The emission band of BiMg₂AsO₆ is slightly red shifted compared to the emission band of BiMg₂PO₆ (the maximum is shifted for 668cm⁻¹). This shift is comparable to the small shift observed for the excitation leading to comparable Stokes shift for the two compounds (18156 and 17770cm⁻¹ respectively for X=P and X=As). Here dealing with relatively different size of tetrahedra (PO₄ vs AsO₄), it is rather difficult to rationalize the effect or not of the LP stereo-activity. Concerning the Stokes shift of BiMg₂VO₆, the large Stokes shift (13340cm⁻¹) gives an idea of the energy difference between the ³T₁ and ¹T₁ states for the vanadate groups (see figure III-37.).

III.5. Solid Solution BiCd₂XX'O₆

The influence of the XO₄ chemical nature on the excitation energy is significant, but dominated by O 2p → V 3d charge transfer in BiMg₂VO₆. In this section, this phenomenology was investigated for mixed XO₄/X'O₄ phases with various X/X' ratio. For reasons of time, the BiMg₂(P,V,As)O₆ phase diagram initiated above has not been investigated, but the very similar BiCd₂(P,V,As)O₆ system with more attractive potentialities was preferred. Indeed, in the first part of this chapter (Influence of M²⁺, III.3), it was shown that increasing the polarizing power of M²⁺ (increasing the size of the cation) leads to shift the excitation band to lower energy whereas the emission energy remains similar. It follows that, in the context of energy saving, investigation of compounds with the largest M²⁺ cation possible (M=Cd or Ca) deserves attention. The hypothetical BiCa₂PO₆ being unstable, BiCd₂(XX')O₆ (X=P, As, V) system have been selected in the frame of this study.

III.5.1. Synthesis

Polycrystalline powder samples of BiCd₂XO₆ (X=P, As, V)^{24,35} phases and mixed compositions were prepared by conventional solid state reaction between Bi₂O₃, CdO, V₂O₅, As₂O₅ and (NH₄)₂HPO₄. The stoichiometric mixtures were heated during 48h at 800°C in alumina crucibles under air. The X=P compound is a white powder whereas X=V is yellowish and X=As is grey. Their purity was checked by XRD. BiCd₂PO₆ and BiCd₂VO₆ are pure whereas for BiCd₂AsO₆ two minor non-assigned reflections are found between 2θ 28° and 29° (figure III-43a). Concerning the mixed compositions, the color of powders depends on

the ratio X/X', for the BiCd₂V_xP_{1-x}O₆ solid solution, BiCd₂V_{0.75}P_{0.25}O₆ is orange whereas BiCd₂V_{0.5}P_{0.5}O₆ and BiCd₂V_{0.25}P_{0.75}O₆ are yellow powders. For BiCd₂As_xP_{1-x}O₆, all the intermediate compounds are dark grey and finally concerning BiCd₂V_xAs_{1-x}O₆ (0.25 ≤ x ≤ 0.75) the powder color varies from pale green to yellow (see figure III-40).

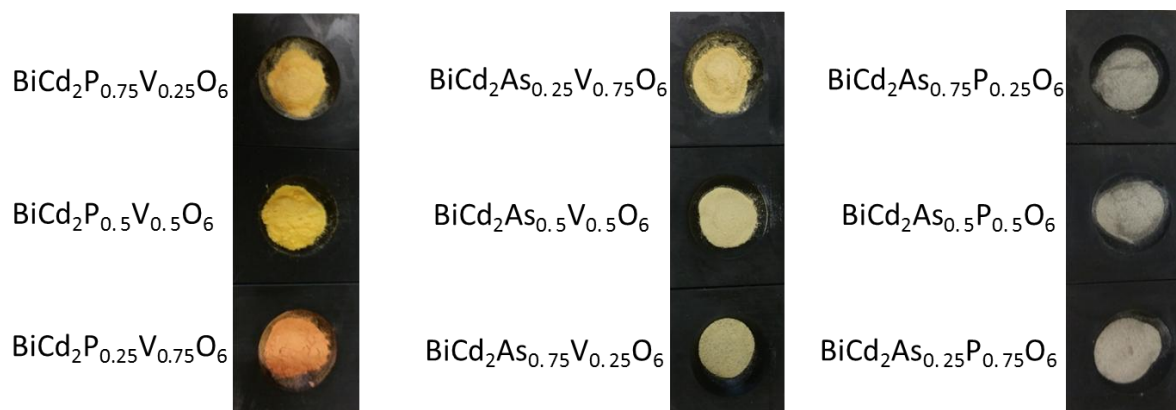


Figure III- 40 Picture of the solid solution powders.

The three BiCd₂XO₆ (X=P, V, As) compounds crystallize in the *Bb2₁m* (63) space group and are mainly isostructural through local differences concerning the effect of varying the XO₄ volume. The figure III-41 represents the structural projection in the (ab). In BiCd₂AsO₆ and BiCd₂PO₆ all the XO₄ tetrahedra have a triangular basis in the (ab) plane such that they all point “up” along the axis c with respect to the NCS *Bb2₁m* symmetry. In BiCd₂VO₆, the VO₄ tetrahedra are tilted such that a triangular basis lies in the (ac) plane. Due to the similar NCS *Bb2₁m* symmetry, a cooperative organization of all VO₄ along the c axis is also true, but here, the XO₄ cannot be considered as “up” but rather as “median”. Here after, the notion of “As or P” versus “V” types will be used to distinguished these two polymorphs. The cell parameters of the three compounds were refined using Fullprof in the pattern matching mode and confirm those of the reported crystal data.^{24,35} All the intermediate samples for each solid solution compositions were also assumed to crystallize in the *Bb2₁m* space group which allow a full pattern indexation. Their refined cell parameters are shown figure III-42.

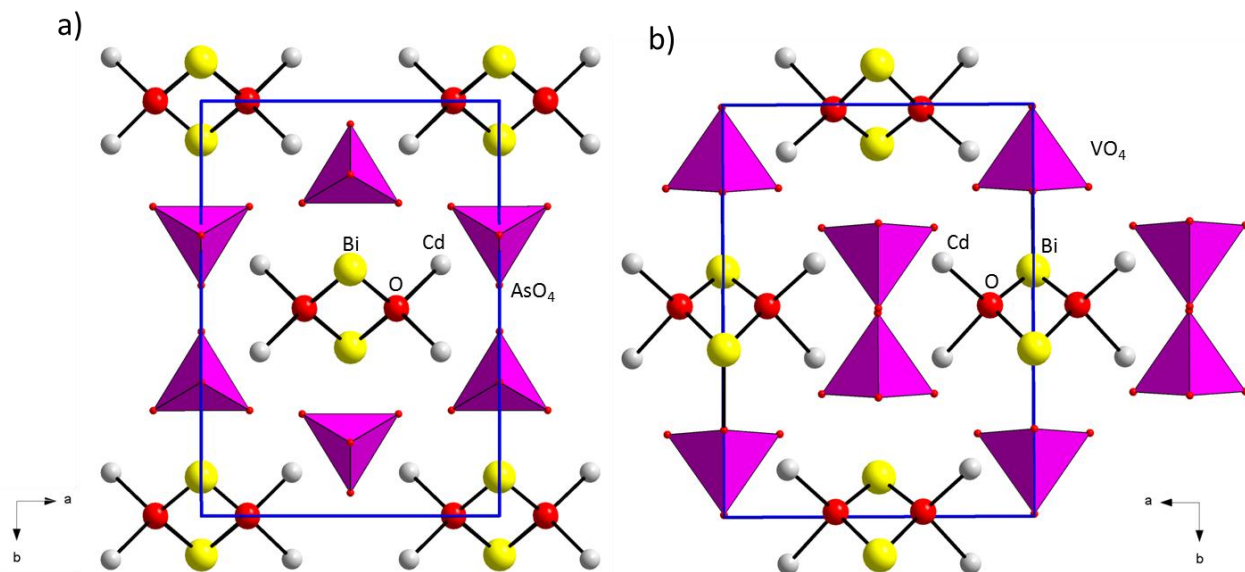


Figure III- 41 Structure representation of BiCd₂AsO₆ (isostructural to BiCd₂PO₆) and BiCd₂VO₆ (right) in the plan (ab). All the arsenate tetrahedra all up in BiCd₂AsO₆ whereas their orientation changes in BiCd₂VO₆.

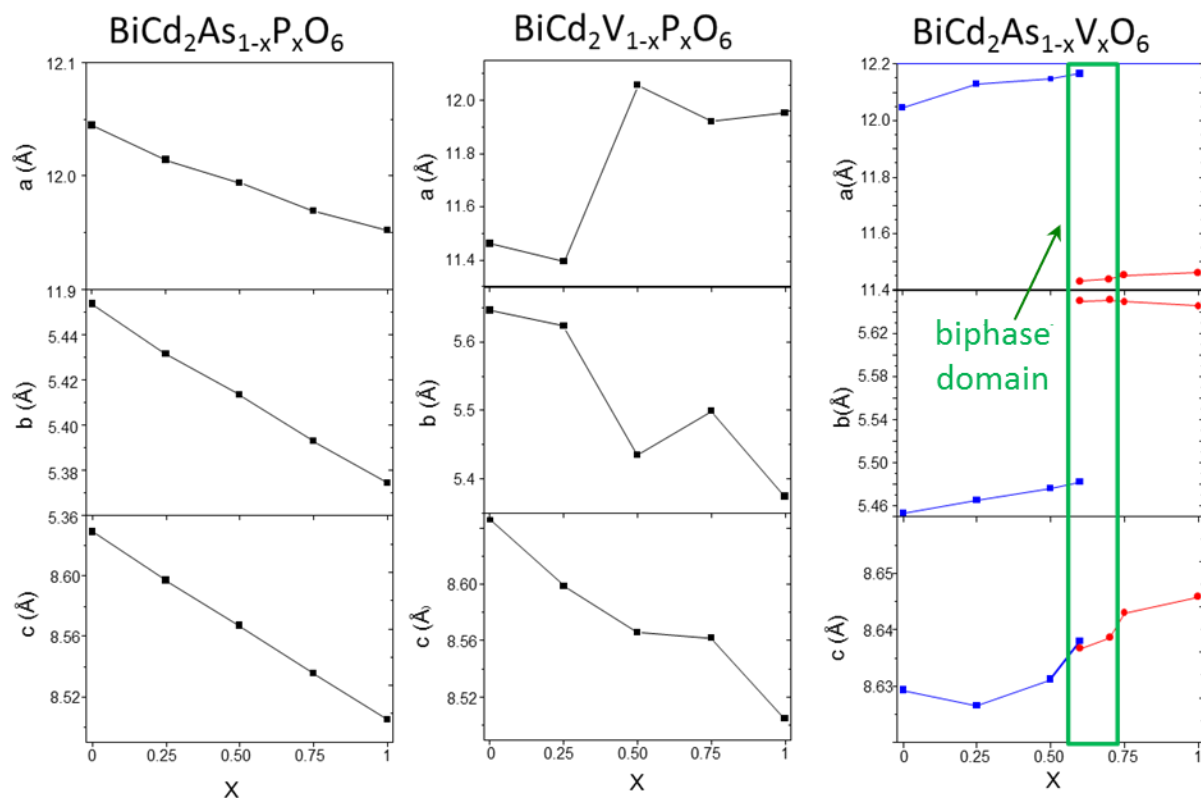
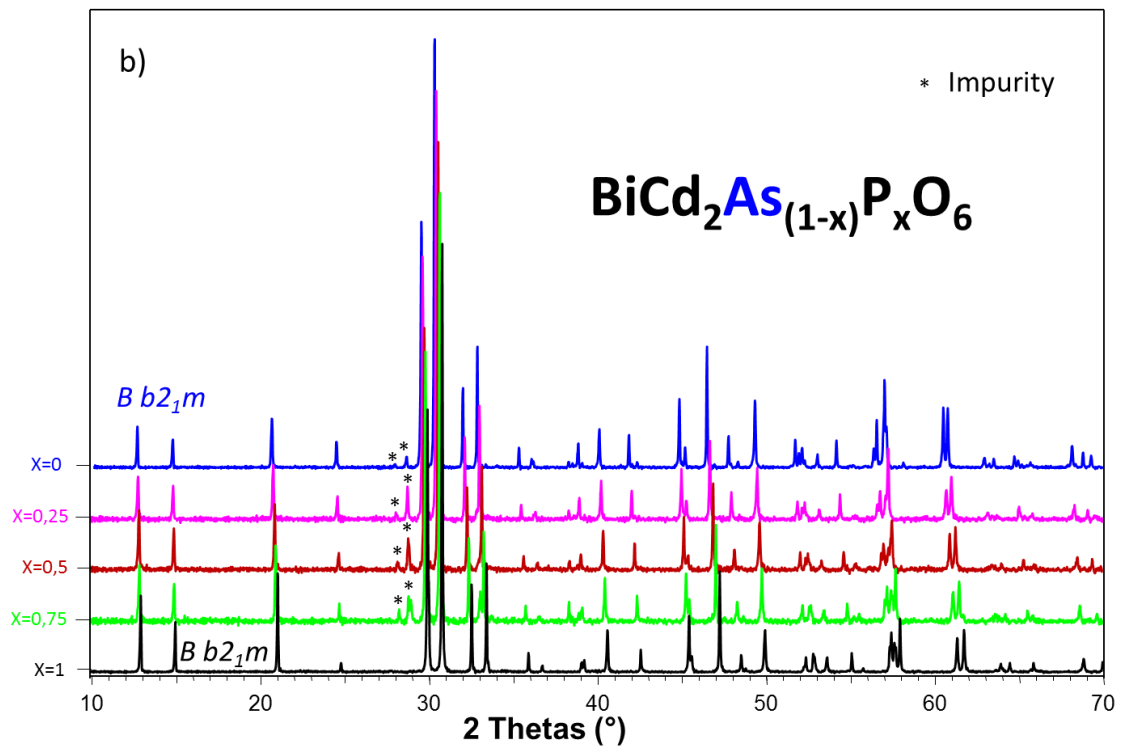
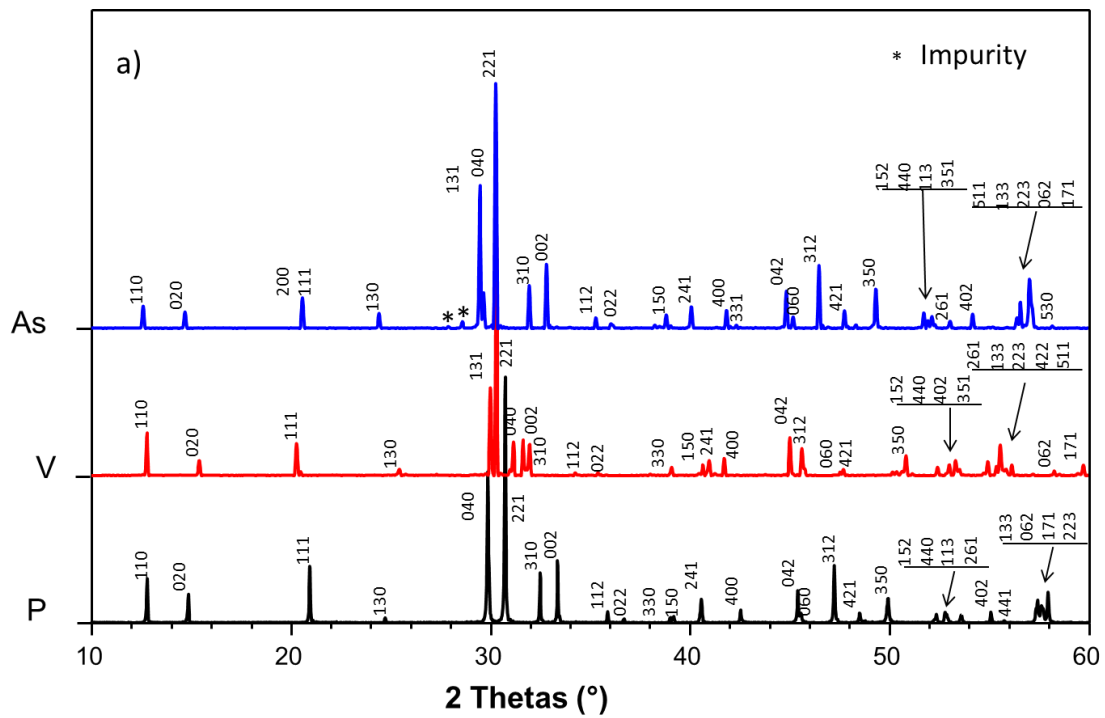


Figure III- 42 Cell parameters of the three solid solutions refined with Fullprof using pattern matching method.



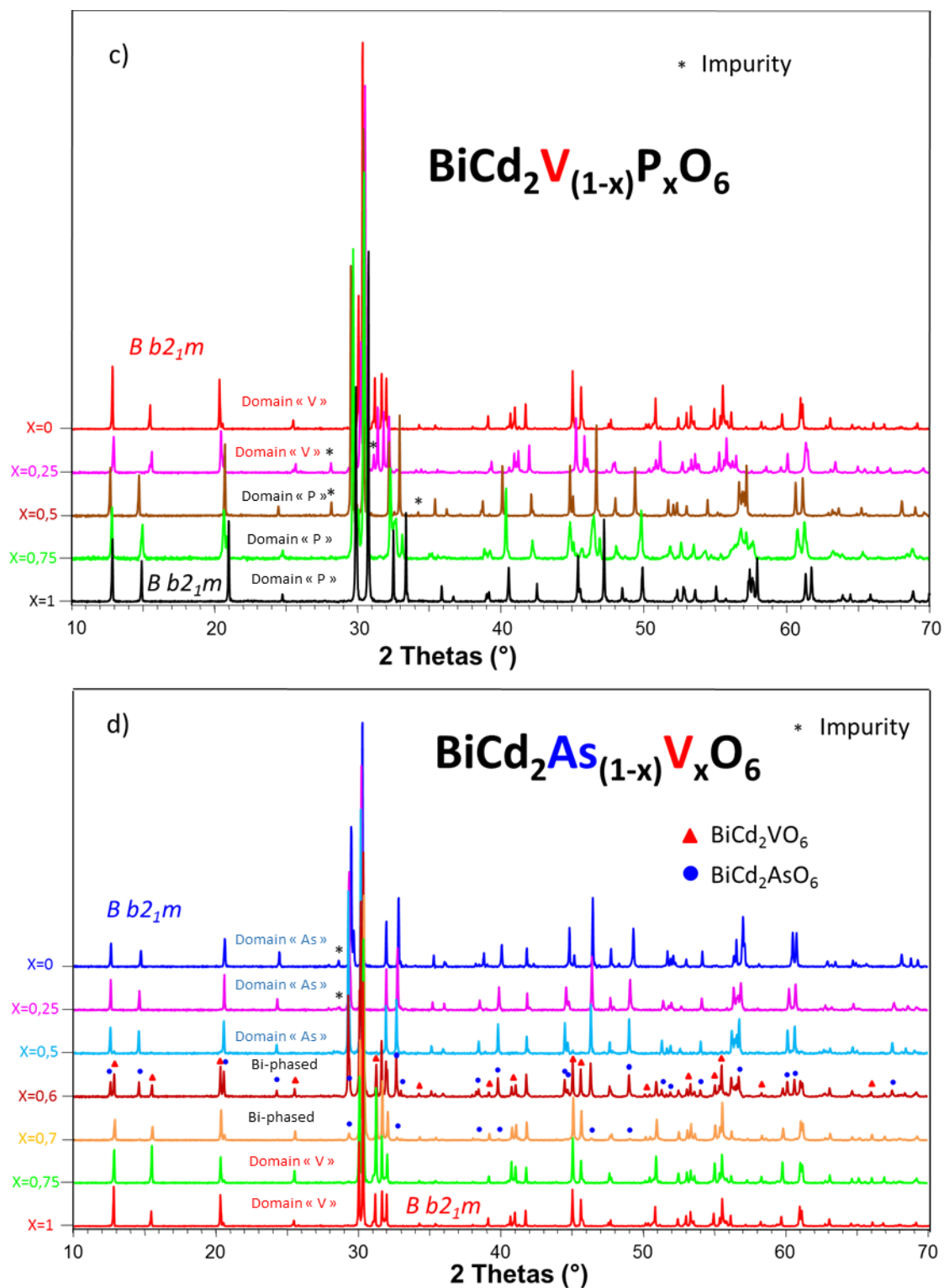


Figure III- 43 a) XRD pattern of BiCd_2XO_6 ($X=\text{P}, \text{As}, \text{V}$) with reflection indexing. b) XRD pattern of the solid solution $\text{BiCd}_2\text{As}_{1-x}\text{P}_x\text{O}_6$ c) XRD pattern of the solid solution $\text{BiCd}_2\text{V}_{1-x}\text{P}_x\text{O}_6$ and d) XRD pattern of the solid solution $\text{BiCd}_2\text{As}_{1-x}\text{V}_x\text{O}_6$.

III.5.2. Structural characteristics of the mixed compositions

BiCd₂As_{1-x}P_xO₆

Concerning the solid solution BiCd₂As_{1-x}P_xO₆, the figure III-43b shows that excluding the minor impurities mentioned above, only a single domain is observed for all the compositions with evidence for a solid solution. All the cell parameters decrease progressively according to x (the ratio P/As) as expected regarding the difference of ionic radius between both cations (As⁵⁺: 0.335 Å and P⁵⁺: 0.17 Å) and the isostructural form of the two end members (“As” or “P” type).

BiCd₂V_{1-x}P_xO₆

Concerning the mixed BiCd₂V_{1-x}P_xO₆ system (figure III-43c), the lattice parameters given figure III-42 show that two distinct domains of solid solution exist depending on the x value. Between x=0 and x=0.25, the phases adopt the “V” type and from x=0.5 to x=1 the “P” type. No biphased composition have been detected, but only three intermediate compounds have been prepared and it is much probable that between x=0.25 and x=0.5, the samples would show multiphased mixtures approaching the “V” to “P” frontier. The cell parameters *b* and *c* “globally” decrease according to x (the ratio P/V, rV⁵⁺: 0.355Å and rP⁵⁺:0.17Å) which is normal due the difference of ionic radius between V⁵⁺ and P⁵⁺. On the other hand, the parameter *a* is very characteristic of the different domains. Between x=0 and x=0.25, it slightly changed (11.4617 to 11.3639Å) while it reaches values close to 12Å in the second domain with a minor evolution afterwards.

BiCd₂As_{1-x}V_xO₆

The evolution of XRD pattern of this last mixed composition BiCd₂V_{1-x}As_xO₆ is shown figure III-43d. This system also presents two structural domains. For x=0, 0.25 and 0.5, the “As” type is stable whereas for x=0.75 and 1 the XRD pattern reveals the “V” type. For x=0.6 and 0.7 a biphased domain can clearly be seen from the figure III-43d. The cell parameters are well characteristic of the domain (figure III-42). *a* and *b* parameters slightly increase from x=0 to x=0.6 and then a jump to values of the antagonist phase occurs (for x=0.6, a=11.4322/12.1650 and b=5.4825/5.6520 respectively for the domain “As” and “V”). Then, further increasing x value, *a* and *b* cell parameters remain nearly constant. Concerning the cell parameter *c*, it is weakly affected by the changing of domain type.

III.5.3. Room temperature PL properties of the mixed compositions

BiCd₂As_{1-x}P_xO₆ self-absorption

As expected, all the intermediate samples from the first solid solution BiCd₂As_{1-x}P_xO₆, as well as BiCd₂AsO₆ do not produce any radiative emissions after photo-excitation due to their color in favor of absorption. The second minor phase (see section 5.2) could play a role in the quenching process but their dark colors are probably the main cause. Such compounds absorb a broad part of the visible light, such that visible emission can be directly reabsorbed by the sample itself. For BiCd₂AsO₆, low temperature photoluminescence tests have been performed, but even at 10K no radiative emission could be detected. As already detailed, only BiCd₂PO₆ which is colorless shows photoluminescence emission at room temperature. Its optical properties are described in the previous section III.4.1.5.

BiCd₂V_{1-x}P_xO₆ photoluminescence

The room temperature photoluminescence spectra of the BiCd₂V_{1-x}P_xO₆ mixed compositions are represented in figure III-44. Focusing on the excitation, one can see that there is a significant difference of the energy position between the excitation of BiCd₂PO₆ (in black) and all the other members of the mixed compositions. There is a red shift of the maximum of the excitation band of about 2000cm⁻¹ for BiCd₂VO₆ compared to BiCd₂PO₆. The behavior is also observed for the emission bands as well as for their FWHM (7820cm⁻¹ for BiCd₂PO₆ and ~5400cm⁻¹ for all the other compounds of the solid solution). All the optical data are gathered table III-13. This phenomenon is reminiscent of what was observed between BiMg₂VO₆ and BiMg₂PO₆ (section III.4.2.4).

Table III-13. Optical data for the mixed composition BiCd₂V_{1-x}P_xO₆.

Compound	BiCd ₂ VO ₆	x=0.25	x=0.50	x=0.75	BiCd ₂ PO ₆
Excitation maximum	30630 cm ⁻¹ (3.80eV)	29900 cm ⁻¹ (3.71eV)	29740 cm ⁻¹ (3.69eV)	30400 cm ⁻¹ (3.77eV)	32680 cm ⁻¹ (4.05eV)
Emission maximum	15500 cm ⁻¹ (1.92eV)	15600 cm ⁻¹ (1.93eV)	15870 cm ⁻¹ (1.97 eV)	15910 cm ⁻¹ (1.97eV)	20048 cm ⁻¹ (2.48eV)
Emission FWHM	5350 cm ⁻¹ (0.66eV)	5410 cm ⁻¹ (0.67eV)	5430 cm ⁻¹ (0.67eV)	5450 cm ⁻¹ (0.68eV)	7820 cm ⁻¹ (0.97eV)
Stokes Shift	15130 cm ⁻¹ (1.88eV)	14300 cm ⁻¹ (1.77eV)	13870 cm ⁻¹ (1.72eV)	14490 cm ⁻¹ (1.80 eV)	12632 cm ⁻¹ (1.57 eV)

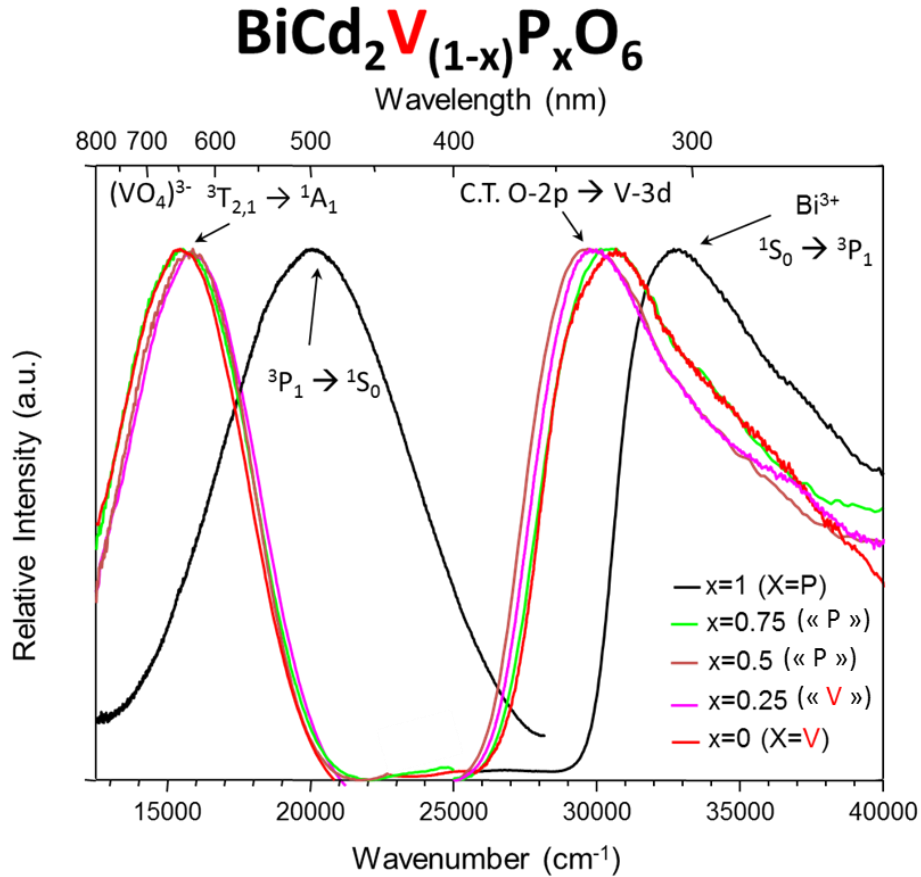


Figure III- 44 Room temperature excitation and emission spectra for the solid solution $BiCd_2V_{1-x}P_xO_6$

In $BiCd_2PO_6$, the activator Bi^{3+} is responsible for the photoluminescence of the material as discussed section 3.4.1.5. ($Bi^{3+}: \ ^1S_0 \rightarrow \ ^3P_1$ (excitation) and $\ ^3P_1 \rightarrow \ ^1S_0$ transitions (emission) whereas for $BiCd_2VO_6$ and all the mixed compositions, the excitation band originates mainly from a charge transfer from O 2p to V 3d states inside the $(VO_4)^{3-}$ groups ($\ ^1A_1 \rightarrow \ ^1T_{1,2}$ transitions). Of course, a contribution of $Bi^{3+}: \ ^1S_0 \rightarrow \ ^3P_1$ transitions cannot be excluded but the emission energies correspond well to $\ ^3T_{2,1} \rightarrow \ ^1A_1$ transitions (of the vanadate groups) as for $BiMg_2VO_6$ presented in the previous part.

Therefore, it can be conclude that as soon as the $BiCd_2PO_6$ is doped with vanadates, the radiative emissions of $(VO_4)^{3-}$ groups predominate in both “V” and “P” types with similar spectral characteristics. This can be explained by the fact that the excitation of the vanadates appears at lower energy than the $Bi^{3+}: \ ^1S_0 \rightarrow \ ^3P_1$ transition. Thus even exciting the Bi^{3+} activators, an energy transfer $Bi^{3+} \rightarrow VO_4^{3-}$ would occur the Bi^{3+} emission would be quenched. The low differences in energy position of excitation and emission bands for the

x=0, 0.25, 0.5 and 0.75 (“vanadate” luminescence) compounds are most probably related to the slightly changes of the vanadium environment (exact V-O bond lengths, O_x-V-O_y angles) and arrangement in the two antagonist structures. For a deeper investigation, it would be very interesting to study the photoluminescence of samples doped with lower concentration of vanadates (x=0.9, 0.95 or even 0.99) to detect fine effects.

BiCd₂As_{1-x}V_xO₆ photoluminescence

The room temperature photoluminescence spectra of the BiCd₂As_{1-x}V_xO₆ mixed composition are represented in figure III-45. BiCd₂AsO₆ as well as the two biphased samples (x=0.6 and 0.7) do not show room temperature photoluminescence. For the biphased samples, this is due to the “presence” of strongly absorbing dark “As” type component.

The excitation bands, situated in the UV range for x=0.25, 0.5 and 1 and UV-blue range for x=0.75, are broad and have a multiplet character, their maximum is listed table III-14. The Stokes shift is important in the entire system (>12000cm⁻¹) and the emission bands are singlet bands peaking in the orange range for x=0.25, 0.5 and 1, and in the red for x=0.75. All the optical data are gathered table III-14.

Table III-14. Optical data for the mixed composition BiCd₂As_{1-x}V_xO₆.

Compound	x=0.25	x=0.50	x=0.75	BiCd ₂ VO ₆
Excitation maximum	29120 cm ⁻¹ (3.61eV)	29780 cm ⁻¹ (3.69eV)	25770 cm ⁻¹ (3.20eV)	30630 cm ⁻¹ (3.80eV)
Emission maximum	16130 cm ⁻¹ (2.00eV)	16130 cm ⁻¹ (2.00 eV)	13100 cm ⁻¹ (1.62eV)	15500 cm ⁻¹ (1.92eV)
Emission FWHM	5250 cm ⁻¹ (0.65eV)	5340 cm ⁻¹ (0.66eV)	-	5350 cm ⁻¹ (0.66eV)
Stokes Shift	12990 cm ⁻¹ (1.61 eV)	13650 cm ⁻¹ (1.69eV)	12670 cm ⁻¹ (1.57eV)	15130 cm ⁻¹ (1.88eV)

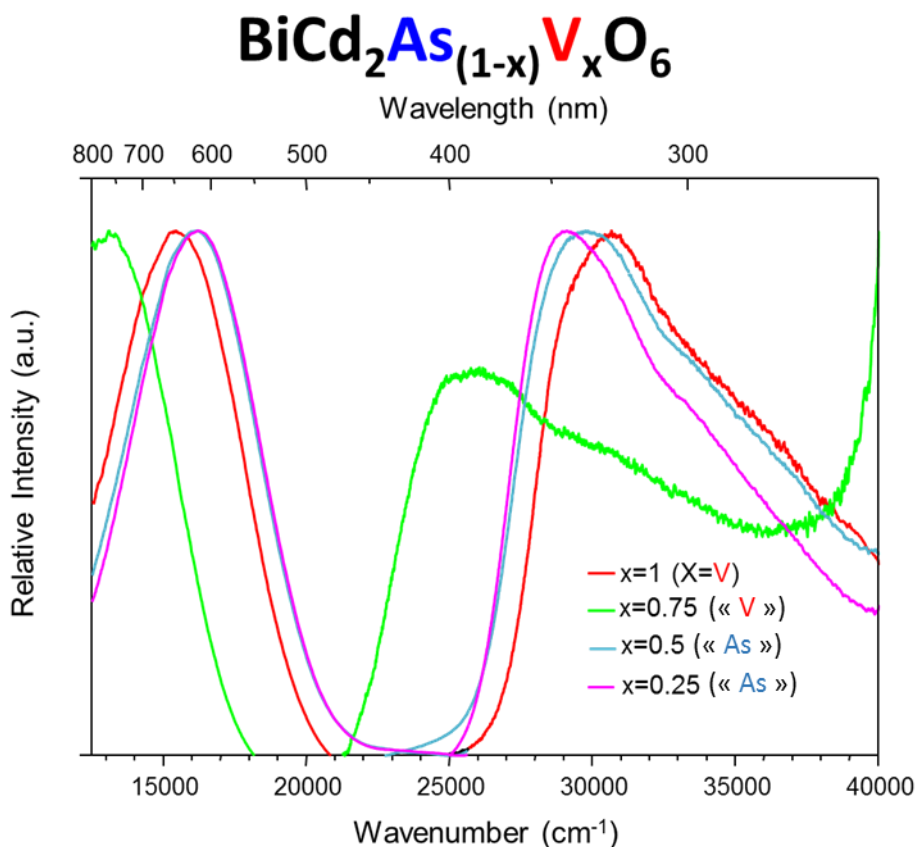


Figure III- 45 Room temperature excitation and emission spectra for the mixed composition BiCd₂As_{1-x}V_xO₆.

Once again, the excitation bands for $x=0.25$ (violet curve), 0.5 (blue curve) and 1 (red curve) (figure III-45) correspond to a charge transfer from O 2p to V 3d states. In the high energy part of the excitation band the Bi³⁺: $^1S_0 \rightarrow ^3P_1$ transition can also be involved.

The emission band for these three samples is ascribed to the “vanadate” emissions ($^3T_{1,2} \rightarrow ^1A_1$ transitions). Concerning $x=0.75$ (green curve), the attribution of transitions for the excitation and emission bands is more ambiguous. The intensities on the figure III-45 were normalized for a better energy position comparison, however it is very important to note that the intensity of excitation and emission bands of $x=0.75$ is much lower than for the others compounds (e.g. its emission is more than 10 times lower compared to $x=0.5$ one with equivalent experimental conditions).

The Stokes shift and the shape of excitation and emission bands match well the vanadate-type luminescence, however the pronounced red shift of both excitation and emission bands compared to the other members of the system as well as the drop of intensity remain unclear. Moreover, decay time measurement trials have been performed but due to the very low

intensity these measurements remain unsuccessful. The strong rise of intensity for the excitation band at $\sim 39000\text{cm}^{-1}$ can probably be attributed to the $^1\text{S}_0 \rightarrow ^1\text{P}_1$ transition because of its very high energy position, however due to the limit of the spectrofluorometer only the beginning of this peak can be observed. Therefore, the highest probably would be to attribute the photoluminescence of $x=0.75$ sample to vanadate groups with a probable contribution of Bi^{3+} cations via a charge transfer from Bi^{3+} to vanadates. From the XRD pattern $x=0.75$ belongs to BiCd_2VO_6 -type domain, but the insertion of AsO_4 could create defects responsible for the lower intensity.

III.5.4. Summary

In this part, as a first step, the relation between the structural and optical properties of BiMg_2XO_6 series was investigated.

It was shown that for BiMg_2VO_6 , the photoluminescence mainly originates from electronic transition within the vanadate complexes whereas the photoluminescence of BiMg_2PO_6 and $\text{BiMg}_2\text{AsO}_6$ originates from the Bi^{3+} activator. Moreover, playing on the chemical nature of X^{5+} situated on the second coordination sphere of the Bi, it is possible to tune the excitation (lowering the polarizing power of X^{5+} shifts the excitation to lower energy).

For more insights, the room temperature photoluminescence properties of the mixed $\text{BiCd}_2\text{X}_{1-x}\text{X}'_x\text{O}_6$ (X or X'=P, As and V) compounds were investigated. It was shown in the solid solution $\text{BiCd}_2\text{As}_{1-x}\text{P}_x\text{O}_6$ ($x=0, 0.25, 0.5, 0.75, 1$) that the darkness of the powder brought by AsO_4 groups quench the photoluminescence.

In other mixed systems with vanadate groups, the emission of Bi^{3+} activator vanishes for the emission of vanadate groups. The excited states of $(\text{VO}_4)^{3-}$ groups are situated at lower energy than the excited state $^3\text{P}_1$ of the Bi^{3+} , then even exciting the Bi^{3+} ions a charge transfer from Bi^{3+} to vanadate groups would occur.

Finally in the $\text{BiCd}_2\text{As}_{1-x}\text{V}_x\text{O}_6$ system, although the charge transfer in the vanadate predominate, the $x=0.75$ compound shows a more unclear PL behavior probably attributed as well to vanadate groups. The figure III-46 summarizes the attribution of luminescence properties of the mixed compositions.

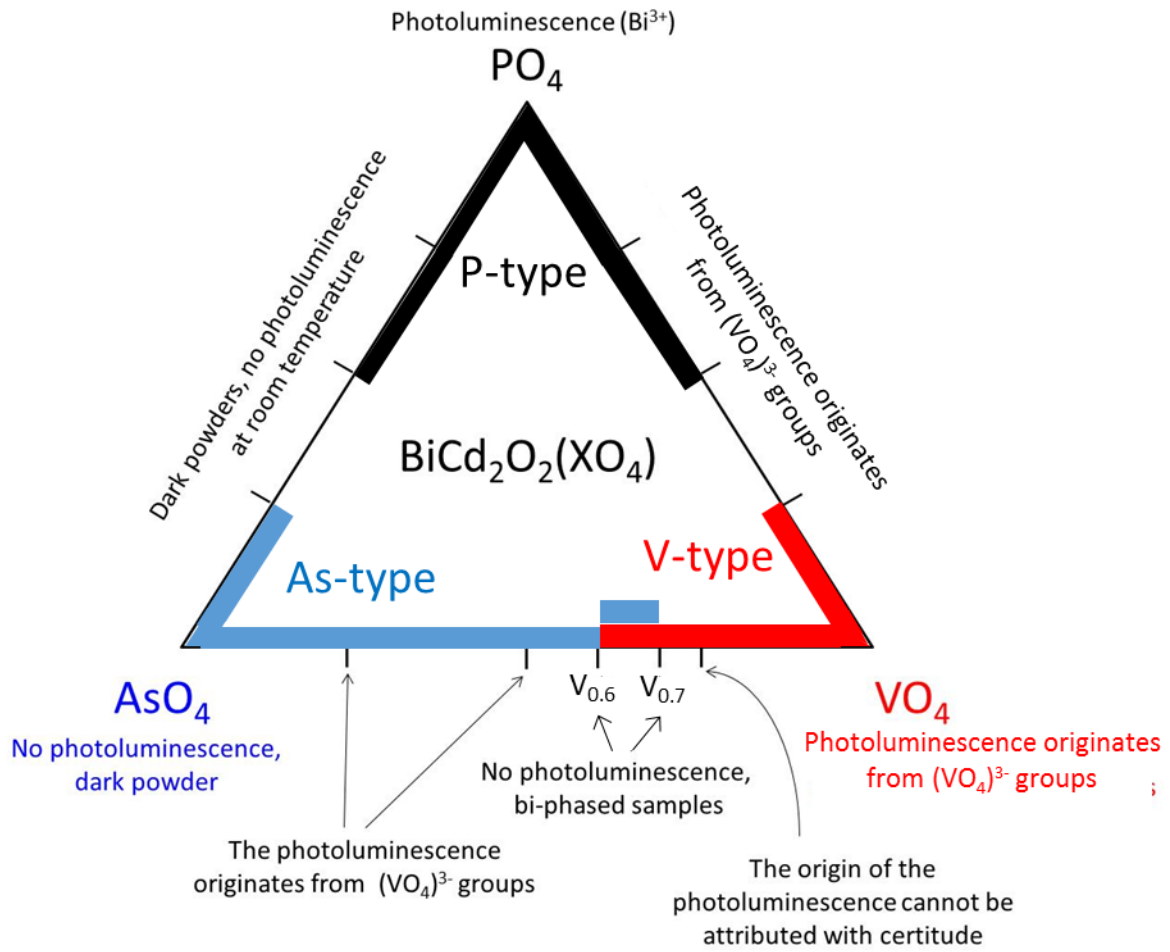


Figure III- 46 Sketch representing the photoluminescence of the studied solid solutions.

III.6. BiMn₂PO₆ photoluminescence

In this section, the optical properties of another BiM₂XO₆ compound are investigated: BiMn₂PO₆.³⁹ Its crystal structure is similar to those of the other members of this family (section III.2), e.g. this compound is isostructural with BiZn₂PO₆.³⁴ BiMn₂PO₆ has the particularity to possess two different activators in stoichiometric amount, Bi³⁺ and Mn²⁺. It was already characterized from the magnetic viewpoint, which shows high spin Mn²⁺ (d⁵, S=5/2) with antiferromagnetic ordering below T_N=30K.⁶⁹ From the optical aspect, divalent manganese plays an important role in the solid state lightening and can be involved as emitter in many applications. When doped in a host lattice, it exhibits a characteristic emission between 500 and 700nm with a small band-width of several tens of nanometers due to the ⁴T₁ (G) → ⁶A₁(S) transition.⁷⁰⁻⁷² However, the exact energy position of the emission depends on the crystal field in the structural lattice.

III.6.1. Synthesis of BiMn₂PO₆

The synthesis of this compound was reported in ref [39] and involves neutral atmosphere for the stabilization of Mn²⁺ ions which prefer Mn³⁺ and Mn⁴⁺ valences. Thus, BiMn₂PO₆ was synthesized under Ar flow using a stoichiometric mixture of Bi₂O₃, MnO and (NH₄)H₂PO₄. After grinding, the mixture was heated in an alumina crucible at 800°C for 36h with intermediate grinding states. The purity of the compound was checked and confirmed by XRD (see figure III-47).

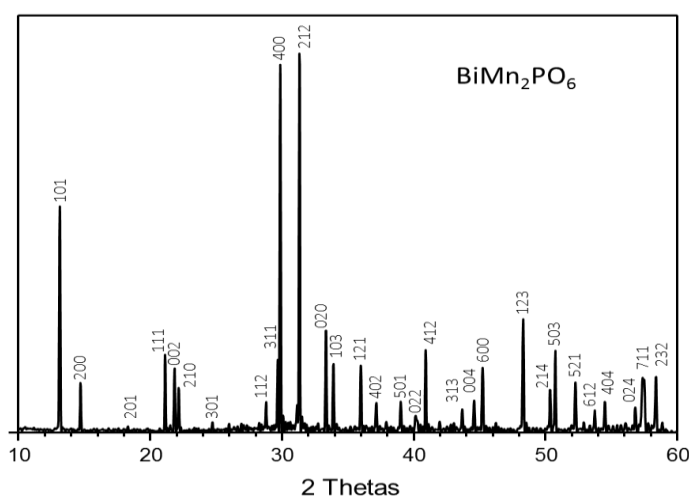


Figure III- 47 X-ray powder pattern of BiMn₂PO₆ including reflections indexation.

III.6.2. d → d luminescence in BiMn₂PO₆

Due to the high amount of emitters in this sample, which causes in general concentration quenching, only low temperature photoluminescence is observed (figure III- 48a). This phosphor displays at 10K a deep red sharp emission with a maximum at 14500cm⁻¹ (692nm) while the excitation spectrum is composed of several peaks from 250nm (40000cm⁻¹) to 600nm (16666cm⁻¹). The CIE chromaticity diagram is represented figure III- 48b.

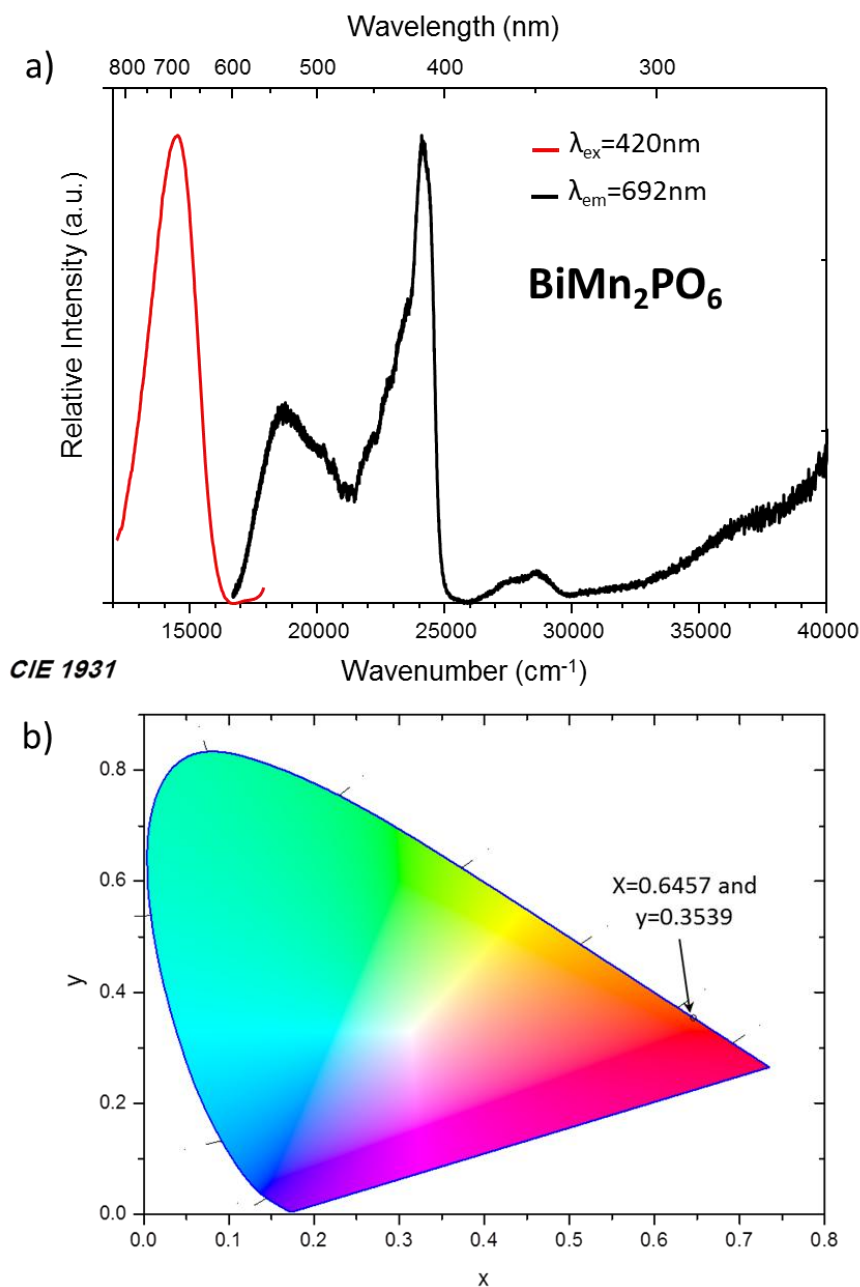


Figure III- 48 a) Emission (left) and excitation (right) spectra of BiMn₂PO₆ at 10K and b) Emission color representation in the CIE diagram.

Due to the position and the shape of the emission band (and comparatively to all other BiM₂XO₆ compounds with either Bi³⁺ or VO₄³⁻ luminescence), this latest can be undoubtedly attributed to the ⁴T₁(G) → ⁶A₁(S) transition of Mn²⁺. It was already shown that increasing the concentration of doping Mn²⁺ shifts the emission band to lower energy (red shift).⁷³ In BiMn₂PO₆, dealing with a high stoichiometric concentration of divalent manganese, one could partially imagine the low energy red emission. Experimentally, the excitation spectrum is composed of 6 peaks, the five higher energy ones are typical from the Mn²⁺ excitation: the band with a maximum at 18700cm⁻¹ is attributed to the ⁶A₁(S) → ⁴T₁(G) transition, the transition ⁶A₁(S) → ⁴T₂(G) peaks at 23400 cm⁻¹, ⁶A₁(S) → ⁴A₁(G),⁴E(G) at 24100cm⁻¹, ⁶A₁(S) → ⁴T₂(D) at 23400cm⁻¹ and finally ⁶A₁(S) → ⁴E₁(D) at 28700cm⁻¹. On the other hand, the last and higher energy excitation band starting at about 34000cm⁻¹ can be attributed to the Bi³⁺: ¹S₀ → ³P₁ transition by analogy with the excitation spectrum of the isostructural BiZn₂PO₆, see the section 3.4.1.3. The figure III-49 represents the electronic transitions of divalent manganese in this compound.

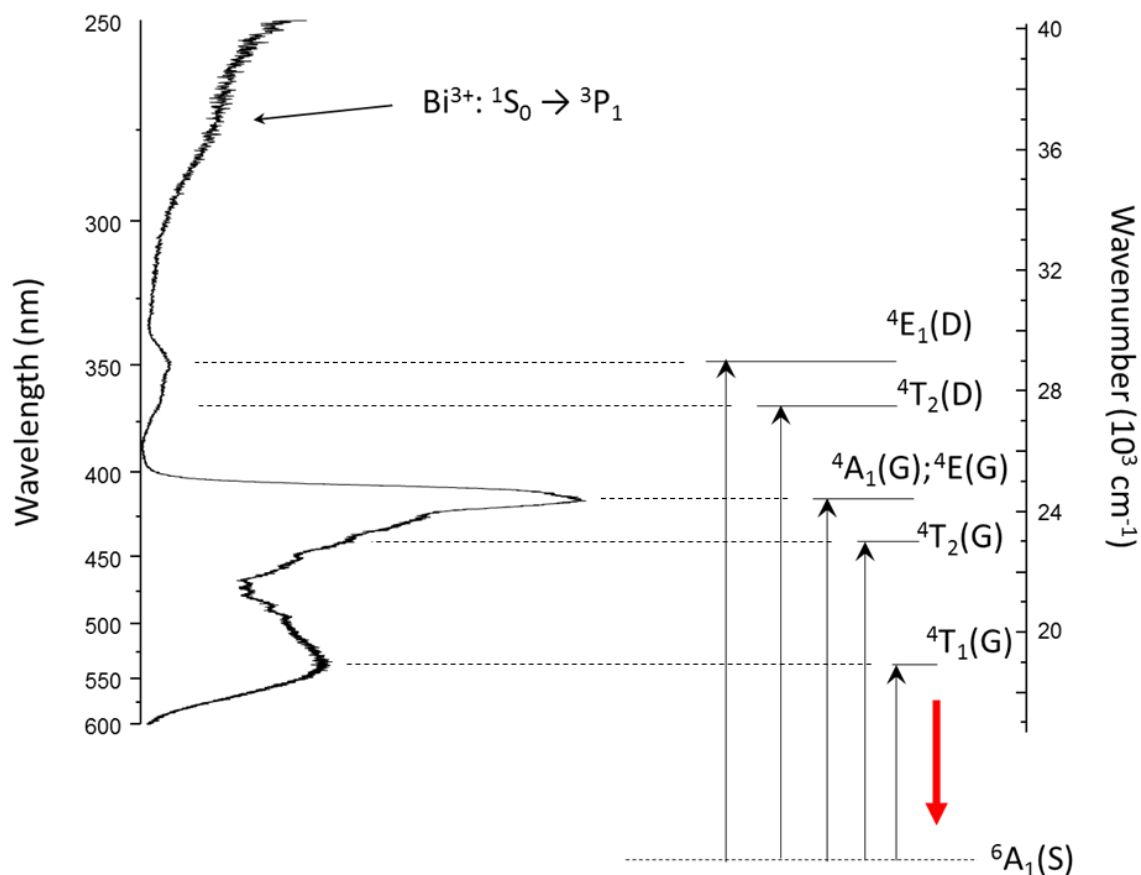


Figure III- 49 Sketch representing the attribution of electronic transitions of Mn²⁺ cation to the excitation spectrum of BiMn₂PO₆.

Luminescence and absorption properties of 3d transition elements were intensively investigated by Tanabe and Sugano in the 50's.⁷⁴⁻⁷⁶ They developed a method to approximate the crystal field by means of Racah methods⁷⁷ in order to explain the absorption bands energy positions leading to the so-called Tanabe-Sugano diagrams, for every dⁿ ions in a octahedral environment. This diagram allows the approximation of the B Racah parameter using the absorption/excitation spectrum.

The figure III-50 represents the Tanabe-Sugano diagram for a d⁵ element. The x axis of this diagram is expressed in terms of the ligand field splitting parameter, Δ (i.e. Dq), divided by the Racah parameter B, which corresponds to the repulsion between the d electrons. The y axis represents the energy (E) of the states also scaled by B. The left side of the diagram corresponds to the high spin configuration whereas the right side to the low spin one. In BiMn₂PO₆, the Mn²⁺ ions have an octahedral coordination and a high spin configuration.⁶⁹ Even if the absorption/excitation peaks are not well defined in this compound, probably due to the high concentration of Mn²⁺ ion, in this case it is possible to approximate the B Racah parameter by contrast to free ion Mn²⁺ or to other Mn²⁺ compounds in order to compare the covalency of Mn-Anion bonds. The more suitable peak corresponds to the ⁴A₁ ⁴E(G) absorption state and its maximum peaks at 24100cm⁻¹, this same state (horizontal line) on the left side of the diagram is situated at E/B=32.5, then the B Racah parameter for the Mn²⁺ in BiMn₂PO₆ is obtained by dividing 24100/32.5 and is equal to 741.5cm⁻¹. This method can be apply here only due to the high spin character of Mn²⁺ ions and the horizontal line for the ⁴A₁ ⁴E(G) absorption in the Tanabe-Sugano diagram. Otherwise, it is possible to determine B using the energy difference of two experimental absorption peaks and comparing it with the energy difference of the two same absorption peaks on the Tanabe-Sugano diagram. The B parameter is equal to 960cm⁻¹ for the free cation, 845cm⁻¹ when Mn²⁺ is coordinated to 6 F⁻ and 785 cm⁻¹ when coordinated to 6 Cl⁻.⁷⁸ Then it is possible to conclude that the Mn-O bonds in BiMn₂PO₆ have a strong covalent character from the excitation spectrum.

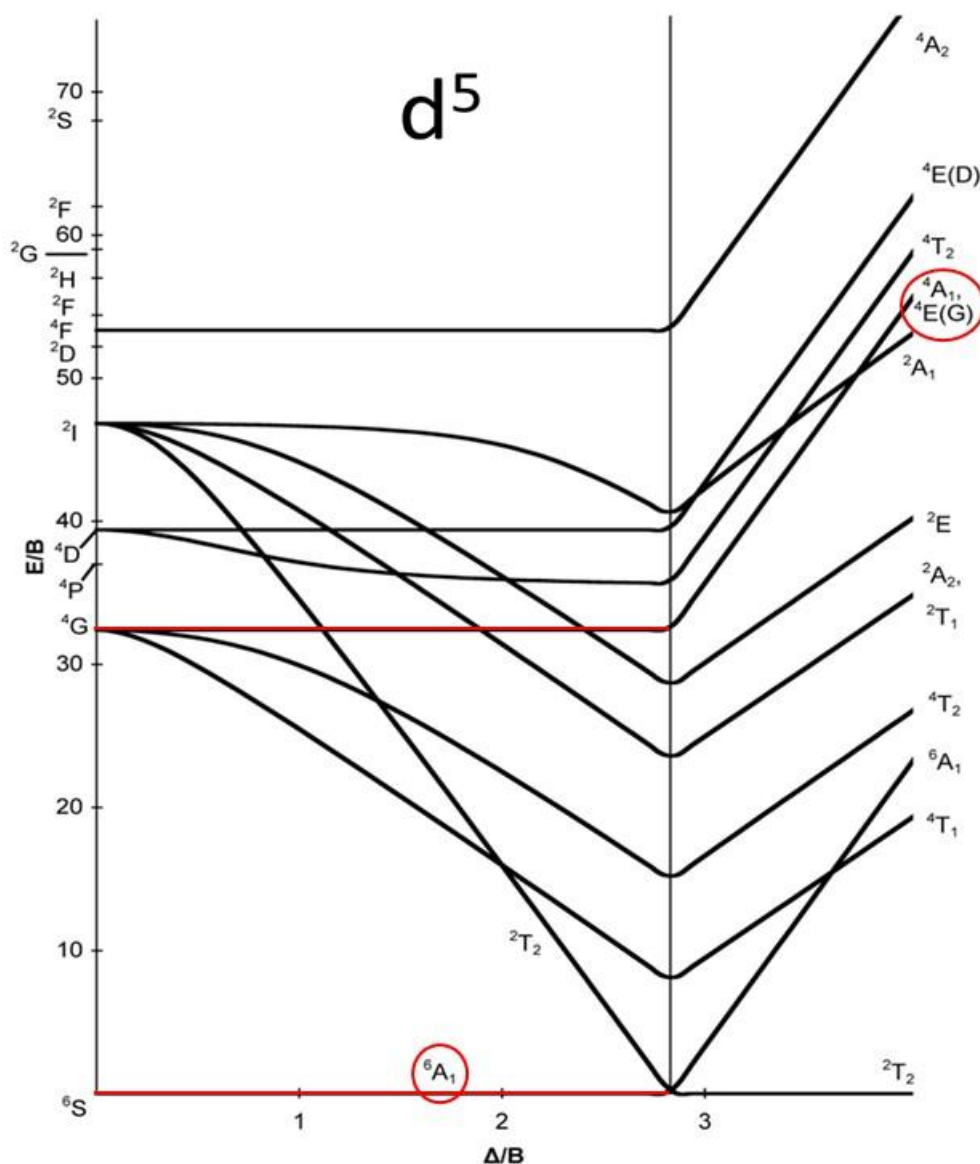


Figure III- 50 Tanabe-Sugano diagram for a d^5 element in octahedral coordination.

In this phosphor, the Bi^{3+} does not show any luminescence even at 10K but serves as sensitizer for Mn^{2+} . After exciting the Bi^{3+} at $\sim 37000\text{cm}^{-1}$ (${}^1S_0 \rightarrow {}^3P_1$ transition), the ns^2 ion transfers its energy (non-radiative) to manganese which will emit in the red range. The GGA DOS calculations have already been made by Nath et al.⁶⁹ and comfort our results: the bottom of the conduction band is mainly occupied by the Mn localized $3d$ states whereas the majority of the Bi density of states is displayed at higher energy (see figure III-51). This case favors energy transfer from Bi^{3+} to Mn^{2+} . This sensitizer role of Bi^{3+} can be very useful for application such as WLED. One of the major problems for WLED is to find out a good red phosphor which can be excited in the UV range (and not absorb in the visible range), this supposes a very large Stokes shift unrealistic for trivalent lanthanides. But this characteristic

perfectly fits to the bismuth, most of the time Bi^{3+} is excited between 250 and 380nm depending on its environment and presents a strong absorption. This makes it a good candidate as sensitizer for optical purposes and that is the reason why nowadays many studies are done on improving the luminescence properties of phosphors by co-doping with Bi^{3+} .⁷⁹⁻⁸¹

R. NATH *et al.*

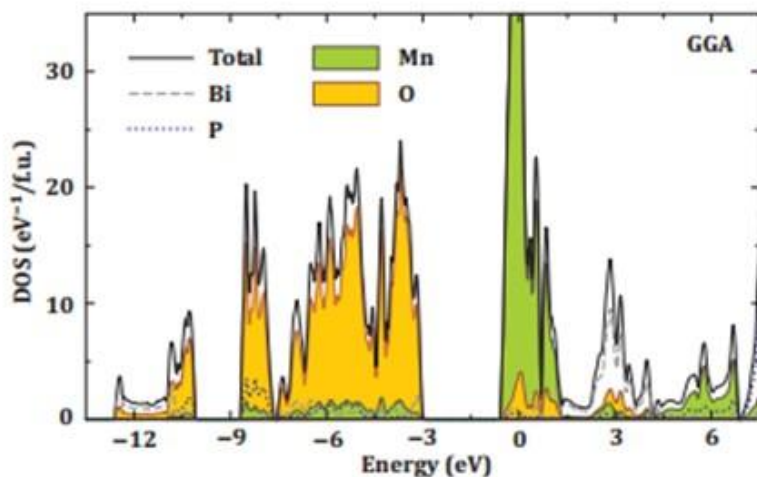


Figure III- 51 TDOS and PDOS representation for BiMn_2PO_6 taken from ref [39].

III.7. Investigation of $\text{BiPb}_2\text{AsO}_6$ photoluminescence properties

In the previous section III.6, it was demonstrated that the emission of Bi^{3+} can be quenched due to the presence of another activator. Here, the luminescence properties of $\text{BiPb}_2\text{AsO}_6$ will be investigated. This time Bi^{3+} is present with another ns^2 type activator: Pb^{2+} . The luminescent properties of Pb^{2+} and Bi^{3+} are very similar, the ground state of divalent lead is composed by a 1S_0 state whereas the excited states correspond to the triplet 3P_0 , 3P_1 , 3P_2 and the singlet 1P_1 states in order of increasing energy. Its optical properties also strongly depend on its chemical environment: a red shift of the excitation band according to the nephelauxetic effect is in general observed and also an emission dependency on the stereo-activity of the lone pair of electrons.⁸²

III.7.1. Synthesis of $\text{BiPb}_2\text{AsO}_6$

According to the preparation detailed in the section 3.3.2, the purity of the prepared sample was verified by XRD measurements. Each reflection of the pattern can be indexed to $\text{BiPb}_2\text{AsO}_6$ calculated pattern from the single crystal data (section III.3.2.) which validates the purity of the sample (figure III-52).

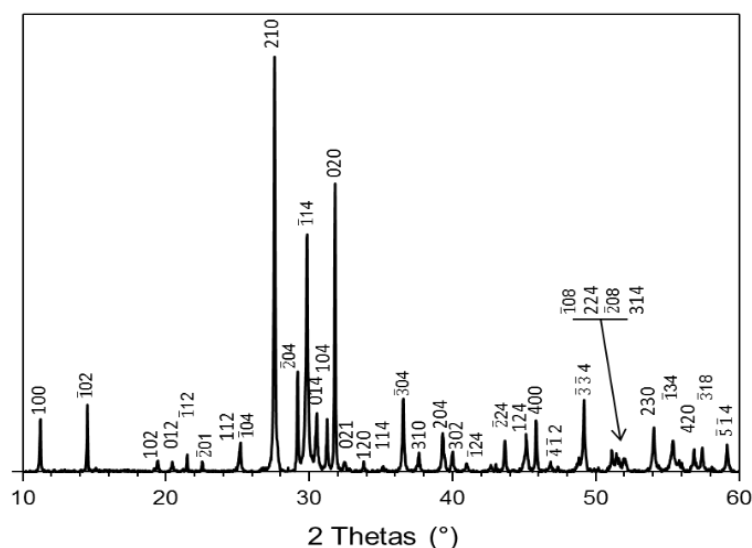


Figure III- 52. X-ray powder pattern of BiPb₂AsO₆ including reflections indexation from the single crystal data (section 3.3.2).

III.7.2. Electronic properties of BiPb₂AsO₆

Density functional theory (DFT) calculations were performed using the Vienna *ab initio* simulation package (VASP).⁴³ The calculations were carried out within the generalized gradient approximation (GGA) for the electron exchange and correlation corrections using the Perdew-Wang (PW91) functional and the frozen core projected wave vector method.⁴⁴⁻⁴⁵ The full geometry optimizations were carried out using a plane wave energy cutoff of 550 eV and 10 *k* points in the irreducible Brillouin zone. All structural optimizations converged with residual Hellman-Feynman forces on the atoms smaller than 0.03 eV/Å and led to reasonable structures regarding the distances and the local geometries. The experimental structure (section III.3.2) fits well the optimized one, the error does not exceed 2.9% on the cell parameter *c* which is acceptable (see table III-15).

Table III-15. Comparison between theoretical (after full relaxation) and experimental crystal data for BiPb₂AsO₆.

BiPb ₂ AsO ₆	Experimental	Theoretical	Deviation from exp.
<i>a</i> (Å)	8.2662 (4)	8.4663	2.4 %
<i>b</i> (Å)	5.6274 (3)	5.6935	1.2 %
<i>c</i> (Å)	14.3152 (7)	14.7376	2.9 %
<i>β</i> (°)	106.66 (2)	109	0.2 %

The relaxed structure was used in order to perform accurate calculations of the electronic structure. For the calculation of the density of states (DOS) and projected density of states

(PDOS), we used a plane wave energy cutoff of 400eV, an energy convergence criterion of 10^{-6} eV and 20 *k* points in the irreducible Brillouin zone. For the band diagram calculations, the *k* points were choosing according to the symmetry of the sample in order to investigate the entire Brillouin zone. Finally, the band diagram calculated for BiPb₂AsO₆ was plotted between -3eV and 5eV and presents an indirect bandgap of 2.59eV between the Y point (VB) and the minimum of the conduction band situated in between Y and C points (see figure III-53b). However, the lowest vertical transition is slightly higher (2.62eV) and takes place in between the Y and C points. The calculated value of the band gap fits well with the one found experimentally using Kubelka-Munk fit and Tauc plot (2.75eV) taking into account the probably underestimation of the calculated one using GGA method (figure III-53c).

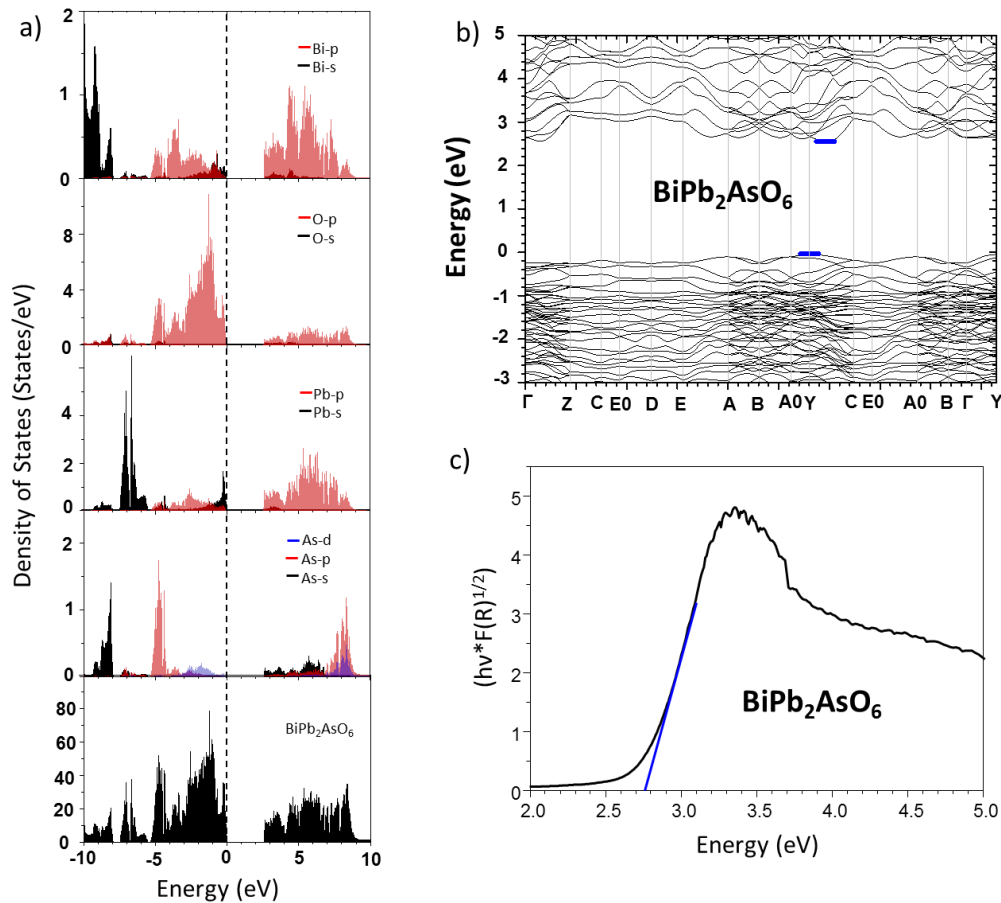


Figure III- 53 . a) TDOS and PDOS representation for BiPb₂AsO₆. b) Band diagram representation of BiPb₂AsO₆, the blue lines localize the minimum of the CB and maximum of the VB and show an indirect character. c) Kubelka-Munk fit and extrapolation of the band gap for BiPb₂AsO₆.

From the density of states representing between -10 and 10eV (figure III-53a.), it is clearly shown that the top of the valence band is mainly composed of Bi 6s-6p, Pb 6s-6p and O 2p

states. A small contribution of As 3d states is found whereas the As 4s and 4p states are localized at lower energies (between -8 and -9.3eV for the 4s states and the higher density of states of As 4p states is situated between -3 and -5.2eV). This hybridization between the Bi 6s-6p and O 2p as well as between Pb 6s-6p and O 2p shows a strong degree of covalency of the Bi-O and Pb-O bonds. On the other hand, the bottom of the CB is mainly composed by O 2p, Bi 6p, Pb 6p and As 4s-4p states. A small contribution of Bi 6s, Pb 6s and As 4p is also found whereas the As d states are localized at higher energies (between 6 and 9eV). Finally, one could consider a very similar role of both Bi³⁺ and Pb²⁺ emitters regarding the energy position of their mixed 6s and 6p states.

III.7.3. Luminescent properties

As expected, BiPb₂AsO₆ does not exhibit any luminescence at room temperature due to too high concentration of ns² ions but shows a low intensity greenish yellow emission at 10K. The CIE coordinates displayed for this phosphor are x=0.3622 and y=0.4693. Figure III-54a shows the photoluminescence spectra of BiPb₂AsO₆ as well as of BiMg₂PO₆ presented before in order to compare the energy position of the bands.

Focusing on the excitation spectrum of BiPb₂AsO₆, the figure III-54a (green curve) clearly shows that it is composed of several bands. At least two bands can be indexed, the higher energy one with a maximum at about 36680cm⁻¹ (272nm) which has the highest intensity and the lower energy which has also the lowest intensity peaking at 23750cm⁻¹ (421nm). Another band appears at higher energy than 40000cm⁻¹ (250nm) but due to the limits of the spectrofluorometer, only a part can be measured. By comparison with the excitation spectrum of BiMg₂PO₆ at 10K, the band with a maximum at 36680cm⁻¹ could be attributed to the Bi³⁺: ¹S₀ → ³P₁ or Pb²⁺: ¹S₀ → ³P₁ since Pb²⁺ has similar optical properties than Bi³⁺. On the other hand, the lower energy excitation band perfectly coincides with the beginning of absorption spectrum (see figure III-54b). This means that it is a band to band absorption, however from the DOS calculations it was shown that the first 6p states of Bi and Pb are situated at the bottom of the conduction band. Therefore, it will be relatively reasonable to attribute this band to the ¹S₀ → ³P₀ forbidden transition of Bi³⁺ or Pb²⁺ cations. On the other hand the emission band can most probably be attributed to the ³P_{0,1} → ¹S₀ transitions of the Bi³⁺ emitters because it coincides with the emission band of BiMg₂PO₆ (see figure III-54a).

Unfortunately, the decay time measurements were not successful due to the very low intensity of the emission and could not bring additional information to validate or not these results.

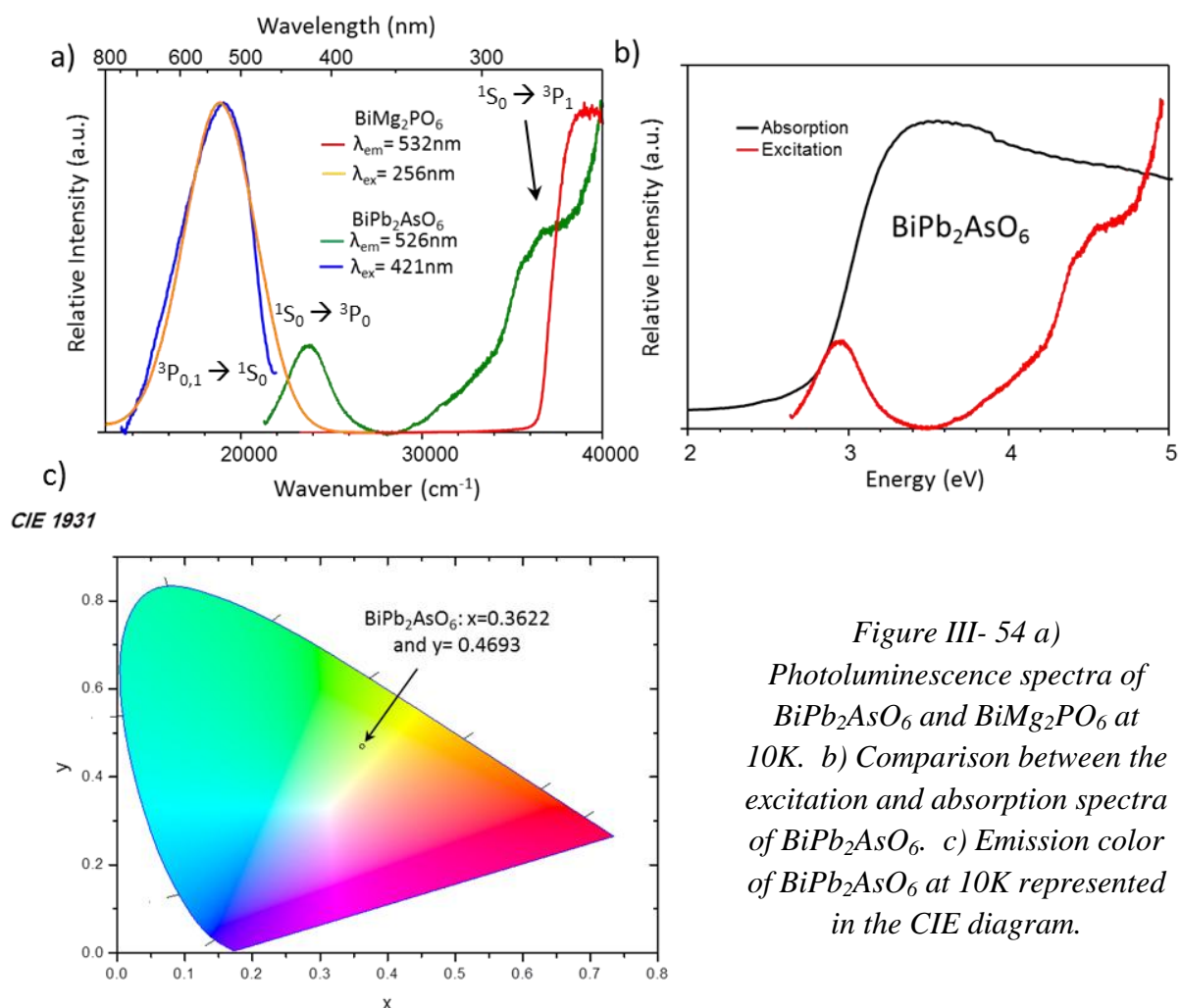


Figure III- 54 a) Photoluminescence spectra of BiPb₂AsO₆ and BiMg₂PO₆ at 10K. b) Comparison between the excitation and absorption spectra of BiPb₂AsO₆. c) Emission color of BiPb₂AsO₆ at 10K represented in the CIE diagram.

III.7.4. Summary

To conclude, the common presence of Bi³⁺ and Pb²⁺ activators in stoichiometric amount in BiPb₂AsO₆ has for effect to nearly completely quench the photoluminescence even at 10K. This compound emits a greenish yellow emission at 10K and the luminescence is totally quenched already at 50K. Due to the similar energy positions of 6s and 6p states of Bi and Pb extracted from the DOS calculations and the lack of information about the decay time, in this case, it is impossible distinguish the optical properties of Bi³⁺ from Pb²⁺. However due to the similarity of them,⁸³ both emitters can be involved in the emission of BiPb₂AsO₆.

References

- [1] Abraham, F.; Debreuillegresse, M.F.; Mairesse, G.; Nowogrocki, G., *Solid State Ionics*, **1988**, 28, 529.
- [2] Abraham, F.; Boivin, J.C.; Mairesse, G.; Nowogrocki, G., *Solid State Ionics*, **1990**, 40/41, 934.
- [3] Huang, J.; Sleight A.W., *J. Solid State Chem.*, **1992**, 97, 228.
- [4] Huang, J.; Sleight A.W., *J. Solid State Chem.*, **1992**, 100, 170.
- [5] Radosavljevic, I.; Evans, J.S.O.; Sleight, A.W., *J. Solid State Chem.*, **1998**, 137, 1.
- [6] Huang, J.; Gu, Q.; Sleight, A.W., *J. Solid State Chem.*, **1994**, 110, 226.
- [7] Radosavljevic, I.; Evans, J.S.O.; Sleight, A.W., *J. Solid State Chem.*, **1998**, 137, 143.
- [8] Radosavljevic, I.; Evans, J.S.O.; Sleight, A.W., *J. Alloys Comp.*, **1999**, 284, 99.
- [9] Radosavljevic, I.; Evans, J.S.O.; Sleight, A.W., *J. Solid State Chem.*, **1998**, 141, 149.
- [10] Radosavljevic, I.; Sleight, A.W., *J. Solid State Chem.*, **2000**, 149, 143.
- [11] Caro, P.E., *Journal of the Less Common Metals*, **1968**, 16, 367.
- [12] Krivovichev, S.V.; Filatov, S.K., *Z. Kristallogr.*, **1998**, 213, 316.
- [13] Krivovichev, S.V.; Filatov, S.K., *Am. Mineral.*, **1999**, 84, 1099.
- [14] Krivovichev, S.V.; Filatov, S.K., *Crystal chemistry of minerals and inorganic compounds with complexes of anion-centered tetrahedra*, St Petersburg University Press, St Petersburg, **2001**.
- [15] Krivovichev, S.V.; Filatov, S.K.; Semenova T.F., *Russ. Chem. Rev.*, **1998a**, 67, 137.
- [16] Huang, J.; Gu, Q.; Sleight, A.W., *J. of Solid State Chem.*, **1993**, 105, 599.
- [17] Shuk, P.; Wiemhöfer, H.D.; Guth, U.; Göpel, W.; Greenblatt, M., *Solid State Ionics*, **1996**, 89, 179.
- [18] Battle, P.D.; Catlow, C.R.A.; Drennan, J.; Murray, A. D., *Journal of Physics C: Solid State Physics*, **1983**, 16, L561.
- [19] Yashima, M.; Ishimura, D., *Chemical Physics Letters*, **2003**, 378, 395.
- [20] Abraham, F.; Nowogrocki, G., *Bull. Soc. Fr. Minéral. Cristallogr.* **1975**, (98).
- [21] Sleight, A. W., *Materials Research Bulletin*, **1974**, 9, 1437.
- [22] Abraham, F.; Tréhoux, J.; Thomas, D., *Materials Research Bulletin*, **1977**, 12, 43.
- [23] Endara D. « Design » et approche prédictive de nouveaux oxyphosphates de bismuth, Université Lille1 - Sciences et Technologies (**2012**).
- [24] Evans, I.R.; Howard, J.A.K., Sleight A.W., *Solid State Science*, **2005**, 7, 299.
- [25] Mentre, O.; Ketatni, E.M.; Colmont, M.; Huve, M.; Abraham, F.; Petricek, V., *J.Am.Chem.Soc.* **2006**, 128, 10857.
- [26] Mentre, O.; Janod, E.; Rabu, P.; Hennion, M.; Leclercq-Hugeux, F.; Kang, J.; Lee, C.; Whangbo, M.H.; Petit, S., *Phys. Rev. B*, **2009**, 80, 180413.
- [27] Tsirlin, A.A.; Rousochatzakis, I.; Kasinathan, D.; Janson, O.; Nath, R.; Weickert, F.; Geibel, C.; Lauchli, A.M.; Rosner, H., *Phys. Rev. B*, **2010**, 82, 144426.
- [28] Barros, A.; Deloncle, R.; Deschamp, J.; Boutinaud, P.; Chadeyron, G.; Mahiou, R.; Cavalli, E.; Brik, M.G., *Opt. Mater.*, **2014**, 36, 1724.
- [29] Krivovichev, S.V.; Mentre, O.; Colmont, M.; Siidra, O.I.; Filatov, S.K., *Chemical Reviews*, **2013**, 113, 6459.
- [30] Walsh, A.; Payne, D.J.; Egdell, R.G.; Watson, G.W., *Chem. Soc. Rev.*, **2011**, 40, 4455.
- [31] Walsh, A.; Watson, G. W.; Payne, D. J.; Edgell, R. G.; Guo, J. H.; Glans, P. A.; Learmonth, T.; Smith, K. E., *Phys. Rev. B*, **2006**, 73, 235104.
- [32] Bosacka, M.; Kurzawa, M.; Rychlowska-Himmel, I.; Szkoda, I., *Thermochimica Acta*, **2005**, 428, 51.
- [33] Nunes, S.E.; Wang, C.H.; So, K.; Evans, J.S.O.; Evans, I.R., *J. Solid State Chem.*, **2015**, 222, 12.
- [34] Ketatni, E.M.; Memari, B.; Abraham, F.; Mentre, O., *J. Solid State Chem.*, **2000**, 153, 48.
- [35] Radosavljevic, I.; Howard, J.A.K., Sleight, A.W., *International Journal of Inorganic Materials*, **2000**, 2, 543.
- [36] Abraham, F.; Ketatni, M.; Mairesse, G.; Mernari, B., *European Journal of Solid State and Inorganic Chemistry*, **1994**, 31, 313.
- [37] Mizrahi, A.; Wignacourt, J.P.; Steinfink, H., *J. Solid State Chem.*, **1997**, 133, 516.
- [38] Roussel, P.; Labidi, O.; Huve, M.; Drache, M.; Wignacourt, J.P.; Petricek, V., *Acta Crystallographica, Section B: Structural Science*, **2009**, 65, 416.
- [39] Xun, X.; Uma, S.; Yokochi, A.; Sleight A.W., *J. Solid State Chem.*, **2002**, 167, 245.

- [40] Tancret N. «Détermination de structures *Ab Initio* par diffraction X sur poudre: Application à quelques oxydes, Université Lille1 - Sciences et Technologies (1995).
- [41] Klasens, H.A., *Nature*, **1946**, 158, 306.
- [42] Yonesaki, Y., *J. Solid State Chem.*, **2013**, 197, 166.
- [43] Kresse, G.; Furthmüller, J., *Vienna Ab-initio Simulation Package (VASP)*; Institut für Materialphysik: Vienna (<http://www.vasp.at/>), **2012**.
- [44] Perdew, J.P.; Wang, Y., *Phys. Rev. B*, **1992**, 45, 13244.
- [45] Kresse, G.; Joubert, D., *Phys. Rev. B*, **1999**, 59, 1758.
- [46] Dash, A.; Sarkar, S.; Adusumalli, V.N.K.B.; Mahalingam, V., *Langmuir*, **2014**, 30, 1401.
- [47] Duffy, J.A., *J. Chem. Soc., Faraday Trans. 2*, **1978**, 74, 1504.
- [48] Setlur, A.A.; Srivastava, A.M., *Opt. Mater.*, **2006**, 29, 410.
- [49] Duffy, J.A.; Ingram, M.D., *J. Chem. Phys.*, **1970**, 52, 3752.
- [50] Colmont, M.; Delevoye, L.; Ketatni, M.; Montagne, L.; Mentre, O., *J. Solid State Chem.*, **2006**, 179, 2111.
- [51] Yeh, C.W.; Liu, Y.P.; Xiao, Z.R.; Wang, Y.K.; Hu, S.F.; Liu, R.S., *J. Mater. Chem.*, **2012**, 22, 5828.
- [52] Orhana, E.; Pontes, F.M.; Pinheiro, C.D.; Boschi, T.M.; Leite, E.R.; Pizani, P.S.; Beltrán, A.; Andrés, J.; Varela, A.; Longo, E., *J. Solid State Chem.*, **2004**, 177, 3879.
- [53] Zhao, L.; Zhang, X.; Fan, C.; Liang, Z.; Han, P., *Phys. B*, **2012**, 407, 3364.
- [54] Polosan, S.; Galca, A.C.; Secu, M., *Solid State Sci.*, **2011**, 13, 49.
- [55] Brixner, L.H., *Mat. Res. Bull.*, **1978**, 13, 563.
- [56] Tanner, P.A.; Jia, G.; Cheng, B.M.; Brik, M.G., *Phys. Status Solidi B*, **2012**, 249, 581.
- [57] Nilk, M.; Nitsch, K.; Velicka, I.; Hybler, J.; Polak, K.; Fabian, T., *Phys. Status Solidi B*, **1991**, 168, K37.
- [58] Folkerts, H.F.; Zuidema, J.; Blasse, G., *Solid State Comm.*, **1996**, 99, 655.
- [59] Srivastava, A.M.; Beers, W.W., *J. Lumin.*, **1999**, 81, 293.
- [60] Xu, W.; Peng, M.; Ma, Z.; Dong, G.; Qiu, J., *Optics Express*, **2012**, 20, 15692.
- [61] Boutinaud, P., *J. Phys.: Condens. Matter.*, **2014**, 26, 405501.
- [62] Kimani, M.M.; Kolis, J.W., *J. Lumin.*, **2014**, 145, 492.
- [63] Song, D.; Guo, C.; Li, T., *Ceramics International*, **2015**, 41, 6518.
- [64] Mulliken, R.S., Spectroscopy, molecular orbitals, and chemical bonding, Nobel Lecture, December 12, **1966**.
- [65] Nakajima, T.; Isobe, M.; Tsuchiya, T.; Ueda, Y.; Manabe, T., *Opt. Mater.*, **2010**, 32, 1618.
- [66] Nakajima, T.; Isobe, M.; Tsuchiya, T.; Ueda, Y.; Kumagai, T., *Nat. Mat.*, **2008**, 7, 735.
- [67] Blasse, G., *Philips Res. Rep.*, **1969**, 24, 131.
- [68] Leppert, J.; Peudenier, S.; Bayer, E.; Grabmaier, B.C.; Blasse, G., *Appl. Phys.*, **1994**, A59, 69.
- [69] Nath, R.; Ranjith, K.M.; Roy, B.; Johnston, D.C.; Furukawa, Y.; Tsirlin, A.A., *Phys. Rev. B*, **2014**, 90, 024431.
- [70] Reisfeld, R.; Kilisev, A.; Jorgensen, C.K., *Chem. Phys. Lett.*, **1984**, 111, 19.
- [71] Sudhakar Reddy, B.; Gopal, N.O.; Narasimhulu, K.V.; Linga Raju, C.; Rao, J.L.; Reddy, B.C.V., *J. Mol. Struct.*, **2005**, 751, 161.
- [72] Yuan, S.; Yang, Y.; Zhang, X.; Tessier, F.; Chevire, F.; Adam, J.L.; Moine, B.; Chen, G., *Opt. Lett.*, **2008**, 33, 2885.
- [73] Da, N.; Peng, M.; Krolikowski, S.; Wondraczek, L., *Optics Express*, **2010**, 18, 2549.
- [74] Tanabe, Y.; Sugano, S., *J. Phys. Soc. Jpn.*, **1954**, 9, 753.
- [75] Tanabe, Y.; Sugano, S., *J. Phys. Soc. Jpn.*, **1954**, 9, 766.
- [76] Tanabe, Y.; Sugano, S., *J. Phys. Soc. Jpn.*, **1956**, 11, 864.
- [77] Racah, G., *Phys. Rev.*, **1942**, 62, 438.
- [78] Riedel, E., *Moderne Anorganische Chemie*, 3. Auflage, Walter de Gruyter, Berlin/New York, **2007**, 446.
- [79] Zhang, Q.; Sun, H.; Kuang, T.; Xing, R.; Hao, X., *RSC Adv.*, **2015**, 5, 4707.
- [80] Maggay, I.V.B.; Lin, P.C.; Liu, W.R., *Journal of Solid State Lighting*, **2014**, 1, 13.

[81] Parthasaradhi Reddy,C.; Naresh,V.; Babu, B.C.; Buddhudu, S.; *Advances in Materials Physics and Chemistry*, **2014**, 4, 165.

[82] Yen, W. M.; Shionoya, S.; Yamamoto, H., *Phosphor Handbook* (second edition), Taylor and Francis, (2006).

[83] Gawande, A.B.; Sonekar, R.P.; Omanwar, S.K., *International Journal of Optics*, **2014**, 2014, 418459.

**Chapter IV. Electronic Structures
and Optical properties of
BiMO(VO₄) compounds**

IV. Electronic Structures and Optical properties of BiMO(VO₄) compounds

IV.1. Crystal structures and interest for optical properties

As for the BiM₂XO₆ described in the previous chapter, the BiMXO₅ series can also be of interest for their optical properties due to the relatively low Bi...Bi connectivity (depending on the BiMXO₅ polytype, each Bi³⁺ is connected to 1 or 2 other Bi³⁺ by Bi-O-Bi bridges (see Chapter III section 1 and figure IV-1) while the oxo-centered chains holding the Bi centers are isolated. It is expected to limit the concentration quenching and may lead to intense room temperature luminescence. According to the oxo-centered description given in the Chapter III, the elementary building units are oxo-centered simple chains, n=1 tetrahedron thick. The table IV-1 gathers all the members of this family reported in the literature so far. Although the large diversity of crystal symmetry and space group of the member of this family, they all can be described as [O₂Bi₂M₂]⁶⁺ ribbons parallel to each others. The ribbons are surrounded by six XO₄ tetrahedra (figure IV-1). The orientation of these tetrahedra compared to the ribbons varies according to the space group and the steric effects of “small” PO₄ or “big” VO₄. In general, M atoms are in *trans* position with respect to edges on the tetrahedra in the ribbons, leading to the Bi...Bi isolated pairs, figure IV-1b. Two exception cases are found, where M atoms are in *cis* position in BiCaVO₅ and BiCdVO₅ (figure IV-1).^{1,2} The *cis* position of M atoms modifies the Bi...Bi connectivity leading to each Bi³⁺ interconnected to two other Bi³⁺ (figure IV-1a). In the past, for several aspects, the BiMXO₅ family have been extensively studied. For instance BiPbPO₅ and BiPbVO₅ show phase transition from triclinic to monoclinic crystal system at high temperature due to drastic VO₄ reorientation.¹² BiCoAsO₅, BiCoPO₅, BiNiPO₅ as well as the solid solution BiNi_xCo_{1-x}PO₅ undergo antiferromagnetic ordering at low temperature (at 11K and 17K respectively for BiNiPO₅ and BiCoPO₅)^{9,13-14}. Concerning the optical aspect at the center of this PhD work, BiMgVO₅ and BiCaVO₅ are room temperature phosphors.^{3,15}

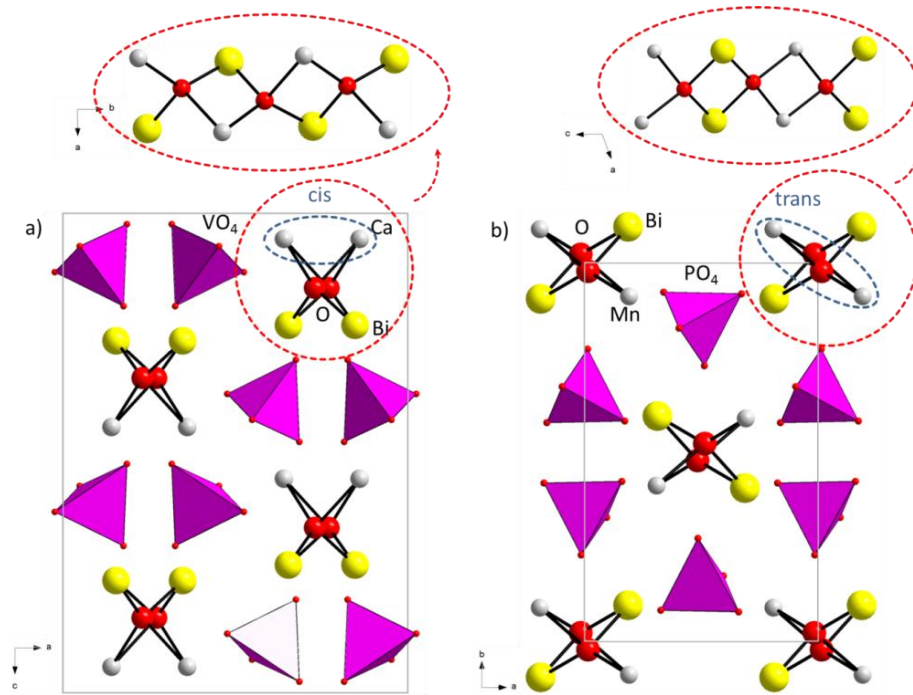


Figure IV- 1 a) The crystal structure of BiCaVO₅ with cis position of M atoms, the projection of the ribbon in the (ab) plan show the Bi...Bi connectivity via Bi-O-Bi bridges b) The crystal structure of BiMnPO₅ with trans position of M atoms, the projection of the ribbon in the (ac) plan show the Bi...Bi connectivity via Bi-O-Bi bridges.

Table IV-1 Crystalline characteristics of BiMXO₅ phases reported in the literature.

Compound	S.G.	a (Å)	b (Å)	c (Å)	α (°)	β (°)	γ (°)	Z
BiCaVO ₅ ¹	<i>P bca</i>	11.202(3)	5.428(2)	15.561(2)	90	90	90	8
BiCdVO ₅ ²	<i>P c2₁n</i>	5.505(2)	11.699(4)	14.276(4)	90	90	90	8
BiMgVO ₅ ³	<i>P 2₁/n</i>	7.542(6)	11.615(5)	5.305(3)	90	107.38(5)	90	4
BiPbVO ₅ ⁴	<i>P -1</i>	7.1082(5)	7.2802(6)	5.6203(4)	111.788(5)	95.207(5)	108.717(5)	4
BiPbPO ₅ ⁵	<i>P -1</i>	5.6158(1)	6.8706(1)	7.1189(1)	109.982(1)	109.817(1)	96.897(1)	2
BiNiPO ₅ ⁶	<i>P 2₁/n</i>	7.1664(8)	11.206(1)	5.1732(6)	90	107.28(1)	90	4
BiNiAsO ₅ ⁷	<i>P -1</i>	6.7127(8)	6.8293(8)	5.2345(6)	107.625(2)	95.409(2)	111.158(2)	2
BiCoPO ₅ ⁸	<i>P 2₁/n</i>	7.2470(1)	11.2851(2)	5.2260(1)	90	107.843(1)	90	4
BiCoAsO ₅ ⁹	<i>P -1</i>	5.2380(3)	6.8286(4)	7.6150(4)	111.631(2)	108.376(2)	108.388(2)	2
BiMnPO ₅ ¹⁰	<i>P 2₁/n</i>	7.4339(3)	11.356(4)	5.3577(2)	90	109.19(2)	90	4
BiMnVO ₅ ¹¹	<i>P -1</i>	6.912(4)	6.991(2)	5.354(1)	108.55(2)	95.98(4)	109.73(4)	2
BiMnAsO ₅ ¹¹	<i>P -1</i>	6.868(1)	6.905(2)	5.360(1)	109.47(2)	95.91(2)	109.32(2)	2

IV.2. Selection of compounds

All the compounds listed in table IV-1 have been tested for their photoluminescence properties. Ni²⁺ and Co²⁺ being known as killer centers,¹⁶ they absorb the visible light and relax via non-radiative path, and hence BiCoXO₅ and BiNiXO₅ (X=P, As) cannot emit light in the visible range at room temperature. It was verified experimentally.

On the other hand, Pb²⁺ and Mn²⁺ are also activator ions as Bi³⁺ and due to the high concentration and the proximity of the activators an energy transfer between activators occurs and finally the energy is lost by cross relaxation. In other words, a concentration quenching occurs.¹⁷ It was also verified experimentally.

Finally among the list given below, only three compounds can produce radiative emission at room temperature: BiCaVO₅, BiCdVO₅ and BiMgVO₅. The point is that the photoluminescence of the three compounds is far from the “Bi³⁺” luminescence context of this thesis work due to the co-presence of Bi³⁺ and luminescent VO₄³⁻ groups. It was already discussed in the chapter III, the luminescence of BiMg₂VO₆ phase is strongly dominated by the vanadate groups originates from O 2p → V 3d charge transfer. In the literature, the photoluminescence of BiCaVO₅ and BiMgVO₅ was already reported.^{3,15}

For BiMgVO₅,³ the authors attribute the emission to Bi³⁺ with the existence of energy transfer from the matrix (VO₄)³⁻ to the emitting centers Bi³⁺ whereas in BiCaVO₅, for the authors, the optical transitions are due to vanadate groups with a certain contribution of Bi³⁺ via metal-metal charge transfer.¹⁵ These two explanations are quite plausible but are the opposite of each other. Moreover, electronic properties or decay time measurements for a complete study are missing in the published works. This is the motivation of this chapter leading to the full investigation of the electronic structures and photoluminescence properties at room temperature of the phases BiMVO₅ (M=Ca, Cd, Mg). The crystal data from the literature are gathered in the Table IV-2.

Table IV-2. Crystal data and selected bond lengths of BiMVO₅ (M=Mg, Ca, Cd).

Compound	BiMgVO ₅ , ref. [3]	BiCaVO ₅ , ref. [1]	BiCdVO ₅ , [2]	
Crystal system	monoclinic	orthorhombic	orthorhombic	
Space group	<i>P2₁/n</i> (14)	<i>Pbca</i> (61)	<i>Pc2₁/n</i> (33)	
<i>a</i> (Å)	7.542(6)	11.2022(25)	5.505(2)	
<i>b</i> (Å)	11.615(5)	5.4283(15)	11.699(4)	
<i>c</i> (Å)	5.305(3)	15.5605(19)	14.276(4)	
β (°)	107.38(5)	-	-	
Cell Volume (Å ³)	443.50(49)	946.22 (40)	546.30(1)	
Refinement type	XRD Single crystal	XRD Single crystal	XRD Single crystal	
Bi-O bonds (Å)	1 x 2.1295	1 x 2.1176	(Bi1)	Bi(2)
(average)	1 x 2.2031	1 x 2.1378	1 x 2.1851	1 x 2.1328
	1 x 2.2681	1 x 2.2737	1 x 2.1961	1 x 2.1839
	1 x 2.4352	1 x 2.3552	1 x 2.2273	1 x 2.3077
	1 x 2.5430	1 x 2.5255	1 x 2.3952	1 x 2.3315
	1 x 2.8135	1 x 3.3806	1 x 2.8396	1 x 2.6281
	1 x 3.2826	1 x 3.4056	1 x 2.9213	1 x 2.7454
	1 x 3.4625	1 x 3.6102	1 x 2.9387	1 x 2.9225
	(2.6422)	(2.7258)	1 x 3.3051	1 x 3.5170
			(2.6261)	(2.5961)
V-O bonds (Å)	1 x 1.6827	1 x 1.6934	(V1)	(V2)
(average)	1 x 1.7075	1 x 1.7001	1 x 1.6880	1 x 1.6824
	1 x 1.7081	1 x 1.7039	1 x 1.7124	1 x 1.7286
	1 x 1.7482	1 x 1.7440	1 x 1.7205	1 x 1.7377
	(1.7116)	(1.7103)	1 x 1.7254	1 x 1.7759
			(1.7115)	(1.7312)

IV.3. Synthesis of BiMVO₅ (M=Mg, Ca, Cd)

Polycrystalline powder samples were prepared by conventional solid state reaction between Bi₂O₃, CdO or MgO or CaCO₃ and NH₄VO₃ in stoichiometric amount. In a first stage, MgO and Bi₂O₃ were heated overnight at 600°C for decarbonatation. After grinding in an agate mortar, mixtures have been placed in alumina crucibles and heated under air. For BiMgVO₅ the mixture was preheated at 500°C for 10h and then the reaction was completed after a last stage of 20h at 850°C. For BiCaVO₅, after a preheating at 450°C during 5h, the reaction was completed at 750°C during 12h. And finally for BiCdVO₅, the mixture was directly heated at 800°C for 45h. Several intermediate grindings were necessary to obtain single crystalline-phases. The XRD measurements confirm the purity of each sample: all the reflections can be indexed to the desired phase (figure IV-2).¹⁻³

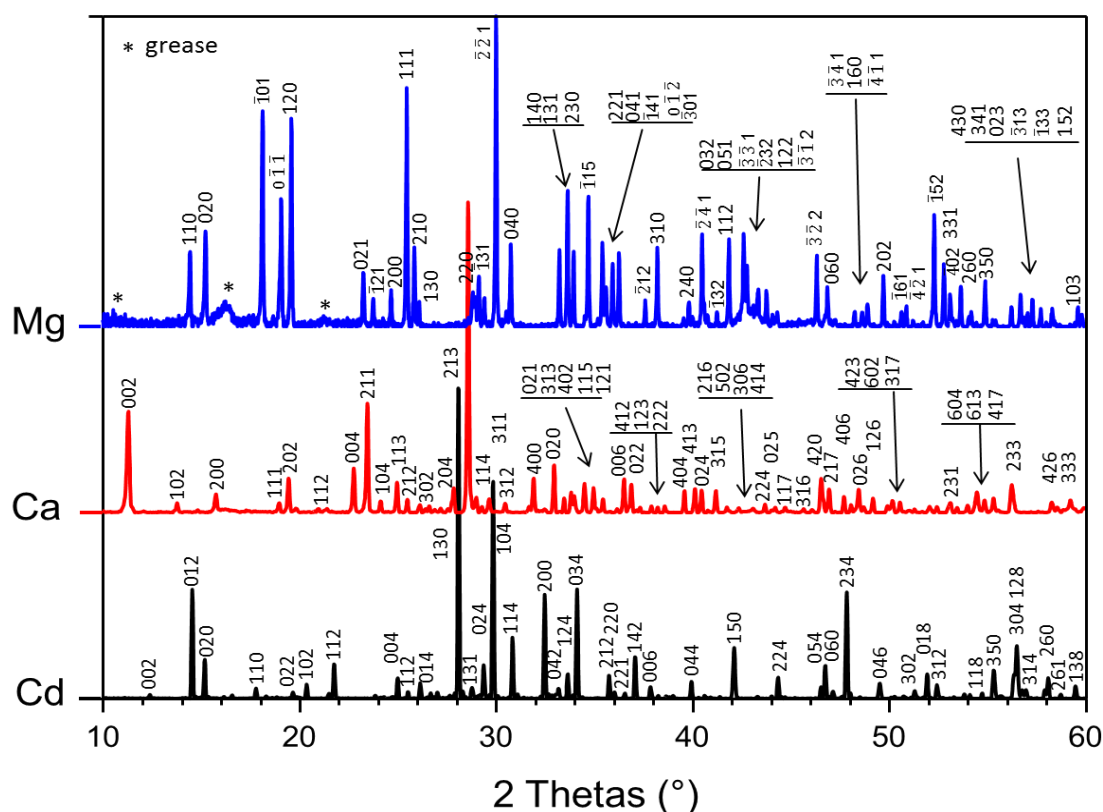


Figure IV- 2 XRD pattern of BiMVO₅ (M=Cd, Ca, Mg) with reflections indexation.

IV.4. Electronic structure calculations

Density functional theory (DFT) calculations were performed using the Vienna *ab initio* simulation package (VASP).¹⁸ The calculations were carried out within the generalized gradient approximation (GGA) for the electron exchange and correlation corrections using the Perdew-Wang (PW91) functional and the frozen core projected wave vector method.¹⁹⁻²⁰ The full geometry optimizations were carried out using a plane wave energy cutoff of 550eV and 9 *k* points in the irreducible Brillouin zone for BiCdVO₅ and BiCaVO₅ (10 *k* points for BiMgVO₅). All structural optimizations converged with residual Hellman-Feynman forces on the atoms smaller than 0.03 eV/Å and led to reasonable structures regarding the distances and the local geometries. The cell parameters found after the full structural relaxation fit well with the experimental one. The error on cell parameters does not exceed 2.3% (on the *a* parameter for BiMgVO₅) (table IV-3) which is relatively low. Then, the relaxed structures were used to perform accurate calculations of the electronic structure. For the later, a plane wave energy

cutoff of 400eV, an energy convergence criterion of 10^{-6} eV and 18 *k* points (20 *k* points for BiMgVO₅) in the irreducible Brillouin zone were used.

Table IV-3. Comparison between experimental and theoretical cell parameters of BiMVO₅ (M= Mg, Ca, Cd) after full structural relaxation.

Compound	Cell parameters	Experimental	Theoretical	Deviation from exp.
BiMgVO ₅	<i>a</i> (Å)	7.542(6)	7.7118	2.3%
	<i>b</i> (Å)	11.615(5)	11.6635	0.4%
	<i>c</i> (Å)	5.305(3)	5.3910	1.6%
	β (°)	107.38(5)	107.43	0.1%
BiCaVO ₅	<i>a</i> (Å)	11.202(3)	11.3519	1.3%
	<i>b</i> (Å)	5.4218(2)	5.5188	1.8%
	<i>c</i> (Å)	15.561(2)	15.7526	1.2%
BiCdVO ₅	<i>a</i> (Å)	5.505(2)	5.5685	1.2%
	<i>b</i> (Å)	11.699(4)	11.8336	1.2%
	<i>c</i> (Å)	14.276(4)	14.4310	1.1%

IV.5. Topology of Density of States

The total and partial density of states are plotted between -5 and 10eV in order to focus on the higher part of the valence band and the lower part of the conduction band (figure IV-4).

- For BiCdVO₅, the highest part of the VB situated between -4.52 and 0eV is formed by Bi 6s and 6p, O 2p, Cd 5s, 4p and 4d and V 3d states. A small contribution of V 4s states can also be observed. The lowest part of the conduction band (2.5 to 5.99eV) is mainly composed of Bi 6p, V 3d, O 2p and Cd 4s states whereas Bi 6s, V 4p and Cd 5p states have only a minor contribution.

- For BiCaVO₅, the highest part of the valence band is situated between -4.15 and 0eV and mainly originates from Bi 6s and 6p, V 3d, O 2p states. The contributions of Ca states can be neglected. The conduction band is divided in two parts. The lowest energy part situated between 3.10 and 3.63eV is essentially dominated by V 3d states, however contributions of Bi 6p and O 2p states are also observed. The higher energy part (3.95 to 8.35eV) is composed of the same states with low additional contributions of V 4p and Bi 6s states.

- The DOS of BiMgVO₅ have the same topology than for BiCaVO₅, here the contributions of the divalent cation (Mg²⁺) states can be neglected. The highest part of the valence band situated between -4.5 and 0eV is mainly formed by Bi 6s and 6p, V 3d and O₂p states. On the other hand, the conduction band is also split in two parts. From 2.95 to 3.56eV it is composed of Bi 6p, O₂p states and a strong contribution of V 3d states whereas the higher energy part (3.92 to 6.98eV) belongs to the contributions of Bi 6p, O₂p, V 3d states. Low contributions of Bi 6s and V 4p states are also observed.

For each compounds, the O 2p states are situated at the Fermi energy whereas a high and rather localized density of V 3d states is situated at the bottom of the CB. This favors the electronic transfer from the O 2p states to V 3d states needed for the excitation process for the vanadate groups (see figure IV-3). The Bi 6s states are each time found at the Fermi level at the top of the valence band whereas their contribution in the conduction band is nearly negligible.

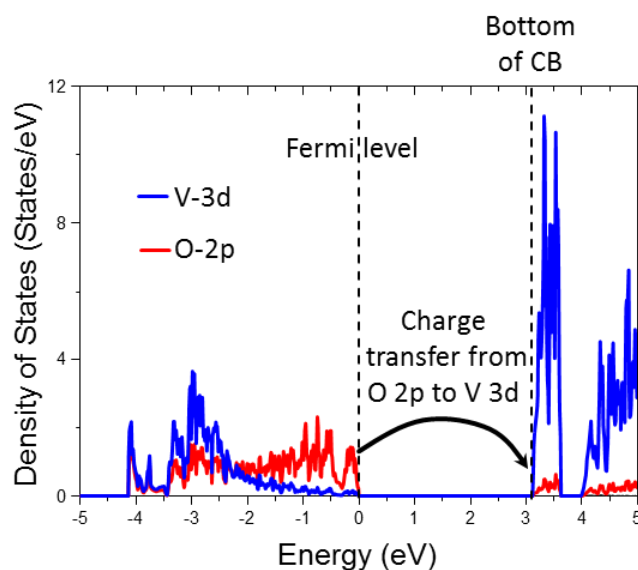


Figure IV- 3 Sketch representing the charge transfer O 2p → V 3d.

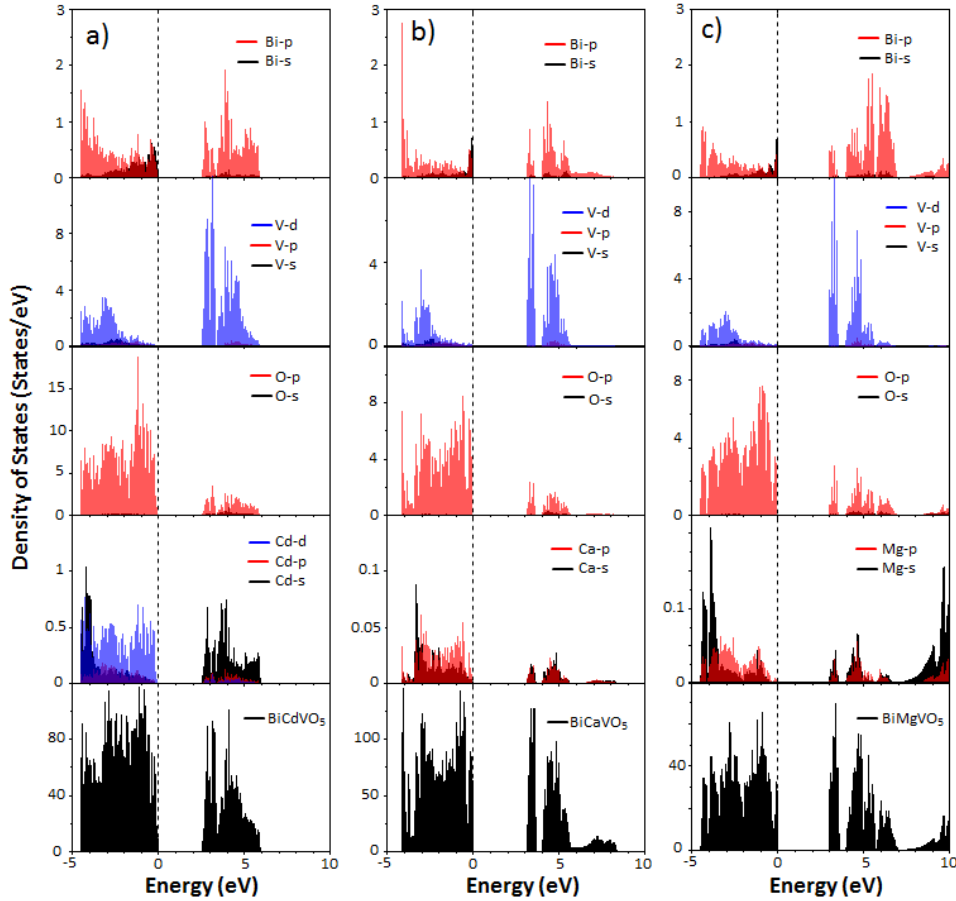


Figure IV- 4 TDOS and PDOS of BiMVO₅ (M=Cd, Ca, Mg).

IV.6. Photoluminescence properties and structural correlation

All the three samples are luminescent at room temperature, BiCaVO₅ ($x= 0.4795$ and $y=0.4533$) emits an orange radiation whereas BiMgVO₅ ($x=0.5246$ and $y=0.4484$) and BiCdVO₅ ($x=0.5345$ and $y=0.4495$) produces a reddish-orange one. The emission colours are given figure IV-5a in the CIE 1931 chromaticity diagram.

The position of excitation and emission bands found in this work for BiMgVO₅ are in good agreement with the literature³ whereas the position of the emission band for BiCaVO₅ is red shifted by $\sim 0.18\text{eV}$ which may be due to the correction for the photomultiplier sensitivity (see table IV-4)¹⁵. Concerning the excitation spectra, it has a similar shape for the three compounds (doublet even if a triplet can be considered for BiCdVO₅) (figure IV-5c). The excitation spectrum of BiMgVO₅ and BiCaVO₅ is situated in the UV range whereas the one of BiCdVO₅ is red shifted and starts in the blue range.

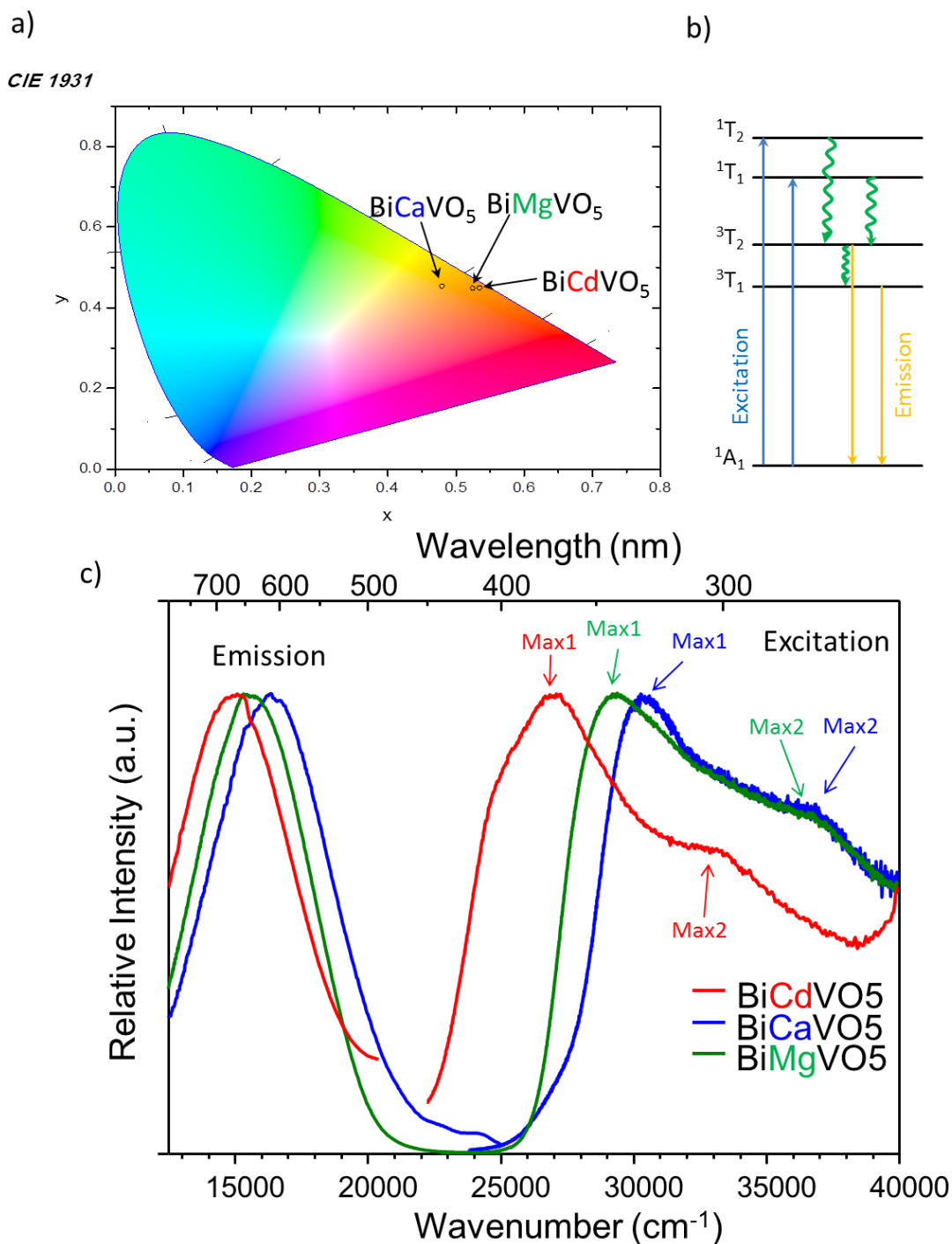


Figure IV- 5 a) Emission color representation on the CIE chromaticity diagram b) Sketch of absorption and emission processes of the VO₄ tetrahedron with T_d symmetry and c) Emission and excitation spectra of BiMVO₅ (M=Cd, Ca, Mg).

The more intense peak is always the one situated at lower energy and although it is difficult to find the exact maximum of the shoulder for each compound, one can remark that the energy difference between the two maxima for each excitation spectra is similar (~6400cm⁻¹, ~6500cm⁻¹ and ~6900cm⁻¹ respectively for M=Cd, Ca and Mg). The emission spectra cover a

large part of the visible range and have similar shapes (FHMW= 5600cm⁻¹, 5500cm⁻¹ and 5100cm⁻¹ respectively for M=Cd, Ca, Mg) (figure IV-5c). All the optical data are gathered table IV-4.

Table IV-4. Optical data for BiMVO₅ (M=Cd, Ca, Mg).

Compound	BiCdVO ₅	BiCaVO ₅	BiCaVO ₅ [15]	BiMgVO ₅	BiMgVO ₅ [3]
Excitation maximum	26910 cm ⁻¹ (3.34eV)	30375 cm ⁻¹ (3.77 eV)	30305 cm ⁻¹ (3.76eV)	29300 cm ⁻¹ (3.64 eV)	29160 cm ⁻¹ (3.62eV)
Emission maximum	14930 cm ⁻¹ (1.85eV)	16360 cm ⁻¹ (2.03eV)	17857 cm ⁻¹ (2.21 eV)	15570 cm ⁻¹ (1.93 eV)	15361 cm ⁻¹ (1.90 eV)
Emission FWHM	5600 cm ⁻¹ (0.69eV)	5500cm ⁻¹ (0.68eV)	- -	5100 cm ⁻¹ (0.63eV)	- -
Stokes Shift	11980 cm ⁻¹ (1.49eV)	14015 cm ⁻¹ (1.74eV)	12448 cm ⁻¹ (1.54eV)	13730 cm ⁻¹ (1.70eV)	13799 cm ⁻¹ (1.71 eV)
Ionic radius M ²⁺	Cd ²⁺ : 0.95 Å	Ca ²⁺ : 1.06 Å	Ca ²⁺ : 1.06 Å	Mg ²⁺ : 0.72 Å	Mg ²⁺ : 0.72 Å
PP of X ⁵⁺	2.1	1.9	1.9	2.8	2.8
CIE coordinates	x= 0.5345 y= 0.4495	x= 0.4795 y= 0.4533	- -	x = 0.5246 y= 0.4484	- -

The excitation and emission bands cannot be attributed easily for these three compounds due to the presence of Bi³⁺ activators and VO₄ groups which are both characterized by broad emission bands in the visible range and large Stokes shifts.²¹⁻²² Moreover both excitation energies for Bi³⁺ and VO₄³⁻ groups are strongly dependent on different crystal lattice structures.²³ The luminescence of vanadates²⁴ was presented in the Chapter III for BiMg₂VO₆.

IV.7. Decay time measurements

In order to get more information on the emitting process, decay time measurements were performed for the three compounds at room temperature (figure IV-6). The decay curves for all are fitting the best with a double exponential behaviour using $I = I_0 + A1 \cdot \exp(-t/\tau_1) + A2 \cdot \exp(-t/\tau_2)$ equation where A1 and A2 are two constants, I₀ the intensity at t=0 and τ₁ and τ₂ the two lifetime values. These lifetime values are gathered in Table IV-5. For M=Cd, the fitting of the decay curve gives τ₁=19μs and τ₂=33μs, for M=Ca τ₁=11μs and τ₂=5μs and finally for M=Mg τ₁=18μs and τ₂=102μs. For BiCaVO₅ and BiCdVO₅ the values of τ₁ and τ₂ are close but a monoexponential fit gives unsatisfactory correlation factors and from the decay curve it can also be seen that there are two linear domains. The value of τ₁ is very similar for the three compounds (19μs, 11μs and 18μs respectively for M=Cd, Ca and Mg) whereas the

value of τ_2 differs more between the studied compounds. Concerning BiMgVO₅, the value of τ_2 (102 μ s) matches perfectly with the lifetime found for BiMg₂VO₆ ($\tau_2=104\mu$ s) in the previous chapter and with the typical lifetime value of the vanadate emission ($\sim 200\mu$ s)²⁵ and thus, τ_1 (18 μ s) can be the most probably be attributed to the charge transfer from Bi³⁺ to VO₄ groups. On the other hand the τ_2 value of BiCdVO₅ (33 μ s) and especially BiCaVO₅ (5 μ s) can fit with both Bi³⁺ and VO₄ emission type (typical decay value of 350ns and 200 μ s respectively). However, for BiCaVO₅ and BiCdVO₅, τ_1 can be the most probably attributed to the charge transfer between Bi³⁺ and VO₄ groups by comparison of the value BiMgVO₅.

Table IV-5. Lifetime values for BiMVO₅ (M=Cd, Ca, Mg) and BiMg₂VO₆.

Compound	τ_1	τ_2
BiCdVO ₅	19 μ s	33 μ s
BiCaVO ₅	11 μ s	5 μ s
BiMgVO ₅	18 μ s	102 μ s
BiMg ₂ VO ₆	18 μ s	104 μ s

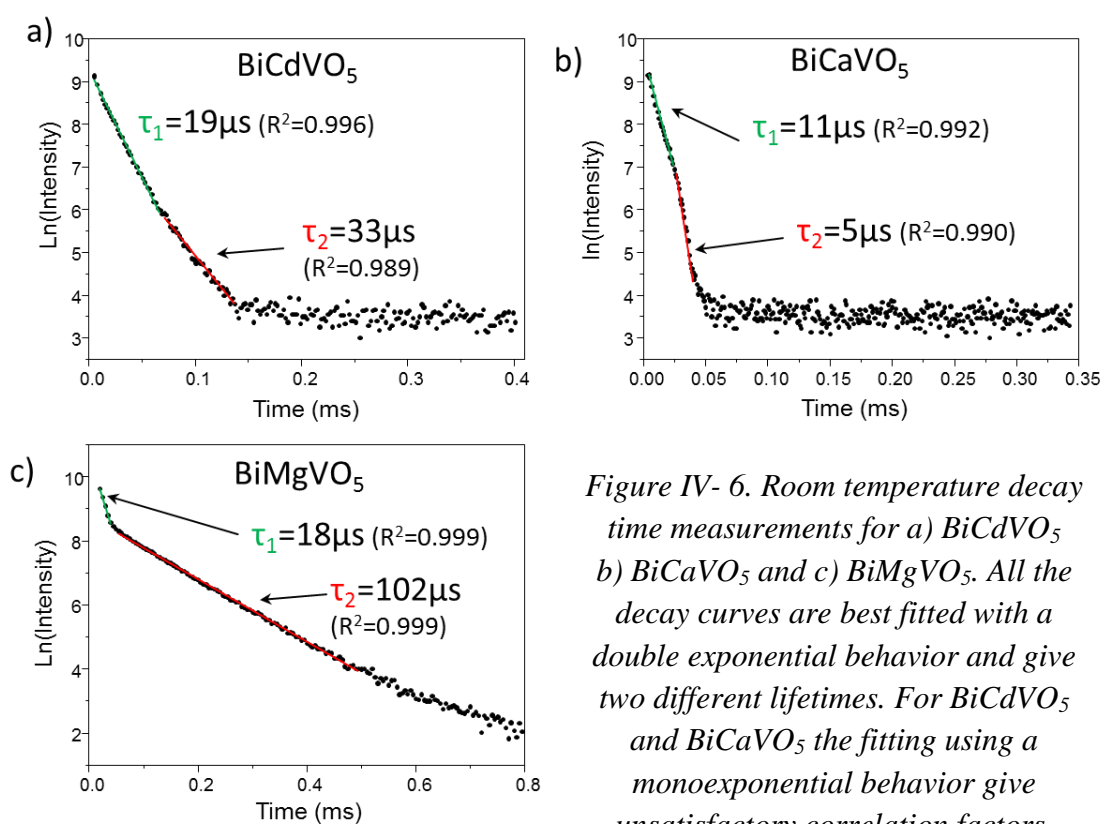


Figure IV- 6. Room temperature decay time measurements for a) BiCdVO₅ b) BiCaVO₅ and c) BiMgVO₅. All the decay curves are best fitted with a double exponential behavior and give two different lifetimes. For BiCdVO₅ and BiCaVO₅ the fitting using a monoexponential behavior give unsatisfactory correlation factors.

IV.8. Discussion

The excitation spectra of the three phosphors can the most probably be attributed to a charge transfer from O 2p to V 3d states due to high contribution of V 3d states at the bottom of the conduction band and the presence of O 2p states at the Fermi energy (figure IV-4). Moreover the quasi-constant energy difference between the two maxima of the excitation spectra can corresponds to the energy difference between the molecular states ¹T₁ and ¹T₂. However a contribution of Bi³⁺: ¹S₀ → ³P₁ transition for the excitation band cannot be completely excluded since from the decay time measurements energy transfer can be observed. One can also note that lowering the bandgap (2.5eV, 2.95eV and 3.10eV respectively for M=Cd, Mg, Ca taken from the DOS calculations) shifts the excitation bands to lower energy.

Concerning the emission process, different things can influence the low value of τ₂ for BiCdVO₅ and BiCaVO₅ and can give more information on the emission process.

First, one can note that the position of Bi atoms in the ribbons is not the same for BiMgVO₅ (*trans* position) than for BiCaVO₅ and BiCdVO₅ (*cis* position) (figure IV-1). Additionally, Mg has a much higher polarizing power (Z/r) than Cd or Ca (table IV-4). Then, by inductive effect this would have for consequence to shift the Bi³⁺ excited states of BiCdVO₅ and BiCaVO₅ to lower energies compared to BiMgVO₅ (nephelauxetic effect, see Chapter III). Thus, the excited states of Bi³⁺ and VO₄³⁻ would be found at comparable energy positions and have more chance to interact on each others (the maximum of the excitation band of VO₄ groups is usually situated between 320 and 370nm)²⁶. In high concentration bismuth doped vanadate compounds, Blasse et al. attribute the emission to bismuth-modified vanadate groups (VO₄³⁻-Bi³⁺ centers).^{15,27} These VO₄³⁻-Bi³⁺ centers act as a trap of the migrating VO₄³⁻ excitation energy²⁸ and then the radiative decay becomes faster than for VO₄³⁻ group because the strong spin orbit coupling at Bi³⁺ ion relaxes the spin-selection rule on the vanadate groups.²⁷ In this case the experimental decay τ₂=5μs for BiCaVO₅ fits well with the literature (4-5μs).^{21,27,29}

IV.9. Summary

Finally, from all the experimental data, it can be concluded that for BiMgVO₅ there is a low interaction between Bi³⁺ and VO₄³⁻ due the energy difference between excited states of Bi³⁺ (³P₁) and of VO₄³⁻ groups. An energy transfer occurs from Bi³⁺ to VO₄³⁻ and the

photoemission of BiMgVO₅ can be predominantly attributed to vanadates. For BiCdVO₅ and BiCaVO₅, the excited states of Bi³⁺ should be situated at a close energy position of molecular excited states of VO₄³⁻ (¹T₁ and ¹T₂) due to higher nephelauxetic effect on Bi³⁺ than in M=Mg compound. This has for consequence to create bismuth-modified vanadate groups which relaxes the spin-selection rule on the VO₄³⁻ groups and lowers the decay time of emission. Then, for M=Ca and Cd compounds, the emission comes from VO₄³⁻-Bi³⁺ centers (see figure IV-7). From the decay time measurements, it is also shown that in BiCaVO₅ the influence of Bi³⁺ on VO₄³⁻ is higher than for BiCdVO₅ which is in good agreement with the nephelauxetic effect expected on Bi³⁺. The polarizing power of Ca²⁺ is lower than this for Cd²⁺ (table IV-4) thus the excited states of Bi³⁺ in BiCaVO₅ should be at lower energy than for BiCdVO₅ and should more overlap with the excited states of the VO₄³⁻ group and by consequence more influence the vanadate emission. The best experimental way to verify these explanations would be to investigate and compare the photoluminescence of isostructural compounds possessing only one activator (Bi³⁺ or VO₄³⁻ groups). However, due to its asymmetric coordination the Bi³⁺ can hardly be substituted by cations with similar charge and ionic radius such as La³⁺ or even Y³⁺. On the other hand, the arsenate compounds BiMAsO₅ (M=Mg, Cd, Ca) could not be successfully synthesized after many trials.

Comparing these results to the original ones, they are in good agreement with the luminescence attribution for BiCaVO₅,¹⁵ however for BiMgVO₅ the authors attributed the emission to a charge transfer from vanadate to the emitting Bi³⁺ activator³ whereas this more complete study shows that the radiative emission comes mainly from VO₄³⁻ groups.

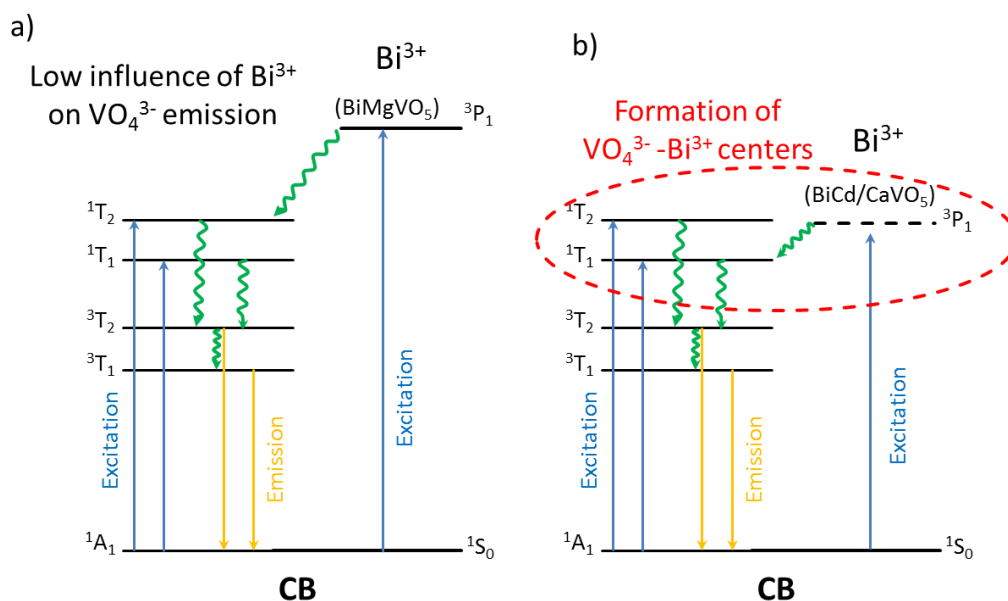


Figure IV- 7 Sketch representing the influence of Bi³⁺ on VO₄³⁻ photoluminescence.

References

- [1] Boje, J.; Mueller Buschbaum, H., *Zeitschrift für Anorganische und Allgemeine Chemie*, **1993**, 619, 521.
- [2] Radosavljevic, I.; Howard, J.A.K., Sleight, A.W., *International Journal of Inorganic Materials*, **2000**, 2, 543.
- [3] Benmokhtar, S.; El Jazouli, A.; Chaminade, J.P.; Gravereau, P.; Guillen, F.; de Waal, D., *J. Solid State Chem.*, **2004**, 177, 4175.
- [4] Brixner, L.H.; Foris, C.M., *Materials Research Bulletin*, **1974**, 9, 273 .
- [5] Labidi, O.; Roussel, P.; Porcher, F.; Drache, M.; Vannier, R.N.; Wignacourt, J.P., *J. Solid State Chem.*, **2008**, 181, 2268.
- [6] Abraham, F.; Ketatni, M., *European Journal of Solid State Inorganic Chemistry*, **1995**, 32, 429.
- [7] Roberts, A.C.; Burns, P.C.; Gault, R.A.; Criddle, A.J.; Feinglos, M.N.; Stirling, J.A.R., *Eur. J. Mineral*, **2001**, 13, 167.
- [8] Ketatni, M.; Abraham, F.; Mentre, O., *Solid State Sciences*, **1999**, 1, 449.
- [9] Aliev, A. «Nouvelles topologies structurales d'oxydes et sels de bismuth ; cristallographie, approche modulaire et propriétés» Université Lille1 - Sciences et Technologies (**2014**).
- [10] Xun, X.; Uma, S.; Sleight, A.W., *J. Alloys and Compounds*, **2002**, 338, 51.
- [11] Xun, X.; Yokochi, A.; Sleight, A.W., *J. Solid State Chem.*, **2002**, 168, 224.
- [12] Giraud, S.; Mizrahi, A.; Drache, M.; Conflant, P.; Wignacourt, J.P.; Steinfink H., *Solid State Sciences*, **2001**, 3, 593.
- [13] Mathews, E.; Ranjith, K.M.; Baenitz, M.; Nath, R., *Solid State Communications*, **2013**, 154, 56.
- [14] Nadir S.; Swinnea, J. S.; Steinfink, H., *J.Solid State Chem.*, **1999**, 148, 295.
- [15] Pei, Z.; Vandijken, A.; Vink, A.; Blasse, G., *J. Alloys and Compounds*, **1994**, 204, 243.
- [16] Klasens, H.A., *Nature*, **1946**, 158, 306.
- [17] Blasse, G. and Grabmaier, B. C., *Luminescent Materials*, Springer, Berlin, (**1994**).
- [18] Kresse, G.; Furthmüller, J., *Vienna Ab-initio Simulation Package (VASP)*; Institut für Materialphysik: Vienna (<http://www.vasp.at/>), **2012**.
- [19] Perdew, J. P.; Wang, Y., *Phys. Rev. B*, **1992**, 45, 13244.
- [20] Kresse, G.; Joubert, D., *Phys. Rev. B*, **1999**, 59, 1758.
- [21] Blasse, G., *Struct. Bond.*, **1980**, 42, 1.
- [22] Blasse, G., *Prog. Solid State Chem.*, **1988**, 18, 79.
- [23] Li, J.; Qiu, K.; Li, W.; Yang, Q.; Li, J., *Materials Research Bulletin*, **2010**, 45, 598.
- [24] Nakajima, T.; Isobe, M.; Tsuchiya, T.; Ueda, Y.; Manabe, T., *Opt. Mater.*, **2010**, 32, 1618.
- [25] Blasse, G., *Philips Res. Rep.*, **1969**, 24, 131.
- [26] Zhou, J.; Huang, F.; Xu, J.; Chen, H.; Wang, Y., *J. Mater. Chem. C*, **2015**, 3, 3023.
- [27] Leppert, J.; Peudenier, S.; Bayer, E.; Grabmaier, B.C.; Blasse, G., *Appl. Phys.*, **1994**, A 59, 69.
- [28] Powell, R.C.; Blasse, G., *Struct. Bonding*, **1980**, 42, 43.
- [29] Boulon, G., *J. Phys.*, **1971**, 32, 333.

Chapter V. Optical properties of Bi³⁺ oxyhalides compounds

V. Optical properties of Bi³⁺ oxyhalides compounds

V.1. The Sillen

After investigation of the correlations between the crystal structures and the optical properties in bismuth oxo-vanadate, phosphate or arsenates described in the previous chapters, now, a focus will be done on mixed anion compounds i.e. essentially bismuth oxyhalides. Previously, using Bi(M,M')₂XO₆ isomorphs (M,M' = Mg, Zn, Cd and X = P, As, V) it was shown the possible controlled tuning of the excitation and emission energies mediated by both the nephelauxetic effect on Bi-O bonds and Bi³⁺ lone pair stereo-activity. Besides the validation of the relatively intense Bi³⁺ optical activity at room temperature in these compounds, these results set a broad playground for control of the optical properties of Bi³⁺ phosphors in well-adapted compounds changing the Bi coordinations. Drastic changes could be achieved by incorporation of heterotypic (O²⁻ and X⁻ halogen) anions within pertinent bismuth oxyhalides. For instance the luminescence of LaOCl:Bi (few percent doping) was undoubtedly ascribed to Bi³⁺ emitters.¹ Dealing with Bi-rich phases, in spite of significant concentration quenching, it was already shown that the Sillen phases ABiO₂Cl (A = Sr, Ba) and BaBiO₂Br display room temperature luminescence where the excitation and emission bands are influenced by the A and halide ions,² while the absence of reported electronic structure calculations did not allow to appreciate their relative effects. More generally on the basis of the enhanced photocatalytic activity of bismuth oxychlorides,³⁻⁸ their optical activity under UV illumination opens a broad field of investigation in this extended chemical/structural series. The CdBiO₂Cl and PbBiO₂Cl/Br phases proved to be active photocatalytically under UV radiations for degradation of methyl orange which questions about its optical activity and effect.⁹⁻¹⁰ This question is fundamentally important due to the duality between the needs for efficient electron-hole pairs separation upon photoexcitation for photocatalysis (PC), while enhanced radiative recombination is wished for light emission. Luminescence may be considered as a competing phenomenon of PEC activity and shed light through a different prism.

V.1.1. Choice and crystal structure of the selected Sillen compounds

The richness of the crystal chemistry of bismuth oxides and salts is governed not only by the labile distorted geometry of coordination of Bi³⁺ due to its stereo-active 6s² lone pair¹¹ but

also by its ability for creating building units made of oxo-centered OBi_n polyhedra as it was shown in the Chapter III.¹² Typically fluorite-type [Bi₂O₂]²⁺ layers are formed by edge-sharing OBi₄ tetrahedra. The easy replacement in these units of Bi³⁺ for aliovalent Mⁿ⁺ cations (see chapter III) offers even broader opportunities for original structural topologies based on O(Bi,M)₄ units.¹² For instance dealing with mixed Bi³⁺/Pb²⁺ oxyhalides, we have recently designed and published the [Pb_nBi_{10-n}O₁₃][Bi₂O₂]_nCl_{4+n} (n=1, 2, 3 and 4) series with 2D crenel-like oxo-centered units isolated by chloride layers,¹³ the photoluminescence properties of PbBi₄O₆Cl₂ will be presented later in this chapter After incorporation of other but compatible structural blocks, a diversity of ordered intergrown structures have been also reported with sequences giving rise to ideal tetragonal structures with $a \sim 3.9 \text{ \AA}$ (i.e., $\sqrt{2}/2a(\text{fluorite})$) and c varying from 6 to 50 Å dependent on the structural complexity.¹⁴⁻²⁰ The Sillen phases^{21,22} consist of [Bi₂O₂]²⁺ layers intergrown with single [X1], double [X2] or triple [M'_xX3] halide layers, where X represents the halide atoms. It produces the rather simple structures of ABiO₂Cl (X1-type) (A²⁺=Cd, Ca, Pb, Sr ...etc)⁶, BiOCl (X2-type)²³ and Ca_{1.25}Bi_{1.5}O₂Cl₃ or LiCa₂Bi₃O₄Cl₆ (X3-type).¹⁶ Dealing with luminescence properties, the Sillen phases are particularly relevant due to the possible control of the Bi³⁺ concentration in the oxo-centered layers, a major parameter for hampering the concentration quenching.

- The X2 series is generally associated to undoped [Bi₂O₂]²⁺ layers with high --Bi-O-Bi-- connectivity which results in a significant quenching of photoemission, i.e. the photoluminescence of BiOCl is quenched at temperature up to 100K.²⁴ They have not been selected for this work.
- In the most rare X3 series the stabilization of triple [M'_xX3] (M=metal) layers involves multiple non stoichiometric substitution in the [Bi₂O₂]²⁺ layers, resulting in disordered character with similar quenching effects. Hence, this series should not be of interest for their optical properties and have not been selected for this work.
- The ABiO₂Cl X1 series is more relevant due to possibilities for ordered A/Bi phases with limited Bi-O-Bi connectivity. Although not well rationalized, the symmetry and disorder in these phases depend on the relative size of Bi, A and X.

Disordered X1 phases: Typically for similar rBi³⁺ and rA²⁺ ionic radii and large X anions the phase is disordered (mixed Bi/A sites) with respect to the *I4/mmm* space group, see Table V-1 and figure V-1 a-c. It was checked during this work that PbBiO₂Br with mixed Bi³⁺/Pb²⁺ sites does not show luminescence at room temperature due to the presence of Pb²⁺ activators

leading to a too high concentration of ns^2 ions and concentration quenching. For CaBiO_2Br , temperature dependence photoluminescence measurements were performed and the radiative emission is completely quenched at temperature above 190K (the results will be presented later in this chapter). Other tetragonal phases are dark such as CaBiO_2I compound which play against the radiative emission. Moreover, CdBiO_2Br and CdBiO_2I have not, so far, been synthesized as single-phase materials using standard methods ⁶ and should not exhibit room temperature photoluminescence due to the presence of mixed sites Bi/A which enhanced the Bi-O-Bi connectivity.

Ordered X1 phases: For larger A^{2+} cations, e.g. $A=\text{Sr}^{2+}$, Ba^{2+} , the structure is fully rearranged with respect to the orthorhombic $Cmcm$ symmetry, whatever the X^- ionic radius is, Table V-1. Here the $[\text{BiAO}_2]^+$ layers consist of stripes of Bi^{3+} along the c -axis alternatively with A^{2+} stripes (figure V-1d). Each Bi^{3+} ion is connected only to two other ones by Bi-O-Bi bridges, in favor of luminescent properties as high as room temperature (figure V-1e). The iodine compounds are dark powders which play against the radiative emission so that they have not been studied here. In the layers, Bi^{3+} are eight coordinated with four short Bi-O bonds and four much longer Bi-X bonds and the Bi^{3+} lone pair points toward the $[\text{Cl}^-]$ interleave (figure V-1f).

Third polytype: Finally the third X1 subgroup deals with the calcium and cadmium bismuth oxychlorides with comparable $r_{\text{Bi}^{3+}}$ and $r_{A^{2+}}$ and relatively small X^- anions. These two compounds crystallize in the monoclinic space group $P2_1/m$ but conserved its layered topology (figure V-1g). However the Bi/A organization is such that double Bi^{3+} stripes and $\text{Cd}^{2+}/\text{Ca}^{2+}$ stripes growing along the b -axis alternate in the layers (figure V-1h). It leads to a restricted Bi-O-Bi connectivity: two Bi^{3+} neighbors connected to each Bi^{3+} position in favor of unquenched luminescence at room temperature. This time, the Bi^{3+} and A^{2+} cations have a seven coordination, four Bi(/A)-O bonds at one side and three Bi(/A)-Cl bonds at the other one, $d(\text{Bi}-\text{Cl})$ are 3.32-3.41Å for CdBiO_2Cl and 3.43-3.47Å for CaBiO_2Cl). Once again the lone pair is active toward the $[\text{Cl}^-]$ interleave (figure V-1i).

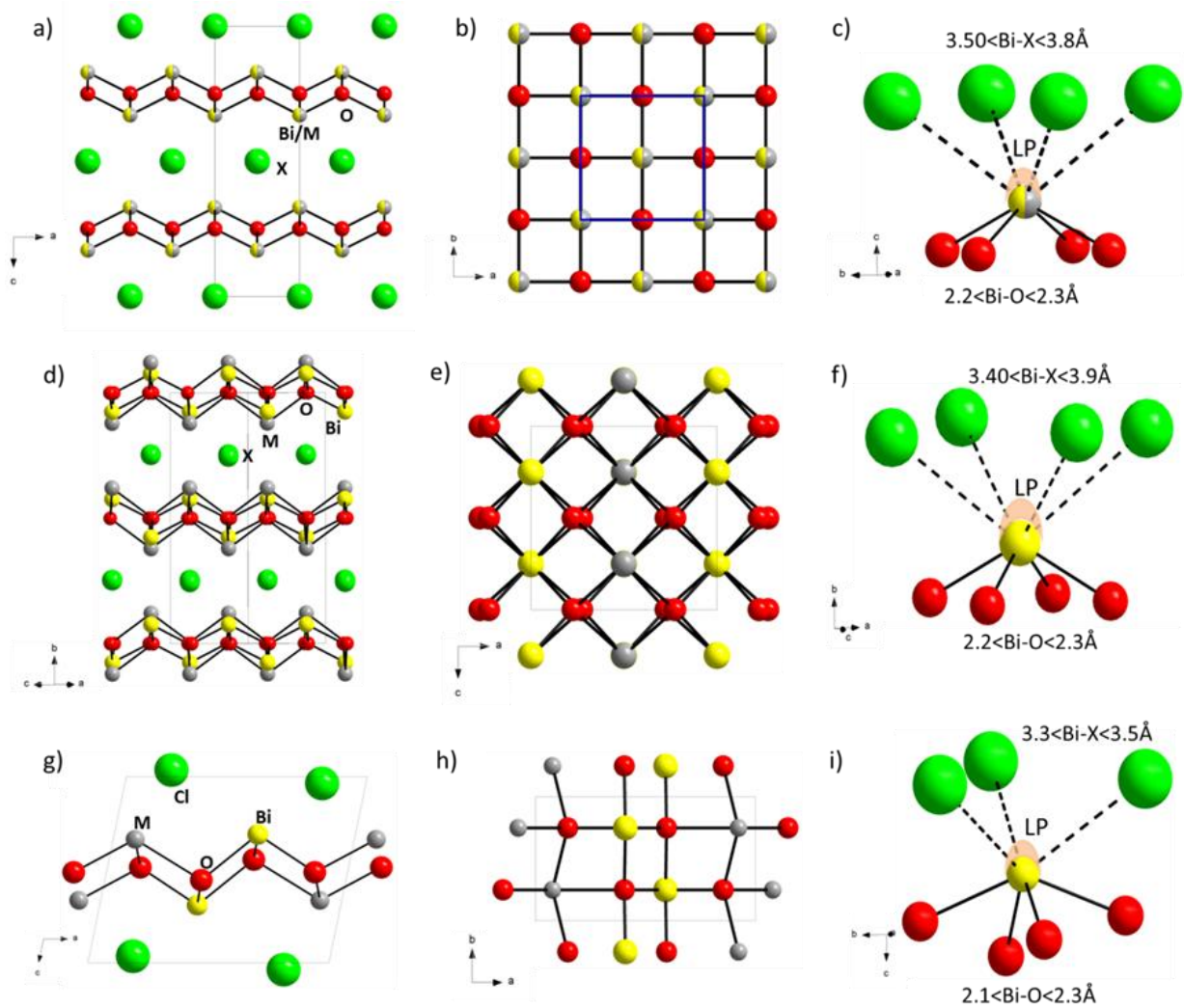


Figure V- 1 a) Structure of $ABiO_2Cl$ (S.G. $I4/mmm$) projected along the b -axis and b) projected along c -axis c) Bismuth-anion coordination and the lone pair position d) Structure of $ABiO_2X$ (S.G. $Cmc21$) and e) projected along b -axis f) Bismuth-anion coordination for $ABiO_2X$ ($M=Sr$ and Ba , $X=Cl$ or Br) and the lone pair position. g) Structure of $ABiO_2Cl$ ($A=Ca$ and Cd , S.G. $P2_1/m$) projected along the monoclinic b -axis and h) projected along c -axis i) Bismuth-anion coordination for $ABiO_2Cl$ ($A=Ca$ and Cd) and the lone pair position.

Table V-1 Reported ABiO₂X compounds where A is a divalent cation and X= Cl, Br or I. The evidence for luminescence at room temperature is mentioned.

S.G.	Samples	a (Å)	b (Å)	c (Å)	β (°)	RT lumin.
<i>I 4/mmm</i>	CaBiO ₂ Br ⁶	3,9617(5)	3,9617(5)	12,584(3)	-	no
	CaBiO ₂ I ⁶	4.01943(4)	4.01943(4)	13.2144(1)	-	no
	CdBiO ₂ Br ²¹	3,943	3,943	12,620	-	-
	CdBiO ₂ I ²⁵	3.9582(3)	3.9582(3)	13.970(2)	-	-
	PbBiO ₂ Cl ²⁶	3,9562(5)	3,9562(5)	12,629(2)	-	no
	PbBiO ₂ Br ²⁶	3.9818(4)	3.9818(4)	12.766(2)	-	no
	PbBiO ₂ I ²⁶	4.0533(4)	4.0533(4)	13.520(2)	-	no
<i>C mcm</i>	BaBiO ₂ Cl ²⁰	5.880(4)	12.945(18)	5.677(3)	-	yes
	BaBiO ₂ Br ⁶	5,968(2)	13,162(6)	5,748(2)	-	yes
	BaBiO ₂ I ⁶	6.0492(1)	14.0224(2)	5.8212(1)	-	-
	SrBiO ₂ Cl ⁴	5.7109(2)	12.4081(5)	5.5888(2)	-	yes
	SrBiO ₂ Br ⁶	5.6460(1)	12.8246(4)	5.7676(1)	-	-
	SrBiO ₂ I ⁶	5,776(3)	13,509(8)	5,863(2)	-	-
	PbBiO ₂ Cl ⁶	5.627(5)	12.425(9)	5.575(2)	-	no
<i>P 2₁/m</i>	CaBiO ₂ Cl ⁴	7,7311(1)	4,1234(1)	6,3979(2)	105,215	yes
	CdBiO ₂ Cl ⁴	7,5878(7)	4,1397(4)	6,0594(6)	101,529(1)	yes

Compounds with “-”RT luminescence could not be synthesized as pure powder during this work.

Preliminary tests: To confirm these assumptions about luminescence or not, several samples belonging to the three different subgroups have been tested to detect room temperature photoluminescence (Table V-1). As expected the five tested compounds adopting the space group “*I4/mmm*” do not show photoluminescence whereas the two other forms (*Cmcm* and *P2₁/m*) show room temperature luminescence as already reported for three of them and announced above.² (The *Cmcm* form of PbBiO₂Cl does not emit radiations at room temperature due to the too high concentration in ns² emitters).

In this chapter, the electronic structure, optical activity and photoluminescence of ordered ABiO₂Cl (A= Ca, Cd, Sr, Ba) and BaBiO₂Br phases will be discussed with respect to their respective crystal structure. Unfortunately, after many efforts, the pure powder of SrBiO₂Br could not be synthesized which explains why this compound is missing to extend this study. All Structural data used for the electronic structure calculations are listed in the Table V-2.

Table V-2. Crystal data and selected Bi-O and Bi-X bonds for the five investigated compounds.

	CdBiO ₂ Cl [4]	CaBiO ₂ Cl [4]	SrBiO ₂ Cl [4]	BaBiO ₂ Cl [20]	BaBiO ₂ Br (this work)
Crystal system	monoclinic	monoclinic	orthorhombic	orthorhombic	orthorhombic
Space group	<i>P</i> 2 ₁ / <i>m</i>	<i>P</i> 2 ₁ / <i>m</i>	<i>C mcm</i>	<i>C mcm</i>	<i>C mcm</i>
a (Å)	7,5878(7)	7,7311(1)	5.7109(2)	5.880(4)	5.9485(7)
b (Å)	4,1397(4)	4,1234(1)	12.4081(5)	12.945(18)	13.3754(15)
c (Å)	6,0594(6)	6,3979(2)	5.5888(2)	5.677(3)	5.7414(6)
β (°)	101,53(1)	105,21 (1)			
Bi-O (Å)	2.1596	2.0603	2.2117 x 4	2.1778 x 4	2.1952 x 4
Bi-O (Å)	2.2231 x 2	2.1958		-	-
Bi-O (Å)	2.2978	2.2627 x 2		-	-
Bi-O	2.2259	2.1954	2.2117	2.1778	2.1952
Bi-X (Å)	3.3201 x 2	3.4299 x 2	3.4906 x 2	3.6528 x 2	3.7388 x 2
Bi-X (Å)	3.4083	3.4700	3.5267 x 2	3.6739 x 2	3.7652 x 2
Bi-X average	3.3495	3.4433	3.5086	3.6633	3.7520
Bi-anion average (Å)	2.6690	2.7302	2.8601	2.9206	2.9736

V.1.2. Synthesis of the X1 phases

Polycrystalline powder samples of all compounds were prepared by conventional solid state reaction between BiOX (X=Cl, Br), CdO or SrCO₃ or CaCO₃ or BaCO₃ in stoichiometric amount. After grinding the reactants in a small amount of acetone, BaBiO₂Cl and CdBiO₂Cl were obtained as single phase materials after heating the mixture at 700°C during 24h in an alumina crucible. For CaBiO₂Cl, SrBiO₂Cl and BaBiO₂Br, the reaction was completed after a further annealing stage at 800°C during 48h. Several intermediate grindings were necessary to obtain single crystalline-phases. The purity of them was checked and confirmed by XRD. All the reflections of each sample could be indexed (see figure V-2a).^{4,20}

V.1.3. Crystal structure of BaBiO₂Br

Due to the absence of reported crystallographic data, the BaBiO₂Br crystal structure (S.G. *Cmcm*) was also investigated by single crystal X-ray diffraction. Only the cell parameters are mentioned in ref [6] whereas on ICSD exclusively an old CIF of BaBiO₂Br crystallizing in the *I4/mmm* space group is available. The synthesized white powder of BaBiO₂Br was then

subsequently melted at 1050°C, cooled to 600°C with a rate of 3°C/h and then to room temperature (rate = 15°C/h) in order to get single crystals. A single crystal was carefully chosen, mounted on a glass rod and collected using a Bruker Apex Duo diffractometer with a Mo-I μ S microfocus tube ($\lambda = 0.71073 \text{ \AA}$). The intensity data have been extracted from the collected frames using the program SAINT-Plus 6.02.²⁷ The lattice parameters have been defined from the complete data set. Absorption corrections have been performed using multiscan methods using SADABS.²⁸ The data collection and pertinent data of the refinements are gathered in the Annex1 part. And finally, the profile fitting refinement of powder BaBiO₂Br was achieved with FullProf²⁹ to avoid all ambiguities concerning the space group. The *Cmcm* model leads to the best fit and no impurities of a hypothetical *I4/mmm* was detected, on the opposite to the initially announced space group.³⁰ (figure V-2b)

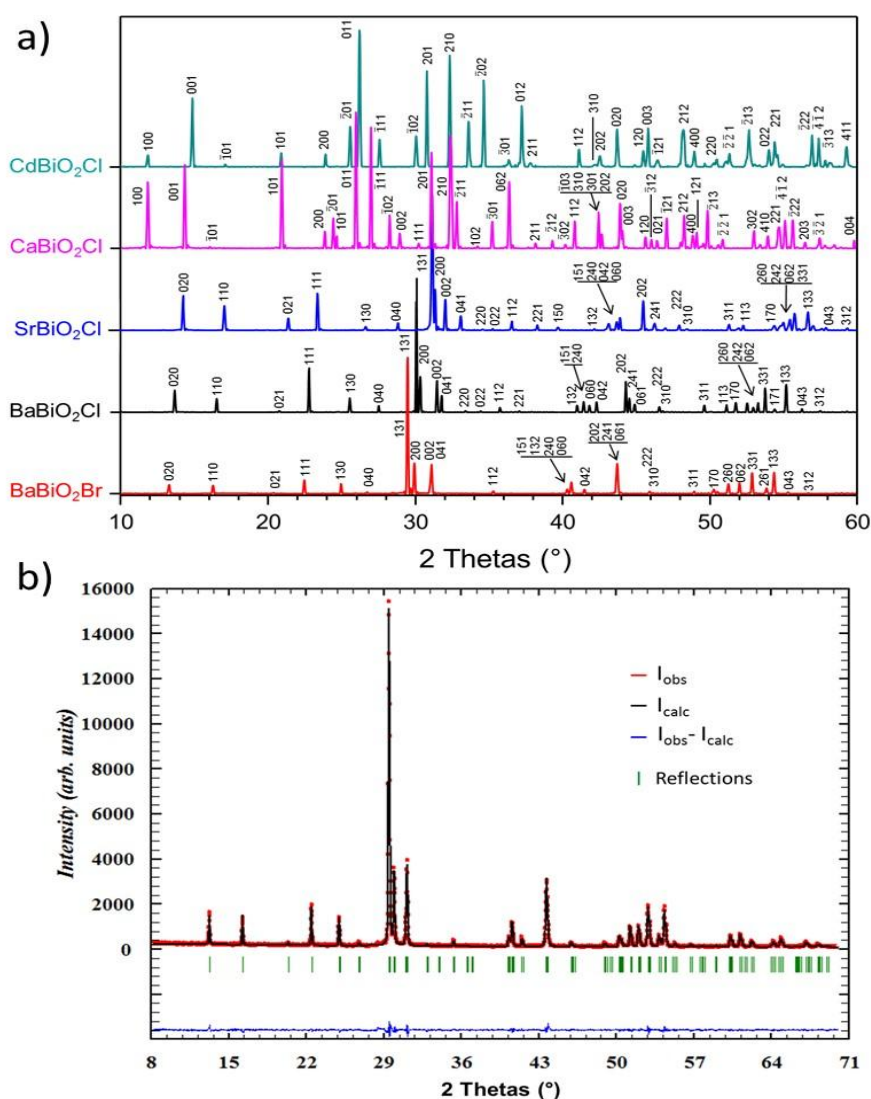


Figure V- 2 a) XRD pattern of $ABiO_2Cl$ ($A=Cd, Ca, Sr, Ba$) and $BaBiO_2Br$ with indexation of the reflections and b) Profile fitting of $BaBiO_2Br$ in the *Cmcm* S.G.

V.1.4. Electronic structures calculations of the Sillen X1 phases

Here again, density functional theory (DFT) calculations were performed using the Vienna *ab initio* simulation package (VASP).³¹ The calculations were carried out within the generalized gradient approximation (GGA) for the electron exchange and correlation corrections using the Perdew-Wang (PW91) functional and the frozen core projected wave vector method.³²⁻³³ The full geometry optimizations were carried out using a plane wave energy cutoff of 550eV and 10 *k* points in the irreducible Brillouin zone. All structural optimizations converged with residual Hellman-Feynman forces on the atoms smaller than 0.03 eV/Å and led to reasonable structures regarding the distances and the local geometries. The experimental structures match well the optimized ones, i.e. within a reasonable error expected for the GGA method (See Table V-3).

Table V-3: Comparison between experimental and calculated cell parameters for $ABiO_2Cl$ ($A=Cd, Ca, Sr, Ba$) and $BaBiO_2Br$.

Compound	Cell parameters	Experimental	Theoretical	Deviation from exp.
CdBiO ₂ Cl	<i>a</i> (Å)	7.5878(7)	7.6519	0.80%
	<i>b</i> (Å)	4.1397(4)	4.2469	2.60%
	<i>c</i> (Å)	6.0594(6)	6.3205	4.30%
	β (°)	101.53(1)	96.90	4.80%
CaBiO ₂ Cl	<i>a</i> (Å)	7.7311(3)	7.8064	1.00%
	<i>b</i> (Å)	4.1234(2)	4.1600	0.90%
	<i>c</i> (Å)	6.3979(2)	6.5102	1.80%
	β (°)	105.21(1)	104.58	0.06%
SrBiO ₂ Cl	<i>a</i> (Å)	5.7109(2)	5.7847	1.30%
	<i>b</i> (Å)	12.4081(5)	12.7007	2.40%
	<i>c</i> (Å)	5.5888(2)	5.6735	1.50%
BaBiO ₂ Cl	<i>a</i> (Å)	5.880(4)	5.9872	1.80%
	<i>b</i> (Å)	12.945(18)	13.3206	2.90%
	<i>c</i> (Å)	5.677(3)	5.7810	1.80%
BaBiO ₂ Br	<i>a</i> (Å)	5.9485(7)	6.0595	1.90%
	<i>b</i> (Å)	13.3754(15)	13.6941	2.40%
	<i>c</i> (Å)	5.7414(6)	5.8385	1.70%

The higher difference between the calculated outputs and the experimental ones concerns CdBiO₂Cl, where the β angle after relaxation decreases significantly, this change should be correlated to the increasing of the *c* cell parameter (exp: 6.0594 → calc: 6.3205Å).

The relaxed structures were used for accurate calculations of the electronic structures. For the later, a plane wave energy cutoff of 400eV, an energy convergence criterion of 10⁻⁶ eV and 20 *k* points in the irreducible Brillouin zone were used. The band diagrams calculated for all the compounds were plotted between -3 eV and 5eV and present an indirect bandgaps (see figure V-3). The all Brillouin zone was each time analyzed, whereas in order to plot continuous bands, only the longer way including the maximum of the VB and the minimum of the CB was plotted.

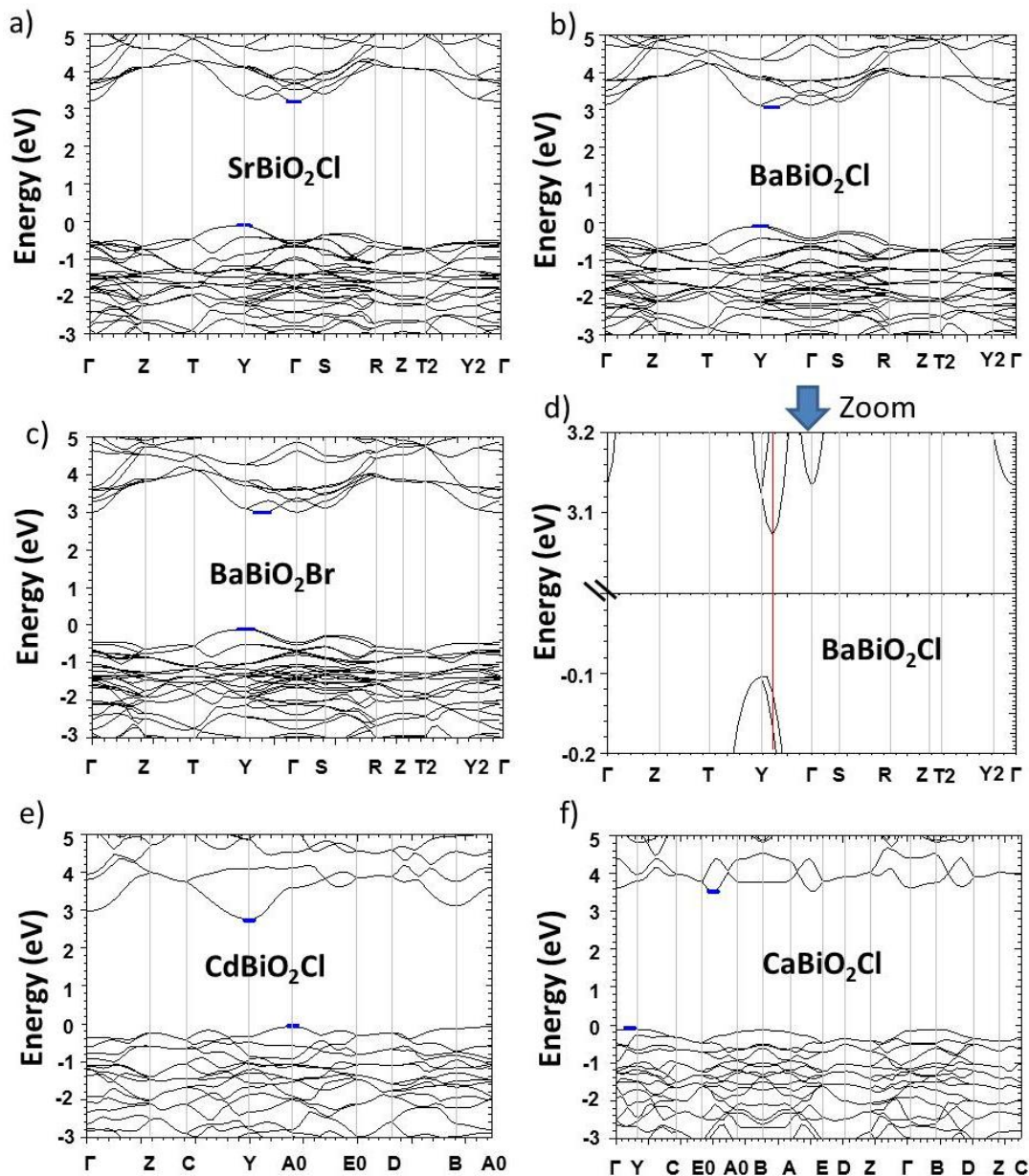


Figure V- 3 a), b), c) Band diagrams of $ABiO_2Cl$ ($A = Sr, Ba$) and $BaBiO_2Br$. d) Zoom on the bottom of the conduction band for $BaBiO_2Cl$. e) and f) Band diagrams of $ABiO_2Cl$ ($A = Cd, Ca$). The blue sticks represent the minima/maxima of the VB/CB, both bandgaps are found indirect.

For SrBiO₂Cl, a minimum indirect bandgap of 3.32eV is found between the VB at the Y point to the CB at the Gamma point, while for BaBiO₂Br, we find an indirect bandgap of 3.11eV defined between the VB at the Y point and the minimum of the CB situated in between the Y and Gamma points. Concerning the BaBiO₂Cl, the indirect character is less pronounced, nevertheless, an indirect bandgap of 3.18eV is found with the maximum of the VB situated at the Y point and the minimum of the CB in between the Y and Gamma points whereas the value of a direct bandgap between the Y points would be 3.23eV which is very close from the value of the indirect bandgap (figure V-3.d). For the monoclinic compounds, indirect bandgaps were also found with values of 3.05 and 3.52eV respectively for CdBiO₂Cl and CaBiO₂Cl. For the cadmium phosphor, the smallest gap is situated between the VB at the point A0 and the CB at Y point, when for the calcium, the maximum of the VB is found in between the Gamma and Y points and the minimum of the CB in between the E0 and A0 points.

V.1.5. UV-visible spectroscopy

The calculated gaps are in good agreement with the experimental ones deduced from the diffuse reflectance spectra (DRS) using the Kubelka-Munk (KM) representation (see figure V-4).³⁴ It is given by $F(R) = (1-R)^2/2R$, where R is the reflectance and F(R) is the Kubelka-Munk function. For bandgap determination KM function and Tauc plots were used as follows: $(F(R)h\nu)^{1/n}$ was plotted against $h\nu$, where the n value depends on the nature of the gap. For an indirect band gap $n = 2$ whereas for a direct one, $n = 1/2$. In this case all the gaps are indirect, then $n = 2$ was used. The line drawn on the linear part of $[F(R)h\nu]^{1/2}$ vs. $h\nu$ curve at $[F(R)h\nu]^{1/2} = 0$ gives the smallest bandgap. The values are reported Table V-4 and compared to the theoretical calculations.

Table V-4. Comparison of the value obtained by DFT and by UV (Kubelka-Munk).

Compound (nature of BG)	UV-KM (bandgap)	DFT bandgap	Error
CdBiO ₂ Cl (indirect)	3.05 eV	2.85 eV	6.6%
CaBiO ₂ Cl (indirect)	3.52 eV	3.59 eV	2%
SrBiO ₂ Cl (indirect)	3.53 eV	3.32 eV	5.9%
BaBiO ₂ Cl (indirect)	3.28 eV	3.18 eV	3%
BaBiO ₂ Br (indirect)	3.15 eV	3.11eV	1.3%

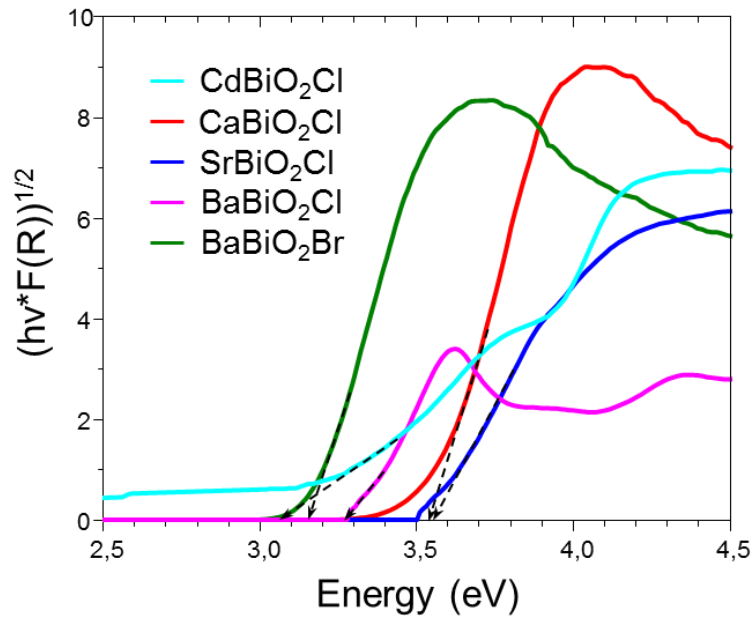


Figure V- 4 Kubelka-Munk representation of $ABiO_2Cl$ ($A=Cd, Ca, Sr, Ba$) and $BaBiO_2Br$ with extrapolation of the bandgap.

Then, it is observed that the experimental results fit well with the calculated taking account that the band gap calculated by DFT is often underestimated using GGA approximation. The error between calculated and experimental does not exceed 6.6% and belongs to the $CdBiO_2Cl$ compound. For each series of polymorphs an important variation depending on A and X elements ($\Delta U \sim 0.4eV$) is observed.

V.1.6. Topology of the Density of States (DOS)

For the DOS diagrams, a focus only on the contribution of the different elements at the top of the valence band and at the bottom of the conduction band is done and hence they are represented between -5eV and 7eV in the figure V-5 concerning orthorhombic and monoclinic phases. The DOS have been shifted to set Fermi energy to 0eV.

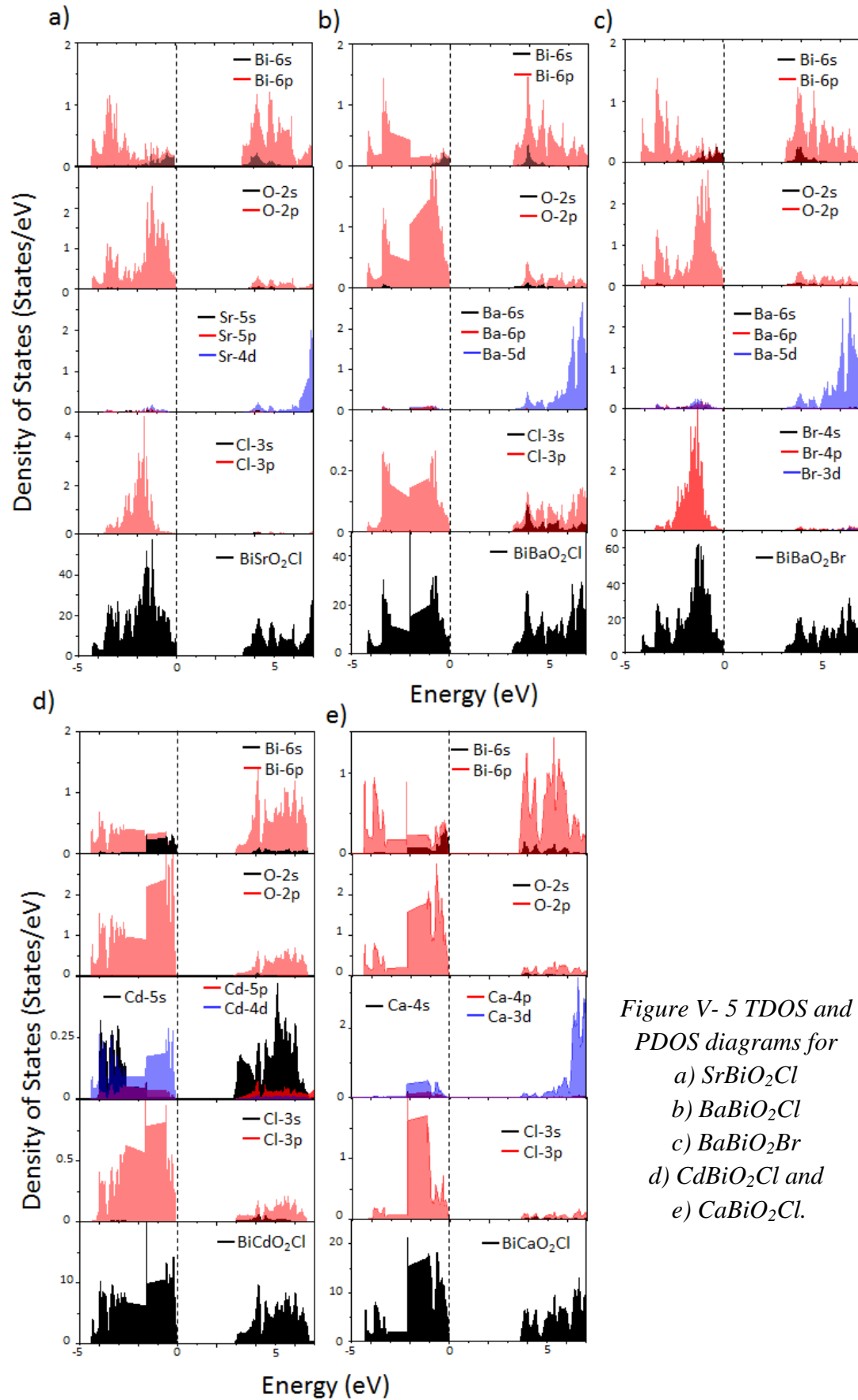


Figure V- 5 TDOS and PDOS diagrams for
 a) SrBiO_2Cl
 b) BaBiO_2Cl
 c) BaBiO_2Br
 d) CdBiO_2Cl and
 e) CaBiO_2Cl .

It is known, for post-transition lone pair metal oxides (Tl⁺, Pb²⁺, Bi³⁺)³⁵⁻³⁶ that:

- i) strong interactions between the cation s and oxygen p orbitals results in anti-bonding states with a great degree of cation s character at the top of the valence band.
- ii) the interactions between nominally empty cation p states (Bi³⁺: 6s² 6p⁰) with the antibonding orbitals result in the familiar lone pair asymmetric electron density within distorted coordination. In all the investigated compounds, this behavior is verified by the presence of mixed O 2p, Bi 6s, Bi 6p states at the Fermi level signing strong oxygen-bismuth electronic transfer and lone pair activity in valence electrons.

Orthorhombic X1 phases : For the orthorhombic phases (figure V-5a-c.) the highest VB part (for SrBiO₂Cl, BaBiO₂Cl and BaBiO₂Br respectively from -4.28, -4.20 and -4.18 to 0eV) is essentially dominated by O 2p, Cl 3p / Br 4p and Bi 6p states, and a small contribution of Bi 6s states is present just below the Fermi level. The 3s, 3p (Cl) or 4s,4p (Br) states of the halide ions show significant mixing with Bi and oxygen states which certify a certain covalency of the Bi-X bonds. On the opposite the main ionic character of the Ba²⁺ and Sr²⁺ cations is shown by their minor contribution in the valence band. The lower part of the CB is represented by Bi 6p, Bi 6s, O 2p, Sr 3d / Ba 4d as well as negligible contribution of Cl 3p / Br 4p. The Bi and O states are situated at the bottom of the CB whereas Sr/Ba states are mainly localized at higher energy

Monoclinic X1 phases: In the two monoclinic phases (figure V-5d-e), the highest part of valence band is situated between -4.45 or -4.33 and 0eV respectively for CdBiO₂Cl and CaBiO₂Cl. As for the orthorhombic phases, it is composed of O 2p, Cl 3p and Bi 6p-6s states, whereas this time the contribution of the divalent metal ion is more significant: non negligible Ca 3d states are displayed at the top of valence band for CaBiO₂Cl as well as intense Cd 4d-5s-5p contributions for CdBiO₂Cl. The Cl 3p states show a significant hybridization with Bi 6p-6s, Ca 3d and Cd 4d-5s states which shows a certain covalent character of Bi-Cl/Ca-Cl and Cd-Cl bonds. The main difference between these two compounds resides on the bottom of the valence band: for CdBiO₂Cl, Cd 5s-5p states are present as well as Bi 6s-6p, O 2p and Cl 3p states whereas for CaBiO₂Cl, only the Bi 6s-6p, O 2p and Cl 3p states are present. The Ca 3d states are mainly situated at higher energy. Then, it can be conclude that there is a significant mixing between Cd 5s-5p with O 2p while the mixing between Ca 3d and O 2p is very low. This induces a higher covalency for the Cd-O than Ca-O bonds.

V.1.7. Photoluminescence properties and correlations to the structure

V.1.7.1. Luminescence properties

All the compounds are excited in the UV range and are characterized by a broad emission band in the visible range at room temperature and they all have a large Stokes shift (between 13710 and 16330cm⁻¹) related to a strong lone pair stereo-activity (figure V-6.) whose implies a strong relaxation of the Bi³⁺ from its off-centered position toward a position closer to the center of the coordination polyhedron upon excitation which has for effect to shift horizontally (towards metal-ligand distances axis) the excited rom the ground state in the potential energy diagram (figure V-7a). The maxima of excitation and emission bands as well as the coordinates representing their emission color on the chromaticity diagram (CIE 1931) are listed Table V-5 as well as the beginning energy of excitation band. The two Ba phosphors emit a greenish-white emission, the Cd and Sr compounds exhibit more a bluish luminescence whereas the Ca one a cyan-white light (Figure V-7b). The emission bands for the entire compounds are broad band typical for a ns² ion and can be attributed to the ³P₁ → ¹S₀ Bi³⁺ transition whereas the excitation is attributed to the A-band (¹S₀ → ³P₁).

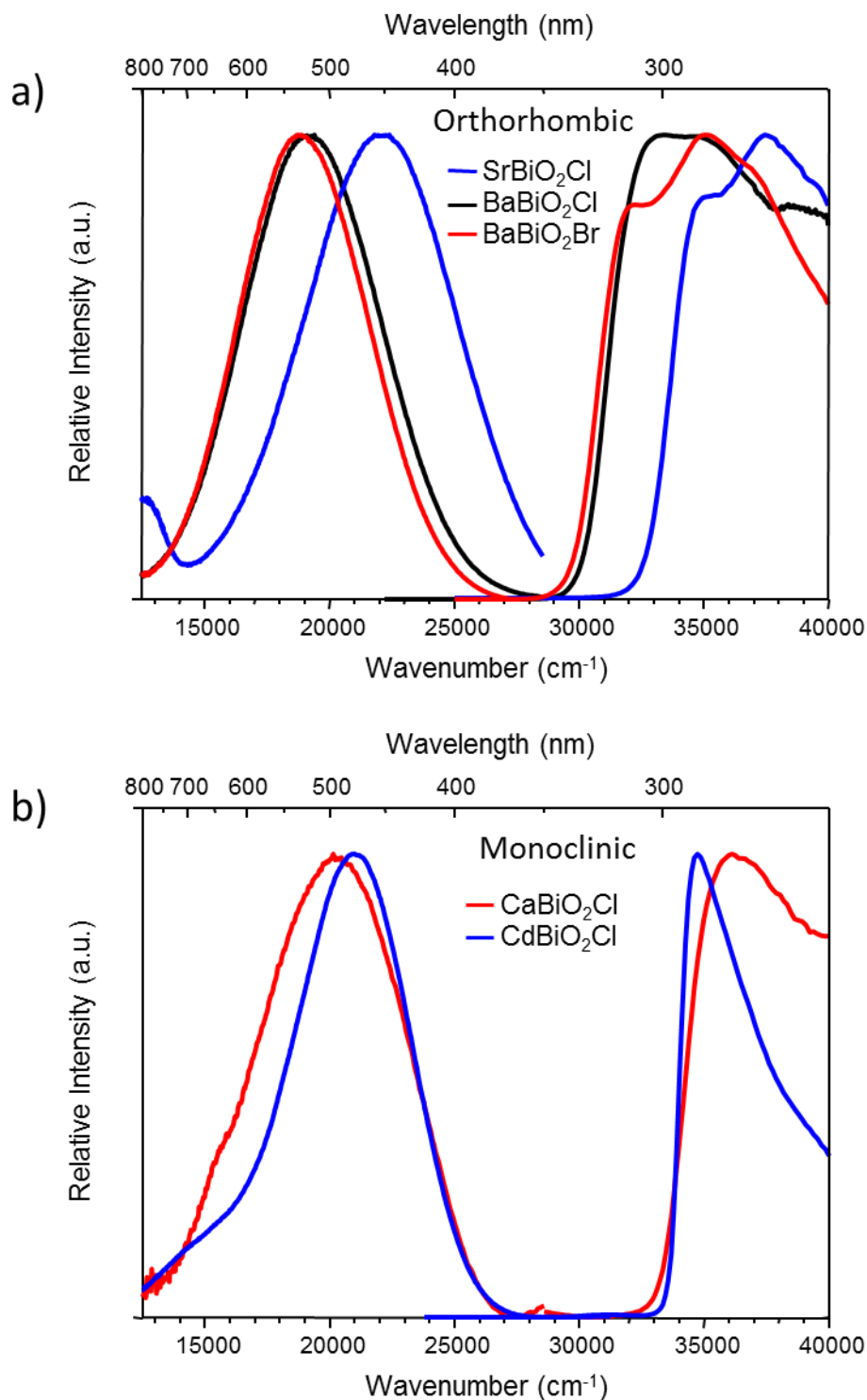


Figure V- 6 a) Room temperature photoluminescence spectra of $ABiO_2X$ ($A=Sr, Ba$ and $X=Cl, Br$), for $BaBiO_2Br$ $\lambda_{ex}=285nm$ and $\lambda_{em}=535nm$, $BaBiO_2Cl$ $\lambda_{ex}=299nm$ and $\lambda_{em}=515nm$, $SrBiO_2Cl$ $\lambda_{ex}=267nm$ and $\lambda_{em}=458nm$ b) room temperature photoluminescence spectra of $ABiO_2Cl$ ($A=Ca, Cd$) for $CdBiO_2Cl$ $\lambda_{ex}=288nm$ and $\lambda_{em}=476nm$, $CaBiO_2Cl$ $\lambda_{ex}=277nm$ and $\lambda_{em}=497nm$. The emission spectra are measured exciting at the maxima of corresponding excitation bands and vice versa.

Table V-5. Optical data for ABiO₂Cl (A= Ca, Cd, Ba, Sr) and BaBiO₂Br.

	CdBiO ₂ Cl	CaBiO ₂ Cl	SrBiO ₂ Cl	BaBiO ₂ Cl	BaBiO ₂ Br
DOS s ² →sp	4.10 eV	3.98 eV	4.12 eV	3.86 eV	3.76 eV
Transition	33070 cm ⁻¹	32100 cm ⁻¹	33230 cm ⁻¹	31130 cm ⁻¹	30320 cm ⁻¹
Max excitation	34720 cm ⁻¹ (4.30 eV)	36100 cm ⁻¹ (4.48 eV)	37450 cm ⁻¹ (4.64 eV)	33450 cm ⁻¹ (4.15 eV)	35090 cm ⁻¹ (4.35 eV)
Ref [8]	-	-	35710 cm ⁻¹ (4.43 eV)	33330 cm ⁻¹ (4.13 eV)	32787 cm ⁻¹ (4.07 eV)
Begin excitation	33000 cm ⁻¹ (4.09 eV)	32100 cm ⁻¹ (3.98 eV)	30870 cm ⁻¹ (3.87 eV)	28900 cm ⁻¹ (3.58 eV)	28300 cm ⁻¹ (3.51 eV)
Max emission/	21010 cm ⁻¹ (2.60 eV)	20120 cm ⁻¹ (2.50 eV)	21840 cm ⁻¹ (2.71 eV)	19420 cm ⁻¹ (2.41 eV)	18760 cm ⁻¹ (2.33 eV)
Ref [8]	-	-	23260 cm ⁻¹ (2.88 eV)	20410 cm ⁻¹ (2.53 eV)	20000 cm ⁻¹ (2.48 eV)
Stokes shift/	13710 cm ⁻¹ (1.70 eV)	15980 cm ⁻¹ (1.98 eV)	15610 cm ⁻¹ (1.94 eV)	14030 cm ⁻¹ (1.74 eV)	16330 cm ⁻¹ (2.02 eV)
Ref [8]	-	-	12450 cm ⁻¹ (1.54 eV)	12920 cm ⁻¹ (1.60 eV)	12790 cm ⁻¹ (1.59 eV)
Ionic radii M ²⁺	1.03 (7)	1.06 (7)	1.26 (8)	1.42 (8)	1.42 (8)
PP of M ²⁺	1.94	1.89	1.59	1.41	1.41
CIE coordinates (x / y)	0.2192/ 0.2705	0.2672/ 0.3222	0.2026/ 0.2231	0.2904/ 0.3786	0.3076/ 0.4320

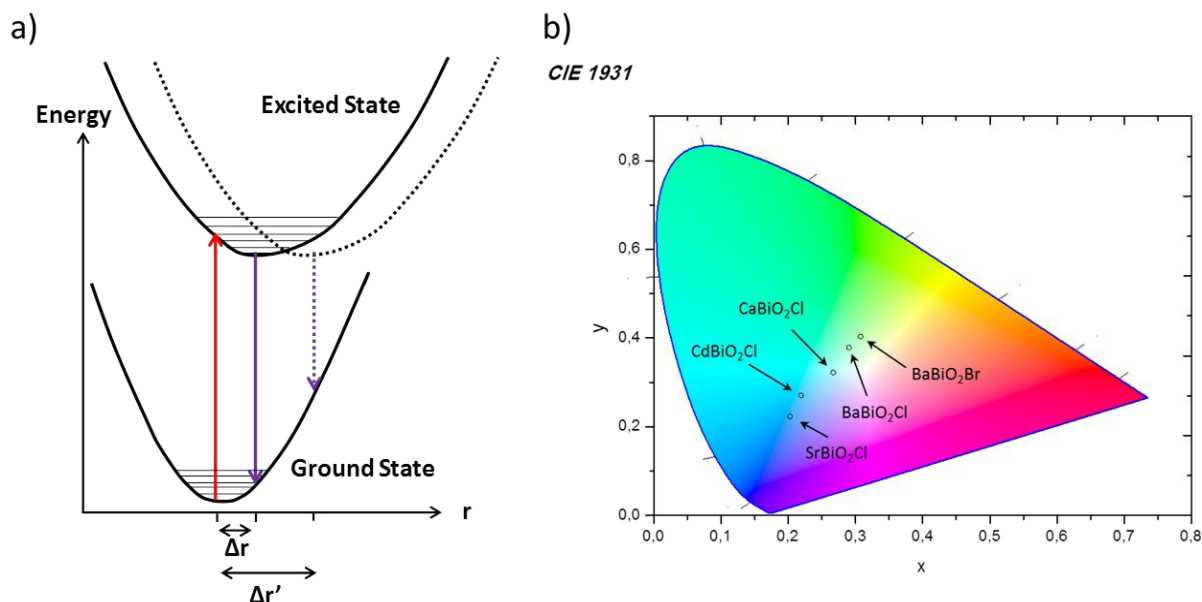


Figure V- 7 Diagram showing the effect of stereo-active lone pair of electrons: a low stereo-activity faintly shifts the excited state $\Delta r \rightarrow$ small Stokes shift (full line). A high stereo-activity induces a larger shift $\Delta r' \rightarrow$ bigger Stokes shift (dashed line). b) Representation of color emission of all the ABiO₂X compounds in the CIE 1931 diagram.

V.1.7.2. Differences with previous works

Compared to the luminescence energies reported by Porter-Chapman *et al.*² for the orthorhombic phases (BaBiO₂Br, BaBiO₂Cl and SrBiO₂Cl), it is found slightly different results in this work, see Table V-5. In this study the emission maxima are systematically red shifted compared to the previous report except for BaBiO₂Cl for which the excitation maximum is blue shifted which enhances a higher Stokes shift. This difference is hard to explain in other way that the type of diffractometer used for the measurement and the spectral corrections. Even taking into account possible particle size differences between both sets of samples, the expected shift should be reduced (2-3nm maximum). For the three orthorhombic compounds the excitation bands clearly show two split maxima whereas it was not mentioned / the case in the previous work.² It is very uncommon to find an experimental doublet structure for the A-band, nevertheless it is theoretically the case.³⁷ In fact, it results from a splitting of the excited state due to the interaction with lattice vibrations (dynamical Jahn-Teller effect).³⁸⁻³⁹ This effect seems to be more pronounced in alkaline earth halide hosts and has no consequences on the emission: exciting at wavelength of one or the other of the maximum of the doublet gives the same emission band.³⁷

V.1.7.3. Excitation energy

The Bi³⁺ excitation strongly depends on the nephelauxetic effect,⁴⁰ generally understood as the decrease of interelectronic repulsion parameters of Bi³⁺ valence electrons due to Bi-anion covalency in comparison with their free-ion value. The increase of this effect leads to a red spectral shift of the excitation transitions. In series of Sillen X1 phases, this effect can be intuitively rationalized using the electronegativity or the polarizing power of the A cation (Bi-O-A next nearest neighbor) or X halide (Bi-X), already discussed in the Chapter III. The two A and X effects can be independently probed.

Influence of the X halide nature

The comparison between the photoexcitation of BaBiO₂Cl (edge at 28900cm⁻¹) and BaBiO₂Br (edge at 28300cm⁻¹) can be used as a direct probe of the X influence, and was already discussed in ref.[2] on the basis of the Stoke shifts, though the slightly different results mentioned above. Inspection of the DOS validates the mixing of bismuth and halide states, within a certain degree of covalency. Still concerning the excitation process, the closest Bi/Br electronegativity favors a slightly less ionic character of the bond compared to Bi-Cl

bonds, see figure V-8b. It involves the experimentally verified redshift (Figure V-6a). However this effect is very weak ($\Delta E_{\text{ex}} = 600\text{cm}^{-1}$) but remains respected in the excitation spectra.

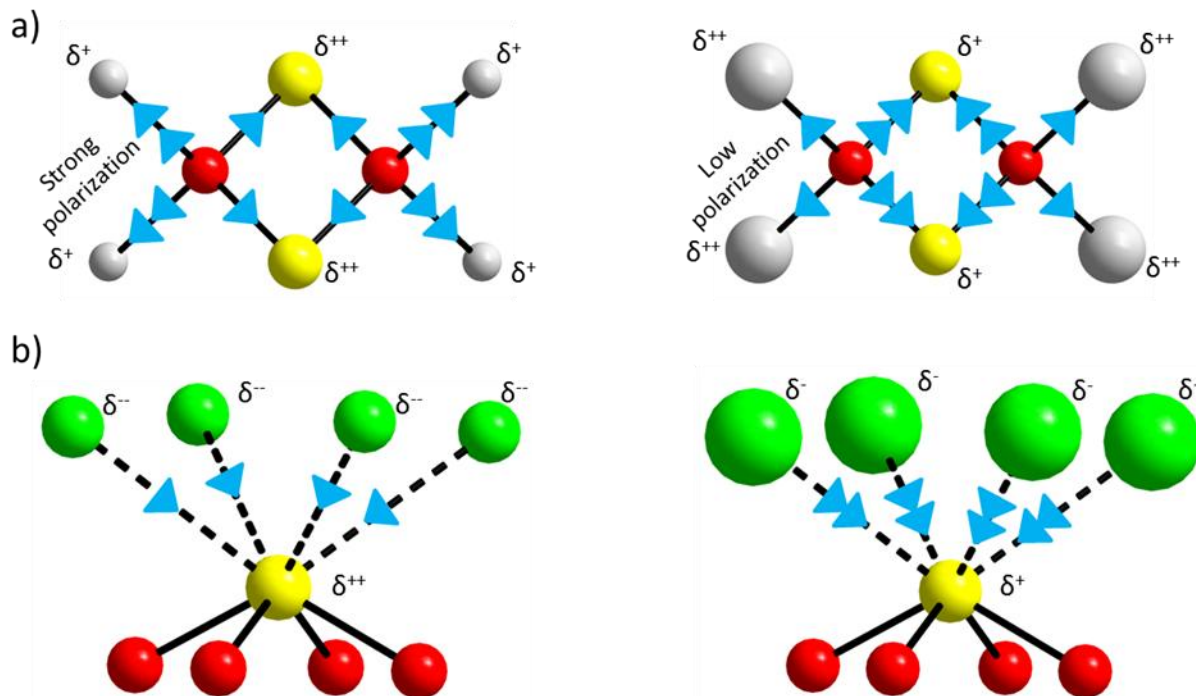


Figure V- 8 . Sketch of the influence of the nature of a) the cation b) the halide. A small cation will strongly polarize the A-O bond and by inductive effect the Bi-O covalency will be lowered. A bigger halide will be more polarized by the Bi and the covalency of Bi-X bond which involves a stronger covalent character.

Influence of A²⁺ on the excitation edge

Here taking into account cations A²⁺ with strong electronegativity differences compared to oxygen, it is rather difficult to reason in terms of degree of bond covalence. However, it was shown for BiM₂PO₆ (M = Mg, Zn, Cd) series of compounds with similar Bi³⁺-O-M²⁺ bridges (Chapter III, section 3.3.1.4), but in 1D oxo-centered units instead of 2D sheets in X1 Sillen phases, that increasing the M²⁺ polarizing power (expressed as z/r, Mg>Zn>Cd) induces a more polarized M-O bond which decreases the oxygen electronegativity,⁴¹ and decreases the next Bi³⁺-O covalency by inductive effect, such that the excitation of the cadmium compound is redshifted by “indirect” nephelauxetic effect (see figure V-8a.).

The inspection of the results on Sillen X1 SrBiO₂Cl and BaBiO₂X (X=Cl, Br) is relevant and shows a similar behavior. Following the ionic radii, the low Ba²⁺ polarizing power increases

the Bi-O covalency, leading to an important redshift by $\Delta E_x \sim 2000\text{cm}^{-1}$ compared to the SrBiO₂Cl compound. Once more although, different spectral behaviors and values, similar tendencies have been observed in ref [2]. However dealing with large and poorly electronegative Ba²⁺ and Sr²⁺ cations, the contrasted A-O bond nature cannot be detected in the DOS (figure V-5) which highlights their main ionic character with no significant mixing between O and A states. Contrarily hierarchical overlapping between M p,d valence states and O 2p states (Mg > Zn > Cd) was evidenced after fine examination of the BiM₂PO₆ DOS.

Concerning the monoclinic phases, CdBiO₂Cl and CaBiO₂Cl show very closed excitation edges and the excitation process starts at lower energy for the calcium compound (32100cm^{-1} against 33000cm^{-1}) even though its maximum is slightly blue shifted. Here again the polarizing power calculated for Cd²⁺ (1.94) and Ca²⁺ (1.89) plays in favor of a stronger nephelauxetic effect for Bi³⁺ in the calcium compound, which fits with the difference in the starting excitation energy.

V.1.7.4. Excitation vs. bandgap

One common and particular feature of these series of phases is highlighted in the figure V-9 which shows that the value of bandgaps from reflectivity measurements (and from DFT calculations) are much lower in energy than the excitation processes. This point was already observed and discussed in the Chapter III for the BiM₂PO₆ (M=Mg, Zn, Cd) phases. This particularity is strongly pronounced in the monoclinic series of oxychlorides with maximum of excitation above the bandgap by $\sim 1\text{eV}$ for CaBiO₂Cl. i) the lowest energetic Bi³⁺ transition $^1S_0 \rightarrow ^3P_1$ is forbidden and hence, not observed in the excitation spectrum and ii) the shift of the excited states along M-ligand axis compared to ground state also shifts the excitation to higher energy. Once again, dealing with $s^2 \rightarrow sp$ transitions, it makes sense to consider transitions from the Fermi level (with strong Bi 6s contribution) to empty Bi 6s-6p mixed states in the conduction band. From the DOS, these “ideal” excitation energies match rather well the experimental values, table V-5. Finally, similar features have been observed in the BiM₂XO₆ series (Chapter III). It suggests that the Bi³⁺ luminescence involves specific energetic states independent of the main band topology. It may be preferred in indirect gap situations, which is a common parameter to BiM₂XO₆ and ABiO₂X phases studied so far.

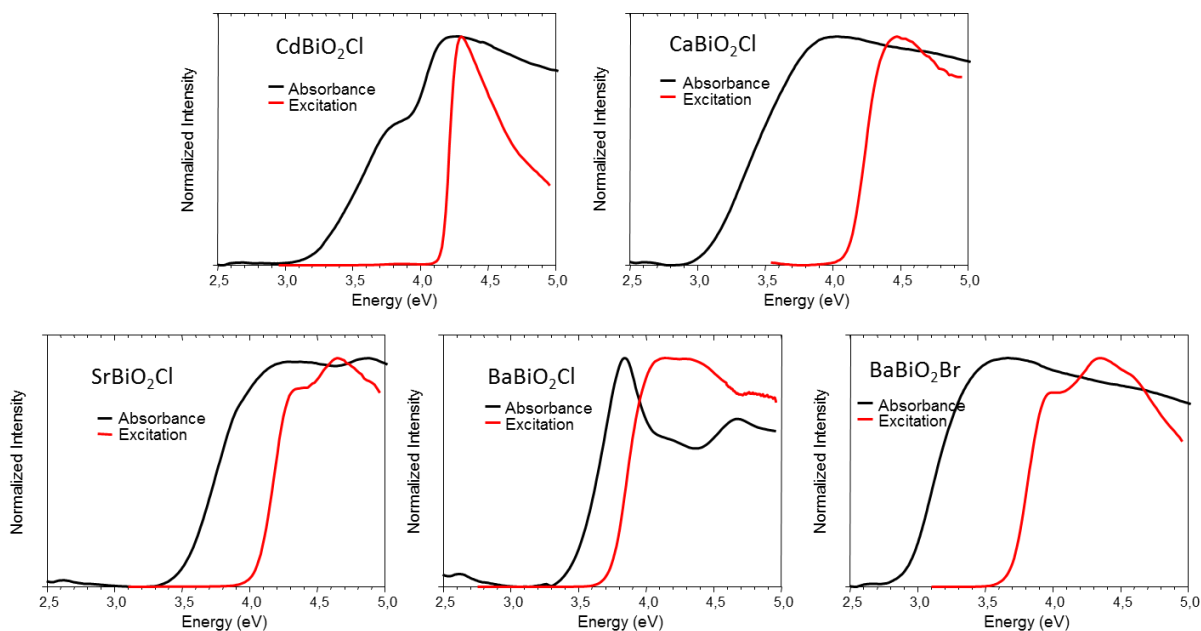


Figure V- 9 Comparison between the absorption and excitation spectra of the five studied compounds.

V.1.8. Emission and lone pair stereo-activity

Emission spectra for all phosphors are situated in a large spectral range of the visible spectrum, even though their comparison should be performed for similar Bi³⁺ point symmetries and coordinations which is not the case between the two polymorphic forms (C_{2v} for orthorhombic and C_s for monoclinic compounds) (see figure V-1).

Monoclinic form: Focusing on the monoclinic series (CaBiO₂Cl and CdBiO₂Cl) the rationalization can be done following the evolution of the *c* cell parameter. As discussed in the BiM₂XO₆ series, chapter III, the lone pair stereo-active effect takes place perpendicularly to the [BiAO₂]⁺ layers, toward the halide ligands, i.e. along the *c* axis. In a rough approximation, increasing the *c* parameter leads to intensify the lone pair stereo-activity (more important structural reorganization after excitation) and to shift the emission toward lower energies (higher Stokes shift). The higher Stokes shift (SS) and lower energy emission for CaBiO₂Cl (SS: 15980cm⁻¹, max emission: 20120 cm⁻¹) compared to CdBiO₂Cl (SS: 13710cm⁻¹, max emission: 21010cm⁻¹) fits well with crystallographic data: for CdBiO₂Cl d(Bi-Cl) are 3.32-3.41Å (cell parameter *c* = 6.06Å) and 3.43-3.47Å for CaBiO₂Cl (cell parameter *c* = 6.40Å). In other words, the higher lone pair stereo-activity, the higher is the Stokes shift.

Orthorhombic form: For the other series SrBiO₂Cl, BaBiO₂Cl and BaBiO₂Br, even though the emission red shift could be rationalized in the same way, following the evolution of the *b* cell parameter this time (lone pair stereo-active along *b*), it will have no sense regarding the pronounced difference of ionic radius between Br⁻ (1.96Å) and Cl⁻(1.81Å) or between Sr²⁺ (1.18Å) and Ba²⁺ (1.42Å) compared to similar Cd²⁺ (1.03Å) and Ca²⁺ (1.06Å) mainly responsible for lattice contraction. Then the evolution of the LP activity is far from obvious, and all one can say is that the Stokes shift is very large and similar (14030cm⁻¹, 15610cm⁻¹ and 16330cm⁻¹ respectively for BaBiO₂Cl, SrBiO₂Cl and BaBiO₂Br) which means that the emission occurs with similar process starting from the excited states. Moreover, with the multiplet character of the excitation bands the rationalization on the Stokes shift could be misrepresented.

V.1.9. Photoluminescence of a disordered X1 phase: CaBiO₂Br

After studying the luminescence of ordered Sillen X1 compounds, optical properties of CaBiO₂Br,⁶ a disordered tetragonal X1 type Sillen will be presented here. This time the crystal structure shows mixed Bi/Ca sites which, depending on cationic distribution can extend locally the -Bi-O-Bi- connectivity or shortcut it by Ca-O-Bi bridges. In the former case, the thermal quenching is expected to turn into a critical situation (Figure V-10).

V.1.9.1. Synthesis of CaBiO₂Br

CaBiO₂Br was obtained as a single polycrystalline phase from the stoichiometric mixture of BiBr₃, Bi₂O₃ and CaO. First of all, CaO was obtained by calcination of CaCO₃ at 1000°C during 24h. Then, the mixture was heated at 750°C in a gold tube placed in a quartz ampoule sealed under vacuum for 4 days. A gold tube was used in order to avoid all reaction between the Ca and the quartz. The XRD analysis confirms the purity of the sample, all the reflections can be indexed to the calculated pattern.⁶ (Figure V-10b, the low intense broad peak at 12° 2θ corresponds to the grease used to glue the sample on the transparent film).

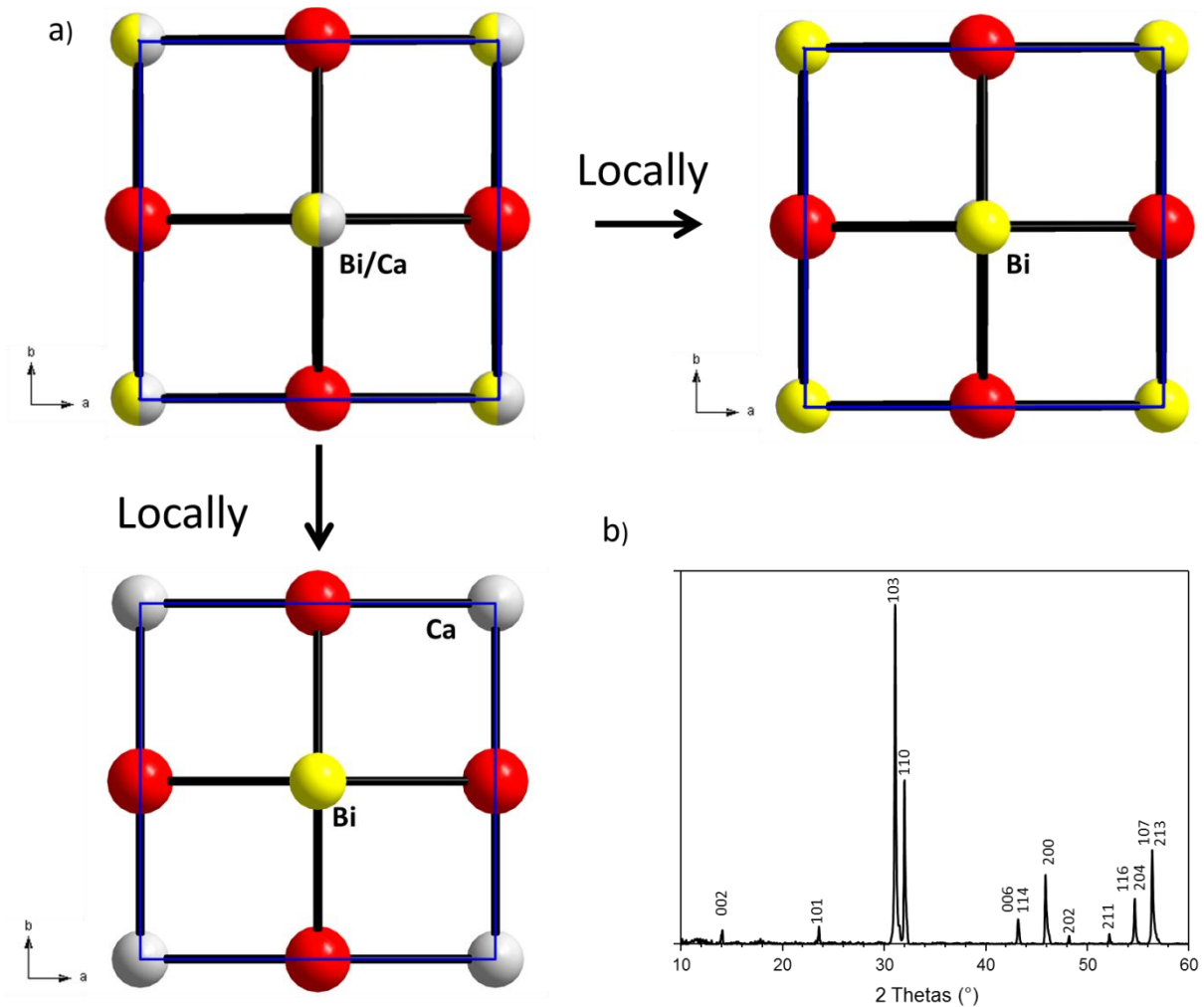


Figure V- 10 a) Example of variable Bi-O-Bi connectivity in CaBiO₂Br due to Bi/Ca mixed sites b) XRD pattern of CaBiO₂Br with full pattern indexation.

V.1.9.2. Low temperature photoluminescence

The luminescence (excitation / emission) of CaBiO₂Br is difficult to compare with the other Sillen seen previously for several reasons:

- i) locally, the Bi have different chemical environments on its first cationic coordination sphere (e.g. only Bi or only Ca) which changes locally the nephelauxetic effect and then the energy position of the excitation band
- ii) the different space group causes a changing of the Bi site symmetry (C_{4v} for CaBiO₂Br, compared to C_{2v} and C_s respectively for the orthorhombic and monoclinic compounds) which strongly influences the emission energy position. Furthermore the local coordination locally lowers the site symmetry.

Optical properties of Bi³⁺ oxyhalides compounds

As expected due to its disordered crystal structure, CaBiO₂Br is not luminescent at room temperature but exhibits a greenish photoluminescence below 190K ($x=0.3348$ and $y=0.4302$ are the coordinates for the CIE 1931 diagram at 10K, see figure V-11). The excitation, situated in the UV range, is represented by a broad band starting between ~ 24000 and 26000cm^{-1} depending on the temperature, and exhibiting a maximum at $\sim 30500\text{cm}^{-1}$. The excitation maximum remains nearly unchanged within the temperature range 10-190K (only a very slight blue shift for 160K and 190K can be numerically observed) whereas its intensity strongly decreases upon heating. The same behavior is observed for the emission band, its maximum persists at $\sim 18700\text{cm}^{-1}$ even if the broad band covers almost the whole visible range and its intensity decreases with increasing temperature (figure V-12).

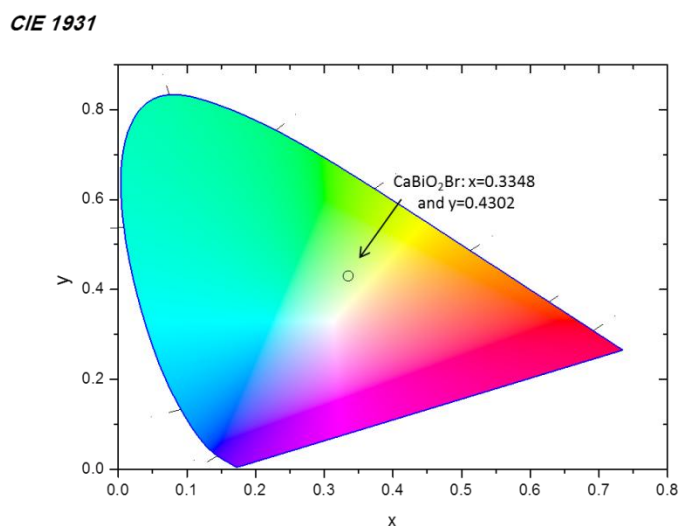


Figure V- 11. Representation of the chromaticity emission at 10K of CaBiO₂Br in the CIE 1931 diagram.

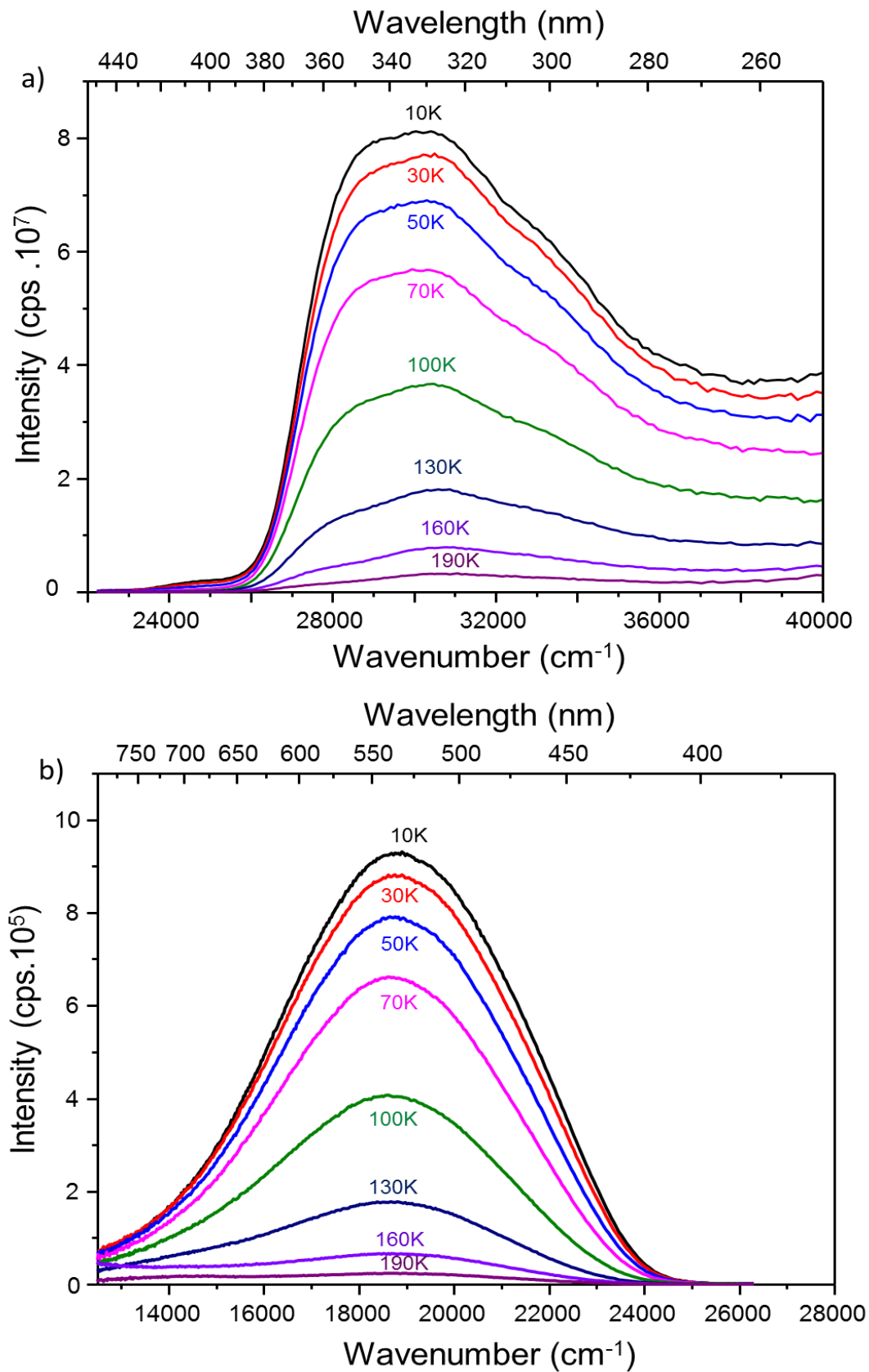


Figure V- 12 Temperature dependence photoluminescence of CaBiO₂Br a) Representation of excitation bands and b) the emission bands.

The excitation bands can be assigned to the Bi³⁺: ¹S₀ → ³P₁ transition as for the other Sillen phases seen previously whereas the emission corresponds to the Bi³⁺: ³P_{1,0} → ¹S₀ transitions. Both the absence of any red shift of the emission on decreasing the temperature and the double exponential lifetime behavior fitted at 10K (see figure V-13.) suggest that already at 190K the ³P₀ → ¹S₀ forbidden transition is observed and a thermal equilibrium between the occupancies of the ³P₁ and ³P₀ states is reached.

At 10K the decay curve ($\lambda_{ex}=330\text{nm}$ and $\lambda_{em}=552\text{nm}$) of CaBiO₂Br was fitted using a double exponential behavior, $I = I_0 + A1*\exp(-t/ \tau_1) + A2*\exp(-t/ \tau_2)$, resulting into two different lifetimes: $\tau_1=99\mu\text{s}$, $\tau_2=1.13\text{ms}$ (see figure V-13). These two lifetimes τ_1 and τ_2 can be attributed respectively to ³P₁ → ¹S₀ (τ_1) and ³P₀ → ¹S₀ (τ_2) transitions. Compared to these found for BiMg₂PO₆ ($\tau_1=37\mu\text{s}$, $\tau_2=0.29\text{ms}$), even if they are higher, they remain in the same order of magnitude.

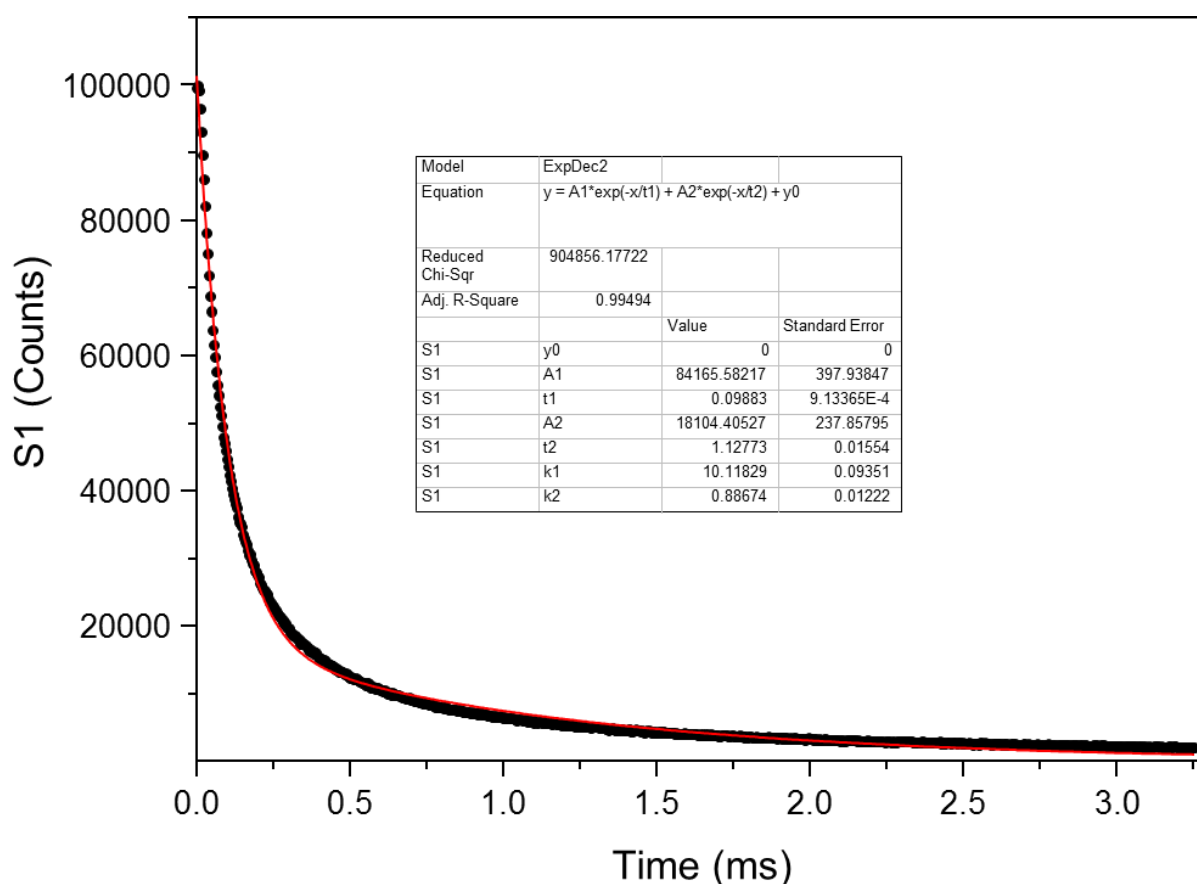


Figure V- 13 Decay time measurement of CaBiO₂Br at 10K ($\lambda_{ex}=330\text{nm}$ and $\lambda_{em}= 552\text{nm}$), the decay curve is fitted with a double exponential behavior ($R^2=0.995$) and gives $\tau_1= 0.099\text{ ms}$ and $\tau_2= 1.128\text{ms}$.

V.1.10. Summary

The X1 Sillen series with formula ABiO₂X is composed of three main crystallographic types, namely the tetragonal form (S.G. *I4/mmm*), the orthorhombic form (S.G. *Cmcm*) and monoclinic form (S.G. *P2₁/m*). Only the two latter show fully ordered Bi/A topologies with a limited Bi-O-Bi connectivity, favorable for unquenched photoluminescence at room temperature. Through this work, it was checked that the monoclinic CdBiO₂Cl, CaBiO₂Cl and orthorhombic SrBiO₂Cl, BaBiO₂Cl and BaBiO₂Br show a bright luminescence at room temperature due to Bi³⁺ activators whereas the photoluminescence of CaBiO₂Br (S.G. *I4/mmm*) is completely quenched at temperature higher than 190K .

The influence of the chemical nature of X on the excitation band energy position is very weak, only a slight redshift is observed for the BaBiO₂Br compared to BaBiO₂Cl. On the other hand, the tuning of the excitation by playing on the chemical nature of A²⁺ via the A-O-Bi bonding scheme is much significant. The shift of the emitting radiation, from bluish to greenish-white color show sizeable properties in possible relation with the degree of lone pair stereo-activity. However, it is clear that the very broad emission band do not highlight lightening application potentialities in these series of compounds.

Specific electronic features already pointed out for BiM₂XO₆ phases are observed here again. It concerns the excitation energy above the bandgap but giving rise to radiative emission. The lowest energetic Bi³⁺ transition ¹S₀ → ³P₁ is forbidden and hence, not observed for the excitation process and the shift of excited states along M-ligand axis compared to ground state has also be considered to explain this phenomena. This specific feature seems related to the 6s² → 6s6p excitation process and may be favored by indirect bandgaps observed for the five studied samples.

V.2. Investigation of other 2D Bi oxychlorides; the BiA₃O₃Cl₃ (A=Sr, Ba) case

These two phases present other 2D topologies of Bi-based phases but this time with a much more Bi³⁺ dilute character since in the layer the Bi/A ratio is equal to 1/3 (ratio of 1 in Sillen X1 phases). Therefore it deserves a strong interest for enhanced luminescence with poor expected quenching, due to the absence of any Bi-O-Bi contacts.

V.2.1. Synthesis

BiSr₃O₃Cl₃ and BiBa₃O₃Cl₃ were synthesized as single polycrystalline phases from the stoichiometric mixture of BiCl₃, BaO and SrO. BaO and SrO were obtained by calcination of respectively BaCO₃ and SrCO₃ at 1400°C during 24h. Then, according to the publication⁴³ the mixtures were preheated in alumina crucibles at 220°C during 4h (below the melting point of BiCl₃), then at 400°C during 4h (below the boiling point of BiCl₃), another 4h at 600°C and finally at 800°C during 12h. The XRD analyses confirm the purity of the sample.⁴²⁻⁴³ (figure V-14).

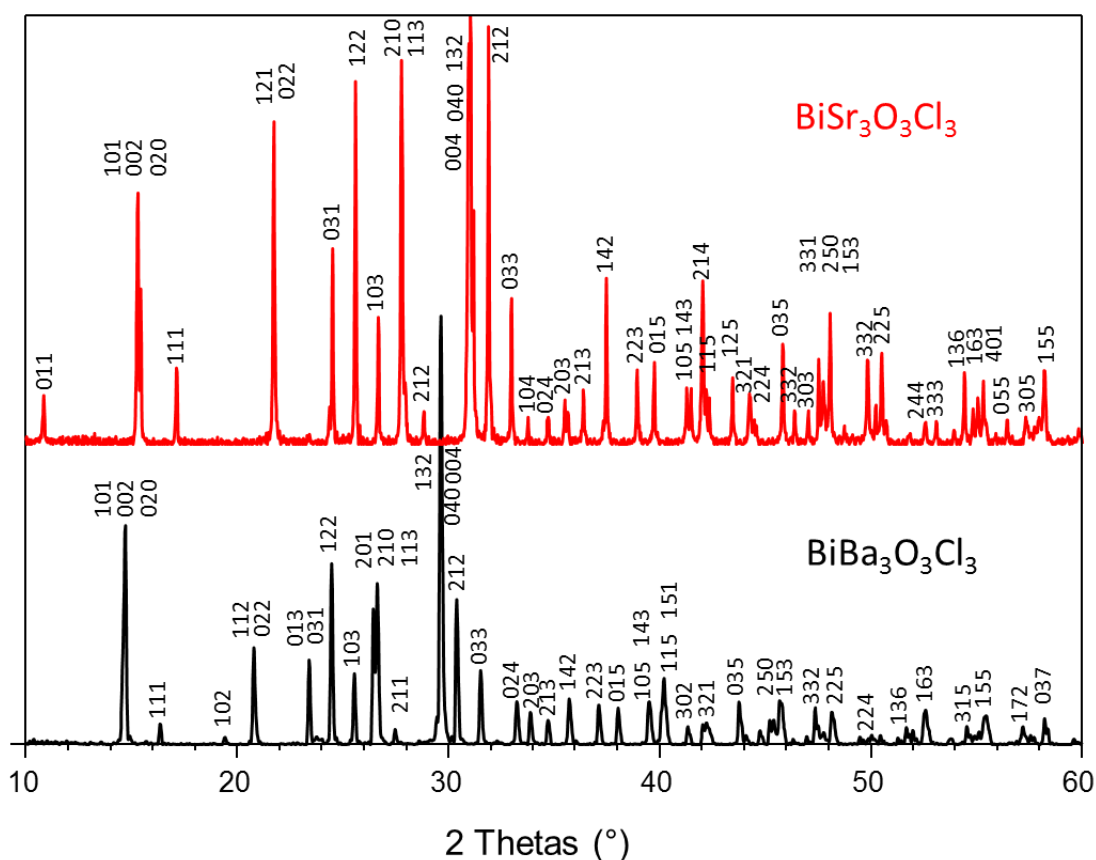


Figure V- 14 XRD pattern of BiA₃O₃Cl₃ (A=Ba, Sr) with reflections indexation from the calculated pattern.

V.2.2. Structural description of isostructural BiSr₃O₃Cl₃ and BiBa₃O₃Cl₃

Both compounds crystallized in the *Pnma* space group and are isostructural (see table V-6), however their crystal structures differ a lot from the Sillen phases investigated previously. In the original report⁴³ BiSr₃O₃Cl₃ as well as BiBa₃O₃Cl₃ were described as the stacking of

layers perpendicular to the *b* axis arranged in sequence /Cl/Sr(Ba)-O/Bi-Sr(Ba)-O-Cl/SrO/Cl/.

These two compounds can also be described using an oxo-centered approach as presented Chapter III but they have a very different topology compared to all the phases investigated until now. Here oxo-centered O(Sr₃Bi) tetrahedral form thick chains containing edge sharing trimers, interconnected by extra common edges. The chains running along the *b*-axis are interconnected by corner sharing into 2d layers in the (*a*,*b*) plane. These chains are separated by Cl⁻ anions (see figure V-15a-b). The Bi³⁺ cation has a low and unusual coordination, it is connected to three oxygens within very short bond lengths (2.02-2.07 Å / 2.06-2.07 Å respectively for BiBa₃O₃Cl₃ and BiSr₃O₃Cl₃) on one side and to two chlorides (Bi-Cl= 3.61 / 3.47 Å respectively for BiBa₃O₃Cl₃ and BiSr₃O₃Cl₃) (see figure V-15d). The bond valence calculated on Bi³⁺ ions give 2.74 and 2.69 respectively for Ba and Sr compounds. This coordination suggests a very strong stereo-activity of the lone pair of electrons. In addition to the Bi...Cl bridges which stabilize the inter-layer bonding, the electrostatic interactions between positive Bi³⁺ centers and the negative lone pairs in the next layer are probably also very important for the structure stabilization (see figure V-15c). Distances between Bi³⁺ cations are Bi-Bi= 4.61 and 4.31 Å respectively for BiBa₃O₃Cl₃ and BiSr₃O₃Cl₃.

Table V-6. Crystal data and selected bond distances for BiA₃O₃Cl₃ (A=Sr, Ba).

Compound	BiBa ₃ O ₃ Cl ₃ , ref. [42]			BiSr ₃ O ₃ Cl ₃ , ref. [43]		
Crystal system	orthorhombic			orthorhombic		
Space group	<i>Pnma</i>			<i>Pnma</i>		
<i>a</i> (Å)	7.0489(18)			6.687(2)		
<i>b</i> (Å)	11.9938(73)			11.4618(8)		
<i>c</i> (Å)	12.0886(61)			11.565(2)		
Cell Volume (Å ³)	1022.01(85)			886.40(31)		
Refinement type	XRD Single crystal			XRD Single crystal		
Bi-O bonds (Å)	1	x	2.018(23)	1	x	2.0613(83)
(average)	2	x	2.0681(232)	2	x	2.0710(65)
			(2.051)			(2.068)
Bi-Cl bonds (Å)	2 x 3.6078(78)			2 x 3.4718(22)		

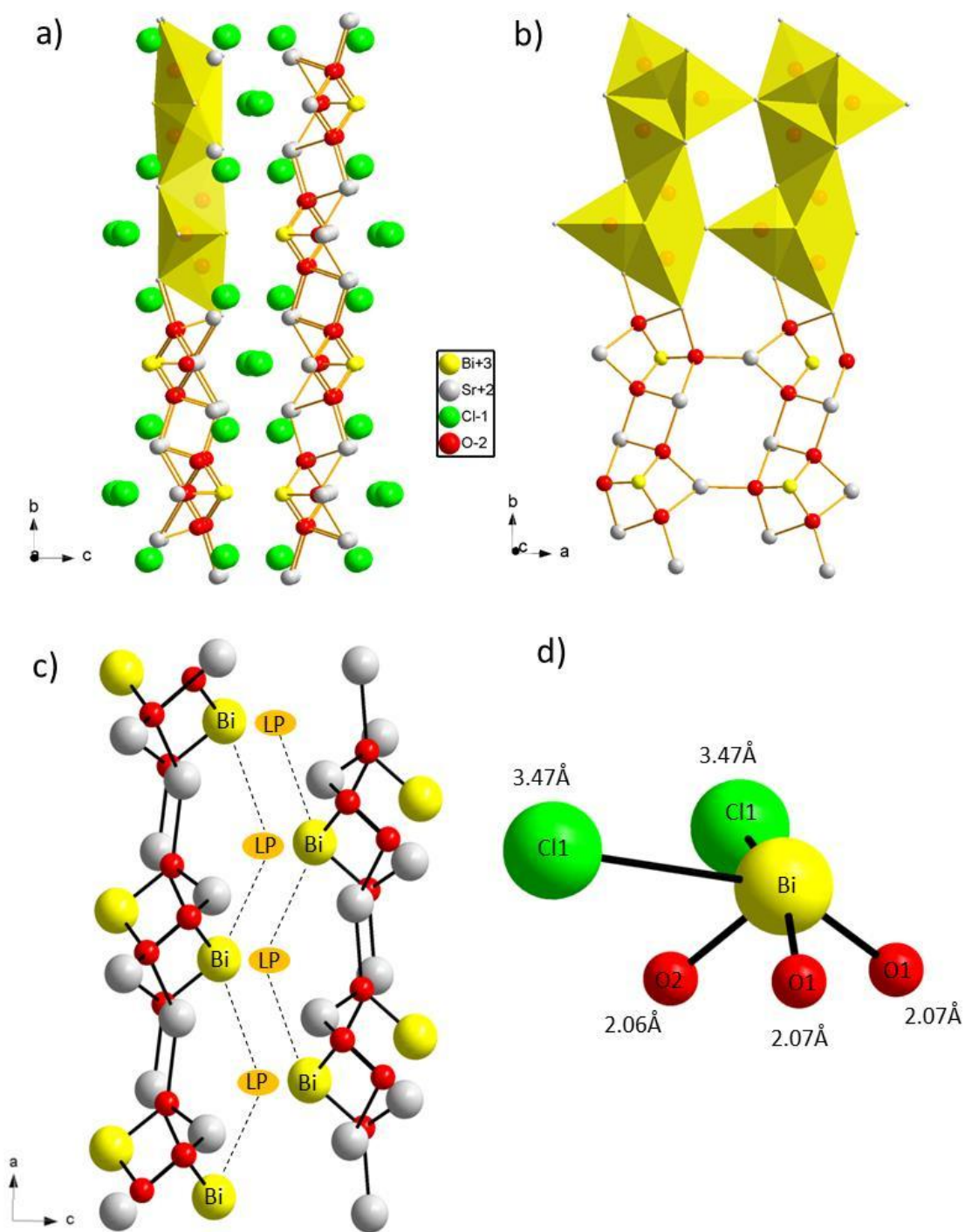


Figure V- 15 Crystal structure of $\text{BiSr}_3\text{O}_3\text{Cl}_3$ with oxo-centered $\text{O}(\text{Sr}_3\text{Bi})$ tetrahedra : (bc) plane (a), (ab) plane (b).
 c) Representation of the interaction between the Bi atoms and the negative lone pairs.
 and d) Coordination of Bi atoms for $\text{BiSr}_3\text{O}_3\text{Cl}_3$.

V.2.3. Electronic calculations and UV-vis spectroscopy

Density functional theory (DFT) calculations were performed using the Vienna *ab initio* simulation package (VASP).³¹ The calculations were carried out within the generalized gradient approximation (GGA) for the electron exchange and correlation corrections using the Perdew-Wang (PW91) functional and the frozen core projected wave vector method.³²⁻³³ The full geometry optimizations were carried out using a plane wave energy cutoff of 550eV and 8 *k* points in the irreducible Brillouin zone. All structural optimizations converged with residual Hellman-Feynman forces on the atoms smaller than 0.03 eV/Å and led to reasonable structures regarding the distances and the local geometries. The experimental structures match well the optimized one, i.e. within a reasonable error expected for the GGA method (see Table V-7). The difference between the calculated and experimental values does not 3.7% and 3.9% for the cell parameter *c* respectively for BiSr₃O₃Cl₃ and BiBa₃O₃Cl₃. The relaxed structures were used for accurate calculations of the electronic structure. For the later, a plane wave energy cutoff of 400eV, an energy convergence criterion of 10⁻⁶ eV and 16 *k* points in the irreducible Brillouin zone were used.

Table V-7. Comparison between experimental and theoretical cell parameter after full relaxation for BiA₃O₃Cl₃ (A=Sr, Ba).

Compound	Cell parameters	Experimental	Calculated	Deviation from exp.
BiSr ₃ O ₃ Cl ₃	a (Å)	6.687 (2)	6.7884	1.5%
	b (Å)	11.4618(8)	11.5447	0.7%
	c (Å)	11.565(2)	11.9929	3.7%
BiBa ₃ O ₃ Cl ₃	a (Å)	7.0489(18)	7.1307	1.1%
	b (Å)	11.9938(73)	12.1686	1.5%
	c (Å)	12.0886(61)	12.5635	3.9%

Bandgaps of BiSr₃O₃Cl₃ and BiBa₃O₃Cl₃: Both materials have a relatively large calculated electronic bandgap, 4.02 and 3.97eV respectively for BiSr₃O₃Cl₃ and BiBa₃O₃Cl₃ and exhibit low-dispersed band at the top at the valence band as well as at the bottom of the conduction band (figure V-16a-b). Concerning the first cited compound, the bandgap is founded indirect; the maximum of the VB is situated at the Gamma point whereas the minimum of the conduction band is localized in between the T and R points. For the barium compound, the lowest energy transition between the valence and conduction bands is a direct transition situated in between the Gamma and X points. However the bands being very flat, the

direct/indirect character is not pronounced. The calculated bandgaps were then compared to the experimental optical bandgap determined by extrapolation of the Kubelka-Munk fits plotted from the reflectivity measurements (figure V-16-e-f.).

The calculated electronic bandgaps and the experimental optical bandgaps strangely differ taking account that the value found by GGA calculations is most of the time underestimated (($E_{\text{ind.}} = 3.62$ (vs. $E_{\text{GGA}} = 3.97\text{eV}$) and 3.58 (vs. $E_{\text{GGA}} = 4.02\text{eV}$) respectively for A=Ba and A=Sr). Different versions of the PAW potentials and some variations in the GGA calculations using functionals such as the revised Perdew-Burke-Ernzerhof (PBE)⁴⁴ or Perdew-Burke-Ernzerhof revised for solids (PBEsol)⁴⁵ were attempted but led to similar results. There are different possible explanations for this difference in the bandgap values:

i) The electronic calculations are not accurate or the GGA method is not adapted for the calculation of these two 2D compounds even if the relaxed structure is in very good agreement with the experimental one and the energy convergence criterion of 10^{-6} eV is reached for the electronic calculations.

ii) A second explanation would be that the electronic and optical bandgaps are not the same in these two compounds. In materials with a large exciton binding energy,⁴⁶⁻⁴⁷ it is possible for a photon to have just barely enough energy to create an exciton (bound electron-hole pair), but not enough energy to separate the electron and hole (which are electrically attracted to each other). This induces that photons with a lower energy than the bandgap can be absorbed by the material. Most of the time the electronic and optical bandgap are similar in inorganic materials, but this possibility cannot be excluded.

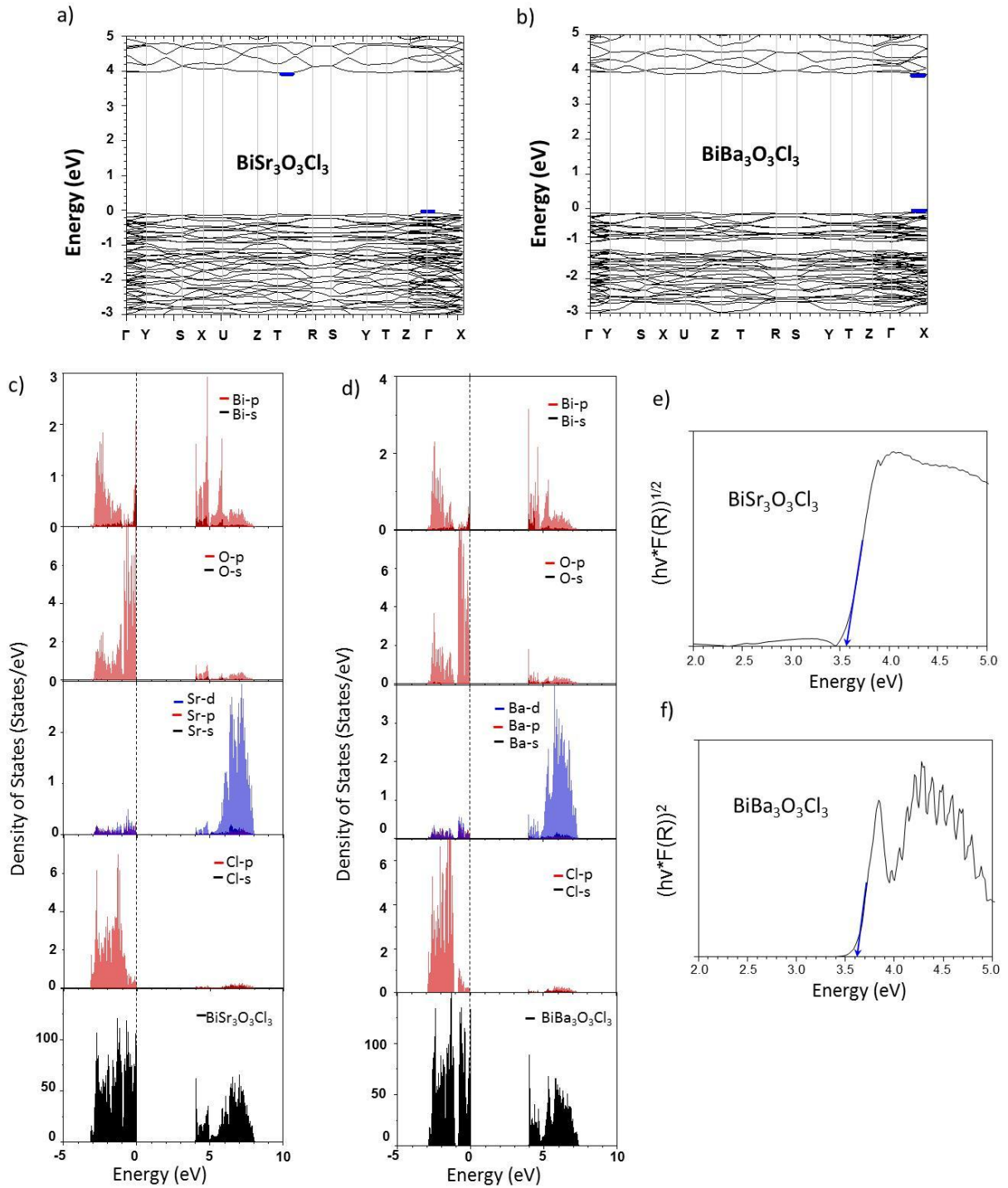


Figure V- 16 a) and b) Band diagrams representation of BiSr₃O₃Cl₃ and BiBa₃O₃Cl₃. TDOS (bottom) and PDOS of c) BiSr₃O₃Cl₃ d) BiBa₃O₃Cl₃. e) and f) represent the Kubelka-Munk fits and Tauc plots with band gap extrapolations for BiSr₃O₃Cl₃ and BiBa₃O₃Cl₃ (for A=Sr, BG=3.58eV and for A=Ba, BG=3.62eV).

V.2.4. DOS topology

BiSr₃O₃Cl₃: (figure V-16c), the highest part of the valence band, situated between -3.2 and 0eV, is essentially composed of O 2p, Cl 3p, Bi 6s and 6p states and a small contribution of Sr 3d and 4p states can also be noticed. There is also a high localized density of Bi 6s states at the Fermi level. The hybridization between the O 2p/Cl 3p and Bi states shows a high degree of covalency of the Bi-O/Cl bonds. The lowest part of the conduction band situated between 4.02 and 8.1eV originates from Bi 6p and 6s, O 2p and Sr 4d states. The contribution of Cl states is negligible. Contrary to the Sillen studied earlier, the Bi 6s states are already present at the bottom edge of the conduction band.

BiBa₃O₃Cl₃: (figure V-16d), the topology of the density of states is similar to that of BiSr₃O₃Cl₃ apart from that the lowest part of the VB is split in two. The two lowest part of the VB situated between ~-3.85 and 1.1eV and ~-0.8 and 0eV are composed of Bi 6p and 6s, O 2p, Cl 3p, Ba 4d and 5p states. The density of O 2p states is higher in the upper energy part (~-0.8 to 0eV) than in the lower energy part (~-3.85 to 1.1eV) of the valence band whereas it is the opposite for the Cl 3p states. Once again a significant and localized density of Bi 6s states is situated at the Fermi level. The lowest part of the CB (~3.98 to 7.5eV) is essentially formed by Bi 6s and 6p, O 2p and Ba 4d states. As for its isostructural strontium compound, the Bi 6s states already hybridize with the Bi 6p at the bottom of the conduction band.

V.2.5. Room temperature photoluminescence and structural correlation

BiSr₃O₃Cl₃ and BiBa₃O₃Cl₃ present photoluminescence properties at room temperature (figure V-17a). The two phosphors exhibit a greenish-white emission as it is represented on the CIE diagram (figure V-17b). However although these phases were expected with very intense emission, the luminescence is very weak and barely observed under an UV lamp. The measurements of the quantum yield lead to ~1% for both phases. So, it is very plausible that the Bi---Bi contacts shown figure V-15c strongly favor the luminescence quenching (see figure V-15c). Especially only ionic Bi-Cl bonds exist at this side in the interleave and the direct Bi-LP-Bi bridges mentioned could be much more drastic than covalent Bi-O-Bi bridges. On the DOS, this feature may be related to the very sharp overlapped Bi 6s and Bi 6p contributions at the fermi levels, which are different to what was observed previously.

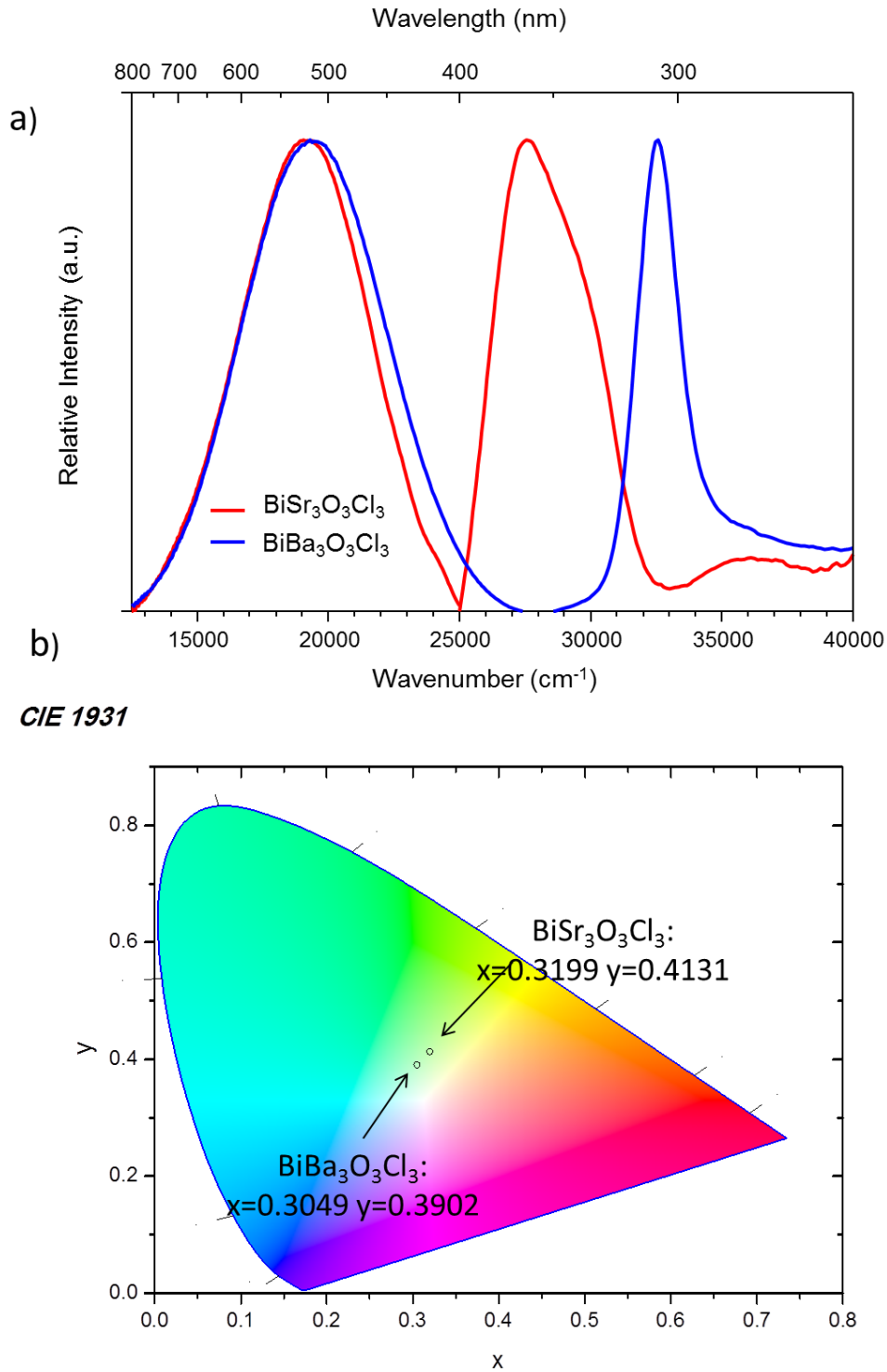


Figure V- 17 a) Room temperature photoluminescence of BiA₃O₃Cl₃ (A=Ba, Sr) and b) Representation of BiA₃O₃Cl₃ (A=Ba, Sr) color emission in the CIE 1931 diagram.

The two samples exhibit a similar broad emission band (FWHM $\approx 5800\text{cm}^{-1}$ for BiSr₃O₃Cl₃ and $\approx 6300\text{cm}^{-1}$ for BiBa₃O₃Cl₃) which covers nearly all the visible range and peaks at 19100cm^{-1} for BiSr₃O₃Cl₃ and 19370cm^{-1} for BiBa₃O₃Cl₃. On the other hand, the excitation differs a lot for the two isostructural samples. For BiBa₃O₃Cl₃, the excitation is represented by

a narrow band with a maximum at 32570cm⁻¹ whereas BiSr₃O₃Cl₃ shows a multiplet split of the excitation. It is composed of a band with a maximum 27550cm⁻¹ which shows a shoulder at higher energies and another band much less intense with a maximum at 36000cm⁻¹. This leads to a much smaller Stokes shift for the strontium compounds (8450cm⁻¹) than for the barium one (13200cm⁻¹).

Such a different behavior of the excitation band for these two isostructural compounds is strange, especially after examination of the excitation and absorption energies (figure V-18).

Concerning BiBa₃O₃Cl₃, the energy position of the excitation band compared to the absorption band is similar to what it was discussed before for the BiM₂PO₆ (M= Mg, Zn, Cd) or ABiO₂Cl (A= Cd, Ca, Sr, Ba) Sillen X1 series. The photoluminescence emission most probably originates from the Bi³⁺: ³P₁ → ¹S₀ transition and the excitation can be attributed to Bi³⁺: ¹S₀ → ³P₁ transition. Even if this compound has a direct bandgap, a semiconductor type photoluminescence (which means band to band transitions) is excluded due to the energy position of the emission band and the too high Stokes shift. Moreover it is possible to notice that the maximum of excitation band (4.06eV) fits with the electronic s² → sp transitions deduced from the PDOS (~4eV). Except the quite narrow excitation band character, the photoluminescence of this compound shows a strong analogy with all the X1 Sillen shown previously.

Contrarily, the excitation band for BiSr₃O₃Cl₃ starts at lower energies than the absorption band, which, for an undoped phosphor is quite strange. And thus makes difficult to assign the emission and excitation bands.

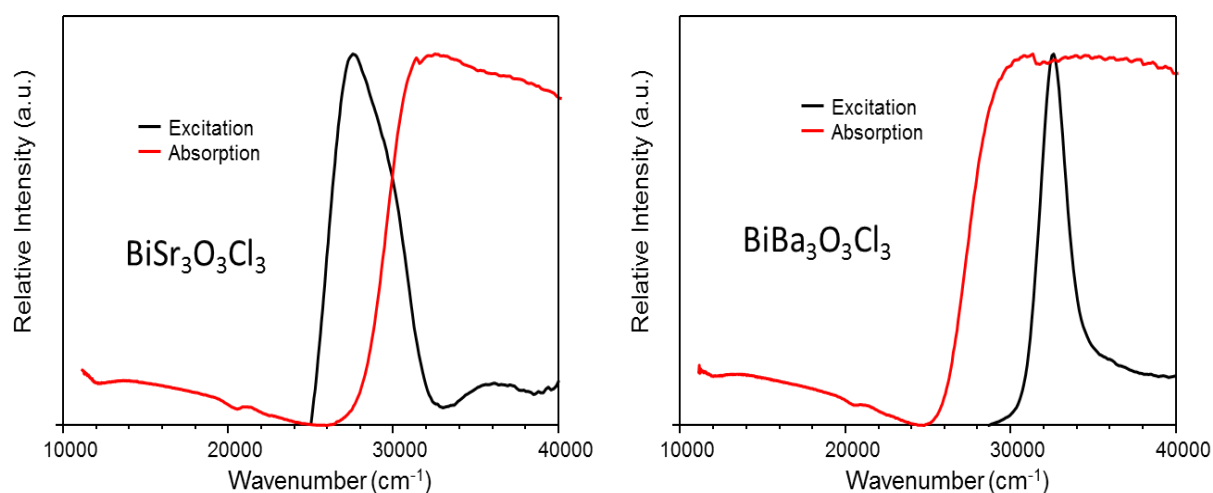


Figure V- 18 Comparison between the absorption and excitation spectra for BiA₃O₃Cl₃ (A=Ba, Sr).

The low intensity excitation band peaking at 36000cm^{-1} should also concern the $\text{Bi}^{3+}: ^1\text{S}_0 \rightarrow ^3\text{P}_1$ transition. By inductive effects the Bi-O bonds should be more covalent in $\text{BiBa}_3\text{O}_3\text{Cl}_3$ than in $\text{BiSr}_3\text{O}_3\text{Cl}_3$ and it matches well with the red shift observed for the Ba^{2+} compound. However the higher intensity excitation band with a maximum at 27550cm^{-1} cannot be attributed with certitude. As the excitation energy is lower than the optical band gap value and the sample is a polycrystalline powder, the highest probability is to ascribe this band to a transition from the top of the valence band to defects situated just below the conduction band which act as electron traps (excitonic luminescence). This type of phenomena was already observed in halide compounds⁴⁸⁻⁴⁹ and moreover the UV spectra show possible defects. It is also of interest to notice the similar energy position of emission band for both phosphors. However the photoluminescence difference between the Sr and Ba phases remain very mysterious.

V.2.6. Summary

Through the investigation of optical and electronic properties of the two isostructural compounds, it was shown that both are photoluminescent at room temperature. The radiative emission of $\text{BiBa}_3\text{O}_3\text{Cl}_3$ most probably originates from the Bi^{3+} activators whereas excitonic states probably situated just under the conduction band should be involved in the photoluminescent process for $\text{BiSr}_3\text{O}_3\text{Cl}_3$. One can just note that may be the indirect bandgap and the low dispersed bands on the bottom of the CB could favorite this luminescent behavior. It is also of interest to notice that the direct connectivity Bi-Bi shown figure V-15c may favor the quenching due to energy transfer between Bi^{3+} activators.

V.3. Luminescence of Bi versus Pb in $\text{PbBi}_4\text{O}_6\text{Cl}_2$ compound

During my thesis, I collaborate with another PhD student from Lille, Almaz Aliev, which synthesized new compounds derived from the Arppe's compound. Especially one of these new compounds, $\text{PbBi}_4\text{O}_6\text{Cl}_2$ seems to be very interesting for me to investigate their luminescence properties. This new compound has the particularity to possess two different kinds of ns^2 ions (Bi^{3+} and Pb^{2+}), while regarding the crystal structure, the lone pair of the Pb^{2+} cation should be not stereo-active. The preliminary luminescence results were already

published in Inorg. Chem.¹³ but in this section, the study was completed by decay time measurement, CIE chromaticity diagram.

V.3.1. Crystal structure of PbBi₄O₆Cl₂

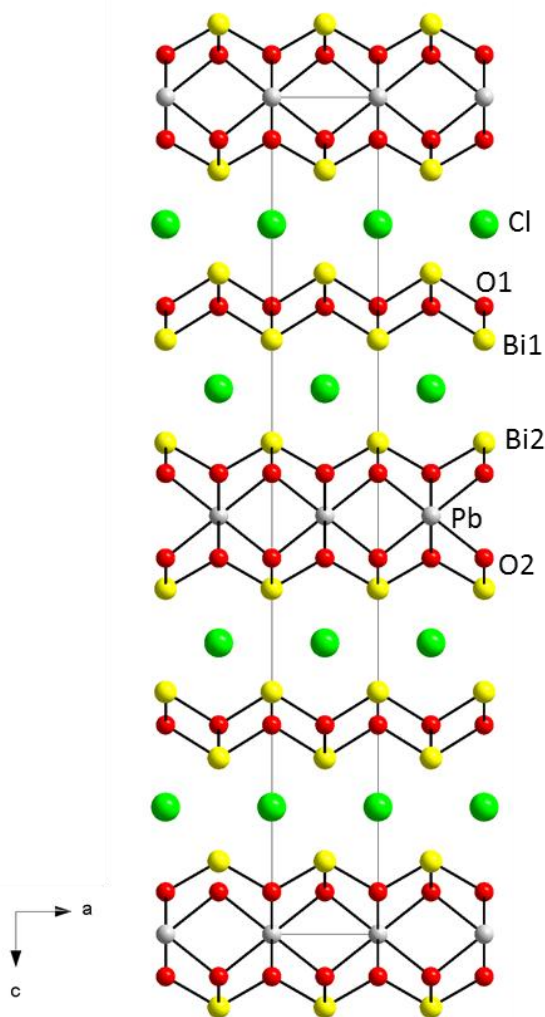


Table V-8. Crystal data and selected bond distances of PbBi₄O₆Cl₂ and BaBi₄O₆Cl₂

Compound	PbBi ₄ O ₆ Cl ₂ , ref. [13]	BaBi ₄ O ₆ Cl ₂ , ref. [50]
Crystal system	tetragonal	tetragonal
Space group	<i>I4/mmm</i>	<i>I4/mmm</i>
<i>a</i> (Å)	3.9488(4)	3.998
<i>c</i> (Å)	31.038(7)	31.370
Cell Volume (Å ³)	483.98 (10)	501.42
Refinement type	XRD Single crystal	XRD Single crystal
Bi1-O bonds (Å)	4 x 2.3241 (17)	4 x 2.2383 (709)
Bi1-Cl bonds (Å)	4 x 3.3324 (103)	4 x 3.0548 (363)
Bi2-O bonds (Å)	4 x 2.2763 (232)	4 x 2.5236 (115)
Bi2-Cl bonds (Å)	4 x 3.4412 (110)	4 x 3.9491 (670)
Pb/Ba-O bonds (Å)	8 x 2.5229 (891)	8 x 2.4292 (891)
Pb/Ba-Cl bonds (Å)	-	2 x 3.5448 (941)

Figure V- 19 Representation of PbBi₄O₆Cl₂ crystal structure along axis *b*.

The new PbBi₄O₆Cl₂ crystallizes in the *I4/mmm* space group (*a*=3.9488(4) Å, *c*=31.038(7) Å) with a layered structure which corresponds to the stacking sequence [Bi₂O₂]²⁺ [Cl]⁻ [PbBi₂O₄]⁰ [Cl]⁻ (figure V-19 and V-20d). [Cl]⁻ layers are simple contrarily to their double thickness in BiOCl, (figure V-20a). It corresponds to an intergrowth between the Bi₂LnO₄Cl⁵¹ and the Sillen ABiO₂Cl (*XI*)⁶ (figure V-20c) structures, but with Pb²⁺ instead Ln³⁺ and Bi³⁺ instead M²⁺ in the two distinct metal layers (figure V-20b). The compound is isostructural with BaBi₄O₆Cl₂ in which neutral [BaBi₂O₄]⁰ layers also exist.⁵⁰ PbBi₄O₆Cl₂ is to our knowledge the first example of Pb²⁺ in the central sites of such layers generally hosting large cations without lone pair electrons (Ba²⁺, Ln³⁺). It follows that in the PbBi₄O₆Cl₂, the lone pair is not active and Pb²⁺ is at the center of a regular PbO₈ quadratic prism (Pb-O bonds: 8x

2.52(3)Å). The Bi/Pb segregation into distinct sites is complete and Bi³⁺ occupies a typical BiO₄Cl₄ tetragonal antiprism (Bi-O: 4x 2.23(2)Å, Bi-Cl: 4x 3.437(9)Å). One should note that in [PbBiO₂] layers of the PbBiO₂Cl - XI (*Cmcm* S.G.)⁶ structure the Pb/Bi ordering is full (Bi-O: 4x 2.27Å vs. Pb-O: 4x 2.44Å and Bi-Cl: 4x 3.42Å vs. Pb-Cl 4x 3.26Å) even though both cations are located in the same layers and both have a stereo-active lone pair (figure V-20c). Typically, this disparity in terms of M-O and M-Cl distances can be regarded as a precious tool to distinguish Bi and Pb in complex mixed Bi/Pb compound as mentioned above. Bond valence calculations using the sums of M-O and M-Cl contributions using bond valence parameters of M-Cl bonds from Brese and O’Keeffe⁵² and more recent ones of M-O bonds revisited by S. Krivovichev⁵³ lead to BVS values almost correct: BVS_{Bi1}=2.67, BVS_{Bi2}=2.97, BVS_{Pb1} =2.25. All the crystal data of PbBi₄O₆Cl₂ and of the isostructural BaBi₄O₆Cl₂ are found Table V-8.

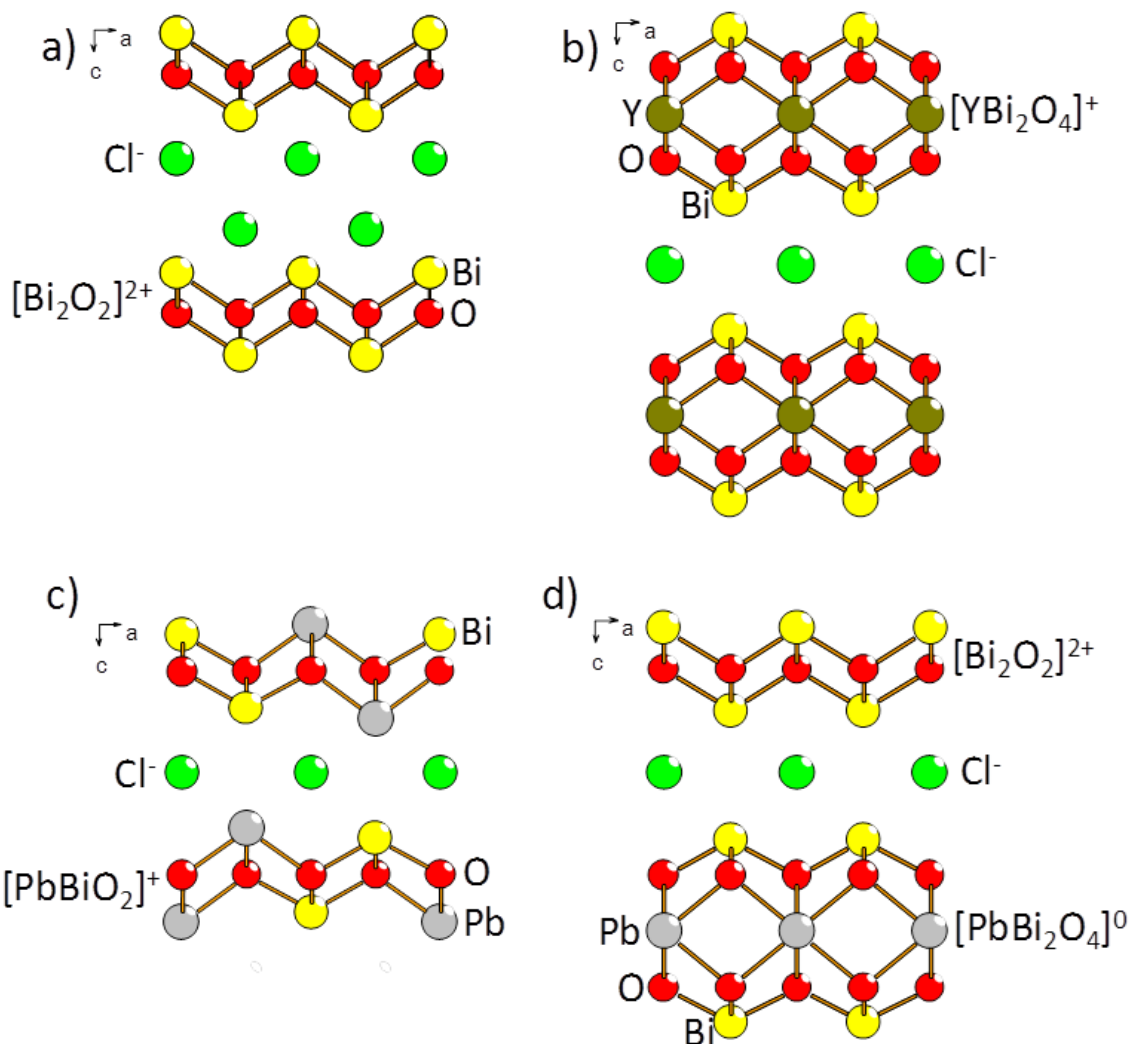


Figure V- 20 Evidence of layered modules in the crystal structures of a) BiOCl, b) Bi₂LnO₄Cl, c) (XI) PbBiO₂Cl and d) PbBi₄O₆Cl₂ (this work).

V.3.2. Photoluminescence properties of MBi₄O₆Cl₂ (M=Ba, Pb)

PbBi₄O₆Cl₂ shows red emission and BaBi₄O₆Cl₂ a reddish-orange one at low temperature (after keeping the sample sealed in a quartz ampoule several seconds in liquid nitrogen) when irradiated using a UV lamp ($\lambda = 365\text{nm}$). This red emission is very unusual for ns² ions stoichiometric compounds and, thus, extremely remarkable. The coordinates representing their emission color on the chromaticity diagram (CIE 1931) are: $x=0.6308$ $y=0.3578$ for PbBi₄O₆Cl₂, $x=0.4552$ $y=0.4273$ for BaBi₄O₆Cl₂ (figure V-21b) and the emission spectrum of PbBi₄O₆Cl₂ filled with corresponding color range is represented (figure V-20c)

Both spectra are plotted in figures V-21a, while the data are gathered in Table IV-9. The emission is, unfortunately, quenched for these two phosphors at room temperature, which prevents their utilization for applications.

PbBi₄O₆Cl₂: the emission band maximum is located at 14450cm^{-1} , while the excitation band starts at about 19000cm^{-1} with a maximum at 22420cm^{-1} (figure V-21a, Table V-9). The Stokes shift can therefore be determined to 7970cm^{-1} . PbBi₄O₆Cl₂ possesses two ns² cations (Bi³⁺ and Pb²⁺). The energetic position of the excited states and, thus, the location of the emission and excitation bands are in general at similar energies.⁵⁴ Therefore, it is difficult to assign excitation and more particularly emission bands to transition of the respective ions. In this way, BaBi₄O₆Cl₂ which is isostructural to PbBi₄O₆Cl₂ and has very comparable cell parameters, and has, thus, the same Bi and Ba/Pb crystallographic sites⁵⁰ was synthesized in order to comparable its luminescence properties with PbBi₄O₆Cl₂.

BaBi₄O₆Cl₂: For this phosphor, two excitation bands with maxima located at 23810 and 31000cm^{-1} could be detected at 10K, and they can be assigned respectively to $^1\text{S}_0 \rightarrow ^3\text{P}_1$ (A-band) and $^1\text{S}_0 \rightarrow ^3\text{P}_2$ (B-band) transitions of the Bi³⁺ ion. The high energy transition $^1\text{S}_0 \rightarrow ^3\text{P}_2$ becomes in general more intense at low temperatures although it is forbidden by selection rules. Additionally, the higher energy transition cannot be attributed to the C-band ($^1\text{S}_0 \rightarrow ^1\text{P}_1$) due to the lower intensity of it compared to the $^1\text{S}_0 \rightarrow ^3\text{P}_1$ transition. The C-band is an allowed dipole transition and its intensity is always found higher than the parity allowed A-band.³⁷ Even if there are two different Bi sites, only one emission band peaking at 14903cm^{-1} is detected. This could be explained by the fact that the two different Bi have a similar coordination. This emission band is assigned to Bi³⁺: $^3\text{P}_{0,1} \rightarrow ^1\text{S}_0$ transitions. All the optical data as the Stokes shift or the FWHM are gathered table V-9.

Table V-9. Photoluminescence characteristics of $MBi_4O_6Cl_2$ ($M=Pb, Ba$) at 10K.

Compound	PbBi ₄ O ₆ Cl ₂	BaBi ₄ O ₆ Cl ₂
Excitation (maximum)	22420 cm ⁻¹ (2.78eV)	23810 cm ⁻¹ (2.95eV)
Emission (maximum)	14450 cm ⁻¹ (1.79eV)	14903 cm ⁻¹ (1.85eV)
Emission FWHM	4300 cm ⁻¹ (0.53eV)	5700 cm ⁻¹ (0.71eV)
Stokes shift	7970 cm ⁻¹ (0.99eV)	8907 cm ⁻¹ (1.10eV)

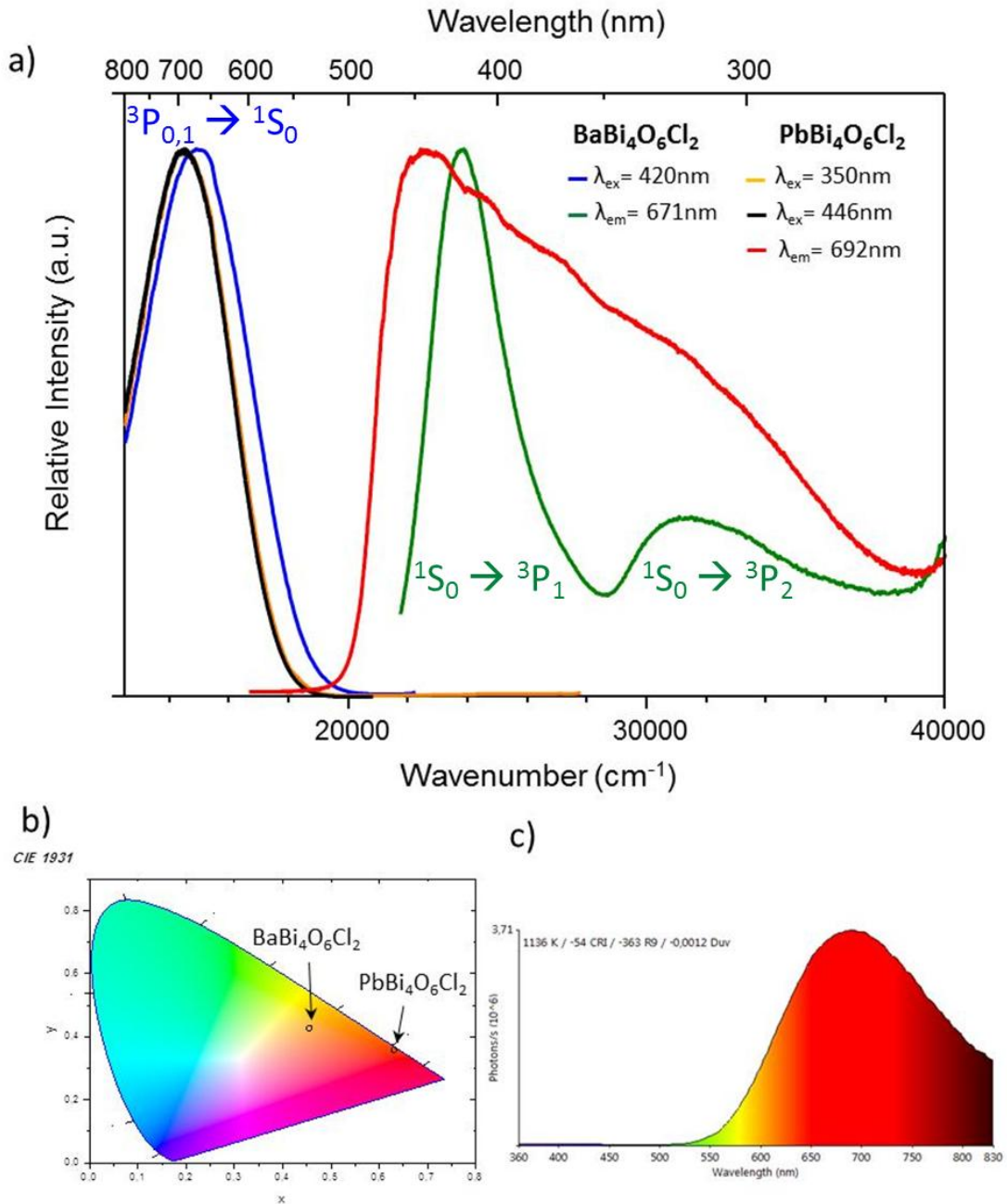


Figure V- 21 a) Photoluminescence spectra of $MBi_4O_6Cl_2$ ($M=Pb, Ba$) at 10K
 b) Representation of $MBi_4O_6Cl_2$ ($M=Pb, Ba$) color emission in the CIE 1931 diagram at 10K
 and c) Representation of $PbBi_4O_6Cl_2$ emission within the color of the spectral range.

Comparison between PbBi₄O₆Cl₂ and BaBi₄O₆Cl₂: The excitation spectrum of PbBi₄O₆Cl₂ is much less defined and should contain some additional bands than the two bands for BaBi₄O₆Cl₂. However, it is very difficult to define the exact number of bands and their energy position due to their strong overlapping (see figure V-21a). Then, it can be assumed that the excitation spectrum of PbBi₄O₆Cl₂ is composed of Bi³⁺:¹S₀ → ³P_{1,2} and most probably Pb²⁺:¹S₀ → ³P_{1,2} transitions. On the other hand, the shape and the energy position of the emission band of PbBi₄O₆Cl₂ are very similar to those of BaBi₄O₆Cl₂ (figure V-21a and table V-9). Thus, by comparison, the emission band of PbBi₄O₆Cl₂ can be the most probably be assigned to the ³P_{1,0} → ¹S₀ transitions of Bi ions as for BaBi₄O₆Cl₂. Moreover, due to the Pb²⁺ coordination, its lone pair is expected to be not stereo-active, this characteristic is in good agreement that PbBi₄O₆Cl₂ shows exclusively Bi emission and a complete Pb–Bi energy transfer after Pb excitation can be assumed. Recently, a study was performed to compare the Bi³⁺ and Pb²⁺ photoluminescence when they are separately doped in the same host lattice.⁵⁵ This study reveals that the excitation A-band as well as the emission band of Bi³⁺ are slightly red shifted compared to respectively excitation the A-band and emission band of Pb²⁺, which means that Pb excited states are situated at higher energy than the Bi ones.⁵⁵ These results are in good agreement with a possible charge transfer from Pb²⁺ to Bi³⁺ when both activators are present in a phosphor even if in PbBi₄O₆Cl₂, the Bi and Pb atoms are not situated in the same crystallographic sites.

As it was stated above, the red emission of PbBi₄O₆Cl₂ is quite unique. Parke and Webb noticed red emission from Bi³⁺ in calcium phosphor glasses⁵⁶, but after recent reinvestigation, Qiu et al.⁵⁷ concluded that this emission is originated by Bi²⁺. More recently, Qiu et al. found a surprising near-to-mid-IR luminescence in Bi₅(AlCl₄)₃, which was attribute to Bi₅³⁺ clusters.⁵⁸ Bi₁₂GeO₂₀ is also reported to show an emission band in the red region at low temperature but also an additional band at higher energy was detected.⁵⁴ To the best of my knowledge PbBi₄O₆Cl₂ is the first example for red emission of Bi³⁺ doped in an oxychloride host. In general, red emission in Bi-doped compounds is usually assigned to Bi²⁺.^{59,60}

V.3.3. Decay time measurement

At 10K the decay curve ($\lambda_{\text{ex}}=418\text{nm}$ and $\lambda_{\text{em}}=665\text{nm}$) for $\text{PbBi}_4\text{O}_6\text{Cl}_2$ was fitted using a triple exponential behavior, $I = I_0 + A1*\exp(-t/ \tau_1) + A2*\exp(-t/ \tau_2) + A3*\exp(-t/ \tau_3)$, giving three different lifetimes: $\tau_1=64\mu\text{s}$, $\tau_2=575\mu\text{s}$ and $\tau_3=12.6\text{ms}$ (see figure V-22). It is important to note that the double exponential profile did not give enough satisfying R^2 coefficient of determination and the simulated curve did not fit well with the experimental one.

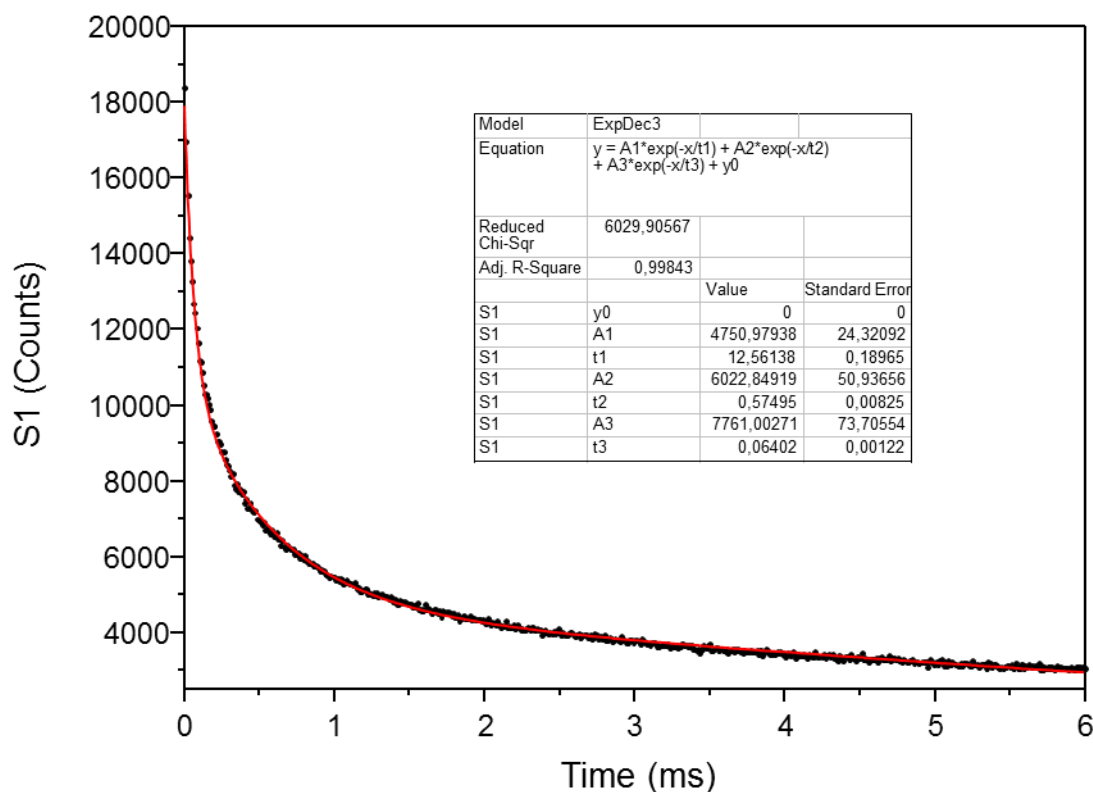


Figure V- 22 Decay time measurement of $\text{PbBi}_4\text{O}_6\text{Cl}_2$ at 10K. The decay curve is fitted with a triple exponential behavior and gives three lifetime values: $\tau_1=64\mu\text{s}$, $\tau_2=575\mu\text{s}$, $\tau_3=12.6\text{ms}$.

- The two lowest lifetime τ_1 and τ_2 are similar to those found for BiMg_2PO_6 ($\tau_1=37\mu\text{s}$ and $\tau_2=286\mu\text{s}$ discussed in Chapter III) and hence, they can be attributed respectively to $^3\text{P}_1 \rightarrow ^1\text{S}_0$ (τ_1) and $^3\text{P}_0 \rightarrow ^1\text{S}_0$ (τ_2) transitions.
- The third lifetime value ($\tau_3=12.6\text{ms}$) is much higher than the two others and should correspond to a strongly forbidden transition due to its high value. For sure, it cannot arise from $\text{Pb}^{2+}/\text{Bi}^{3+}$: $^3\text{P}_2 \rightarrow ^1\text{S}_0$ out of the experimental range. Finally, the third lifetime cannot be attributed with certitude. However, exciting at 418nm could involve the Pb^{2+} : $^1\text{S}_0 \rightarrow ^3\text{P}_1$

transitions, then this third life time may be related to the processes feeding the excited states of Bi³⁺ from Pb²⁺ excited states.

V.3.4. Summary

Finally, through the comparison with BaBi₄O₆Cl₂, it was shown that in spite of the presence of Pb²⁺ activators, the low temperature photoluminescence of PbBi₄O₆Cl₂ should arise essentially from Bi³⁺: ³P_{0,1} → ¹S₀ transitions. The red emission exhibited is quite uncommon for Bi³⁺ emitters and to the best of my knowledge, is observed for the first time in bismuth oxyhalides compounds. The lone pair of Pb²⁺ is non stereo-active regarding the crystal structure of the compound and its activation transfers its energy to Bi³⁺ via non radiative relaxation (figure V-23). This transfer most probably arises from particular values of all the energetic levels. It is most probable that the non-stereo-active LP for Pb²⁺ in this phase plays a role in the absence of its radiative emission.

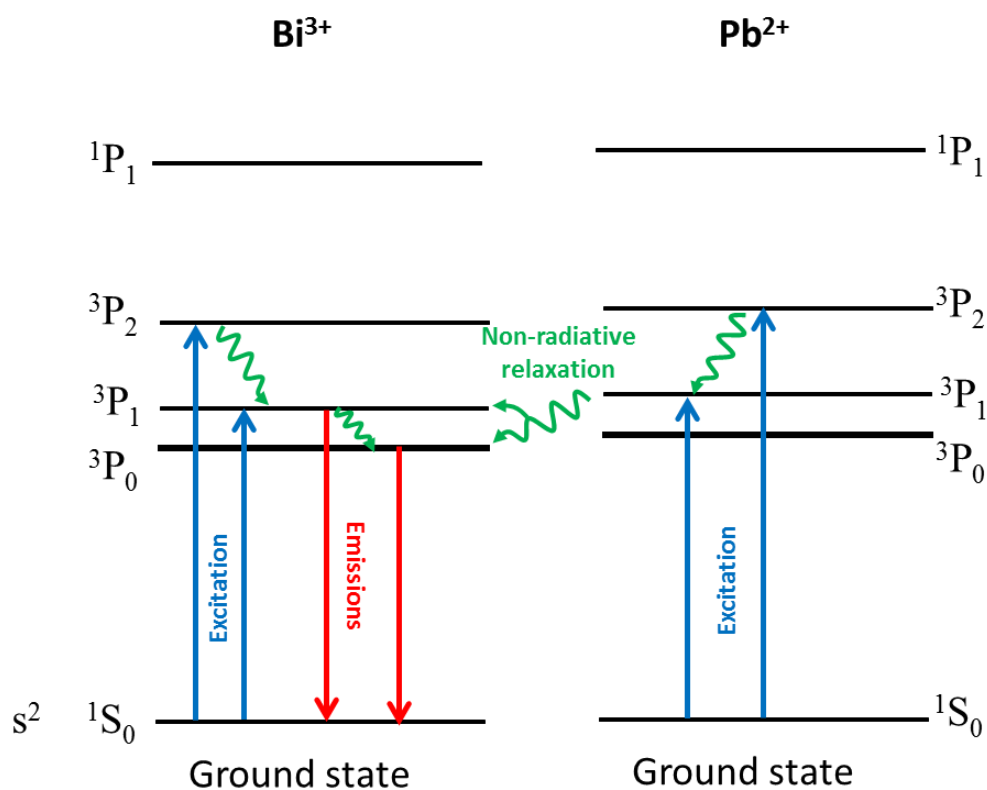


Figure V- 23 Sketch representing the energy transfer from Pb²⁺ to Bi³⁺.

References

- [1] Jacquier, B., *J. Lumin.*, **1975**, *10*, 95.
- [2] Porter-Chapman, Y.; Bourret-Courchesne, E.; Derenzo, S.E., *J. Luminescence*, **2008**, *128*, 87.
- [3] Dolgikh, V.A.; Kholodkovskaya, L.N., *Russ. J. Inorg. Chem.*, **1992**, *37*, 488.
- [4] Fray, S.M.; Milne, C.J.; Lightfoot, P., *J. Solid State Chem.*, **1997**, *128*, 115.
- [5] Kusainova, A.M.; Zhou, W.; Irvine, J.T.S.; Lightfoot, P., *J. Solid State Chem.*, **2002**, *166*, 148.
- [6] Charkin, D.O.; Berdonosov, P.S.; Dolgikh, V.A.; Lightfoot, P., *J. Solid State Chem.*, **2003**, *175*, 316.
- [7] Thomas, J.M.; Ueda, W.; Harris, K.D.M., *Faraday Discuss. Chem. Soc.*, **1989**, *87*, 33.
- [8] Burch, R.; Chalker, S.; Loader, P.; Thomas, J.M.; Ueda, W., *Appl. Catal.*, **1992**, *A 82*, 77.
- [9] Shan, Z.; Wang, W.; Lin, X.; Ding, H.; Huang, F., *J. Solid State Chem.*, **2008**, *181*, 1361.
- [10] Shan, Z.; Lin, X.; Liu, M.; Ding, H.; Huang, F., *Solid State Sciences*, **2009**, *11*, 1163.
- [11] Cornei, N.; Tancret, N.; Abraham, F.; Mentré, O., *Inorg. Chem.*, **2006**, *45*, 4886.
- [12] Krivovichev, S.V.; Mentré, O.; Colmont, M.; Siidra, O.I.; Filatov, S.K., *Chemical Reviews*, **2013**, *113*, 6459.
- [13] Aliev, A.; Olchowka, J.; Colmont, M.; Capoen, E.; Wickleder, C.; Mentré, O., *Inorg. Chem.*, **2013**, *52*, 8427.
- [14] Gilberg, M., *Ark. Kemi Mineral. Geol.*, **1960**, *B2*, 565.
- [15] Kirik, S.D.; Yakovleva, E.G.; Shimanskii, A.F.; Kovalev, Y.G., *Acta Crystallographica Section C Crystal Structure Communications*, **2001**, *57*, 1367.
- [16] Lopatin S., S., *Žurnal neorganičeskoj himii*, **1987**, *32*, 1694.
- [17] Dolgikh, V. A.; Kholodkovskaya, L. N., *Russ. J. Inorg. Chem.*, **1992**, *37*, 488.
- [18] Ketterer, J.; Krämer, V., *Materials Research Bulletin*, **1985**, *20*, 1031.
- [19] Deschanvres, A.; Gallay, J.; Hunout, J.M.; Thiault, M.T.; Victor, C., *C. R. Acad. Sci. Paris*, **1970**, *270*, 696.
- [20] Kennard, M.A.; Darriet, J.; Grannec, J.; Tressaud, A., *J. Solid State Chem.*, **1995**, *117*, 201.
- [21] Sillén, L. G., *Zeitschrift für anorganische und allgemeine Chemie*, **1939**, *242*, 41.
- [22] Sillén, L. G., *Naturwissenschaften*, **1942**, *30*, 318.
- [23] Keramidis, K.G.; Voutsas, G.P.; Rentzeperis, P.I., *Zeitschrift für Kristallographie*, **1993**, *205*, 35.
- [24] Bletskan, D.I.; Kopinets, I.F.; Rubish, I.D.; Turyanitsa, I.I.; Shtilikha, M.V., *Soviet Physics Journal*, **1973**, *16*, 646.
- [25] Sillén, L.G.; Joernstad, E., *Zeitschrift für Anorganische und Allgemeine Chemie* (1950) (DE), **1942**, *250*, 173.
- [26] Ketterer, J.; Krämer, V., *Mater. Res. Bull.*, **1985**, *20*, 1031.
- [27] SAINT: Area-Detector Integration Software; Siemens Industrial Automation, Inc.: Madison, **1996**.
- [28] SADABS: Area-Detector Absorption Correction; Siemens Industrial Automation, Inc.: Madison, **1995**.
- [29] Rodriguez-Carvajal, J., Recent developments of the program FULLPROF, **2001**.
- [30] Sillén, L.G.; Gjoerling-Husberg, A.S., *Zeitschrift fuer Anorganische und Allgemeine Chemie* (1950) (DE), **1941**, *248*, 135.
- [31] Kresse, G.; Furthmüller, J., *Vienna Ab-initio Simulation Package (VASP)*; Institut für Materialphysik: Vienna (<http://www.vasp.at/>), **2012**.
- [32] Perdew, J. P.; Wang, Y., *Phys. Rev. B* **1992**, *45*, 13244.
- [33] Kresse, G.; Joubert, D., *Phys. Rev. B* **1999**, *59*, 1758.
- [34] Kubelka, P.; Munk, F., *Zeit. für Tekn. Physik*, **1931**, *12*, 593.
- [35] Walsh, A.; Payne, D.J.; Egdell, R.G.; Watson, G.W., *Chem. Soc. Rev.*, **2011**, *40*, 4455.
- [36] Walsh, A.; Watson, G.W.; Payne, D.J.; Edgell, R.G.; Guo, J.H.; Glans, P.A.; Learmonth, T.;

- Smith, K.E., *Phys. Rev. B*, **2006**, 73, 235104.
- [37] Yen, W.M.; Shionoya, S.; Yamamoto, H., *Phosphor Handbook* (seconde edition), Taylor and Francis, (2006)
- [38] Toyozawa, Y.; Inoue, M., *J. Phys. Soc. Japan*, **1966**, 21, 1663.
- [39] Toyozawa, Y., *Optical Processes in Solids*, Cambridge University Press, London, 53, (2003).
- [40] Tchougreeff, A.L.; Dronskowski, R., *International Journal of Quantum Chemistry*, **2009**, 109, 2606.
- [41] Duffy, J.A., *J. Chem. Soc., Faraday Trans. 2*, **1978**, 74, 1504-1514.
- [42] Lenz, A.; Mueller Buschbaum, H., *Zeitschrift für Anorganische und Allgemeine Chemie*, (1950) (DE), **1990**, 582, 25.
- [43] Huang, J.; Sleight, A.W., *J. Solid State Chem.*, **1992**, 96, 154.
- [44] Perdew, J.P.; Burke, K.; Ernzerhof, M., *Phys. Rev. Lett.*, **1996**, 77, 3865.
- [45] Perdew, J.P.; Ruzsinszky, A.; Csonka, G.I.; Vydrov, O.A.; Scuseria, G.E.; Constantin, L.A.; Zhou, X.; Burke, K., *Phys. Rev. Lett.*, **2008**, 100, 136406.
- [46] Wang, X.; Jones, A.M.; Seyler, K.L.; Tran, V.; Jia, Y.; Zhao, H.; Wang, H.; Yang, L.; Xu, X.; Xia, F., *Nature Nanotechnology*, **2015**, 10, 517.
- [47] Dvorak, M.; Wei, S.H.; Wu, Z., *Phys. Rev. Lett.*, **2013**, 110, 016402.
- [48] Kondo, S.; Ohsawa, H.; Asada, H.; Saito, T., *Journal of Applied Physics*, **2010**, 107, 103526.
- [49] Marrone, M.J.; Kabler, M.N., *Phys. Rev.*, **1968**, 176, 1070.
- [50] Aurivillius, B., *Chemica Scripta*, **1987**, 27, 397.
- [51] Schmidt, M.; Oppermann, H.; Hennig, C.; Henn, R.W.; Gmelin, E.; Söger, N.; Binnewies, M., *Zeitschrift für anorganische und allgemeine Chemie*, **2000**, 626, 125.
- [52] Brese, N.E.; O'Keeffe, M., *Acta Crystallographica Section B Structural Science*, **1991**, 47, 192.
- [53] Krivovichev, S.V., *Zeitschrift für Kristallographie - Crystalline Materials*, **2012**, 227, 575.
- [54] Timmermans, C.W M.; Blasse, G., *J. Solid State Chem.*, **1984**, 52, 222.
- [55] Gawande, A.B.; Sonekar, R.P.; Omanwar, S.K., *International Journal of Optics*, **2014**, 2014, 418459.
- [56] Parke, S.; Webb, R.S., *Journal of Physics and Chemistry of Solids*, **1973**, 34, 85.
- [57] Xu, W.; Peng, M.; Ma, Z.; Dong, G.; Qiu, J., *Opt. Express*, **2012**, 20, 15692.
- [58] Cao, R.; Peng, M.; Wondraczek, L.; Qiu, J., *Opt. Express*, **2012**, 20, 2562.
- [59] Hamstra, M.A.; Folkerts, H.F.; Blasse, G., *J. Mater. Chem.*, **1994**, 4, 1349.
- [60] Peng, M.; Wondraczek, L., *Journal of the American Ceramic Society*, **2010**, 93, 1437.

Chapter VI. Photoluminescence of BiCdS₂Br

VI. Photoluminescence of BiCdS₂Br

In the previous chapters the photoluminescence of bismuth oxides or oxyhalides was investigated. However, in view of applications, i.e. for important redshift of the Bi³⁺ the excitation band, it should be preferred to bond this emitter with more polarizable anions in order to significantly increase the nephelauxetic effect. Best adapted anions should be as big as possible with important local negative charge according to Fajans' rules.¹⁻³. Unfortunately, the most stable anions associated with Bi³⁺ are rarely highly charged. For instance, a higher nephelauxetic effect would occur for bismuth nitrides (N³⁻) as bismuth bonding anion, but it requires drastic synthesis conditions⁴ out of the experimental setup used in this work. Therefore, sulfide or selenide anions are the most suitable to replace the oxygen ones. For this purpose a focus was done on an interesting of the literature: BiCdS₂Br.⁵ At least, the full analysis of this compound using the same tools than for the oxides or oxyhalides shown previously is helpful to understand the main differences that can bring anions such S²⁻ in the electronic structure and optical properties.

VI.1. Synthesis

The polycrystalline sample was synthesized according to the published method,⁵ a stoichiometric mixture of Bi, BiBr₃, CdS and S was thoroughly grounded in an agate mortar and sealed in quartz ampoule under vacuum.



Then the mixture was first slowly (~0.5 °C/min) heated to 250 °C, isothermed for 10h and after that heated at 1 °C/min to 420 °C and isothermed for 4 days. The reaction was then slowly cooled (~0.1 °C/min) to room temperature and the purity of the sample checked and confirmed by XRD. All the reflections are indexed to BiCdS₂Br theoretical powder pattern.⁵

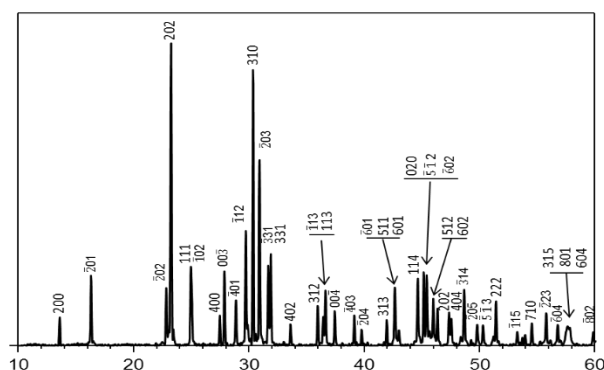


Figure VI- 1 X-ray powder pattern of BiCdS₂Br with full reflection indexation.

VI.2. Structure description of BiCdS₂Br

BiCdS₂Br crystallizes in the *C2/m* space group with a framework structure far different from the corresponding oxides such as the Sillen X1 CdBiO₂Br with *I4/mmm* space group.⁶ Due to the size of S²⁻, the anion centered description is not valid anymore and the classical cation centered approach is relevant. BiCdS₂Br can be described by Cd containing chalcobromide slabs in the (bc) plane interlinked by the Bi³⁺ cations (figure VI-2a). These slabs are composed of infinite [CdS₃]⁴⁻ and [CdSBr₂]²⁻ chains along b axis linked alternatively by a common S1 anion (figure VI-2b). The two cadmium cations adopt octahedral Cd1S₆ / Cd2S₄Br₂ coordinations (figure VI-2b). The Bi atom is found in a distorted eight-fold coordination: five Bi-S bonds from 2.59 to 3.01 Å and three longer Bi-Br bonds from 3.56 to 3.73 Å (figure VI-2c). The charge calculations using Pacha (figure VI-2) compared to BiCdO₂Br (different structure, similar formula) evidence a most important partial charge on O²⁻ than on S²⁻ with respect to the stronger electronegativity of the former. Logically Bi local charge is more important in the BiS_n coordination. The crystal data are gathered table VI-1.

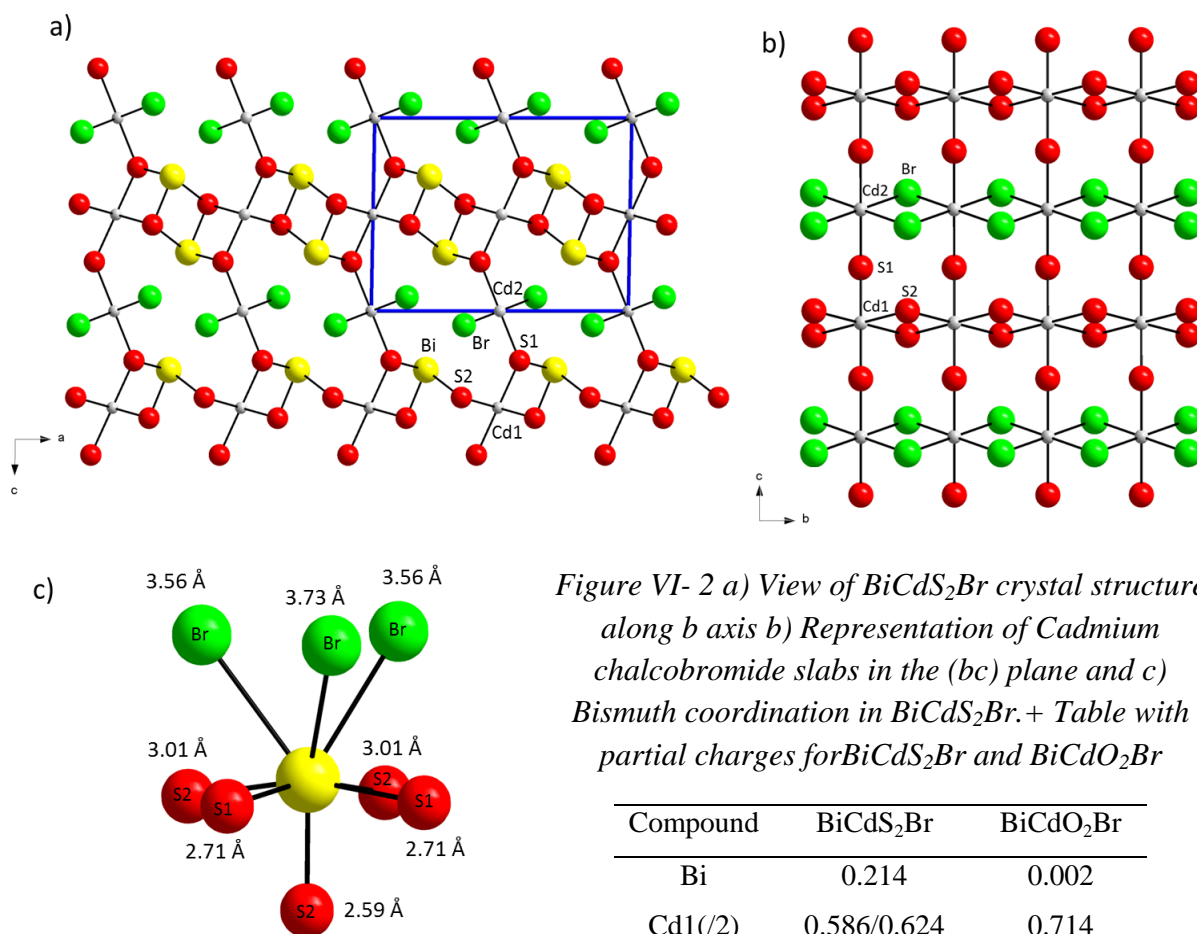


Table VI-1 Crystal data of BiCdS₂Br and comparison with calculated data after full relaxation.

BiCdS ₂ Br	Experimental	Theoretical	Deviation from exp
Crystal system	<i>monoclinic</i>	<i>monoclinic</i>	
Space group	<i>C 2/m</i>	<i>C 2/m</i>	
<i>a</i> (Å)	12.977 (3)	13.2322	6.7%
<i>b</i> (Å)	4.0120 (8)	4.0538	1%
<i>c</i> (Å)	9.5840 (19)	9.6907	1.1%
β (°)	91.07(3)	91.65	0.1%
Cell Volume (Å ³)	498.89 (18)	519.59	4.1%

VI.3. Electronic calculations

As for all the other calculation in this thesis, density functional theory (DFT) calculations were performed using the Vienna *ab initio* simulation package (VASP).⁷ The calculations were carried out within the generalized gradient approximation (GGA) for the electron exchange and correlation corrections using the Perdew-Wang (PW91) functional and the frozen core projected wave vector method.⁸⁻⁹ The full geometry optimizations were carried out using a plane wave energy cutoff of 550eV and 11 *k* points in the irreducible Brillouin zone. All structural optimizations converged with residual Hellman-Feynman forces on the atoms smaller than 0.03 eV/Å and led to reasonable structures regarding the distances and the local geometries. The experimental structure matches well the optimized one, i.e. within a reasonable error expected for the GGA method (see table VI-1). The difference between the calculated and experimental values does not exceed 6.7% for the cell parameter *c*. The relaxed structures were used for accurate calculations of the electronic structure. For the later, a plane wave energy cutoff of 400eV, an energy convergence criterion of 10⁻⁶ eV and 22 *k* points in the irreducible Brillouin zone were used. The *k* points for the band diagram calculation were chosen according to the space group (*C 2/m*) in order to examine the all Brillouin zone.

Figure VI-3 represents the band diagram of BiCdS₂Br plotted between -3 and +5eV. This compound is a semiconductor with a direct band gap of 1,72eV between the Gamma points. It means a more “narrow” bandgap compared to all oxides discussed before, as expected. Even if no numerical value is given in the reference [5], the calculated bandgap seems to be in good

agreement with those experimentally found by reflectance measurements by Wang et al.⁵ While a direct bandgap is not suitable for photocatalysis purposes due to the easy radiative recombination of the photo-generated electrons and holes, it is necessary for semiconductor luminescence, such as for the famous GaN blue LEDs, the origin of a late Nobel prize (in 2014). Actually, most of the commercial blue LEDs are direct bandgap nitride semiconductors/insulators with high photoluminescence quantum yield as well as a fairly high thermal conductivity.¹⁰

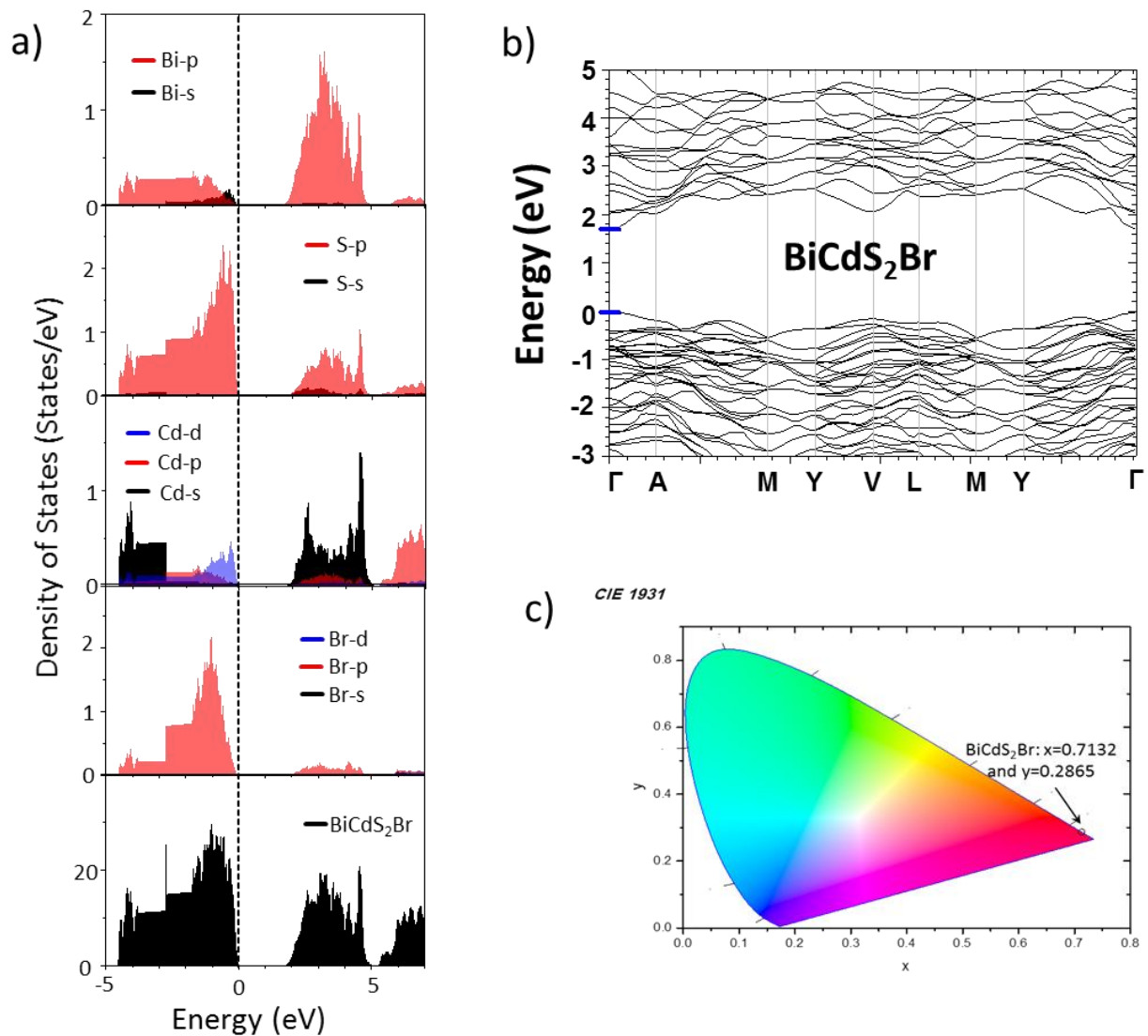


Figure VI- 3 a) DOS of BiCdS₂Br, b) Representation of the band diagram of BiCdS₂Br, a direct bandgap of 1.72eV is found and c) Color emission of BiCdS₂Br at 10K representation in the CIE chromaticity diagram.

VI.4. DOS topology

The partial and total density of states for BiCdS₂Br are represented figure VI-3a between -5 and 7eV. The higher part of the valence band (between -4.6 and 0eV) is composed of Bi 6s/6p, S 3p, Br 4p states and small contributions of Cd s/p and d states. As for the Sillen X1, the Bi 6s states are situated at the Fermi level and they hybridize with Bi 6p and S 3p states which show a high degree of covalency for the Bi-S bonds. The lower part of the CB situated 5.1eV mainly originates from Bi 6p, S 3p, Cd 5s. Low contribution of Cd 5p, Br 4p and S 3s are also found. Strangely, nearly no contribution of Bi 6s states in the lowest part of the CB are observed. This is expected to be prejudicial for the luminescence dealing with $s^2 \rightarrow sp$ Bi³⁺ transitions. Another singularity is the strong/broad contribution of Bi 6p states in the conduction band, compared to more localized states in oxides. The full DOS topology shows a more “flat” and narrow character in the VB and CB.

VI.5. Photoluminescence properties of BiCdS₂Br

BiCdS₂Br shows luminescence only at low temperature below 130K, it exhibits a red emission as represented in the CIE 1931 diagram (figure VI-3c).

Focusing on the excitation band (figure VI-4), it looks very different from what it was presented before for the Sillen ABiO₂X series (A=Cd, Ca, Sr, Ba and X=Cl, Br) (Chapter V). The extremely broad and noisy excitation is composed of several overlapping bands localized in the range 17500 – 40000cm⁻¹ (250-575nm) with a maximum at ~ 20000cm⁻¹ (500nm), it is comparable to the excitation band of PbBi₄O₆Cl₂ (seen Chapter V, section III.3) except that time there is only one Bi³⁺ site and no Pb²⁺ cations.

The intensity of the band slightly increases heating from 10 to 50K and then roughly decreases to completely quench the photoluminescence at temperature above 130K. The emission band is a relatively narrow (FWHM ≈ 800cm⁻¹ at 10K) and the Stokes shift is relatively low ≈ 4200cm⁻¹ which implies a poor energy loss during the PL process. The same thermal dependence behavior is observed for the emission and excitation bands

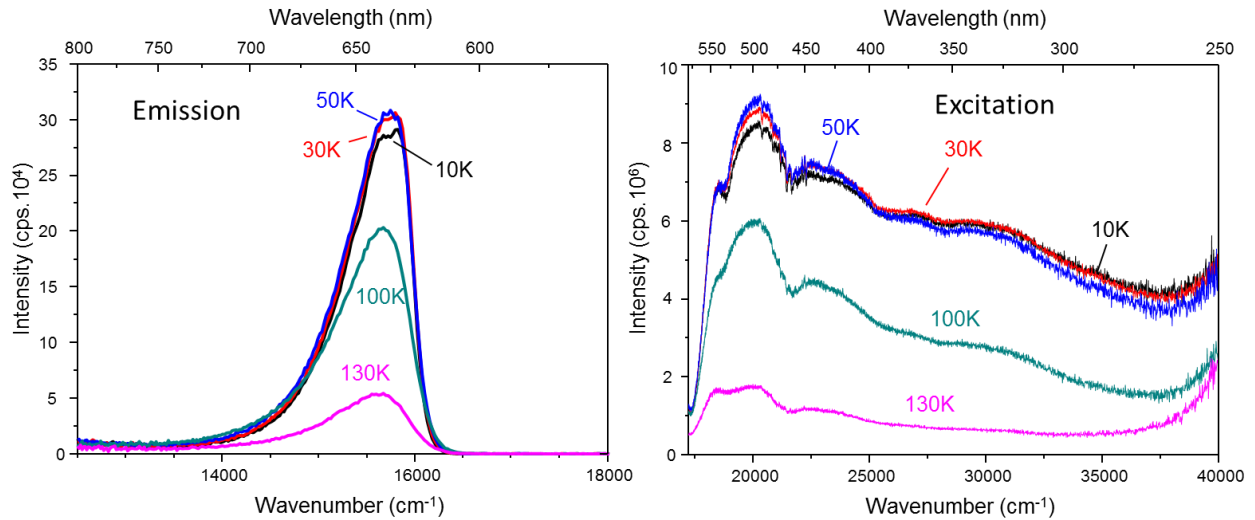


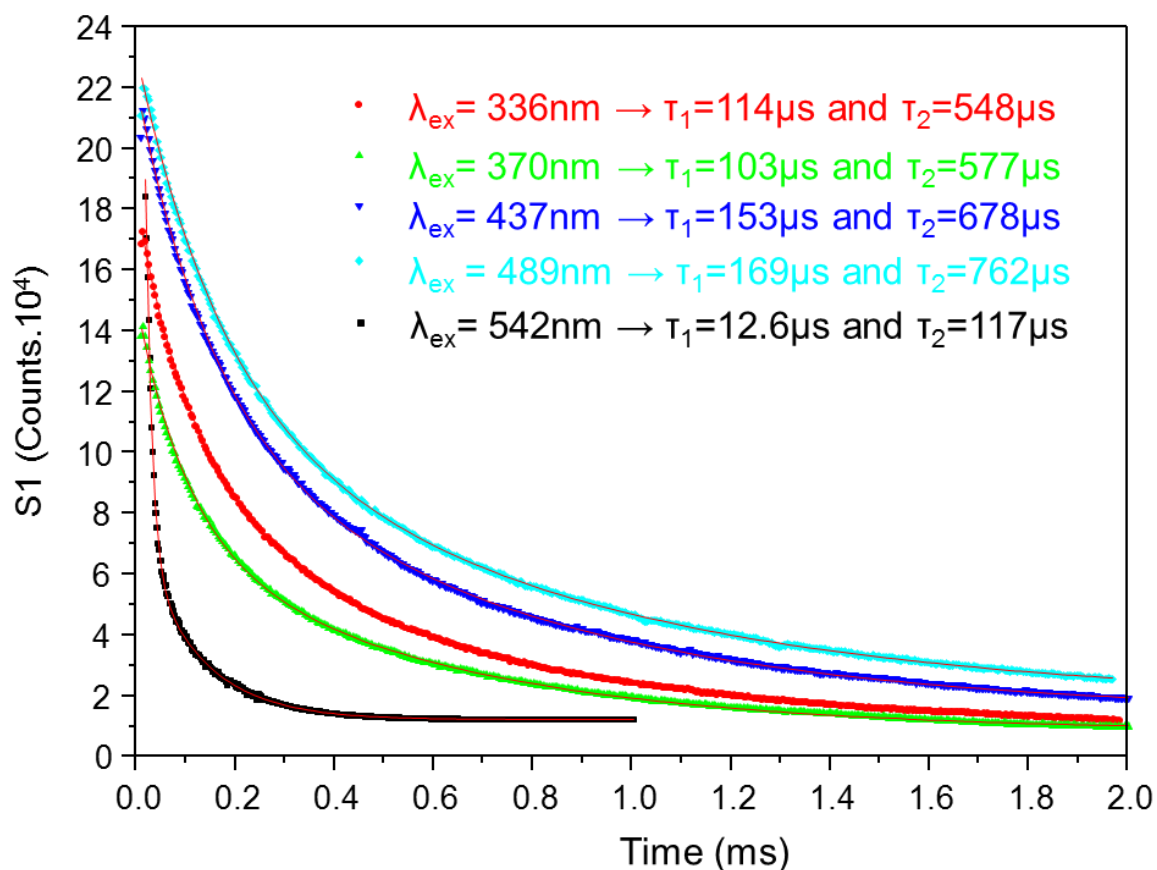
Figure VI- 4 Temperature dependence of emission spectra (left) and excitation spectra (right) of BiCdS₂Br.

VI.6. Decay time

Due to the very broad and multiplet character excitation band, the decay time was measured using different excitation energies but detecting each time the emission at 633nm (15800cm⁻¹). All decay time were measured at 10K and can be fitted with a biexponential behavior using the $I = I_0 + A1 \cdot \exp(-t/ \tau_1) + A2 \cdot \exp(-t/ \tau_2)$ equation. For each excitation energies, a very good correlation fitting parameter ($R^2=0.99$) was found. The four higher energies excitation give rise to lifetimes in the same order of magnitude (see table VI-2). Basically, τ_1 and τ_2 increase decreasing the excitation energy, however these changes are rather weak. On the other hand, exciting at still lower energy 542nm (18450cm⁻¹) (beginning of the excitation band) significantly decreases the lifetime values, $\tau_1=12.6\mu\text{s}$ and $\tau_2=117\mu\text{s}$.

Table VI-2. Decay time values using different excitation energies and detecting the emission at 633nm (15800cm⁻¹).

Excitation energy	τ_1	τ_2
336nm (29762cm ⁻¹)	114 μs	548 μs
370nm (27027cm ⁻¹)	103 μs	577 μs
437nm (22883cm ⁻¹)	153 μs	678 μs
489nm (20450cm ⁻¹)	169 μs	762 μs
542nm (18450cm ⁻¹)	12.6 μs	117 μs



Decay time measurements of BiCdS₂Br at 10K. All the decay curves can be fitted with a double exponential behavior (for each fit $R^2=0.99$).

VI.7. Discussion

All the experimental and theoretical results let be assumed that the photoluminescence exhibited by BiCdS₂Br is a typical semiconductor PL (band to band transition and not localized on Bi³⁺).

In fact, the absence of Bi 6s states in the lower part of the conduction band should be prejudicial for Bi³⁺ emission dealing with s²

(1000cm⁻¹) does not for Bi³⁺ emission which involves transitions from different vibrational level and leads to broad band as it was seen previously for all the compounds.

On the other hand, all the optical data and calculations fit with a semiconductor-type PL:

First, in semiconductors, a radiative recombination implies that both the energy and momentum must be conserved.¹¹ The conservation of momentum is guaranteed, upon the photoexcitation of the electron which only involves a UV or visible photon in this case, thanks to the direct bandgap character (the top of the valence and the bottom of the conduction bands have the same wave vector, (situated at the same k point of the Brillouin zone). Concerning the phonon needed to realize the absorption process, its wave vector is negligible compared to the electron wave vector.¹² The excess of energy during the electron-hole recombination is released by photon emission which also implies the energy conservation.

Secondly, the relatively low Stokes shift is characteristic of semiconductor photoluminescence¹¹ and moreover one can also remark that the emission band is comprised between 1.73 and 2eV (14000 and 16150cm⁻¹) which is in good agreement with the bandgap calculated (1.72eV) taking into account the probable underestimation of this latter value. Basically, the emission of semiconductors is situated around the bandgap value.¹¹

Moreover, it is known that the decay time of semiconductor (with a direct bandgap) photoemission is fast due to the allowed character transition¹¹ and exciting at energy corresponding to the bottom of the conduction band, the decay time fits with this specificity ($\tau_1=12\mu\text{s}$ and $\tau_2=117\mu\text{s}$ at 10K). Whereas exciting at higher energies, the lifetime becomes much longer due to relaxation processes for the electron to reach the bottom of the conduction band.

Finally, the temperature behavior of the emission also tends to confirm the semiconductor photoluminescence character. Globally, increasing the temperature has the effect to decrease the emission intensity due to the basic thermal quenching, heating the phosphor leads to the activation of non-radiative recombination centers. Whereas the behavior of excitation and emission intensity between 10 and 50K could most probably be explained by the presence of an excitonic state situated just below the conduction band which acts as an electron trap at low temperature.

VI.8. Summary

To conclude, even if this compound is Bi³⁺ based, the activator is not directly implied in the photoluminescence of BiCdS₂Br. All the data from measurements tend to validate the semiconductor luminescence behavior (direct band gap, lifetime, temperature behavior, low Stokes shift).

References

- [1] Fajans, K., *Naturwiss.*, **1923**, *11*, 165.
- [2] Fajans, K.; Joos, G., *Z. Phys.*, **1924**, *23*, 1.
- [3] Fajans, K., *Z. Kristallogr.*, **1924**, *61*, 18.
- [4] Xie, R.J.; Li, Y.Q.; Hirotsaki, N. and Yamamoto, H., *Nitride Phosphors and Solid State Lightening*, Taylor and Francis, (**2011**).
- [5] Wang, L.; Hung, Y.C.; Hwu, S.J.; Koo, Y.J.; Whangbo, M.H., *Chem. Mater.*, **2006**, *18*, 1219.
- [6] Sillén, L.G., *Zeitschrift für anorganische und allgemeine Chemie*, **1939**, *242*, 41.
- [7] Kresse, G.; Furthmüller, J., *Vienna Ab-initio Simulation Package (VASP)*; Institut für Materialphysik: Vienna (<http://www.vasp.at/>), **2012**.
- [8] Perdew, J. P.; Wang, Y., *Phys. Rev. B* **1992**, *45*, 13244.
- [9] Kresse, G.; Joubert, D., *Phys. Rev. B* **1999**, *59*, 1758.
- [10] Bloom, S.; Harbeke, G.; Meier, E.; Ortenburger, I.B., *Phys. Status Solidi b*, **1974**, *66*, 161.
- [11] Bergman, L.; McHale, J.L., *Handbook of Luminescent Semiconductor Materials*, Taylor and Francis, (**2011**).
- [12] Schattke, W.; Van Hove, M.A., *Solid-State Photoemission and Related Methods*, Wiley, (**2008**).

Summary and Outlook

This work aims on investigating the correlations between optical and structural properties of Bi^{3+} based compounds. Most of the studied materials are photoluminescent at room temperature which is already a remarkable point due to the stoichiometric concentration (large amount) of activator ions without full quenching. Through this work, different series of isostructural compounds or solid solutions were investigated and key parameters to tailor the luminescence properties were pointed out when possible. For this, synthetic, experimental works and empirical or ab initio calculations were combined for a full overview of the problematic.

- In the first series of isostructural compounds investigated (BiM_2PO_6 where $\text{M}=\text{Mg, Zn, Cd}$) and $\text{BiMM}'\text{PO}_6$ solid solution, it was shown that the arrangement of Bi^{3+} ions in 1D-zigzag chains results in a limited Bi-Bi connectivity and together with important Stokes shifts play against self-quenching of the radiative emission. All the samples are luminescent at room temperature and their emission bands are attributed to $\text{Bi}^{3+}: {}^3\text{P}_1 \rightarrow {}^1\text{S}_0$ transitions. For the BiM_2PO_6 ($\text{M}=\text{Mg, Zn, Cd}$) compounds, it is also shown that a significant tuning of the excitation energy ($\text{Bi}^{3+}: {}^1\text{S}_0 \rightarrow {}^3\text{P}_1$ electronic transitions) is allowed by substitution of M^{2+} cations, through inductive covalent effects inside the M-O-Bi subunits accordingly to the nephelauxetic effect. When the polarizing power of M^{2+} increases ($\text{Mg} > \text{Zn} > \text{Cd}$), the covalent Bi-O character decreases, shifting the excitation band to higher energy. It was confirmed by 1st principle calculations.

In these series, it was also shown that, due to Bi^{3+} photoluminescence specificities, the excitation bands are situated at higher energies than the absorption edge. This phenomena was confirmed for most of the compounds investigated in this work and already pointed out in the literature but never discussed before. Two reasons have been argued for such observations arising from the particular Bi^{3+} emitters: 1) The low energy reflectance spectra may correspond to forbidden transitions (not observed in the luminescence excitation process ${}^1\text{S}_0 \rightarrow {}^3\text{P}_0$ transition) 2) The important Bi^{3+} configurational change after excitation results in large Stokes shift which moves the excitation above the bottom of the conduction band.

Additionally, to the best of my knowledge it is shown for the first time experimentally the dependence of the emission energy on the lone pair stereo-activity: In the atypical $\text{BiCd}_x\text{Mg}_{2-x}\text{PO}_6$ solid solution, we have used a pertinent lattice parameter as an indicator of the LP

Summary and Outlook

activity and we have correlated this activity to the emission edge, such that less pronounced LP stereo-chemical activities lead to a shift of the emission band to higher energies.

Temperature dependence measurements for BiMg_2PO_6 showed that a thermodynamic equilibrium between the $^3\text{P}_1$ and $^3\text{P}_0$ states is created at low temperature which has for consequence to shift the emission spectra to lower energies due to the contribution of $^3\text{P}_0 \rightarrow ^1\text{S}_0$ transitions during the emission process.

- In the BiMg_2XO_6 (X=P, V, As) series, the same specificities as previously are found for X=P and As. In X=As compound, the lower polarizing power of As compared to P shifts the excitation band originated from Bi^{3+} ($^1\text{S}_0 \rightarrow ^3\text{P}_1$ transitions) to lower energies and the difference between the absorption and excitation spectra can be explained as for the previous series.

On the other hand, the co-presence of VO_4^{3-} groups induces an energy transfer from Bi^{3+} to vanadates groups which quenches the Bi^{3+} luminescence but reinforces the “standard” $\text{V}_{3d} \rightarrow \text{O}_{2p}$ charge transfer and PL activity. This result was comforted by the decay measurements and also validated by first principle calculations. The study of $\text{BiCd}_2\text{XX}'\text{O}_6$ (X=P, V, As) solid solutions also confirmed this tendency. While $\text{BiCd}_2\text{AsO}_6$ as well as $\text{BiCd}_2\text{As}_{1-x}\text{P}_x\text{O}_6$ solid solution do not emit radiative emission in the visible range due to their dark color and light absorption, VO_4^{3-} doped BiCd_2PO_6 directly causes a strong red shift of the luminescence process.

- Similar interactions between Bi^{3+} emitters and vanadate groups has been observed in the BiMVO_5 series (M=Mg, Ca, Cd). However sizeable topologies have been analyzed:

- When the excited states of Bi^{3+} are situated at higher energies than those of the vanadate groups (molecular states), a classic energy transfer from Bi^{3+} to VO_4^{3-} groups occurs and the vanadate emission is nearly not perturbed by the presence of Bi^{3+} (Mg case).

- When the Bi^{3+} states are situated at similar energies than VO_4^{3-} ones, mixed $\text{VO}_4^{3-}\text{-Bi}^{3+}$ centers are formed which strongly decrease the emission lifetime (Cd, Ca cases).

- Changing the Bi coordination sphere to mixed oxyhalide anions, a correlation between the structure and the room temperature photoluminescence for Sillen X1 ABiO_2X series (A=Ca, Cd, Sr, and X=Cl, Br, I) was performed: A/Bi disordered compounds with the $I4/mmm$ space group do not emit at room temperature whereas ordered ones crystallizing in $Cmcm$ or $P2_1/m$ space group are luminescent at room temperature.

For the ABiO_2X (A=Sr, Ba, Ca, Cl and X=Cl, Br) series, the (previously established) influences of the first cationic Bi coordination sphere as well as spectral specificities of the Bi^{3+} luminescence were checked. The influence of the halide nature was also investigated using nephelauxetic arguments.

- In the next $\text{BiA}_3\text{O}_3\text{Cl}_3$ (A=Sr, Ba) phases, which are luminescent at room temperature, the direct Bi...Bi interactions show drastic quenching effects on the emission intensity. Some discrepancies were observed for these two compounds:
 - The calculated band gap has a value much higher than the experimental one. Either, the GGA calculations are not well adapted to these compounds or the electronic and optical band gaps may differ.
 - Such difference may be highlighted in $\text{BiSr}_3\text{O}_3\text{Cl}_3$ the excitation band being situated at lower energies than the absorption edge. We proposed that the emission of $\text{BiSr}_3\text{O}_3\text{Cl}_3$ originates from defects (excitonic states) contrary to $\text{BiBa}_3\text{O}_3\text{Cl}_3$ for which Bi^{3+} would be the emitter.
- For the compounds with co-presence of other activator ions, it was demonstrated that:
 - For BiMn_2PO_6 , the room temperature luminescence is quenched due to a too high concentration of activators, however a charge transfer from Bi^{3+} to Mn^{2+} is observed at 10K and this compound exhibits at low temperature a typical Mn^{2+} red emission.
 - For $\text{BiPb}_2\text{AsO}_6$ and $\text{PbBi}_4\text{O}_6\text{Cl}_2$ the room temperature photoluminescence is also quenched and at low temperature charge transfer from Pb^{2+} to Bi^{3+} are detected as well as green emission for $\text{BiPb}_2\text{AsO}_6$ and red one for $\text{PbBi}_4\text{O}_6\text{Cl}_2$.
- Finally after investigation of several series oxides, oxo-anionic salts and oxyhalides, we have decided to initiate drastic changes in the electronic structure of our target compounds, focusing on a bromo-sulfide phase. BiCdS_2Br is a narrow direct band gap semiconductor compared to all previous phases (large and indirect BG). Here the Bi^{3+} activators have no primal influence on the luminescence properties. The direct band gap character induces a typical semiconductor emission in the red range at low temperature.

It is also important to notice that investigation of the effect of particle sizes was studied for BiCd_2PO_6 dealing with various attrition times (10min to 5h). However, no influence could be found on its luminescence properties and this work is not presented in this thesis.

Summary and Outlook

Finally, the future challenge would be to synthesize the ideal stable series of compounds which will be characterized by a low Bi...Bi connectivity in order to decrease the concentration quenching, a Bi-ligand strongly covalent bond character in order to minimize the excitation energy (energy saving) and an adjustable lone pair stereo-activity via chemical substitution in order to tailor the desired emission. However, even if this series of compounds could be synthesized, it has a very low probability that Bi based compounds can be used in LEDs applications especially due to concentration quenching induced in stoichiometric activator materials.

However, some of the studied compounds have the characteristics to be well suitable for scintillator applications, e.g. BiMg_2PO_6 :

This compound is thermally stable (high temperature melting point)

Good absorber due to the presence of Bi (high density)

Fast decay time due to the parity allowed transition

Bright emission in the visible range.

And quantum yield higher than the commercial BGO (22.8% against 15%)

Annex1

Table S1. Crystal data, measurement and refinement parameters for BaBiO₂Br.

BaBiO₂Br	
Crystal data	
Crystal symmetry	Orthorhombic
Space group	<i>C mcm</i> (63)
a (Å)	5.9485 (7)
b (Å)	13.3754(15)
c (Å)	5.7414(6)
V (Å ³)	456.81 (9)
Z	4
Dx (g/cm ³)	6.6606
(mm ⁻¹) (0.7107Å)	55.614
Appearance	Colorless platelet
Crystal size (mm)	0.10 x 0.09 x 0.03
Data collection	
λ (Mo Kα) (Å)	0.71073
Scan mode	ω and φ
θ(min-max)(°)	3.75 – 46.69
R(int) (%)	5.43
	-10 ≤ h ≤ 12
Reciprocal space recording	-27 ≤ k ≤ 26
	-11 ≤ l ≤ 11
Refinement	
Meas., obs./indep.all	5084,
(obs=I>3σ(I))	1154/889
No. of Refined parameters	92
Refinement method	F
R1(F ²)(obs) / R1(F ²)(all) (%)	3.98 / 5.57
wR2(F ²)(obs) / wR2(F ²)(all) (%)	4.09 / 4.27
GOF(obs) / GOF(all)	1.49/ 1.37
Δρmax/ Δρmax (e Å ⁻³)	6.225 / -5.98
Extinction coefficient	'none'

Table S2.. Fractional atomic coordinates and equivalent isotropic displacement parameters of BaBiO₂Br.

Atom	Wyckoff	S.O.F.	x	y	z	U _{eq} (Å ²)
Bi	16g	1	1/2	0.42585(2)	1/4	0.01139(8)
Ba	8f	1	1/2	0.61312(4)	1/4	0.01378(13)
Br	8f	1	0	0.25323(9)	1/4	0.0207(3)
O	8e	1	0.7240(10)	1/2	0	0.0162(12)

Table S3. Atomic displacement parameters (Å²) for BaBiO₂Br.

	U11	U22	U33	U12	U13	U23
Bi	0.01340(18)	0.01269(12)	0.00808(10)	0.00000	0.00000	0.00000
Ba	0.0131(3)	0.0178(2)	0.01045(16)	0.00000	0.00000	0.00000
Br	0.0241(6)	0.0211(4)	0.0169(3)	0.00000	0.00000	0.00000
O	0.021(3)	0.0167(18)	0.0112 (15)	0.00000	0.00000	0.0026(13)

Table S4. Selected bond distances for BaBiO₂Br.

Atom1	Atom2	Distance (Å)
Bi	O	4x 2.1953(36)
	Br	2x 3.7387(8)
	Br	2x 3.7652(8)
Ba	O	4x 2.6542(37)
	Br	2x 3.3818(7)
	Br	2x 3.3818(7)

Annex 2

This annex part deals with the crystallographic aspect. In fact, during my experimental work, I had the opportunity to point out and isolate new compounds I decided to characterize structurally. But unfortunately after many attempts the pure polycrystalline phases could not be successfully synthesized and as a consequence, optical properties were not investigated. Here, the crystal structures of two new compounds will be presented and discussed.

Single crystal X-Ray Diffraction

Crystals of respective compounds were mounted on glass fibers and studied on a Bruker X8 APEX II diffractometer equipped with a micro-focus X-ray tube with the MoK α radiation at 50 kV and 40 mA. The collected data were integrated using the Bruker program Saint Plus 6.025.¹ The unit-cell parameters were refined from the full data set. Multiscan absorption correction was performed for the three compounds using SADABS.² The structures were solved using Superflip methods. Jana 2006 program was used for structure refinements.³

BiPb_{0.5}Zn_{0.5}PO₅ compound

Synthesis

The ulterior motive of the prior synthesis of this new phase was to synthesize BiZnPO₅ (isostructural with BiCoPO₅)⁴ by analogy with BiZn₂PO₆⁵ in order to get infinite single zinc-oxygen chains not yet stabilized for the moment.

In that way, a mixture of Bi₂O₃, ZnO and (NH₄)₂HPO₄ with molar ratio Bi/Zn/P of 1/1/1 was ground and heated at 500°C during 12h to decompose the (NH₄)₂HPO₄ and then finally at 700°C for 24h in an alumina crucible. Intermediate grindings were done to homogenize the phase but the corresponding X-Ray diagram was different from the expected BiCoPO₅ and has not correspondence in the database. Then, the synthesis of single crystal was tempted. The sample was heated to 900°C with a rate of 150°C/h, kept at this temperature during 1h, cooled down to 450°C with a rate of 3°C/h and finally cooled to the room temperature under air. Yellowish platelets crystals were found in the melt and analyzed by single crystal measurements.

In a first time, the structure refinement led to relatively good correlation factor for a compound with the $\text{Bi}_{1.5}\text{Zn}_{0.5}\text{PO}_5$ formula. However, this compound is not neutral (total charge +10.5 for the cations and -10 for the anions). Then, several possibilities can be considered to get a neutral compound:

The first one is the presence of $\text{Bi}^{3+}/\text{Zn}^{2+}$ mixed sites instead of full Bi^{3+} sites, however in this case the bond lengths Zn-O does not fit and moreover due to the high electronic density of these sites, the refinement excluded the presence of Zn.

The second option is the presence of partial occupancy on the two “Bi” sites which would give the $\text{Bi}_{1.33}\text{Zn}_{0.5}\text{PO}_5$ neutral formula. The refinement leads to acceptable correlation factors but the bond valence sum of one of the two bismuth is too low (~2.05) and also the bond lengths Bi-O are too long. Moreover, from a crystallo-chemical point of view the presence of partial occupancy sites in BiMXO_5 structure-type remains strange.

The last option and the more plausible is the presence of impurities in the crucible during the synthesis of crystals. It was already the case in the lab to find lead impurities in some preparation due to the contamination by the crucibles. A lead atom would fit much better regarding the BVS, the asymmetric coordination and the bond lengths. Due to our knowledge on such materials it appears unrealistic to consider Bi with non-full occupancy rate. A lack of time didn't allow us to check this point before submission of the thesis but it will be performed later. And that is the reason why the third option was taken for the structural refinement.

The measurement and refinement data are gathered in the table S-5, the atomic positions in the table S-6, and atomic anisotropic displacements in the table S-7.

Structure description

$\text{BiPb}_{0.5}\text{Zn}_{0.5}\text{PO}_5$ crystallizes in a monoclinic unit cell parameters $a=5.6417(1)$ Å, $b=11.9142(3)$ Å, $c=6.9746(1)$ Å and $\beta=104.4520(8)$ (space group $P 2_1/m$). This unit cell is similar to BiMXO_5 ($M=\text{Mn, Ca, Co, Cu...}$ and $X=\text{P, As, V}$) compounds seen chapter IV. This compound can be described as oxo-centered infinite ribbons along a -axis, parallel to each other's and surrounded by isolated PO_4^{3-} tetrahedra (see figure S-1). The ribbons are built from $[\text{O}_2\text{Bi}_2\text{PbZn}]^{6+}$ building units however both. For the BiMXO_5 family, the ribbon is formed by $[\text{O}_2\text{Bi}_2\text{M}_2]$ building units, then in the case of $\text{BiPb}_{0.5}\text{Zn}_{0.5}\text{PO}_5$ the two positions of

M^{2+} cations in the ribbon are occupied by different divalent cations (one by Pb^{2+} and the other one by Zn^{2+}).

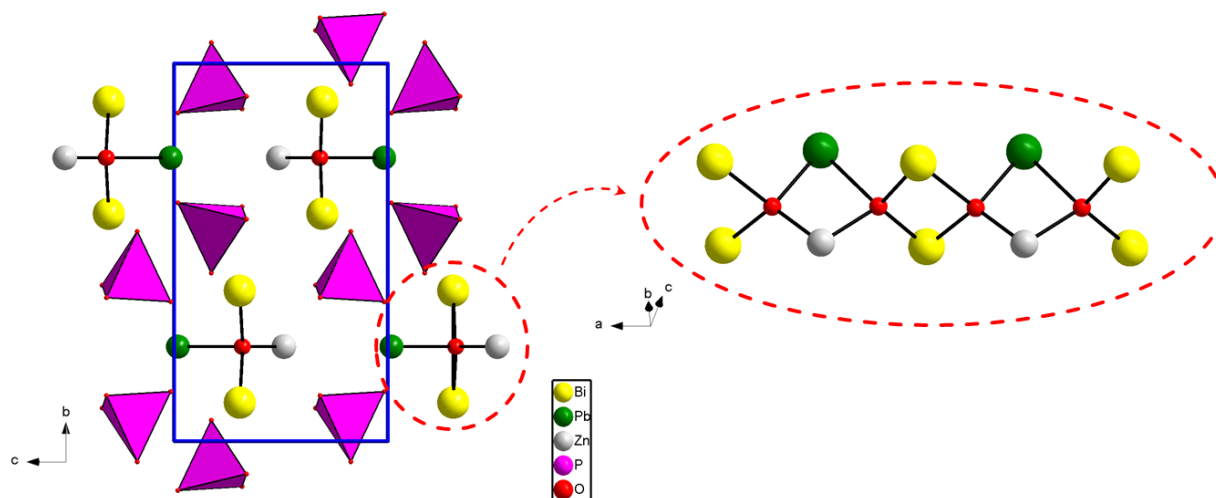


Figure S- 1 View in the (bc) plan of the crystal structure of $BiPb_{0.5}Zn_{0.5}PO_5$ and zoom on the infinite ribbon along a-axis.

The Bi atom is eight-coordinated (with oxygen) and has a typical asymmetric environment characterized by a stereo-active lone pair of electrons with five short Bi-O bonds on one side going from 2.1466Å to 2.4303Å and three more longer Bi-O bonds on the other side (from 2.9109Å to 3.6135Å) (figure S-2a). In this coordination the bond valence sum of Bi1 is equal to 3.055.

Pb atoms are ten-coordinated (to oxygen). Its coordination also presumes a lone pair stereo-activity due to the asymmetric coordination (figure S-2b). Six Pb-O bonds with length between 2.3809Å and 2.6632Å are situated on one side of the lead whereas four longer Pb-O bonds are found on the other side (3.271Å /3.4123Å). The bond valence sum of Pb is equal to 1.994.

Zn is found in a four-coordination environment (center of a slightly distorted tetrahedra) with bond lengths to oxygen from 1.9241 to 2.0175 Å, and giving rise to a bond valence sum of 1.995 (figure S-2c).

The P atoms which have a bond valence sum of 4.86, are localized in a regular tetrahedral environment with P-O bonds ranging from 1.5378 to 1.5517Å and angles comprised between 104.31 and 114.07°. (see figure S-2d)

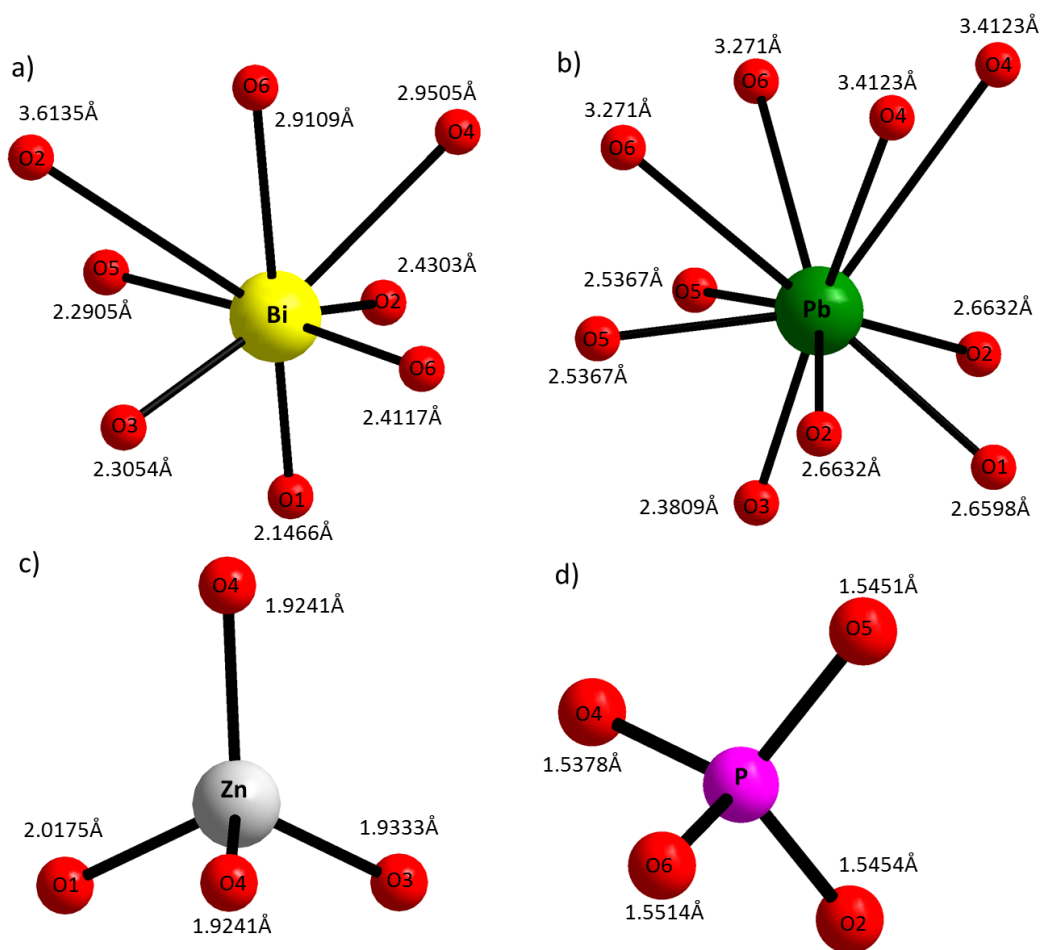


Figure S- 2 Coordination of Bi b) Pb c) Zn and d) P.

Unfortunately, no pure polycrystalline phase could be obtained after many trials. Nevertheless, because of the co-presence of Bi^{3+} and Pb^{2+} activators in high concentrations, the probably for this compound to present room temperature photoluminescence properties is very low.

Table S-5. Crystal data, measurement and refinement parameters for $\text{BiPb}_{0.5}\text{Zn}_{0.5}\text{PO}_5$.

$\text{BiPb}_{0.5}\text{Zn}_{0.5}\text{PO}_5$	
Crystal data	
Crystal symmetry	Monoclinic
Space group	$P 21/m$
a (Å)	5.6417 (1)
b (Å)	11.9142(3)
c (Å)	6.9746(1)
β (°)	104.4520(8)
V (Å ³)	453.9732 (16)
Z	4
Dx (g/cm ³)	7.7329
(mm ⁻¹) (0.7107Å)	81.064
Appearance	Yellow platelet
Crystal size (mm)	0.15 x 0.07 x 0.02
Data collection	
λ (Mo K α) (Å)	0.71073
Scan mode	ω and ϕ
θ (min-max)(°)	3.02 – 33.26
R(int) (%)	4.0
	$-8 \leq h \leq 8$
Reciprocal space recording	$-18 \leq k \leq 18$
	$-10 \leq l \leq 10$
Refinement	
Meas., obs./indep.all	12030,
(obs= $I > 3\sigma(I)$)	1806/1701
No. of Refined parameters	80
Refinement method	F
R1(F ²)(obs) / R1(F ²)(all) (%)	2.72 / 2.90
wR2(F ²)(obs) / wR2(F ²)(all) (%)	4.56 / 4.61
GOF(obs) / GOF(all)	2.06 / 2.10
$\Delta\rho_{\text{max}} / \Delta\rho_{\text{min}}$ (e Å ⁻³)	3.49 / -3.12
Extinction coefficient	170 (30)

Table S-6. Fractional atomic coordinates and equivalent isotropic displacement parameters of $\text{BiPb}_{0.5}\text{Zn}_{0.5}\text{PO}_5$.

Atom	Wyckoff	x	y	z	Ueq (\AA^2)	BVS
Bi	4f	0.79071(4)	0.60185(2)	0.30656(3)	0.01295(9)	3.055(19)
Pb	2e	1.17829(7)	3/4	0.01713(6)	0.02259(12)	1.944(14)
Zn	2e	0.37067(17)	3/4	0.51288(15)	0.0166(3)	1.995(17)
P	4f	0.6856(2)	0.56950(11)	0.28663(17)	0.0021(3)	4.86(4)
O1	2e	0.5774(11)	3/4	0.3161(10)	0.0124(17)	2.385(15)
O2	4f	0.3619(10)	0.5550(5)	0.1732(10)	0.0303(19)	1.84(2)
O3	4f	1.0574(11)	3/4	0.3207(9)	0.0120(16)	2.129(14)
O4	4f	0.4362(11)	0.6204(5)	0.6825(12)	0.036(2)	1.90(2)
O5	2e	0.7972(12)	0.6310(6)	-0.0167(10)	0.034(2)	2.12(2)
O6	4f	0.8752(12)	0.5873(7)	0.6621(10)	0.036(2)	1.77(3)

Table S-7. Atomic displacement parameters (\AA^2) for $\text{BiPb}_{0.5}\text{Zn}_{0.5}\text{PO}_5$.

	U11	U22	U33	U12	U13	U23
Bi	0.01398(14)	0.01299(15)	0.01181(15)	0.00266(6)	0.00309(9)	0.00056(7)
Pb	0.02079(19)	0.0300(2)	0.0174(2)	0.00000	0.00572(14)	0.00000
Zn	0.0104(4)	0.0153(4)	0.0088(4)	0.00000	0.0020(3)	0.00000
P	0.0045(5)	0.0019(5)	0.0009(5)	-0.0013(4)	-0.0007(4)	0.0004(4)
O1	0.014(2)	0.006(2)	0.020(3)	0.00000	0.009(2)	0.00000
O2	0.028(3)	0.016(2)	0.048(4)	0.001(2)	0.010(3)	0.001(2)
O3	0.009(2)	0.018(3)	0.006(2)	0.00000	-0.0041(19)	0.00000
O4	0.023(3)	0.028(3)	0.050(4)	-0.010(2)	-0.003(3)	0.022(3)
O5	0.044(3)	0.040(3)	0.023(3)	-0.027(3)	0.015(3)	-0.008(3)
O6	0.027(3)	0.065(5)	0.018(3)	-0.007(3)	0.008(2)	0.001(3)

Table S-8. Selected distances (Å) of $\text{BiPb}_{0.5}\text{Zn}_{0.5}\text{PO}_5$.

Bond	Distance (Å)	Bond	Distance (Å)
Bi-O1	2.1466(37)	Pb-O3	2.3809(68)
Bi-O5	2.2905(72)	Pb-O5 (*2)	2.5367(69)
Bi-O3	2.3054(41)	Pb-O1	2.6598(57)
Bi-O6	2.4117(69)	Pb-O2 (*2)	2.6632(59)
Bi-O2	2.4303(53)	Pb-O6 (*2)	3.271(7)
Bi-O6	2.9109(78)	Pb-O4 (*2)	3.4123(81)
Bi-O4	2.9505(61)		
Bi-O2	3.6135(64)	P-O3	1.5378(59)
		P-O6	1.5441(67)
Zn-O4 (*2)	1.9241(68)	P-O2	1.5454(62)
Zn-O3	1.9333(55)	P-O4	1.5514(78)
Zn-O1	2.0107(75)		

Bi₂BaIO₄H compound

Synthesis

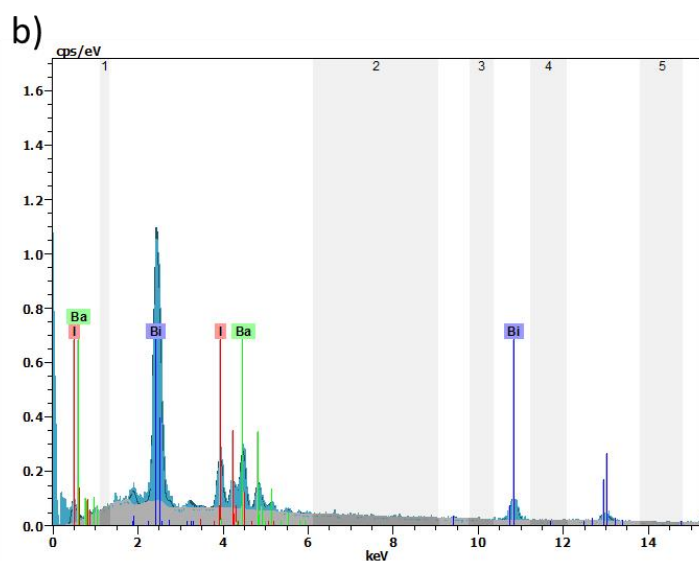
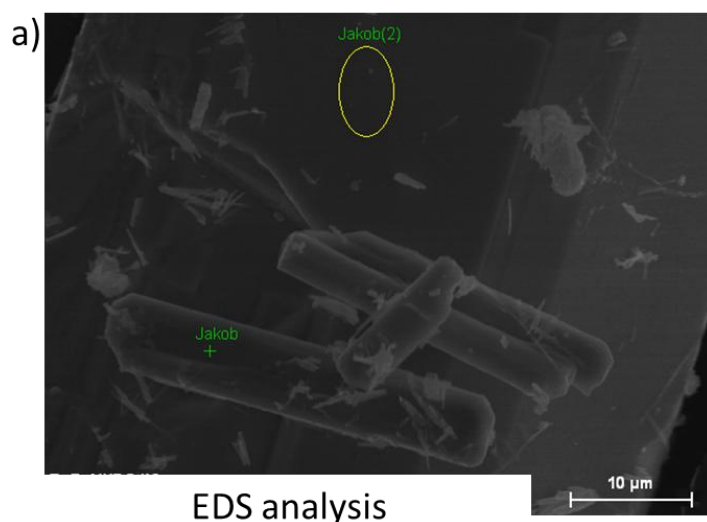
Most of the oxyhalide Sillen in the literature are synthesized by conventional solid state reactions (see Chapter IV). While the oxychlorides and even several oxybromides can be synthesized under air (see Chapter IV), all the oxyiodides have to be heated during several days under vacuum in a sealed ampoule in order to keep the stoichiometry during the heating process.⁶ In this way, during my thesis, I tried to synthesize oxyiodides by hydrothermal or solvothermal way.

Crystals of Bi₂BaIO₄H were obtained by hydrothermal synthesis. Bi(NO₃)₃·5H₂O and BaI₂·2H₂O (with a molar ratio Bi/Ba =1) were placed in a 23 mL Teflon-lined Parr autoclave filled with 4mL of distilled water and 1mL of 0.5M NaOH solution and heated statically at 170°C under autogenous pressure during 82 h. After the reaction was completed, the solution was filtered under air and a mixture of white powder and yellowish crystals appear on the filter-paper. A crystal was isolated, washed with ethanol and mounted on a rod glass in order to proceed to the data collection. The crystals found in the mixture correspond to the Bi₂BaIO₄H phase whereas the powder could not be identified. The crystal data and measurement parameters are gathered Table S-9. The atomic positions and atomic displacements are gathered Table S-10 and 11.

Energy-dispersive X-ray spectroscopy

Due to some difficulties to solve the crystal structure (problem with final electroneutrality), quantitative energy-dispersive X-ray spectroscopy (EDS) analyses were performed in order to get more information especially on the elemental composition and their ratio.

The EDS analyses were performed on a Hitachi S4700 microscope equipped with a microanalysis EDS system. The quantitative EDS analyses show the presence of Bi, Ba and I elements respectively in a ratio ~2:1:1 (see figure S-3a-d). The oxygen K α peak appears at ~0.5eV and is overlapped with the Ba and I peaks. Moreover, any traces of Na present as reactant were found during the analyses. (figure S-3b)



c) Spectrum: Jakob

Element	Series	norm. C [wt.%]	Atom. C [at.%]
iode	L-series	18.41	24.72
baryum	L-series	20.63	25.59
bismuth	L-series	60.96	49.69
Total:		100.00	100.00

d) Spectrum: Jakob(2)

Element	Series	norm. C [wt.%]	Atom. C [at.%]
baryum	L-series	19.47	24.38
iode	L-series	17.62	23.87
bismuth	L-series	62.91	51.75
Total:		100.00	100.00

Figure S- 3 a) Image of $\text{Bi}_2\text{BaIO}_4\text{H}$ crystals b) EDS spectrum of selected crystals: all the peaks can be indexed to Bi, Ba or I elements c) and d) Tables showing the quantification of the elements.

Infrared measurements

As hydrogen cannot be detected by EDS and its presence cannot be undoubtedly confirmed by single crystal refinement due to its very low electronic density compared to Bi, I or Ba elements, IR measurements is a good alternative to detect the vibrations of O-H bonds, for example.

Infrared spectra of $\text{Bi}_2\text{BaIO}_4\text{H}$ were measured between 4000 and 400 cm^{-1} with a Perkin-Elmer Spectrum TwoTM spectrometer equipped with a diamond attenuated total reflectance (ATR) accessory at room temperature (figure S-4).

The IR spectrum presents a medium band peaking at 1430cm^{-1} , a low intense band at 1082cm^{-1} and small peaks at 855 , 690 and 640cm^{-1} . Basically, the metal-oxygen or metal-halogen vibrations are situated at low wavenumber ($<1000\text{cm}^{-1}$).⁷ Whereas the four peaks 640 , 690 , 855 and 1082cm^{-1} are the most probably attributed to Bi-O, Ba-O or Bi-I vibrations, the peak situated at 1430cm^{-1} can be attributed to the O-H (hydroxyl) bending vibration.⁷ There is no broad band at $\sim 3400\text{cm}^{-1}$ which excludes presence of free O-H bonds (e.g. H_2O molecules).

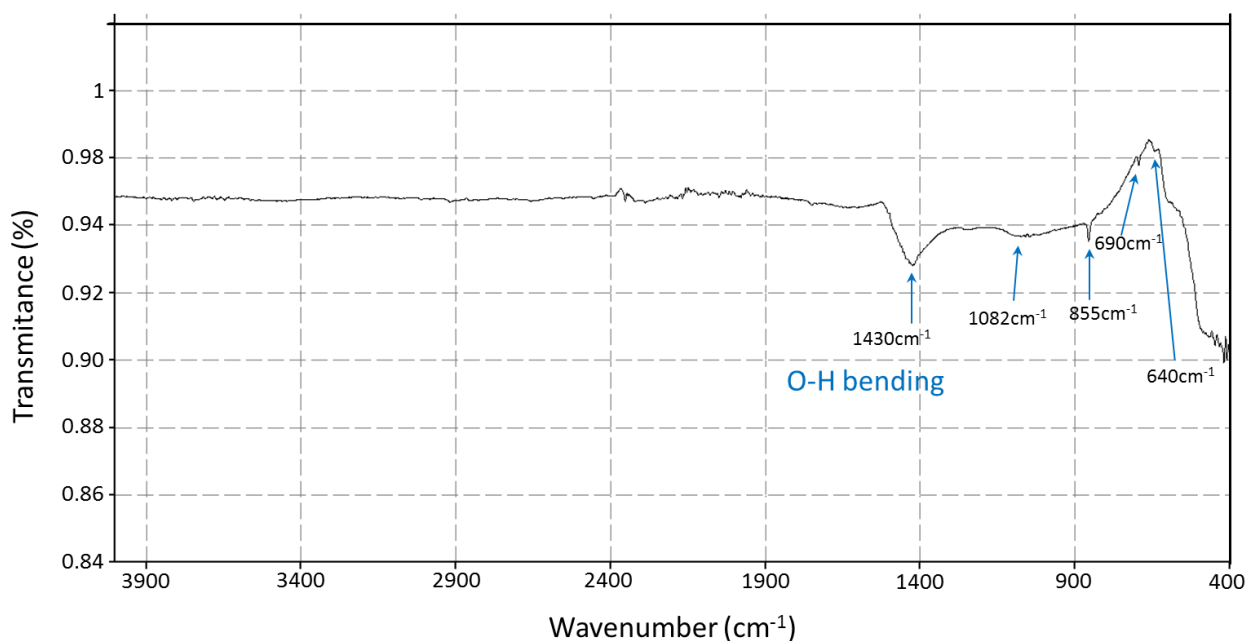


Figure S- 4 Infrared spectrum of $\text{Bi}_2\text{BaIO}_4\text{H}$, O-H bending vibration is evidenced at 1430cm^{-1}

Structure description

$\text{Bi}_2\text{BaIO}_4\text{H}$ crystallizes in the orthorhombic $Cmca$ space group with cell parameters of $a=8.6913(5)$ Å, $b=18.6881(9)$ Å and $c=8.8943(5)$ Å. This structure can be described in terms of cationic layers pile up along b -axis and separated by iodide sheets (see figure S-5a). These cationic layers are formed of edge sharing oxo-centered tetrahedra $\text{O1}(\text{Bi}_2\text{Ba}_2)$, $\text{O2}(\text{Bi}_2\text{Ba}_2)$ and $\text{O3}(\text{BiBa}_3)$. These tetrahedra are strongly disordered (see figure S-5b) compared to the cationic layers found for orthorhombic Sillen X1 (figure S-5c). The Bi and Ba cations are slightly shifted from more symmetrical positions. Inside this cationic layer, the O3 atom is bonded to a hydrogen forming hydroxyl groups. It was hard work to localize the H atoms required to get the neutrality from the successive difference Fourier maps. Then they were placed bonded to O3 after calculating the BVS on each atom (see Table S-12).

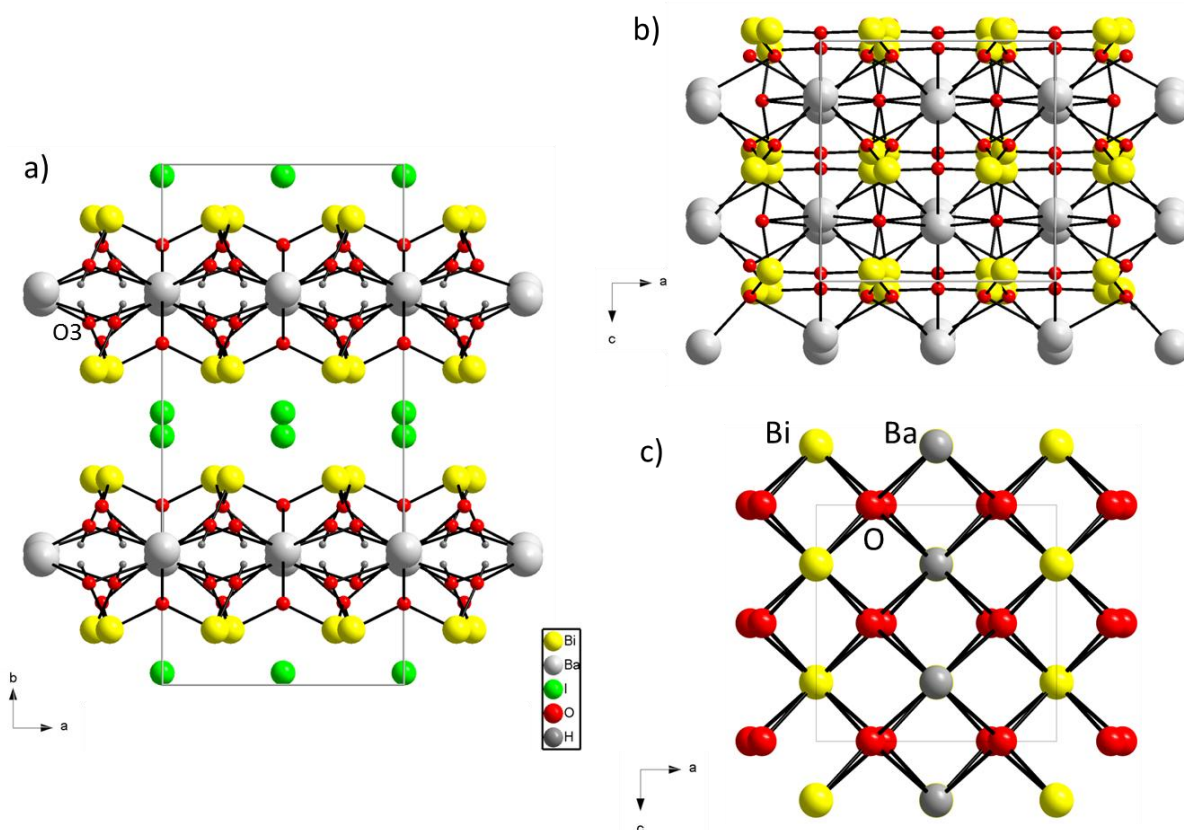


Figure S- 5 a) Representation of $\text{Bi}_2\text{BaIO}_4\text{H}$ crystal structure in (a,b) plane, b) Cationic layer represented in (a,c) plane and c) Cationic layer of the X1 Sillen BaBiO_2Br (S.G. Cmcm) (Chapter V).

The Bi atoms are found seven-coordinated, and have a typical asymmetric environment characterized by the stereo-activity of its lone pair of electrons (figure S-6a and table S-12). On one side, Bi is bonded to three oxygen atoms with bond lengths from 2.0551 to 2.1196Å and on the other side four longer Bi-I bonds are observed going from 3.6571 to 3.8309Å. A bond valence sum of 3.352 is found in that coordination. The Ba atoms are found in an eight-coordinated environment with oxygen (see figure S-6b). Ba-O bonds are comprised between 2.6802 and 3.1236Å giving a bond valence sum for Ba of 1.861. The O3 is bonded to an hydrogen atom forming hydroxyl group (confirmed by IR measurements). To the best of my knowledge, the presence of a hydroxyl group inside the cationic layer of oxyhalides compounds was never observed before. This phenomena is however possible due to the synthesis method while most of the time the oxyhalides are synthesized by solid state reactions. It would be also of interest to do proton solid state NMR measurements to confirm undoubtedly the presence of H elements.

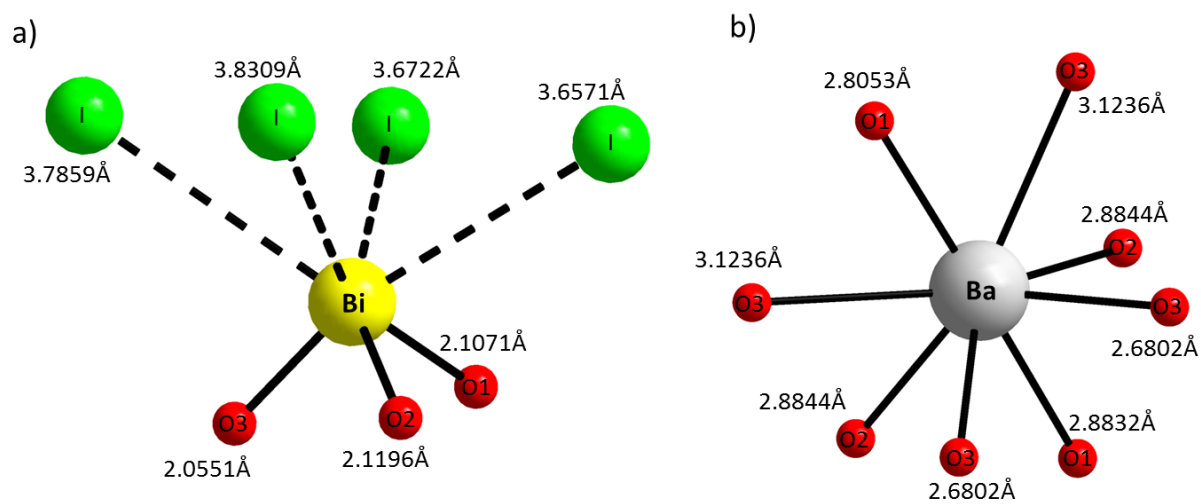


Figure S- 6 a) Coordination of the Bi and b) Ba atoms.

Table S-9. Crystal data, measurement and refinement parameters for $\text{Bi}_2\text{BaIO}_4\text{H}$.

$\text{Bi}_2\text{BaIO}_4\text{H}$	
Crystal data	
Crystal symmetry	Orthorhombic
Space group	<i>C mca</i>
a (Å)	8.6913 (5)
b (Å)	18.6881(9)
c (Å)	8.8943(5)
V (Å ³)	1444.65(14)
Z	8
Dx (g/cm ³)	6.8688
(mm ⁻¹) (0.7107Å)	58.21
Appearance	Yellow needle
Crystal size (mm)	0.23 x 0.08 x 0.052
Data collection	
λ (Mo K α) (Å)	0.71073
Scan mode	ω and φ
θ (min-max)(°)	2.18 – 42.3
R(int) (%)	5.52
	$-16 \leq h \leq 13$
Reciprocal space recording	$-30 \leq k \leq 34$
	$-16 \leq l \leq 16$
Refinement	
Meas., obs./indep.all	17919,
(obs= $I > 3\sigma(I)$)	2679/2150
No. of Refined parameters	43
Refinement method	F
R1(F ²)(obs) / R1(F ²)(all) (%)	4.03 / 5.26
wR2(F ²)(obs) / wR2(F ²)(all) (%)	4.35 / 4.48
GOF(obs) / GOF(all)	1.94 / 1.79
$\Delta\rho_{\text{max}} / \Delta\rho_{\text{min}}$ (e Å ⁻³)	2.80 / -3.07
Extinction coefficient	182 (19)

Table S-10. Fractional atomic coordinates and equivalent isotropic displacement parameters of $\text{Bi}_2\text{BaIO}_4\text{H}$.

Atom	Wyckoff	S.O.F.	<i>x</i>	<i>y</i>	<i>z</i>	U _{eq} (Å ²)
Bi	16g	1	0.21718(2)	0.10554(1)	0.04039(2)	0.00925(5)
Ba	8f	1	1/2	0.24185(2)	-0.27420(5)	0.00992(10)
I	8f	1	0	0.47754(3)	0.23225(6)	0.01612(13)
O1	8e	1	0	0.1555(3)	0.0322(6)	0.0105(12)
O2	8e	1	¼	0.1573(3)	¼	0.0151(15)
O3	16g	1	0.8029(5)	0.8049(3)	0.4357(5)	0.0203(12)
H	16g	0.5	0.83704	0.76913	0.39395	0.0243

Table S-11. Atomic displacement parameters (Å²) for $\text{Bi}_2\text{BaIO}_4\text{H}$.

	U11	U22	U33	U12	U13	U23
Bi	0.01144(9)	0.00585(8)	0.01046(9)	0.00222(5)	-0.00081(6)	-0.00204(6)
Ba	0.01237(17)	0.00984(17)	0.00754(16)	0.00000	0.00000	-0.00257(13)
I	0.0184(2)	0.0168(2)	0.0132(2)	0.00000	0.00000	-0.00020(17)
O1	0.010(2)	0.007(2)	0.014 (2)	0.00000	0.00000	-0.0005(17)
O2	0.024(3)	0.012(3)	0.010(2)	0.00000	-0.008(2)	0.00000
O3	0.027(2)	0.0097(18)	0.024(2)	0.0048(16)	0.0165(18)	-0.0017(16)

Table S-12. Selected bond distances for $\text{Bi}_2\text{BaIO}_4\text{H}$ and bond valence sum for each atoms.

Bond	Distance (Å)	Bond	Distance (Å)	Atom	BVS
Bi-O3	2.0551(52)	2x Ba-O3	2.6802(46)	Bi	3.352
Bi-O1	2.1071(25)	Ba-O1	2.8053(54)	Ba	1.861
Bi-O2	2.1196(26)	Ba-O1	2.8832(55)	I	0.6885
Bi-I	3.6571(5)	2x Ba-O2	2.8844(37)	O1	2.2374
Bi-I	3.6722(5)	2x Ba-O3	3.1236(45)	O2	2.262
Bi-I	3.7859(5)	Bi-Bi	3.7721(3)	O3/ O3 without H	2.003
				bonding	/1.615
Bi-I	3.8309(5)	O3-H	0.8202(52)	H	0.765

Reference

- [1] *SAINT: Area-Detector Integration Software*; Siemens Industrial Automation, Inc.: Madison, **1996**.
- [2] *SADABS: Area-Detector Absorption Correction*; Siemens Industrial Automation, Inc.: Madison, **1995**.
- [3] Petricek, V.; Dusek, M.; Palatinus, L., *JANA2006. Structure Determination Software Programs*, Institute of Physics, Praha, Czech Republic, **2006**.
- [4] Ketatni, M.; Abraham, F.; Mentre, O., *Solid State Sciences*, **1999**, *1*, 449.
- [5] Ketatni, E.M.; Memari, B.; Abraham, F.; Mentre, O., *J. Solid State Chem.*, **2000**, *153*, 48.
- [6] Charkin, D.O.; Berdonosov, P.S.; Dolgikh, V.A.; Lightfoot, P., *J. Solid State Chem.*, **2003**, *175*, 316.
- [7] Shimanouchi, T., *J.Phys. Chem.*, **1977**, *6*, 993.

+33 636 735 115

jakub.olchowka@ed.univ-lille1.fr

Date of birth: 17/08/1988

Marriage status: single

French citizen

Jacob OLCHOWKA

EXPERIENCE

Since October 2012: Common Ph.D. project in academic research laboratories under the supervision of Prof. C. WICKLEDER, Prof. Dr. O. MENTRE, and Dr. M. COLMONT (defense planned the 29th of October 2015); UCCS, University of Lille1, France and Anorganische Chemie II, University of Siegen, Germany

“New Rare-Earth free photoluminescent materials”

Feb - Jul 2012: 6 month internship under the supervision of Prof. Dr. T. LOISEAU; *University of Lille1, France*

“Study of metallic and organic precursor influence on uranyl reduction”

Apr - Jul 2011: 3 month internship in industry; Esterra, Lille, France

“Study of the water treatment”

EDUCATION

2010-2012: **Master degree (with honors): Chemistry, Energy and Environment**
University of Lille1 – France

2006-2010: **Bachelor of Science in physics/ chemistry**
University of Lille1 – France

SKILLS

Areas of research: Crystallography, luminescence, solid state chemistry, DFT calculations, Actinide chemistry

Synthesis methods: Hydrothermal and solvothermal synthesis
Solid state and sol-gel synthesis
Air-sensitive synthesis (glove-box)

Analytical: Expert in XRD (structure determination - single crystal and powder X-ray diffraction)
Expert in Luminescence (measurement and interpretation, decay time, quantum yield) Very good knowledge UV-Visible and IR spectroscopies, Thermal analysis (TGA-DTA)
Good knowledge in first principle calculations (DFT using VASP)

Computer: Crystallographic software (APEX2, JANA2006, EVA, Wingx, Fullprof) Spectroscopic software (Spectrum, Origin)

Linguistic: French: mother tongue
Polish: mother tongue
English: very good knowledge
Spanish: basic communication skills
German: basic communication skills

Teaching experience: Teacher Assistant at the National Graduate School of Engineering Chemistry of Lille- 160 hours of practical courses of analytical chemistry and mineral chemistry for chemical engineers, supervisor of Master student during their internship.

PUBLICATIONS

- 1- Lü, M., Aliev, A., Olchowka, J., Colmont, M., Huve, M., Wickleder, C., Mentre, O. «Multi-dimensional open-frameworks: Combinations of 1D-channels and 2D-layers in novel Bi/M oxo-chlorides» *Inorg. Chem.*, **2014**, *14*, 528-536.
- 2- Aliev, A., Olchowka, J., Colmont, M., Capoen E., Wickleder C., Mentre O. «New [PbBi₂O₄][Bi₂O₂]Cl₂ and [Pb_nBi_{10-n}O₁₃][Bi₂O₂]_(n)Cl_{4+n} Series by Association of Sizable Subunits: Relationship with Arppe's Compound Bi₂₄O₃₁Cl₁₀ and Luminescence Properties» *Inorg. Chem.*, **2013**, *52*, 8427-8435.
- 3- Olchowka, J.; Volkringer, C.; Henry, N., Loiseau T. « Crystal structures of tetravalent uranium fluorides obtained in the presence of hydrazine from uranyl source » *J. Fluorine Chem.*, **2014**, *159*, 1-7.
- 4- Olchowka, J., Volkringer, C., Henry, N., Loiseau, T. « Synthesis, Structural Characterization, and Dehydration Analysis of Uranyl Zinc Mellitate, (UO₂)/Zn(H₂O)₄(H₂mel)center dot 2H₂O» *Eur. J. Inorg. Chem.*, **2013**, *12*, 2109-2114.
- 5- Olchowka, J., Falaise, C., Volkringer, C., Loiseau T. « Structural Observations of Heterometallic Uranyl Copper(II) Carboxylates and Their Solid-State Topotactic Transformation upon Dehydration» *Chem. Eur. J.*, **2013**, *19*, 2012-2022.

CONFERENCE CONTRIBUTIONS

Oral communications:

- 1- Olchowka, J.; Colmont, M.; Kabbour, H.; Wickleder, C.; Mentré, O. « *Relations structure/luminescence in bismuth based compounds* » Oral, EMRS Spring Meeting, (2015), Lille, France.
- 2- Olchowka, J.; Colmont, M.; Kabbour, H.; Wickleder, C.; Mentré, O. « *Relations structure/luminescence dans les oxyphosphates de Bismuth* » Oral, Matériaux 2014, (2014), Montpellier, France.
- 3- Olchowka, J.; Colmont, M.; Wickleder, C.; Mentré, O. « *Luminescent Rare Earth-Free Bismuth Oxyphosphates* » Oral, ECSSC14, (2013), Bordeaux, France.
- 4- Olchowka, J.; Henry, N.; Volkringer, C.; Loiseau, T. « *Etude de l'influence de précurseurs métalliques et organiques pour la réduction de l'uranyle UO₂²⁺* » Oral, JOENJC, (2012), Lille, France.

Posters:

- 1- Olchowka, J.; Colmont, M.; Mentré, O. Wickleder, C. «*Relation structure/optical properties of Bi³⁺ based compounds*» Poster, IKSS15 (2014), Krutyn, Poland
- 2- Olchowka, J.; Colmont, M.; Mentré, O. Wickleder, C.; « *Tailoring the Optical Properties of Bi³⁺ Ions* » Poster, IKSS14 (2013), Krutyn, Poland.

Workshops/Summer Schools

- 1- FluoroFest Horiba 2015, Workshop, (2015), Starnberg (Munich), Germany.
- 2- Summer School, Lanthanide-based photonic materials and structures/ breakthrough applications and cutting edge systems (IKSS16) (2014), Krutyn, Poland

- 3- Summer School, Optical Lanthanide Materials: New Horizons by Tailored Designs (IKSS14), (2013), Krutyn, Poland
- 4- Winter School, Formation PTRX (Crystallography), (2012), Lille, France